

**CHARACTERIZING PLASTIC DEFORMATION MECHANISMS IN
METAL THIN FILMS USING *IN SITU* TRANSMISSION
ELECTRON MICROSCOPY NANOMECHANICS**

A Dissertation
Presented to
The Academic Faculty

by

Sandra Stangebye

In Partial Fulfillment
of the Requirements for the Degree
Doctor of Philosophy in
Materials Science and Engineering
School of Materials Science and Engineering

Georgia Institute of Technology
May 2023

COPYRIGHT © 2023 BY SANDRA STANGEBYE

**CHARACTERIZING PLASTIC DEFORMATION MECHANISMS IN
METAL THIN FILMS USING *IN SITU* TRANSMISSION
ELECTRON MICROSCOPY NANOMECHANICS**

Approved by:

Dr. Josh Kacher, Co-Advisor
School of Materials Science and
Engineering
Georgia Institute of Technology

Dr. Olivier N. Pierron, Co-Advisor
George W. Woodruff School of
Mechanical Engineering
Georgia Institute of Technology

Dr. Ting Zhu
George W. Woodruff School of
Mechanical Engineering
Georgia Institute of Technology

Dr. Hamid Garmestani
School of Materials Science
and Engineering
Georgia Institute of Technology

Dr. Naresh Thadhani
School of Materials Science and
Engineering
Georgia Institute of Technology

Date Approved: March 10, 2023

To all the hardworking women in STEM who paved the path before me

ACKNOWLEDGEMENTS

I would like to begin by expressing my sincere gratitude to my advisors, Dr. Josh Kacher and Dr. Olivier Pierron, for their invaluable mentorship and support throughout my graduate years. Their insightful feedback and weekly encouragements have been instrumental in shaping me into the scientist I am today. Their excitement for science made it easy to look forward to the next experiment and truly made earning this PhD enjoyable. I will carry this excitement and valuable experience forward with me throughout my career.

I would also like to thank my collaborators for their contributions to the work covered in this thesis. Thank you to Dr. Ting Zhu, Dr. Yin Zhang, Dr. Xing Lui, and Kunqing Ding for the modeling work done to complement the experimental work. I would also like to thank Dr. Khalid Hattar and Dr. Eric Lang from Sandia National Laboratories for their help on irradiating specimens and interpreting the exciting results, as well as providing a fruitful experience at Sandia during my research practicum. I would like to especially thank Dr. Yong Ding for his continual support operating the FEI Tecnai F30 TEM at Georgia Tech. His dedication and approachability were instrumental in helping me obtain great *in situ* TEM results.

I am also grateful to the additional members on my PhD committee, Dr. Naresh Thadhani and Dr. Hamid Garmestani for their guidance and support on this thesis work. I would also like to thank my past and current lab mates, Dr. Alejandro Barrios, Dr. Gabe Cahn, Dr. Katie Koube, Dr. Jahnavi Dasai, Dr. Sarah Lombardo and Lina Daza Llanos for providing support throughout the years. I would like to especially thank Dr. Saurabh Gupta for the guidance and mentorship during my first year at Georgia Tech.

Additionally, this endeavor would not have been possible without the generous support of the Department of Energy National Nuclear Security Administration Stewardship Science Graduate Fellowship (DOE NNSA SSGF). I am very fortunate to have been a part of the community of graduate students and scientists and look forward to continued collaborations.

Finally, I am extremely grateful for the love and support received from my family. I would like to especially thank my parents, Lars and Jenny, for providing me with the confidence and opportunity to pursue my dreams. I would also like to thank my closest friends for providing a healthy distraction from research and for the constant encouragement.

TABLE OF CONTENTS

ACKNOWLEDGEMENTS	iv
LIST OF TABLES	ix
LIST OF FIGURES	x
LIST OF SYMBOLS AND ABBREVIATIONS	xxi
SUMMARY	xxiv
CHAPTER 1. Background and Motivation	1
1.1 Introduction	1
1.2 Mechanical Properties of NC and UFG Metal Thin Films	2
1.2.1 Yield Strength	3
1.2.2 Ductility	6
1.2.3 Strain Rate Sensitivity	7
1.2.4 Strain Hardening	9
1.2.5 Strategies for Obtaining Optimal Mechanical Properties	9
1.3 Deformation Mechanisms	11
1.3.1 Dislocation-Based Mechanisms	12
1.3.2 Grain Boundary Sliding	13
1.3.3 Grain Rotation	14
1.3.4 Stress-Assisted Grain Boundary Migration	15
1.4 Activation Volume	16
1.4.1 Theory	16
1.4.2 Activation Volume Values for NC and UFG Metals	18
1.4.3 Conrad's Model	21
1.5 Grain Boundary Kinetics	23
1.5.1 Grain Boundary Migration Driving Force	24
1.5.2 Grain Boundary Mobility	26
1.5.3 Disconnections	29
1.5.4 Influence of Triple Junctions	33
1.6 Radiation-Induced Changes	36
1.6.1 Radiation Tolerance in NC and UFG Metals	37
1.7 Motivation and Thesis Objectives	38
CHAPTER 2. Experimental Methods	41
2.1 Overview	41
2.2 <i>In Situ</i> MEMS-Based Technique	41
2.2.1 MEMS Geometry and Capacitive Sensing	41
2.2.2 Stress and Strain Calculation	43
2.2.3 Experimentally Measuring Activation Volume	45

2.2.4	MEMS-Device Limitations	47
2.3	Updated MEMS-design: Imaged-Based Sensing	50
2.3.1	Comparing Data from Electrical- and Imaged-based Sensing Techniques	54
2.4	Specimen Fabrication and Manipulation	57
2.5	Specimen Irradiation	58
2.6	Characterization	59
2.6.1	Transmission Electron Microscopy	59
2.6.2	Scanning Electron Microscopy	60
CHAPTER 3.	Investigating Electron Beam Effects on <i>in situ</i> TEM Experiments	61
3.1	Overview	61
3.2	Common Electron Beam Effects	61
3.3	Electron Beam Influence on Deformation of Metal Thin Films	63
3.3.1	Electron Beam Effects in NC Al	63
3.3.2	Electron Beam Effects in UFG Au	75
3.4	Discussion	78
3.5	Conclusion	85
CHAPTER 4.	Plastic Deformation Mechanisms in Aluminum	87
4.1	Overview	87
4.2	Initial Microstructure	87
4.3	Monotonic Response	88
4.4	<i>In Situ</i> TEM Observation of Deformation Mechanisms	90
4.4.1	200 nm-thick NC Al	90
4.4.2	100 nm-thick NC Al	99
4.5	<i>In Situ</i> TEM Activation Volume Measurements	102
4.5.1	200 nm-thick NC Al	102
4.5.2	100 nm-thick NC Al	104
4.6	Discussion	105
4.7	Conclusion	108
CHAPTER 5.	Plastic Deformation Mechanisms in Gold	110
5.1	Overview	110
5.2	Initial Microstructure	110
5.3	Monotonic Response	113
5.4	<i>In Situ</i> TEM Observation of Deformation Mechanisms	115
5.4.1	As-deposited UFG Au	115
5.4.2	Annealed UFG Au	119
5.5	<i>In Situ</i> TEM Activation Volume Measurements	123
5.5.1	As-deposited UFG Au	123
5.5.2	Annealed UFG Au	130
5.6	Discussion	135
5.7	Conclusion	137
CHAPTER 6.	Stress-Induced Grain Boundary Migration	138
6.1	Introduction	138
6.2	Documenting Grain Boundary Migration	138

6.3	Comparing Initial Microstructure	138
6.4	Grain Boundary Migration in As-deposited Gold	140
6.5	Grain Boundary Migration in Annealed Gold	147
6.5.1	Microstructural Features	151
6.6	Discussion	156
6.7	Conclusion	163
 CHAPTER 7. Stress-Assisted Self-Healing of Radiation Damage in Ultrafine-Grained Metal Thin Films		 164
7.1	Overview	164
7.2	Initial Microstructure	164
7.2.1	Defect Spacing Measurement	166
7.3	Mechanical Properties	167
7.4	Deformation Mechanisms	168
7.4.1	Dislocation-Based	168
7.4.2	Grain Boundary-Based	170
7.5	<i>In Situ</i> TEM Measurements of Activation Volume	178
7.6	Discussion	183
7.7	Conclusion	187
 CHAPTER 8. Interpretation of Measured Activation Volume		 188
8.1	Overview	188
8.2	Summary of All Activation Volume Values	188
8.2.1	Gold	188
8.2.2	Aluminium	192
8.3	Relating Experimentally Measured V^* to Deformation Mechanisms	194
8.3.1	Atomistic Modeling	195
8.4	Discussion	199
8.4.1	General Trends in Activation Volume	201
8.5	Conclusion	207
 CHAPTER 9. Conclusions		 209
9.1	Recommendation for Future Work	213
 REFERENCES		 216

LIST OF TABLES

Table 1 – Comparison of activation volume V^* measurements reported in literature across different metals with varying grain size (d), thicknesses (t), microstructure, and strain rates.	21
Table 2 – Measurements of MEMS features compared to the nominal dimensions.	54
Table 3 – Detailed description of the fabrication steps and specifications for the thin film fabrication.	57
Table 4 – True activation volume measurements V^* for three different relaxation segments with varying e-beam condition during repeated stress-relaxation experiment for NC Al.	73
Table 5 – Summary of tensile properties determined by <i>in situ</i> monotonic experiments for Al-100 and Al-200.	89
Table 6 – Summary of activation volume values and contributing components (strain rate ratio and reloading stress) for 3 of the relaxations in Figure 37.	104
Table 7 – <i>In situ</i> monotonic tensile properties for as-deposited, A350, and A700 UFG Au specimens.	114
Table 8 – Parameters used in estimating defect spacing.	167
Table 9 – Average strain rate sensitivity values determined using V^* for all UFG Au specimens.	191
Table 10 – Summary of all True V^* values for the as-deposited, annealed (A350 and A700), and irradiated UFG Au and NC Al specimens.	194
Table 11 – A summary of V^* values calculated from the FENEB models for different deformation mechanism.	199

LIST OF FIGURES

Figure 1 – Schematic of dislocation pile-up at a GB [8].	4
Figure 2 – Compiled yield stress vs. % elongation of different (a) NC metals and (b) ufg metals [10,29].	6
Figure 3 – Deformation mechanism map for FCC metals across different grain sizes from [69]. Strength curve is based on copper.	12
Figure 4 – Grain boundary sliding and its basic accommodation mechanisms in nanograined materials (from [77]). (a) NC UFG specimen under tensile load. Magnified insets (b-i) illustrating local accommodation mechanisms. (b-e) Accommodation through transformation of defects (GB dislocations and disconnections) at TJs and local migration of GB. (f-g) Accommodation through GB dislocation/disconnection pile up at TJ leading to emission of lattice dislocation in adjacent grain. (i-h) Accommodation through diffusion-controlled rotational deformation.....	14
Figure 5 – Grain size dependence of reciprocal activation volume V^* calculations for Ni and Cu [96].	23
Figure 6 – Schematic of strain energy density driving force that leads to grain coarsening [102]. Diagrams in (a) and (b) show the unstrained and strained free energy state for grains G1, G2 and G3 (all grains have different grain sizes). When a load is applied, the energy density increases by the increase in strain energy density, which varies across the different grain sizes due to size-dependent yielding (c).	25
Figure 7 – Schematic diagram of (a) pure tilt grain boundary where the axis of rotation is parallel to the grain boundary plane, (b) pure twist grain boundary (axis of rotation is perpendicular to grain boundary plane), (c) coherent boundary and (d) incoherent boundary (a-b) taken from [103] and (c-d) taken from [104].	27
Figure 8 – Mobility as a function of (a) disorientation angle and (b) Σ value for Ni at 1400K for all 388 boundaries simulated [99].	29
Figure 9 – (a) A bicrystal GB containing a disconnection dipole, (b) Schematic of a nucleated disconnection dipole, (c) quantized disconnection formation energy for $\Sigma 5$, $\Sigma 13$, $\Sigma 37$ grain boundaries [97].	30
Figure 10 – (a) 1D representation of TJ structure where γ is the line tension for each GB and θ is the angle between GBs [104], (b) 3D geometry of a TJ where the three GBs ($GB^{(1)}$, $GB^{(2)}$, and $GB^{(3)}$) meet along line direction ξ . $J^{(1)-(3)}$ are disconnection fluxes from the three GBs to TJ [98].	34
Figure 11 – Effect of neutron irradiation (3 dpa) on the engineering stress-strain curve for annealed 316LN austenitic steel [124,130].	37
Figure 12 – MEMS device tensile testing operation. (a) SEM image of the MEMS device with the thermal actuator (TA), capacitive sensor one (CS1), capacitive sensor two (CS2), and the load sensor (LS) beams labeled. The specimen gap (SG) is outlined in magenta and shown at a higher magnification in (b). (b) SEM image of a specimen on MEMS device	

	clamped with glue. (c) Schematic of the MEMS device showing the key components.	42
Figure 13	– Physical drift in XA during a paused segment (constant Vin). (a) Full XA data for the Vin loading scheme. The loading was paused at (b) Vin = 3V and (c) Vin = 6V . In both cases, XA increases during the paused segment by the amount represented with the red double-arrow.	49
Figure 14	– SEM images of image-based MEMS device. (a) Full device with the thermal actuator (TA), SiO ₂ bridge (SiO₂ B), stationary beam (SB), and load sensor (LS) labeled. The specimen gap is outlined and shown in more detail in (b). The displacement of the actuator XA and load sensor XLS are indicated. (c) schematic of the MEMS operation.	51
Figure 15	– <i>In situ</i> operation of image-based MEMS during monotonic tensile test. The stationary beam is labeled and remains in the same position. (b)-(d) images captured throughout the experiments. The time stamp, far-field stress levels, nominal and local strain are provided. The local strain is estimated by measuring the distance between the two indicated edge features. (d) XA and XLS are indicated.	53
Figure 16	– Comparing electrical- and image-based sensing results under monotonic loading conditions for an UFG Au specimen.	55
Figure 17	– Comparing electrical- and image-based sensing results during stress-relaxation experiment. (a) Stress vs. time data for full experiment until specimen failure, (b)-(d) individual relaxation segments. The solid lines are logarithmic fits of the corresponding datasets.	56
Figure 18	– Specimen geometry. (a) Schematic of the specimen with nominal dimensions labeled, (b) SEM image of the released specimens.	58
Figure 19	– SRIM-estimated damage profile (black) and Au implantation profile (red) for 100 nm-thick Au film irradiated with 2.8 MeV Au ions. Shaded area in the plot indicates the thickness of the Au film, offering a visual guide. Average dpa in the film is ~0.65 dpa and peak implantation level is 30 appm.	59
Figure 20	– Behavior of NC Al under monotonic testing for 5 different specimens tested under different beam condition and strain rates. (a) The strain rates for each specimen are: (#1) 1.2 × 10⁻⁴ s⁻¹ , (#2) 6 × 10⁻⁴ s⁻¹ , (#3) 1.8 × 10⁻⁴ s⁻¹ , (#4) 1.5 × 10⁻⁵ s⁻¹ , (#5) 2.7 × 10⁻⁴ s⁻¹ . (b-g) Bright-field TEM micrographs of the fracture surfaces with the white numbers assigning the micrograph to the corresponding curve on (a). (e) Bright-field and (f) dark-field TEM micrographs of a fracture surface for a specimen tested in beam-off condition with a strain rate of 1.5 × 10⁻⁵ s⁻¹ which exhibit large grains within the necked region, closely resembling that of (g). (b-g) are all taken at the same magnification.	65
Figure 21	– Monotonic deformation of NC Al under alternating beam-off and -on conditions for TEM accelerating voltages of 300 and 80 kV. Stress-strain behavior during a monotonic test with alternating beam-on (grey) and -off (green) conditions every 30 seconds for experiments conducted during (a) 300 kV and (b) 80 kV TEM accelerating voltage.	

Accumulated plastic strain throughout the experiment showing an increase in plastic strain rate during beam-on conditions for (c) 300 kV and (d) 80 kV accelerating voltages. (e,f) Bright-field TEM images showing the (e) initial microstructure and (f) final microstructure of the specimen. The black box in (e) outlines the region of the specimen exposed to the e-beam during beam-on conditions.....	68
Figure 22 – Behavior of NC Al during a multiple stress-relaxation experiment with alternating beam on- and -off condition. (a) Stress-strain curve with 20 total segments of paused loading (for stress-relaxation) of length 30-60 seconds alternating between beam-on (grey) and beam-off (green) conditions until specimen failure. (b,c) Stress-strain data scaled to show (b) the first four and (c) the last five segments of paused loading in detail. Grey diamonds correspond to the beam-on relaxation data while green diamonds are the beam-off relaxation data. (d) The stress-relaxation data for the first four relaxation segments. The first two occur during beam-on condition with substantial stress-relaxation. The second two (green) segments occur during beam-off condition with negligible stress-relaxation. (e) Stress-relaxation data for the last five relaxation segments where the first two occur during the beam-on condition and the last three occur during beam-off condition. All segments are fitted with a logarithmic fit with R^2 values shown.	71
Figure 23 – True activation volume V^* measurements for NC Al specimens tested under beam-off (green squares) and beam-on (grey circles) conditions. The open square data points correspond to the activation volume measurements shown in Table 2 and Figure 12(c) and (e).	74
Figure 24 – Stress-strain response during monotonic testing of UFG Au specimen with alternative beam-on and beam-off conditions with a TEM e-beam accelerating voltage of (a) 300 kV and (b) 80 kV. Accumulated plastic strain during the experiments conducted at TEM accelerating voltages of (c) 300 kV and (d) 80 kV. The strain rates for (a) and (b) are 1.4×10^{-4} and $1.1 \times 10^{-4} \text{ s}^{-1}$, respectively.	76
Figure 25 – TEM micrographs of the microstructural evolution of a UFG Au specimen tested under monotonic loading with alternating beam-on and beam-off conditions every 30 seconds. (a) Initial microstructure with black box indicating region of specimen that was repeatedly exposed to the e-beam. (b) Final microstructure after failure.	77
Figure 26 – True activation volume V^* measurements from different UFG Au specimens and relaxation segments for <i>ex situ</i> /beam-off (red squares) and <i>in situ</i> /beam-on (grey circles) conditions.	78
Figure 27 – Initial microstructure of the NC Al specimens. BF TEM images of (a) 200 and (b) 100-nm thick specimens. (c) PED map of a 200 nm-thick specimen indicating a random out-of-plane texture. (d) grain size distribution of the 200 nm-thick (gray) and 100 nm-thick (green) specimens with the weighted average indicated by dashed line.	88
Figure 28 – <i>In situ</i> monotonic tensile curves for Al-100 (green) and Al-200 (gray) specimens tested at $\dot{\epsilon} \sim 1 - 3 \times 10^{-4} \text{ s}^{-1}$	89

Figure 29 – Bright-field TEM images showing the microstructure evolution of a 200-nm-thick Al microspecimen under uniaxial load (direction of applied load indicated by red arrows). The frames taken at (a) 0%, (b) 4.7%, (c) 8.5%, (d) 12.1% and (e) 14.4% strain [176].	91
Figure 30 – Low magnification TEM images showing microstructure evolution at different strain values [120]. The frames are taken at (a) 1.9%, (b) 4.9%, (c) 10%, (d) 14.5%, (d) 16.5% and (f) 18.7% total strain. Arrowhead in each designating the same feature. (g) Engineering stress-strain curve with the total strain of (a-f) indicated by the colored squares [176].	92
Figure 31 – GBM during uniform deformation. (a) Low magnification TEM image showing no neck developed. Circle indicates location of grain marked by arrow in (b-c). (b) and (c) are digitally magnified snapshots taken 34 seconds apart during the highlighted portion in the stress-strain curve (d).	94
Figure 32 – Fast GBM after neck develops. (a) Low magnification TEM image showing developed neck near top of snapshot. White circle indicates location of highlighted grain in (b-d). (e) Stress-strain curve with highlighted region corresponding to when snapshots (a-d) were recorded. Change in grain size as a function of time for (f,g) a grain in uniform region and (h,i) necked region (from b-d).	95
Figure 33 – (a) Cumulative area fraction grain size plots for different strain values post neck formation compared to the initial microstructure (red data). Data with circle markers and solid lines are taken from grains within the uniform region while data with triangle markers and dashed lines are from grains within the necked region. (b) Low magnification TEM micrograph designating regions defined as ‘Necked’ (in between white lines) and the remaining ‘Uniform’ region.	97
Figure 34 – Rapid GB motion ahead of crack tip. (a) the beginning of recorded segment. (b) $t = 63.2\text{s}$, slight grain growth. (c) $t = 63.8\text{ s}$. Top boundary migrated 3.6 nm in the 0.6s separating (b) and (c) resulting in migration speed of 6 nm s^{-1} . (d) $t = 95\text{ s}$, final grain structure prior to failure [176].	98
Figure 35 – Post-mortem TEM analysis of fracture surface (a) multiple large grains near fracture surface, (b-e) enlarged dark-field TEM images of highlighted grains with evidence of dislocation structures indicated by arrowheads [176].	99
Figure 36 – <i>In situ</i> TEM observations of deformation of Al-100 during tensile loading. BF TEM images of the gauge length (a) prior to an applied load, (b) while straining, and (c) after failure. Microstructure after failure in the region of (d) ‘uniform’ (far from necked region) and (e) near the necked/fracture surface. (f) grain size distribution in terms of cumulative area fraction for the pre-strain state (gray), region far from neck (blue), and necked/fractured (green).	100
Figure 37 - <i>In situ</i> measurement of activation volume in Al-200 NC Al. (a) The full stress-strain curve until the specimen was unloaded. Gaps in the data	

	correspond to stress-relaxation segments which are shown in (b). The measured (c) true and (d) apparent activation volumes values.....	103
Figure 38	– <i>In situ</i> repeated stress-relaxation experiment and activation volume measurements for Al-100 specimen. Full (a) stress-strain and (b) stress-time (relaxation) data for the experiment, (c) true and (d) apparent activation volume values determined from the relaxations in (b) with $R2 > 0.9$	105
Figure 39	– Initial microstructure of UFG Au specimens. Bright-field TEM images of (a) as-deposited and specimens that have been annealed at (b) 350°C (30 minutes) and (c) 700°C (5 minutes) with corresponding orientation maps for (a) and (b) in (d) and (e), respectively. The legend for the orientation and GB orientation is provided to the right. (f) Grain size distribution for each shown in terms of cumulative area fraction and (g) GB misorientation distribution from (d) and (e).....	112
Figure 40	– <i>In situ</i> monotonic tensile curves for as-deposited (red), A350 (blue), and A700 (green) tested under similar strain rates.	114
Figure 41	– Emission of leading and trailing partial dislocation from a GB during a stress relaxation segment. Arrowhead in (a) indicates the stacking fault region between leading and trailing partial dislocation. (b) Trailing partial is emitted and perfect dislocation transverses the grain. (c) Arrow indicates direction of dislocation glide leading to pileup at the nearby GB [92].	115
Figure 42	– Dislocation cross-slip resulting in a transition from transgranular to intergranular dislocation glide. Arrowhead in each frame tracks a single dislocation. (a) Dislocation is emitted from GB and glides transgranular in direction indicated by arrow. (b)-(c) transgranular dislocation glide. (d) dislocation cross-slips onto GB and subsequently glides on GB in direction indicated by arrow. Experimental time is given in each frame [92]......	116
Figure 43	– TEM micrograph of dislocations on multiple slip systems during late stage deformation [92].	117
Figure 44	– Sequence of snapshots taken from a TEM video recording documenting separate instances of nearby GBM. (a) – (d) Grain G1 expands and makes contact with G5, (e) the progression of boundary migration in direction of the arrow from (a) to (d). (f) – (i) Grain G2 expands via progression shown in (j) while G3 shrinks. Time stamps are given on each snapshot.	119
Figure 45	– Dislocation emission, pile-up, and absorption in A350 UFG Au specimen. Dislocations are emitted from GB ₁ and glide in the direction of white arrow. Black arrowhead tracks the same dislocation until it is absorbed by GB ₂ . Progression of the dislocation emission/absorption after (b) 17s, (c) 33s, (d) 40s, and (e) 82s. Given time is in terms of elapsed time since first frame of the video (a).The grain marked by the star in (a) is removed during this process.	121
Figure 46	– GBM and dislocation glide active during <i>in situ</i> TEM straining of A700 Au specimens. The GB marked by the white arrowhead in (a) undergoes	

stress-induced GBM through the progression of images. The white arrow marks the initial location of the GB in each frame. Dislocations glide is denoted by black arrowheads in (b) and (d). Time is provided in terms of seconds since first frame of the sequence.....	122
Figure 47 - <i>In situ</i> measurement of activation volume in as-deposited UFG Au. (a) stress-strain curve with both loading (red) and unloading (grey) data. Gaps in the data correspond to stress-relaxation segments which are shown in (b). The dashed box identifies the region in which the relaxations shown in (c)-(f) occur. The apparent and true activation volume values are printed on each relaxation segment.	125
Figure 48 – <i>In situ</i> measurement of activation volume in as-deposited UFG Au using image-based technique for stress measurements. (a) stress-strain curve constructed from points throughout the experiment and (b) stress-time data for all the relaxations.....	127
Figure 49 – <i>In situ</i> activation volume measurements for as-deposited UFG Au measured using image-based sensing technique. Results are displayed for relaxation number (a) 1, (b), 2, (c) 10, (d) 11, (e) 17, and (f) 18. The displayed apparent and true activation volume values have units of b3	128
Figure 50 – A summary of <i>in situ</i> values of (a) true and (b) apparent activation volume vs. stress for as-deposited UFG Au.....	130
Figure 51 – <i>In situ</i> repeated stress-relaxation experiment on A350 Au specimen. (a) stress-strain curve, (b) stress-time data displaying all the relaxation segments. Relaxation number (c) 15, (d) 16, (e) 18, and (f) 19. Apparent V_a and true V * activation volume values are shown for each relaxation along with the R₂ values corresponding to the fit (solid black line).....	131
Figure 52 – <i>In situ</i> (a) true and (b) apparent activation volume measurements for A350 specimens. The blue data is all the values from the experiment shown in Figure 30 and the gray data is from a purely electrical-based sensing experiment on a separate specimen (stress-strain data not shown).....	132
Figure 53 – <i>In situ</i> repeated stress-relaxation experiment on an A700 specimen. (a) full stress-strain curve, (b) stress-time data for the relaxation segments. Relax # (c) 4, (d) 5, (d) 7, and (f) 8 shown in more detail with the measured apparent and true activation volume values displayed.	134
Figure 54 – <i>In situ</i> (a) true and (b) apparent activation volume values for A700 Au.	135
Figure 55 – TEM images of initial microstructure of (a) as-deposited and (b) annealed Au thin films with corresponding orientation map for each region in (c) and (d), respectively. (e) Area fraction grain size and (f) GB misorientation distribution for the as-deposited (grey) and annealed (orange) films. The average grain size is indicated by the vertical dashed lines and highlights the change in grain size after annealing.....	140
Figure 56 – Stress-induced grain growth and the removal of small grains. BF TEM images of (a) initial microstructure with grain traces outlined. The outlined grain undergoes extensive grain growth in the direction of the red arrows (stress is applied in the vertical direction as indicated). (b)	

microstructure after 31 minutes under a tensile load. The outline represents the final grain size/shape. (c) corresponding orientation map of the region with the initial and final grain outline overlaid. (d)-(f) similar analysis of a second region.	141
Figure 57 – Analysis of the grain growth and shrinkage of a cluster of grains. (a) initial microstructure with GB cluster outlined with certain grains that are constant throughout the transformation identified by letters. Same region with the GB network outlined (b) 16, (c) 31, and (d) 63 minutes after an applied load. The grains are labeled to help identify how the grains have been rearranged. (e) Overlays of the GB network between (a) (dashed) and (b) (solid) with the grains that are removed during the transition highlighted in red. (f) overlay of (b) (dashed) and (c) (solid). (g) overlay of (c) (dashed) and (d) (solid) showing minimal changes for the last 32 minutes of the experiment.	143
Figure 58 – Detailed analysis of grain growth and shrinkage due to mechanical loading. (a) Outlined GB network with grains color coded based on if the grain disappears (red), shrinks (blue), grows (green), or undergoes minimal change (grey) throughout the 63-minute experiment. Grains colored white could not be tracked with confidence so are omitted from the analysis. (b) Distribution of grain sizes that grew (green) vs. disappeared (red-thatched), showing a strong grain size dependence. Out-of-plane orientation for the grains that (c) disappeared, (d) grew, and (e) experienced minimal change are plotted on IPFs, in addition to the in-plane orientation along the vertical loading direction for the grains that (f) disappeared, (g) grew, and (h) experienced minimal changes. The crystal direction for each color is shown in (c).	146
Figure 59 – IPF orientation of all grains in the specimen with grain sizes (a) less than 50 nm and (b) greater than 50 nm.	147
Figure 60 – GBM in A350 Au film. (a) BF TEM image of the initial microstructure with the GB network outlined, (b) same region after 47 minutes under load and specimen failure. The current GB network is outlined. (c) orientation map of the same region. Red arrows indicate direction of GBM and black arrow point to small grains that disappear. (d) overlaid outline from (a) (dashed) and (b) (solid) to show the instances of GBM (red arrows) and grain removal (red highlighted grains).	149
Figure 61 – GBM distances in an annealed specimen during stress-relaxation. The initial GB network is outlined and color coded based off of the migration distance. Color legend is provided on the figure. The white boundaries did not experience measurable migration and the black boundaries could not be confidently identified so are omitted from the analysis. The dashed boundaries are identified as $\Sigma 3$ twin boundaries using the orientation map. Examples of clusters of large migration distances are indicated by arrows.	151
Figure 62 – GB misorientation angle distribution for (a) mobile and (b) immobile GBs during the stress-relaxation experiment. Number fraction is given in terms of the fraction of GBs for a given misorientation angle that are	

	mobile or immobile compared to the total number of GBs that were manually tracked during the experiment. The GB distribution for the full specimen is shown on each with the dashed bars (same distribution is shown in Fig. 1(f)). (c) Distribution of the tracked twin boundaries for both mobile (gray) and immobile (orange) twin boundaries.	153
Figure 63	– GB migration distribution in terms of the GB trace angle for mobile (gray) and immobile (orange) tracked boundaries. The schematic to the right indicates how the GB trace angle is defined with respect to the vertical loading axis for a model grain.	154
Figure 64	– Grain coarsening ability with respect to the initial grain Schmid factor for the grains that grew (green) and shrunk (red). The coarsening ability is defined as the absolute value of the total change in grain size (Δd) divided by the initial grain size (d_0).	155
Figure 65	– GBM behavior in terms of grain size ratio across a given boundary. Grain size ratio defined as the maximum grain size divided by the minimum grain size on either side of a given boundary.	156
Figure 66	– An example of GB network effects where intergranular dislocation glide leads to triple junction migration during stress-relaxation. (a) intergranular dislocation glide on two GBs (direction of both indicated by red arrows). The white arrowhead marks the triple point that undergoes migration throughout the series of TEM images. (b)-(d) continued intergranular dislocation glide resulting in migration of TJ. White arrowhead in (b) marks visible dislocations. (e) schematic of the initial (black) and final (red dashed) trace of the GBs with arrow indicating TJ migration.	162
Figure 67	- Initial microstructure of irradiated UFG Au specimens. TEM micrographs of (a) non-irradiated Au film and (b) irradiated Au film. Most grain interiors contain ‘black-spot’ radiation damage. Scale bar is the same as in (a). (c) BF TEM micrograph of a grain interior of irradiated film to exhibit radiation damage. (d) Cumulative grain size distribution of non-irradiated (black circles) and irradiated (magenta diamonds) films prior to straining. (e) Indexed diffraction pattern of irradiated Au film exhibiting characteristic ring structure for NC and UFG FCC metals.	166
Figure 68	– Monotonic tensile curve for irradiated UFG Au specimen. (a) Stress-strain curves from <i>in situ</i> TEM tensile tests of non-irradiated and irradiated specimens. Both were conducted at a strain rate of $\sim 10^{-4} \text{ s}^{-1}$. TEM micrographs of a (a) non-irradiated and (c) irradiated specimen tested under tension to show the differences in fracture surface.	168
Figure 69	– Radiation defects serving as obstacles to dislocation glide. (a) Grain containing multiple radiation-induced defects with one specific defect indicated by white arrowhead. (b) After 3 seconds, dislocations are emitted from the indicated GB and partially transverse the grain until being pinned by defects. One pinned dislocation (indicated by black arrowhead) is pinned by the defect that is indicated by white arrowhead	

in both (a) and (b) and the leftmost GB. (c) After two additional seconds, the left end of the dislocation (black arrowhead) glides while a portion remains pinned by a defect (white arrowhead). (d) a portion of the dislocation continues to glide until being pinned by an additional defect indicated by the second white arrowhead. 169

Figure 70 – Stress-assisted GB migration leading to radiation damage healing and defect-free regions capable of supporting extensive dislocation glide. (a) Microstructure prior to an applied load with a single grain outlined. (b) GBM has led to grain growth of the outlined grain resulting in defect-free regions where GB migration occurred. The radiation defects remain where the original grain was (no migrating GB passed through this region). Arrows indicate direction of continued GB migration. (c) GB migration continues and leads to a further increase in grain size and defect-free region. Arrow indicates a dislocation pinned on radiation defects. (d) The indicated dislocation becomes de-pinned and glides unrestricted in the radiation-free region until being absorbed by a nearby GB. (e) Continued GB migration leading to an increasing defect-free area. (f) The defect-free region can now support dislocation-dislocation interactions, indicated by both arrowheads. Time stamp in each indicate the total time (in minutes) under a tensile stress (both during loading and stress-relaxation). (g) GB migration distance data for all the involved boundaries during the transition from (c) to (f). The far-field stress values are provided on the secondary axis to demonstrate how migration behavior varies with stress. 172

Figure 71 – “Steady” grain boundary migration documented in irradiated film during repeated stress-relaxation experiment. (a) Microstructure prior to an applied load. The outlined grain is one of the grains tracked throughout the experiment with two migrating boundaries labeled 1 and 2. The red arrows indicate direction of GBM. (b)-(d) the same grain shown in 10-minute increments, (e) final microstructure with the original grain outline from (a) overlaid to show the change in grain size and shape due to GB migration. The scale bar in (a) is the same for all frames. (f) GBM distance data throughout the experiment from six boundaries recorded simultaneously. The instantaneous far-field stress levels are shown with the stress scale on the right y axis. Average velocity (nm/s) is recorded to the right of each curve. Time is given in terms of time since initial recording of the grains, which began 3 minutes after initial load was applied. 174

Figure 72 – “Rapid” stress-induced grain boundary migration in non-irradiated films during a stress-relaxation experiment. (a) Initial microstructure of a collection of grains. The outlined grain undergoes significant grain growth due to GBM in the direction indicated by red arrows. (b)-(c) the same grain in 10-minute increments. (d) Final grain microstructure with original grain outline from (a) overlaid to show the significant stress-induced grain growth. (e) GBM distance for different boundaries tracked simultaneously. The manually measured stress levels are plotted

on the secondary axis. Vertical grey lines represent reload instances in which the stress was increased. Time is given in terms of seconds since first recording of given set of grains which occurred 2.5 minutes after load was first applied. The velocity of the GB represented by the red data points is shown for the final three reloading segments (i.e. velocity of the GB as it migrates after promoted by an increase in stress until stagnation again).	176
Figure 73 - Comparison of stress-assisted grain boundary migration distances and velocity in irradiated and non-irradiated Au films. (a) GB migration distance data from the irradiated film in Figure 71(diamonds) and non-irradiated specimen in Figure 72(circles) scaled to show first 5 minutes only. The stress levels for both are shown with the stress scale on the right y axis to show that the initial stress levels are similar followed by an increase in stress in the irradiated film and decrease in stress in non-irradiated. The average velocity is provided for each non-irradiated GB showing a range of 0.04 – 0.30 nm/s. (b) “Instantaneous” velocity for one GB in irradiated specimen and two GBs in non-irradiated specimen. “Instantaneous” velocity is defined as the velocity for a 30-60 second interval. The schematic of the grain shape change outline of (c) non-irradiated grain in Figure 72 and (d) irradiated Figure 71 to compare migration behavior at the same length scale (scale bar the same for both). The solid outline represents the initial grain size with the two dashed outlines representing the grain shape after 10 and 20 minutes. The red arrow indicates direction of migration. The black ‘x’ represents radiation damage. The stress ranges during migration are provided underneath the schematics.	178
Figure 74 – <i>In situ</i> repeated stress-relaxation experiment and activation volume measurements for an irradiated Au specimen. (a) full stress-strain curve with stress-relaxation segments shown in (b). The four relaxations within the dashed boxes correspond to (c) Relax 12, (d) 13, (e) 17, and (f) 18.....	180
Figure 75 – All <i>in situ</i> true V^* and apparent V_a activation volume measurements on irradiated UFG Au specimens.....	181
Figure 76 – Successive <i>in situ</i> stress-relaxation experiments to investigate how true activation volume V^* varies with evolving microstructure. Stress-time data for (a) Test 1 and (b) Test 2 for the same specimen. The measured V^* values for both tests are shown in (c).	183
Figure 77 – GB migration data for migrating boundaries in a UFG annealed Au specimen. (a) TEM image of initial microstructure of UFG annealed Au. Migration behavior of annealed Au compared with the migrating boundaries in (b) irradiated specimen and (c) non-irradiated as-deposited.	186
Figure 78 – All <i>in situ</i> true activation volume measurements made on UFG Au specimens (as-deposited, A350, A700, and irradiated). True activation volume V^* versus (a) the initial stress level, (b) plastic strain (%), and (c) plastic strain rate ($\dot{\epsilon} - 1$) for each given relaxation segment. (d)	

strain rate sensitivity m calculated using V^* for each relaxation segment.	189
Figure 79 – All <i>in situ</i> V^* measurements made on NC Al specimens (Al-100 and Al-200). True activation volume V^* versus (a) the initial stress level, (b) plastic strain (%), and (c) plastic strain rate ($\dot{\epsilon} - 1$) for each given relaxation segment. (d) strain rate sensitivity m calculated using V^* for each relaxation segment.	193
Figure 80 – Atomistic FENEB simulation setup for GB dislocation nucleation in an Au bicrystal. (a) An initial defect-free configuration containing a symmetric tilt GB. The tensile load is applied on $[415]$ direction. (b) A typical free-end state with an embryonic partial dislocation loop at the intersection between the GB and surface (from Ref. [95]).	196
Figure 81 – FENEB results for GB dislocation nucleation in an Au bi-crystal. (a) MEPs at different applied resolved shear stresses, (b1-b4) Atomic configurations (marked in (a)), (c) Activation energy as a function of resolved shear stress. (d) Activation volume as a function of resolved shear stress.	198
Figure 82 – Schematic of the stress-dependent activation energy for two competing thermally activated processes [200].	203

LIST OF SYMBOLS AND ABBREVIATIONS

A350	Gold specimens annealed at 350°C
A700	Gold specimens annealed at 700°C
ACOM	Automated crystal orientation mapping
Al-100	100 nm-thick Aluminum
Al-200	200 nm-thick Aluminum
BF	Bright field
CI	Confidence index
CSL	Coincidence site lattice
DOF	Degrees of freedom
FCC	Face-centered cubic
FIB	Focused ion beam
GB	Grain boundary
GBM	Grain boundary migration
HAGB	High angle grain boundary
IPF	Inverse pole figure
LAGB	Low angle grain boundary
LS	Load sensor
MD	Molecular dynamics
MEMS	Microelectromechanical systems
MEP	Minimum energy path
NBED	Nanobeam electron diffraction
NC	Nanocrystalline
PED	Procession electron diffraction

SAD	Selected area diffraction
SEM	Scanning electron microscopy
SFT	Stacking-fault tetrahedron
SG	Specimen gap
TA	Thermal actuator
TB	Twin boundary
TEM	Transmission electron microscopy
TJ	Triple junction
UFG	Ultrafine-grained
UTS	Ultimate tensile strength
UV	Ultraviolet
WBDF	Weak beam dark field
$\Delta\sigma$	Amount of stress relaxation
ΔG	Activation energy
V_a	Apparent activation volume
k	Boltzmann constant
b	Burgers vector
CS_1	Capacitive Sensor 1
CS_2	Capacitive Sensor 2
α	Calibration constant
v	Dislocation velocity
τ^*	Effective stress
E	Elastic Modulus
d	Grain size
X_{LS}	Load sensor displacement
K_{LS}	Load sensor stiffness

ρ_m	Mobile dislocation density
ε_0	Permittivity of free space
$\dot{\gamma}_p$	Plastic shear strain rate
$\dot{\varepsilon}_p$	Plastic strain rate
κ	Relative permittivity of air
X_S	Specimen displacement
m	Strain rate sensitivity
T	Temperature
X_A	Thermal actuator displacement
V_{in}	Thermal actuator input voltage
V^*	True activation volume
σ_y	Yield stress

SUMMARY

The plastic deformation mechanisms that govern the mechanical properties of nanocrystalline (NC) and ultrafine-grained (UFG) metal thin films were investigated through *in situ* transmission electron microscopy (TEM) nanomechanical experiments. This technique allows for the simultaneous observation of the active deformation mechanisms and quantification of the mechanical properties during monotonic and stress-relaxation experiments. Experiments were performed on NC Al and UFG Au specimens with different microstructure (grain sizes, thickness, texture), including irradiated UFG Au. For the NC Al specimens, it was documented that stress-assisted grain boundary migration (GBM) leads to grain growth. Grain growth was enhanced in regions of increased stress such as within the necked region or ahead of a growing crack. For the UFG Au specimens, a mixture of dislocation-based and GB-based mechanisms were identified, including dislocation nucleation and absorption at GBs and GBM. The radiation damage in the irradiated UFG Au served as effective pinning points for transgranular dislocation glide which resulted in a measurable increase in strength. Stress-assisted GBM was observed to effectively remove radiation damage as the defects were absorbed by the GB during migration. This resulted in defect-free ('cleaned') regions that can support unrestricted dislocation glide, suggesting that stress-assisted GBM is a healing mechanisms for radiation damage in UFG metals.

True activation volume calculations were performed for all of the UFG Au and NC Al specimen variations to further quantify the plastic deformation mechanisms. For Au, it was found that V^* increases from $25 \pm 14b^3$, to $35b^3$, and finally to $96 \pm 5b^3$ as the

average grain size increases from 142, 287, and 768 nm respectively. Average V^* for the NC Al specimens was $22 \pm 11b^3$ and $6 \pm 2b^3$ as the average grain size decreased from 95 to 55 nm. These results indicate that there is a grain size effect on activation volume. An existing model was used to interpret the activation volume values and propose that there is likely a competition between active displacive- and diffusive-type deformation mechanisms. For all of the specimens, there was a strong stress-dependence of decreasing V^* with increasing stress.

In situ TEM straining experiments were conducted combined with orientation mapping for a detailed analysis of stress-assisted GBM/grain growth in the UFG Au specimens (as-deposited and annealed). In the as-deposited films, GBM was shown to be largely dominated by the removal of the small grains ($d < 50$ nm). Stress-assisted GBM in the annealed films was analyzed in terms of microstructural features that might impact the propensity for migration, such as GB character, grain orientation, Schmid factor, and GB trace angle with respect to the loading direction. However, there were no trends observed for any of the investigated microstructural features, suggesting a complicated interplay between driving forces and microstructures. It is postulated that the consistent small grain removal is due to an increase in GBM driving force related to a reduction in strain energy density. Grain size-dependent yielding leads to yielded large grains and elastically-deformed small grains and as a result, the large grains (low strain energy density) will grow at the expense of the small grains (with high strain energy density).

The technique was also used to quantify the effect of the TEM electron beam during an *in situ* experiment. It was determined that the observed increase in plastic strain rate and decrease in activation volume during electron beam exposure was due to increased atomic

fluctuations. The additional atomic activation accelerates the stress-driven, thermally-activated deformation mechanisms by reducing the barrier to plastic deformation which resulted in the observed increase in plasticity. These results indicate that there is non-negligible e-beam effect that must be considered for accurate interpretation of *in situ* experiment results.

CHAPTER 1.

BACKGROUND AND MOTIVATION

1.1 Introduction

The demand for smaller, smarter and faster devices has motivated continued research into understanding the mechanical behavior of small-scale materials used to create micron-sized features for devices such as flexible or stretchable electronics or micro electromechanical systems (MEMS). MEMS utilize both electrical and mechanical components for ultra-sensitive monitoring and control, with MEMS-based devices expanding to include sensors [1], actuators [2], biomedical devices [3], and micropower generators [4]. Typical MEMS devices are fabricated with silicon as the primary structural material, however due to its inherent brittle behavior, next-generation MEMS devices require more robust materials capable of withstanding extreme temperatures and surface wear conditions.

The intrinsic strength and toughness of metals make metallic thin films a viable solution for structural components or electrical contacts [5,6]. Operational demands on the thin films can lead to mechanical and/or thermal stresses that may result in plasticity, friction or wear, creep, fatigue, fracture, etc [7]. As such, understanding the mechanical properties of metal thin films is needed in order to overcome the critical issue of reliability.

This chapter aims to introduce the unique mechanical properties of metal thin films in terms of characterizing the active deformation mechanisms followed by a detailed

description of stress-induced GBM. The chapter finishes with a description of radiation-induced defects and their influence on the mechanical properties of metal thin films.

1.2 Mechanical Properties of NC and UFG Metal Thin Films

Thin films used in the microelectronic industry typically have thickness dimensions ranging from several microns (μm) down to one nanometer (nm). The small dimensions of metal thin films lead to differences in mechanical properties compared to their bulk counterparts. Size-effect material property changes in metals are generally attributed to dislocations and their interactions with defects (GBs, precipitates or second phase particles) along different internal or external characteristic length scales such as grain size or film thickness/geometry, respectively [8]. One important distinction between thin film testing and bulk testing is the influence of the free-surface. The free-surface can serve as a stress concentrator for dislocation nucleation or crack initiation as well as a means for dislocation escape. The limited dimensions also lead to a high sensitivity to fabrication processing, as different processing steps can impart significant stresses in the thin films and alter the properties. Most notably, however, the thin film fabrication typically produces films with grain size dimensions controlled by the thickness of the film due to the “specimen thickness effect” [9]. This leads to films with smaller grain sizes compared to their bulk counterparts, which has a significant impact on the mechanical properties.

Nanocrystalline (NC) metals have grain sizes ranging from a few nm's up to ~ 100 nm and metals with slightly larger grain sizes of $100\text{ nm} - 1\text{ }\mu\text{m}$ are classified as ultrafine-grained (UFG). Decades of research has shown that altering the grain size of a metal has a large impact on the mechanical properties, including the yield strength, ductility, fracture

toughness, fatigue life, etc. Metal thin films may not be load bearing in application, but understanding their mechanical properties is important in order to ensure the reliability of microelectronics. Furthermore, thin films are required to observe the deformation mechanisms directly.

1.2.1 Yield Strength

The stress which marks the transition between elastic and plastic deformation is defined as yield strength and is used as a metric to compare mechanical performance across different materials. It has been repeatedly shown that decreasing the grain size into the NC and UFG regimes results in a notable increase in yield strength [10–13]. This behavior is explained using the well-known Hall-Petch relationship [14–16]:

$$\sigma_y = \sigma_0 + k/\sqrt{d} \quad (1)$$

which states that yield strength (σ_y) scales inversely with grain size (d), where σ_0 is the friction stress below which dislocations are immobile and k is a constant. The most common mechanistic interpretation of this relationship involves the dislocation pile-up model [17–19]. Under an applied load, dislocations glide through the crystalline lattice until reaching a barrier, such as a GB. The schematic below shows that successive dislocation glide will lead to a pile-up of length L_p at that GB, where L_p is half of the grain diameter d_g [8].

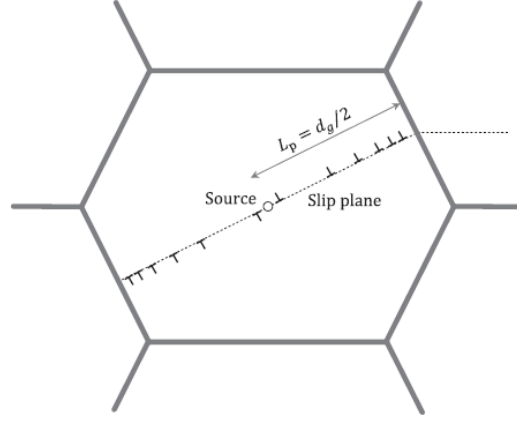


Figure 1 – Schematic of dislocation pile-up at a GB [8].

The number of dislocations n in the pile-up is related to the applied stress τ_s and L_p following:

$$n = \frac{\tau_s L_p}{\alpha G b} \quad (2)$$

where α is a constant, G is the shear modulus, and b is the Burgers vector [8]. This process continues until the stress concentration caused by the dislocation pile-up τ_p (where $\tau_p = n\tau_s$) reaches a critical stress τ_{cr} . At this point, the dislocations in the pile-up either pass the GB or the stress concentration leads to dislocation nucleation in the adjoining grain. Since the number of dislocations in a pile-up is related to both the applied stress and the grain size ($L_p = d_g/2$), this implies that a decrease in grain size results in fewer dislocations in a pile-up at a given stress level and thus a smaller pile-up stress. Thus, higher stress levels are necessary to reach the critical stress required to continue deformation in the adjoining grain and explains the observed increase in strength at diminishing grain sizes.

The increase in strength with decreasing grain size has sparked interest and significant research has been done to characterize this phenomenon using a variety of different mechanical testing platforms, including uniaxial tension/compression and micro- or nano-indentation [12,13,20,21]. It is important to note that the reported mechanical properties can be highly sensitive to specimen geometry and fabrication techniques. Under uniaxial tension of microsamples, Gianola *et al.* reported an increase in yield strength of Al from 91 to 116 MPa as the grain size decreased from 90 to 40 nm [20], which is ~15-20 times larger than the yield strength for bulk coarse-grained Al [22]. NC Cu ($d \sim 22$ nm) is reported to have a yield strength of 360 MPa which is 10 times larger than the strength reported for Cu counterpart with $d \sim 20 \mu\text{m}$ [12]. NC Pd shows a similar increase in strength (40 to 660 MPa) as the grain size is decreased from $20 \mu\text{m}$ to 47 nm [12]. Compressive testing is useful in cases where the specimen suffers from brittle fracture under tension. Very large compression strengths for NC Cu ($d \sim 19 - 54$ nm) have been reported to be on the order of 1 GPa (coarse-grained value ~ 50 MPa) [21].

Decreasing the grain size further has been found to lead to softening known as the “inverse” Hall-Petch effect [23,24]. The threshold grain size for this is not well-defined but it has been postulated that the transition occurs when the grain size is too small to support lattice dislocations and thus the dislocation pile-up model breaks down. *In situ* TEM straining experiments have shown dislocation activity in NC Au and Ag specimens with 100 nm grains whereas no dislocation activity was observed in specimens with 10 nm-sized grains and instead grain rotation and GB sliding occurred to accommodate deformation [25]. Molecular dynamic (MD) simulations have also predicted that the deformation is dominated by GB processes, such as GB sliding [26–28].

1.2.2 Ductility

As discussed in the previous section, the increase in strength of NC and UFG metals owes itself to the fact that GBs serve as effective blockages to extended dislocation glide. Unfortunately, this also leads to a decrease in ductility which limits the direct usability of such metal thin films. Sanders *et al.* reported a decrease in elongation-to-failure from >8% to 1-4% when the grain size in Cu decreased from 110 to 50 nm [12]s. **Figure 2** shows compiled data of normalized yield strength (strength/strength of conventional coarse-grained) versus percentage elongation in tension for a variety of metals with grain sizes in the NC (**Figure 2(a)**) and UFG (**Figure 2(b)**) regime [10,29]. Despite the fact that the specimens were fabricated following different processes, the data clearly shows a severe decrease in % elongation accompanying the increase in strength for specimens within the NC regime. The data shown for the UFG specimens (**Figure 2(b)**) indicates that most specimens show an increase in strength without a drastic loss in ductility, indicating that UFG metals appear to be less susceptible to the severe decrease in ductility.

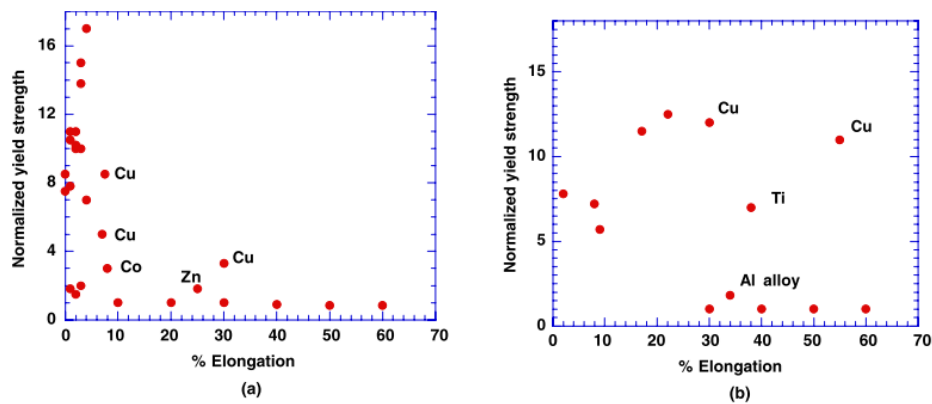


Figure 2 – Compiled yield stress vs. % elongation of different (a) NC metals and (b) ufg metals [10,29].

It has been shown that ductility (strain at failure) is heavily dependent on the active deformation mechanisms. For example, Gianola *et al.* found that NC Al specimens (40 nm grain size) show increased ductility if stress-assisted GBM is activated compared to counterparts that experience no grain growth [20]. The exact reason behind this is unclear, however, one hypothesis is that the early stress-assisted grain growth leads to grains that are then large enough to support dislocations. Following along the same lines, bimodal grain size distributions (i.e. a mixture of micron-sized grains within a NC/UFG matrix) has been proposed to optimize the tensile ductility and yield strength [30]. Additionally, it has been proposed that non-equilibrium GBs can contribute to increased ductility due to excess dislocation nucleation at such boundaries or facilitate grain sliding and GB rotation [31].

1.2.3 Strain Rate Sensitivity

Strain rate sensitivity is the dependence of flow stress on the applied strain rate and can be expressed as:

$$m = \frac{\partial \ln \sigma}{\partial \ln \dot{\epsilon}} = \frac{1}{\sigma_y} \frac{\partial \sigma}{\partial \ln \dot{\epsilon}} \quad (3)$$

where $\dot{\epsilon}$ is the strain rate [10,32]. This value is typically on the order of 0.01 or smaller for polycrystalline FCC metals [33]. However, there are numerous reports of increased strain rate sensitivity as the grain size decreases to the NC/UFG regime for a variety of FCC metals regardless of fabrication process, including Cu [34–37], Ni [38–40], and Al [33,41]. Values typically range from 0.015-0.103 [35,37,39,40,42,43] with larger values reported for experiments conducted at elevated temperatures. For example, May *et al.* reported $m \sim 0.25$ for UFG Al under compression testing conducted at 523K [33] and Duhamel *et al.*

reported values as large as $m \sim 0.17$ for NC Cu tested at $\dot{\epsilon} = 10^{-5} \text{ s}^{-1}$ and $T = 393 \text{ K}$ [44]. The increased strain rate sensitivity is usually attributed to a change in rate-controlling deformation mechanism and the competition between diffusion- and dislocation-based mechanisms. GB mechanisms such as GB sliding or diffusional creep are expected to have $m \sim 0.5$ and $m \sim 1$, respectively [40]. This indicates that diffusion-controlled processes may be more important at smaller grain sizes and slower strain rates. The strain rate sensitivity can also be expressed in terms of the activation volume V^* :

$$m = \frac{\sqrt{3}kT}{\sigma V^*} \quad (4)$$

where k is the Boltzmann constant, T is the absolute temperature and σ is the flow stress [40]. This relationship implies an increase in strain rate sensitivity is related to a corresponding decrease in activation volume and further points to a change in deformation mechanisms as grain size decreases leading to the increase in m .

Strain rate sensitivity can be related to ductility through the Hart stability criteria ($\gamma \geq 1 - m$, where $\gamma = (1/\sigma)(\partial\sigma/\partial\epsilon)$ and describes the strain hardening) [45–47]. This has been further simplified to give an estimate of the strain in which the microstructure becomes unstable (ϵ_u), which is given by:

$$\epsilon_u = \frac{n}{1 + m} \quad (5)$$

where $n = \gamma\epsilon$. This equation implies that as strain rate sensitivity increases, ϵ_u decreases which indicates a decrease in ductility. Since V^* is related to m , investigating true activation volume V^* can aid in the effort to increase m and thus improve ductility.

1.2.4 Strain Hardening

Strain-hardening describes the ability of a material to continue to ‘harden’ or strengthen with additional strain. In conventional coarse-grained metals, this occurs due to dislocation generation and storage which leads to dislocation entanglement and thus restriction in dislocation glide [48]. It has been shown that NC and UFG metals exhibit low strain hardening for a variety of metals and processing techniques, including electrodeposition [49,50], equal channel angular pressing [30,51,52], and severe plastic deformation [51,53]. This is due to the saturation of dislocation density which is a result of both dislocation annihilation at GBs and dynamic recovery. The small grain sizes make it difficult for the grains to store dislocations, with some predictions indicating that no dislocation pile-up occurs for grain sizes below 20 nm [54].

The lack of strain hardening ($d\sigma/d\varepsilon = 0$) leads to localized deformation [10] which contributes to the loss of ductility and limited uniform elongation of NC/UFG metals [55,56]. The combination of high flow stress and low work hardening in NC metals promotes neck formation, resulting in ‘unusable’ elongation and reduced tensile ductility.

1.2.5 Strategies for Obtaining Optimal Mechanical Properties

As discussed in the previous sections, decreasing the grain size can lead to certain favourable mechanical properties (increased yield strength), however, this is unfortunately accompanied by a wealth of unfavourable properties (decreased ductility and strain hardening) which limits the direct application of NC/UFG metals. There are several approaches to optimize both the increase in yield strength while minimizing the deleterious effects of decreasing the grain size.

1.2.5.1 Controlling Grain Size Distribution

One of the postulated ways to retain the auspicious result of decreasing the grain sizes without suffering from limited ductility or strain hardening is to control the grain size distribution. Specifically, groups have investigated the effect of a bi-modal or multi-modal grain size distributions [30,57–59]. The general idea is that the small grains ($d < 300$ nm) can contribute to an increase in strength due to dislocation pile-up and/or inability to support dislocations while the larger grains ($d > 1$ μm) can contribute to increased ductility/strain hardening by supporting dislocation pile-up and dislocation interactions and storage. For example, Wang *et al.* reported that a bi-model grain size distribution in ECAP-Cu can lead to a significant increase in ductility (increase in failure strain from 15% to 65%) while still maintaining a 5-6 time increase in strength compared to coarse-grained Cu [30].

1.2.5.2 Controlling Deformation Mechanisms

Researchers have postulated that activating additional deformation mechanisms, namely GB mechanisms, could lead to increased ductility and strain hardening in NC and UFG metals. Studies have shown that superplasticity (high elongation without necking) in NC/UFG metals can be achieved through GB sliding [60–62]. In this model, GB dislocations and disconnections move along GBs to facilitate GB sliding and pile-up at TJs. This then leads to stress-concentration that can promote dislocation nucleation and slip in the neighbouring grain [60].

An additional GB mechanism that has been proposed to help increase ductility is stress-assisted GBM [20,63]. The reasoning is that GBM can facilitate grain growth and

allow grains to reach sizes that can then support dislocations. Both of the aforementioned GB deformation mechanisms will be discussed in detail in the next section.

1.3 Deformation Mechanisms

In conventional coarse-grained metals ($d > 1 \mu\text{m}$), plastic deformation is primarily dictated by the glide of unit dislocations through grain interiors. Inhibiting this dislocation glide can effectively halt plastic deformation, which explains the observed increase in strength as grain size decreases. The underlying theory is that as the grain size decreases, GBs serve as obstacles to dislocation glide and thus prevent extended plasticity. Because of the increased volume fraction of GBs, it is expected that the propensity for dislocation-GB interactions will play a profound role in the plastic deformation of metals with small grain sizes. As grain size continues to decrease, GBs contribute directly to plastic deformation. As such, GB dislocation emission and absorption, which may be accompanied by GB sliding [26], grain rotation [64–67], atomic shuffling [27] and stress-assisted GBM [20,63,68] have all been proposed as deformation mechanisms. **Figure 3** shows the deformation mechanisms map across all grain sizes for FCC metals [69].

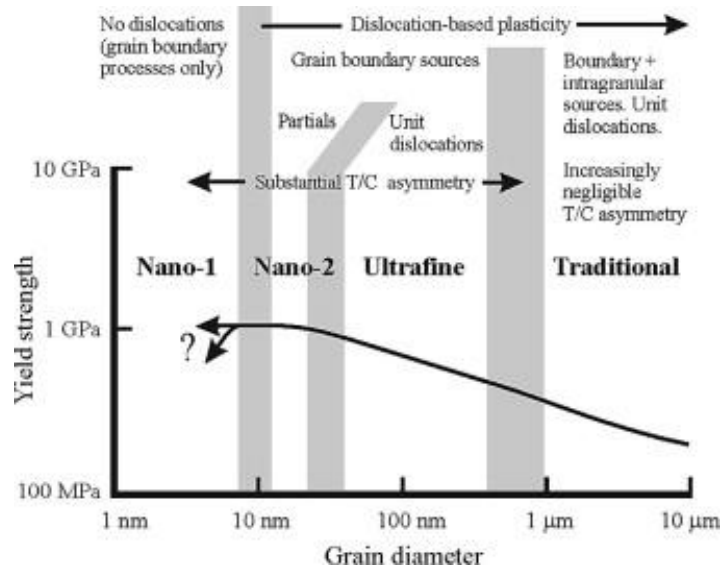


Figure 3 – Deformation mechanism map for FCC metals across different grain sizes from [69]. Strength curve is based on copper.

1.3.1 Dislocation-Based Mechanisms

In coarse-grained metals, deformation is controlled by dislocation-based mechanisms involving the slip and storage of dislocations in grain interiors. As grain size decreases into the NC and UFG regime, intragranular dislocation glide still occurs, but due to limited space within the small grains, conventional intragranular Frank-Read dislocation sources are not operable which leave GBs as the primary source for dislocation nucleation [26,69]. Previous investigations have shown that dislocations are emitted from GBs in both UFG [16] and NC metals [70–72]. However, as the grain size decreases below a critical value (typically $d < 20$ nm), the propensity for partial dislocation nucleation outweighs that of full dislocation nucleation [71]. Dislocation nucleation usually occurs at regions of stress concentration, such as GB ledges or TJs, as these features lower the stress required for dislocation nucleation [16,73]. Experimental evidence provided by Momprou *et al.* suggests that GB dislocation nucleation can lead to intergranular dislocation glide early in

deformation (2% plastic strain) which is transferred to transgranular glide at larger strains for UFG Al [16]. This particular study suggested that intergranular dislocation glide occurs irrespective of GB character and that the activation of GB dislocation sources controls the onset of plastic deformation.

1.3.2 Grain Boundary Sliding

GB sliding is an active deformation mechanism in UFG and NC metals documented both by MD simulations [27] and experiments [16,74,75] and is the principle mechanism in superplasticity. GB sliding is defined as the relative shear of one grain with respect to a neighboring grain in response to an applied stress. A schematic of different accommodation mechanisms for GB sliding is shown in **Figure 4**. When this occurs without any grain shape change (as opposed to occurring by stress-directed diffusion of vacancies [62]), it requires accommodation via GB dislocation and/or disconnection glide [16]. In some cases, this can lead to local GB and/or TJ migration [27] (**Figure 4(b)-(e)**) as TJs serve as restrictions to GB sliding. GB dislocation and disconnection glide can also lead to pile-ups at TJs and subsequent lattice dislocation emission and pile-up in adjacent grain (**Figure 4(f)-(g)**). Other accommodation mechanisms involve local diffusion processes (**Figure 4(h)-(i)**). In fact, MD simulations have predicted that on the atomic scale, GB sliding occurs via atomic shuffling or stress-assisted free-volume migration [27].

There is evidence to suggest that the transition from GB dislocation emission to GB sliding at a certain diminishing grain size is based on stacking fault energy and strain rate [76]. Other studies have shown that dislocation nucleation from non-equilibrium GBs allow grains to slide or rotate to accommodate deformation [31]. Low-energy GBs are less

susceptible to GB sliding [27] and as a result, GB sliding is more commonly observed in high-angle GBs (HAGB) or non-coincident site lattice (CSL) Σ boundaries [16,60].

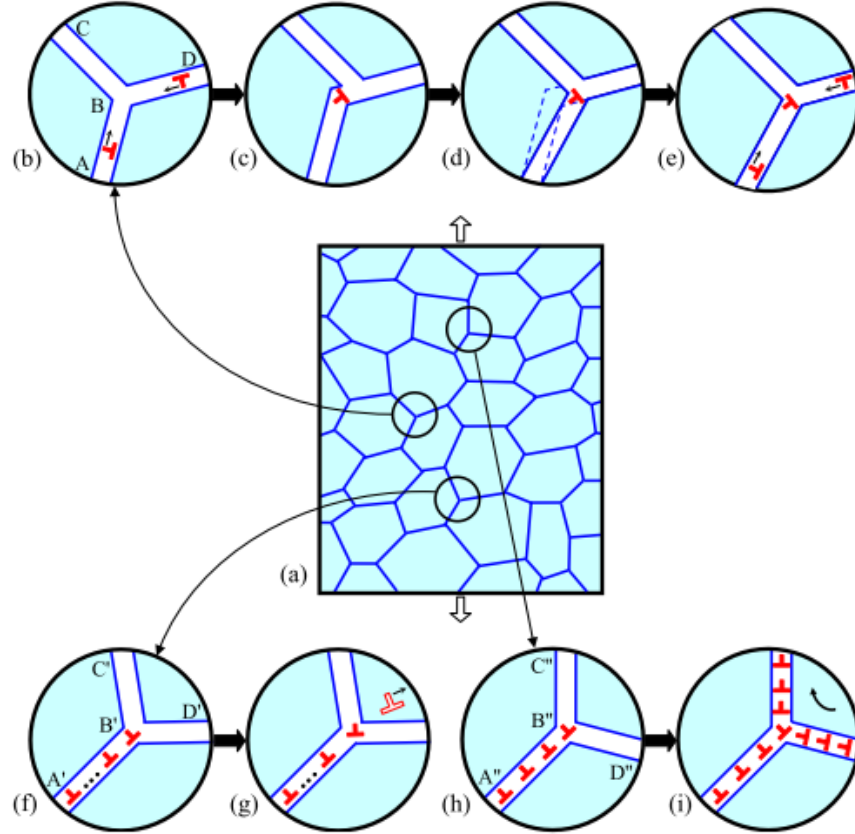


Figure 4 – Grain boundary sliding and its basic accommodation mechanisms in nanograined materials (from [77]). (a) NC UFG specimen under tensile load. Magnified insets (b-i) illustrating local accommodation mechanisms. (b-e) Accommodation through transformation of defects (GB dislocations and disconnections) at TJs and local migration of GB. (f-g) Accommodation through GB dislocation/disconnection pile up at TJ leading to emission of lattice dislocation in adjacent grain. (h-i) Accommodation through diffusion-controlled rotational deformation.

1.3.3 Grain Rotation

Another deformation mode in NC/UFG metals is plastic flow accompanied by grain rotation. This rotational deformation is facilitated by GB disclination flow along GBs that

causes local rotations of the crystal lattice and is typically driven by a reduction in GB energy. GB disclinations are line defects that are characterized by rotation of the crystal lattice around its line [77]. Due to geometric restrictions, the motion of GB disclinations either absorb pre-existing dislocations or cause emission of new lattice dislocations, indicating that grain rotation is accommodated by dislocation emission and slip in adjacent grains [77]. GB dislocations can also mediate grain rotations due to a transition from GB dislocation glide to disconnection climb that can occur at TJs [77,78].

By combining *in situ* TEM straining with nanobeam electron diffraction (NBED), Wang *et al.* observed crystal lattice rotations initiated by GB sliding in NC Ni and suggests that grain rotation can lead to grain coalescence (grain growth) [67]. More detailed analysis of grain rotation has been done by combining *in situ* TEM straining with automated crystal orientation mapping (ACOM) to investigate the time-dependent grain orientation changes in UFG Al with random texture. This study found that the number of grains and magnitude of orientation change both increased with increasing strain [64]. They postulated that the large stress difference and plastic strain mismatch between neighbouring ‘hard’ and ‘soft’ grains leads to the rotating of grains to maintain strain compatibility.

1.3.4 Stress-Assisted Grain Boundary Migration

A growing number of studies have reported stress-assisted GBM as a contributor to both plastic flow and grain growth in UFG/NC metals. In particular, studies have suggested that grain growth mediated by GBM occurs prior to transgranular dislocation activity. For example, *in situ* TEM straining of NC Al has shown fast GB-migration near a crack tip prior to dislocation activity [63] while other studies have shown that grain

coarsening occurs in the immediate vicinity of an indenter tip during *in situ* TEM nanoindentation, with the coarsening halting once grains are large enough to accommodate dislocation mechanisms [79]. Stress-assisted GBM is thought to be mediated by the nucleation and glide of GB disconnections [16], but the nucleation and subsequent glide itself likely depends on GB structure. Stress-assisted GBM will be discussed in detail in Section 1.5.

1.4 Activation Volume

1.4.1 Theory

The basic theory behind thermally activated deformation is based on the barriers to dislocation glide [80,81]. The flow stress (τ) of a crystal can be broken into two separate contributions:

$$\tau = \tau_i + \tau^* \quad (6)$$

where the former (τ_i) is due to long-range elastic interactions and the latter (effective stress τ^*) is due to short-range barriers and is responsible for the flow stress dependence on temperature and strain-rate. The stress required to overcome the short-range barriers (τ^*) is much smaller than that required to overcome long-range barriers and thus can be provided from thermal fluctuations (hence the term ‘thermally’ activated). This explains why the yield strength of a material decreases with increasing temperature. The plastic strain rate ($\dot{\gamma}_p$) is given by the Orowan equation below:

$$\dot{\gamma}_p = \alpha \rho_m b v \quad (7)$$

where α is a geometric coefficient, ρ_m is the mobile dislocation density, and b is the dislocation Burgers vector. The dislocation velocity v can be expressed as

$$v = dv \exp(-\Delta G^*/kT) \quad (8)$$

where d is the distance the dislocation moves and the remaining term ($v \exp(-\Delta G^*/kT)$) is the probability that thermal vibrations occurring at frequency v lead to a dislocation successfully overcoming the required energy barrier (ΔG^*). Using this, the plastic strain rate can be expressed as:

$$\dot{\gamma}_p = \dot{\gamma}_o \exp(-\Delta G^*/kT) \quad (9)$$

with $\dot{\gamma}_o = \alpha \rho_m b d v$. This equation captures the dependence of deformation on the ability of a dislocation to overcome the local energy barrier (ΔG^*). However, separate dislocation slip mechanisms may have similar ΔG^* values and therefore it is useful to further study how ΔG^* varies with the stress needed to overcome the barrier (τ^*), as this will be unique for distinct mechanisms. This relationship is referred to as the true activation volume V^* and is shown below.

$$V^* = -\left(\frac{\delta \Delta G^*}{\delta \tau^*}\right)_T \quad (10)$$

V^* is unique for a specific deformation mechanism, as it captures the relationship between the energy barrier and stress required to overcome a specific obstacle. Physically, V^* is related to the area swept by a dislocation as it overcomes the local barrier and is proportional to the number of atoms involved in the process [80,82]. Ultimately, V^* is

considered a characteristic value for specific dislocation mechanisms and can thus be used to differentiate between different mechanisms. By combining Eqn. (9) and Eqn. (10) and assuming constant dislocation density, V^* can be written as:

$$V^* = kT \frac{\delta \ln \dot{\gamma}_p}{\delta \tau^*} \quad (11)$$

Experimentally, V^* can be measured via stress-relaxation tests [83–85] and determined using the following equation,

$$V^* = kT \frac{\ln(\dot{\gamma}_{p2}/\dot{\gamma}_{p1})}{\Delta \tau^*} \quad (12)$$

where $\dot{\gamma}_{p1}$ and $\dot{\gamma}_{p2}$ are the initial and final plastic shear strain rate during a relaxation segment, respectively and $\Delta \tau^*$ is the decrease in effective stress during the relaxation. However, the assumption of constant dislocation density during reloading may not necessarily always be valid. To avoid this assumption, the apparent activation volume (V_a) can be determined by fitting the stress relaxation segment with a logarithmic fit as follows:

$$V_a = - \frac{\sqrt{3}kT \ln\left(1 + \frac{t}{c_r}\right)}{\Delta \sigma} \quad (13)$$

where V_a and c_r are fitting constants, t is time, and $\Delta \sigma$ is the decrease in applied stress during relaxation segment. The apparent activation volume represents the variation of free energy ΔG with the total stress (rather than τ^* only, $V_a = \frac{\delta \Delta G}{\delta \tau}$)

1.4.2 Activation Volume Values for NC and UFG Metals

Dislocation mechanisms that involve a large area (and thus many atoms) typically have high activation volume values. These mechanisms, such as a dislocation cutting through forest dislocations, have activation volumes of the order of hundreds to several thousand b^3 [40,86]. As a result, conventional FCC metals typically have $V^* \sim 10^2 - 10^3 b^3$ [10]. Other traditional dislocation mechanisms, such as cross-slip, have been reported to have $V^* = 10 - 100 b^3$ [40]. As the deformation becomes more localized and involve fewer atoms, the activation volume decreases accordingly. For example, diffusional processes are estimated to have an activation volume $V^* \sim 1 b^3$ [87], with GB diffusion processes having $V^* \sim 1 - 10 b^3$ [10].

Experimentally determined activation volume for NC and UFG metals is limited and inconclusive. Karanjgaokar *et al.* has reported activation volume values of $6.4 b^3$ within the strain rate range of $10^{-5} - 10^{-2} \text{ s}^{-1}$, which increases to $19.7 b^3$ when the strain rate is increased to $10^{-3} - 10 \text{ s}^{-1}$ for Au films with an average grain size of 64 nm [88]. They attributed the low activation volume during the slow strain rate tests to diffusion-based mechanisms, whereas dislocation depinning was identified as the rate-controlling mechanisms at higher strain rates. Wang *et al.* has reported activation volume of $20 b^3$ for NC Ni ($d \sim 30 \text{ nm}$) under a strain rate of 10^{-4} s^{-1} [40]. They attributed the rate-controlling mechanisms to dislocation interaction with GBs while specifically discrediting diffusion-based mechanisms since the activation volume is not $\sim 1 b^3$.

Other researchers have reported activation volume values of 4.5 and $12.5 b^3$ for Au films (0.85 mm thick, $d \sim 40 \text{ nm}$) at strain rates lower and higher than 10^{-4} s^{-1} , respectively [89]. They also reported that the activation volume values increased to 8.1 and

14.6 b^3 for similar films as the thickness increased to 1.76 mm. The reduced activation volume at higher strain rates was attributed to GB processes, although the researchers were not able to conclude which specific processes. Lu *et al.* has showed that activation volume for nanotwinned (nt) Cu varies depending on thickness between adjacent TBs λ from 16 to 30 b^3 as λ increases from 15 to 35 nm, whereas UFG Cu had $V \sim 309 b^3$ [90]. They attribute the large decrease in V due to a switch in deformation mechanism from traditional dislocation forest cutting to dislocation cross-slip/accumulation at TB.

Determining activation volume is further complicated by the fact that the atomic processes involving dislocation-GB interaction differs based on GB structure, and thus it is likely that activation volume values are further affected by the specifics of a GB [90,91]. Overall, there is not a clear consensus in determining the dominant deformation mechanisms and corresponding activation volume. Reported activation volumes range across specimens of different material, grain size, thickness, texture, etc. **Table 1** summarizes activation volume measurements reported in literature. Most of the abovementioned studies were conducted *ex situ*, and careful assumptions are required in order to link measured activation volume values with the corresponding rate-controlling mechanism [40,84]. Thus, *in situ* activation volume measurements are ideal for correlating rate-controlling deformation processes with measured activation volumes.

Table 1 – Comparison of activation volume V^* measurements reported in literature across different metals with varying grain size (d), thicknesses (t), microstructure, and strain rates.

Strain Rate (s^{-1})	Material	d (t)	V (b^3)	Proposed Rate-controlling Mechanisms	Ref.
$< 10^{-4}$	NC Au	40 nm (0.86 μm)	4.5	GB processes	[89]
	NC Au	40 nm (1.76 μm)	8.1	GB processes	[89]
	NC Au	64 nm (850 nm)	6.4	GB-diffusion processes	[88]
10^{-4}	NC Ni	30 nm (120 μm)	20	Dislocation interaction with GBs	[40]
	UFG Au	150 nm (100 nm)	8-14	GB-dislocation interactions	[92,93]
	nt-15 Cu	400 nm (20 μm)	16	Dislocation cross-slip at twin interface	[90]
	nt-35 Cu	400 nm (20 μm)	30	Intra-twin and inter-twin processes	[90]
	UFG Cu	400 nm (20 μm)	309	Intersection of forest dislocations in bulk	[90]
	NC Al	62 nm (150 nm)	35	Stress-assisted grain growth	[94]
	UFG Al	104 nm (300 nm)	10 - 55	Stress-assisted grain growth	[94]
$> 10^{-4}$	NC Au	40 nm (0.86 μm)	12.5	Dislocation nucleation/pinning/depinning	[89]
	NC Au	40 nm (1.76 μm)	14.6	Dislocation nucleation/pinning/depinning	[89]
	NC Au	64 nm (850 nm)	19.7	Dislocation depinning from GB	[88]

1.4.3 Conrad's Model

As discussed in the previous section, relating the experimentally measured activation volume to a rate-controlling deformation mechanism is a difficult task. Some researchers have attempted to use models to explain the experimentally measured (sample-level) V^* . The Conrad model relates the experimentally measured sample-level activation volume (V^*) to grain size (d), and the individual activation volume from intragranular mechanisms (V_i^*) and processes at GBs (V_c^*) [26,86,95].

$$\frac{1}{V^*} = \frac{1}{V_i^*} + \frac{M^2 \mu b}{K_{H-P} \sqrt{d}} \frac{1}{V_c^*} \quad (14)$$

In the above equation, M is the Taylor factor, μ is the shear modulus, K_{H-P} is the Hall-Petch coefficient and α is a dimensionless parameter in the dislocation pileup model. This model is based on the amplified local stress at the GB due to dislocation pile-up (similar to the Hall-Petch relationship discussed in Section 1.2.1). Since the pile-up length (i.e. number of dislocations) is proportional to grain size d , the Conrad relationship implies a similar Hall-Petch type relationship for V^* .

At large grain sizes ($d > 1\mu m$), the V_c^* term is negligible and the sample-level V^* is dominated by V_i^* only ($V^* \sim V_i^*$) [26,95]. Mechanisms contributing to V_i^* are dislocation-based, such as cutting of forest dislocations by glide dislocations. V_i^* usually scales with $\sim lb^2$ and does not have a direct grain size dependence. For a typical dislocation density of 10^{14} nm^{-2} , this results in $V_i^* \sim 500b^3$. As grain size decreases, the V_c^* term increases (due to the increasing $\frac{M^2 \mu b}{2\pi \alpha K_{H-P} \sqrt{d}}$ coefficient) and thus, the contribution to V^* from V_c^* increases. Examples of V_c^* mechanisms include dislocation nucleation @ GBs or disconnection glide. At the smallest of grain sizes ($d < 10 \text{ nm}$), intragranular dislocation activity is absent and the second term is considerably larger than the first and $V^* \sim \frac{2\pi \alpha K_{H-P} \sqrt{d}}{M^2 \mu b} V_c^*$. In intermediate grain sizes ($10 \text{ nm} < d < 1000 \text{ nm}$), there is likely a unique interplay (weighting) of both V_i^* and V_c^* . Experimentally measuring V^* with specimens with different grain sizes can be helpful in validating this Conrad model. Decreasing V^* with decreasing grain size is consisted with previous experimental data and models summarized in **Figure 5** [96].

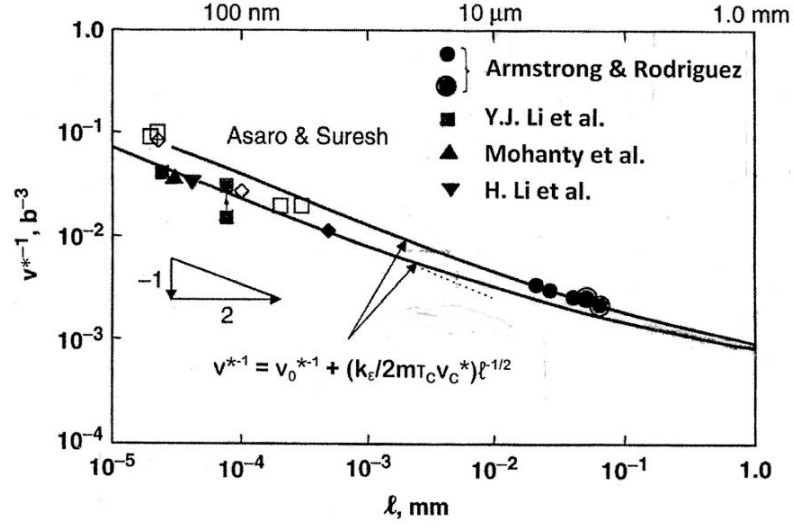


Figure 5 – Grain size dependence of reciprocal activation volume V^* calculations for Ni and Cu [96].

1.5 Grain Boundary Kinetics

It is clear that GBs serve an important role in NC and UFG metals and characterizing the specific behavior of the GB network is crucial for understanding the plastic deformation mechanisms and mechanical properties. GB kinetics dictate the evolution of a GB network and structure and is paramount in understanding how a material evolves during deformation. The fundamental kinetic equation used to describe GBM is:

$$v_{\perp} = M_z F \quad (15)$$

where v_{\perp} is GBM velocity defined normal to GB plane, F is the applied driving force and M_z is the intrinsic GB mobility that relates v_{\perp} to F [97]. This equation implies that GBM velocity is linearly related to the driving force, however, MD simulations have suggested that this may not be true, particularly at lower temperatures [98]. The intrinsic mobility is

an equilibrium GB property that only depends on material parameters, temperature, and/or bi-crystallography and in addition to driving force, controls the evolution of grain morphology and crystallography.

1.5.1 Grain Boundary Migration Driving Force

In general, the driving force for GBM is an overall decrease in the total free energy of the system. The specifics of the driving forces are divided into two categories: energy-jump and stress-driven [97]. Energy-jump driven GBM occurs when the free energy density of two grains differs and as a result, the boundary migrates towards the grain with higher free energy (in attempt to lower the overall energy). Energy differences between grains can arise from elastic anisotropy, variation in surface energy between different crystallographic grain orientations, excess defect density, magnetic free energy density and capillary forces acting to reduce GB free energy due to GB curvature [97,99]. Stress-driven GBM occurs when a boundary migrates in response to an applied stress and has been observed both through MD simulations and experimentally on bicrystals and polycrystals.

In reality, multiple driving forces are active simultaneously which makes fully understanding GBM complicated. For example, stress can promote defect (dislocation) generation which can in turn influence the defect density and lead to an additional driving force related to defect energy, although this is typically not expected to be a significant factor until high levels of deformation are met. In addition, elastic anisotropy arises when a stress is applied to the system and grains are elastically deformed. Grains of different orientations will have different strain energy densities which can promote GBM towards the grain with the higher strain energy [97]. This has been reported to be a significant

driving force particularly under cyclic loading, as the different studies have shown that a favourable texture (with lower strain energy density) develops during cycling [100,101]. Grain size also influences stored strain energy, and in particular, a variation in grain size leads to a variation in stored strain energy and thus an energy-jump driven driving force for GBM. This phenomenon is explained well by the figure below (from [102]). Under the no-stress state, grains G1, G2, and G3 all have the same free energy density (**Figure 6(a)**), however, after a load is applied the free energy density increases by the amount of elastic strain energy density which is different across grains, **Figure 6(b)**. Grain-to-grain variation in strain energy density arises from grain size dependent yielding (Hall-Petch effect, summarized in **Figure 6(c)**). Under an applied stress, each grain deforms elastically until eventually, the larger grains will yield through dislocation generation and slip. This yielding occurs at a lower stress level than the yielding stress required in the smaller grains and as a result, the elastic strain energy density within the larger grains is smaller than that of the smaller grains. This results in a difference in strain energy density across a GB and can promote GBM towards the small grain and eventually lead to the complete removal of small grains.

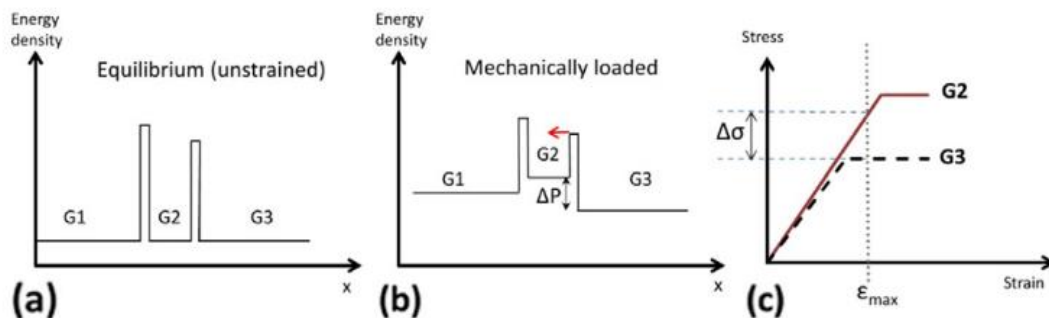


Figure 6 – Schematic of strain energy density driving force that leads to grain coarsening [102]. Diagrams in (a) and (b) show the unstrained and strained free

energy state for grains G1, G2 and G3 (all grains have different grain sizes). When a load is applied, the energy density increases by the increase in strain energy density, which varies across the different grain sizes due to size-dependent yielding (c).

1.5.2 Grain Boundary Mobility

The atomic nature of the GB mobility is believed to be independent of the type of driving force and instead, relies heavily on the structure of the GB. Understanding GB mobility, however, is a difficult task because it depends on the GB structure, which itself is defined by five degrees of freedom (DOF) [99]. Specifically, there are three macroscopic DOF that describe crystallographic orientation (one DOF for rotation angle and two DOF for axis of rotation) and two DOF that describe the GB plane. This leads to a large number of different types of GBs. Based on the change in crystal orientation $\Delta\theta$ about a common rotation axis (i.e. misorientation angle), boundaries are either classified as low-angle GB (LAGB) when $\Delta\theta < 15^\circ$ or high-angle GB (HAGB) when $\Delta\theta > 15^\circ$. Boundaries are further classified as pure tilt, twist, or a mixed type depending on the relationship between rotation axis and GB normal. A schematic for a pure tilt and twist boundary is shown in **Figure 7(a)** and (b), respectively [103]. Pure tilt and twist GBs are frequently engineered in bicrystals, but boundaries are more commonly of mixed tilt/twist type in polycrystalline materials. When the boundary plane is also a plane of symmetry, the GB is called symmetrical (only possible in pure tilt boundaries) and if this is not the case, the boundary is otherwise referred to as asymmetrical. GBs can be further classified by the coherency of the interface between two grains. A coherent boundary (shown in **Figure 7(c)**) occurs when the atoms along the GB plane match perfectly with the neighbouring grains. An incoherent boundary is when this perfect alignment does not occur (**Figure 7(d)**) [104]. Coherency

terminology is most commonly used to describe twin boundaries, with most twin boundaries being coherent.

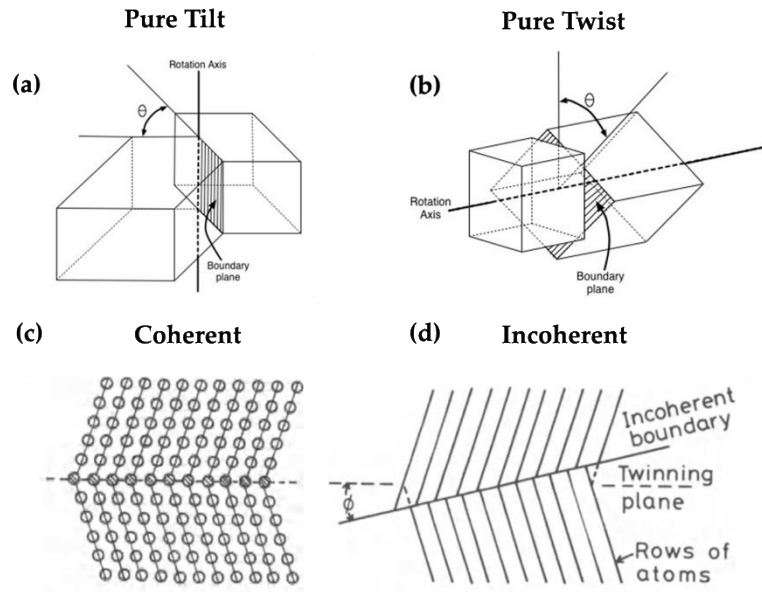


Figure 7 – Schematic diagram of (a) pure tilt grain boundary where the axis of rotation is parallel to the grain boundary plane, (b) pure twist grain boundary (axis of rotation is perpendicular to grain boundary plane), (c) coherent boundary and (d) incoherent boundary (a-b) taken from [103] and (c-d) taken from [104].

Another common convention for classifying GBs is the coincident site lattice (CSL) model [105]. According to this model, boundaries are assigned a number (Σ) that relates to the reciprocal number density of lattice sites that coincide between lattices of both grains. For example, a $\Sigma 5$ boundary indicates that 1 in every 5 atoms in the lattice is common (coincident) in both grains. Boundaries with low Σ values indicate a relatively high level of atomic fit between the joining crystal orientations and as a result are expected to have lower energy than random GBs. Based on the fact that the GB plane undoubtedly influences the extent of atomic overlap, only pure tilt or twist boundaries are typically expected to

have a high density of CSL. However, this model does not specifically specify the GB plane, so it only captures three of the five DOFs.

The study of GB mobility has primarily been centered on the study of bicrystals due to the inherent simplicity but have provided valuable insight into GB mobility nonetheless [106–108]. **Figure 8(a)** shows the mobility of 388 distinct GBs with varying misorientation and type (tilt, twist, mixed) predicted by MD simulations on Ni bicrystals under energy-jump driving force at 1400K [99]. The results indicate that there is a slight increase in mobility with decreasing misorientation angle. This is contrary to the generally accepted view that mobility increases for HAGB compare to LAGB [77,109], but the researchers claim this discrepancy could be a result of limitations in mobility resolution at small misorientations and as a result, the data set does not include LAGB below 10° misorientation. The results do effectively illustrate that different boundaries have different mobilities, with $\langle 111 \rangle$ twist boundaries showing the lowest mobility. It was also found that shear-coupled motion is strongly related to boundary mobility, with the boundaries showing highest mobility also moving by a coupled shear mechanism, although this was not found to remain true for the highly mobile $\Sigma 3$ twin boundaries. Olmsted *et al.* also determined that GB mobility is not closely correlated with Σ value (**Figure 8(b)**) with the single exception of $\Sigma 3$ boundaries [99]. Other MD simulations on a flat GB in an Al bicrystal have determined that the mobility of mixed-type boundaries is markedly higher than that of a pure twist or tilt boundary which is expected due to the increased disorder of mixed-type boundaries [109]. The simulations also showed that two GBs with the same misorientation angle-axis pair but different boundary planes can have very different mobilities. This indicates that the boundary plane could be a major factor that influences

mobility and in general it was found that mobility increased as the GB plane deviated from (111), with high-coincidence and LAGB as exceptions. Other GB processes have also been found to be dependent on GB structure. For example, MD simulations on nickel bicrystals have shown that dislocation transmission through a boundary is heavily dependent on GB misorientation angle, with high-angle tilt boundaries showing unlikely transmission when compared to low-angle tilt boundaries [110].

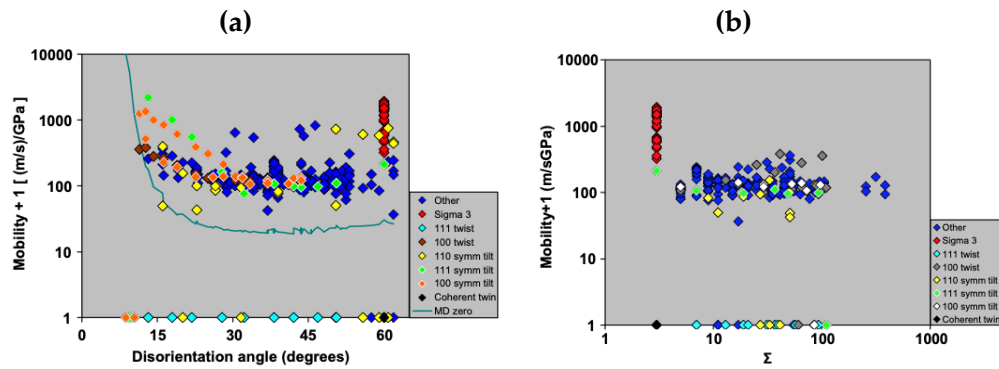


Figure 8 – Mobility as a function of (a) disorientation angle and (b) Σ value for Ni at 1400K for all 388 boundaries simulated [99].

1.5.3 Disconnections

Understanding the different structures of GBs is important because the bicrystallography heavily influences the overall kinetics of the GB. One of the widely accepted models of GB kinetics, first proposed in the 1970s, involves the dynamics of GB disconnections [111–113]. Disconnections are line defects that contain both a step h and dislocation character \mathbf{b} . An example of a GB with a disconnection is shown in **Figure 9(a)**, with both \mathbf{b} and h indicated. In this model, the glide of disconnections facilitates both GBM (through the step height h) and GB sliding (through the Burger's vector \mathbf{b}). Because disconnections are defects that lie within a boundary, it is not surprising that the specifics

of a disconnection ($\{\mathbf{b}_n, h_{nj}\}$) are directly influenced by the bicrystallography of the GB. In fact, the bicrystallography of a boundary defines the set of permissible disconnection modes $\{\mathbf{b}_n, h_{nj}\}$ [97].

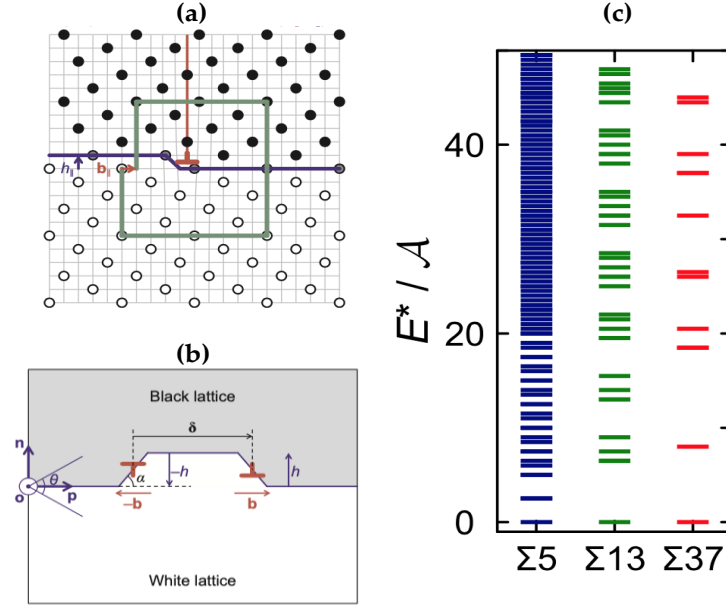


Figure 9 – (a) A bicrystal GB containing a disconnection dipole, (b) Schematic of a nucleated disconnection dipole, (c) quantized disconnection formation energy for $\Sigma 5$, $\Sigma 13$, $\Sigma 37$ grain boundaries [97].

In this model, GBM occurs by the nucleation and glide of permissible disconnections which is inherently controlled by GB bicrystallography. The energy required to form a pair of disconnections (a disconnection dipole) depends directly on both \mathbf{b} and h based on the following relationship and the schematic shown in **Figure 9(b)** [97]:

$$E = 2E_{step} + 2E_{core} + E_{int} = 2[\Gamma_s |h|] + 2[\zeta K \mathbf{b}^2] + 2K \mathbf{b}^2 \ln(\delta/r_0) \quad (16)$$

In this equation, Γ_s is the excess surface energy due to the creation of a step, ζ is a core energy scale factor, $K \equiv \mu/4\pi(1 - \nu)$ (μ is shear modulus, ν is the Poisson's ratio), δ is the

disconnection separation and r_0 is the disconnection core size. The above equation is considering only 2D disconnection modes, however, a generalized energy barrier can take the form:

$$E_{nj}^* = A|\widetilde{h_{nj}}| + B\widetilde{\mathbf{b}_n^2} \quad (17)$$

where A is the excess energy density due to the step and B includes dislocation core energy and elastic interaction between the two components of the disconnection pair [97]. For tilt GBs, $B \propto \Sigma^{-1}$ which inherently implies that the character of \mathbf{b} is most important. This means that for low- Σ tilt GBs, disconnection modes with small \mathbf{b} are most favorable. Conversely, GB step dominates disconnection mode/energy for high- Σ tilt GBs and thus small h is most favorable [97].

The above equations show that disconnection nucleation is not energetically favorable and that disconnection dipoles will collapse immediately following nucleation [97]. However, stable disconnection dipoles can be nucleated in the presence of a driving force based on the following equation for the energy of formation:

$$E = 2E_{step} + 2E_{core} + E_{int} - \tau\mathbf{b}\delta - \psi h\delta \quad (18)$$

where τ is the applied stress, and ψ is the energy jump across the boundary. This equation implies that there is a critical dipole size δ^* in which the energy decreases with further separation and that the critical separation decreases with increasing driving force (stress and chemical potential difference) [97].

The probability of disconnection nucleation of mode $\{\mathbf{b}_n, h_{nj}\}$ is proportional to the Boltzmann factor $\exp(-L_x E_{nj}^*/k_B T)$, where L_x is the periodic of the simulation supercell along the x-axis [97]. Since there are a finite set of $\{\mathbf{b}_n, h_{nj}\}$ allowed for a specific boundary based on the bicrystallography, the formation energy spectrum is quantized and unique for every possible boundary. Three example energy spectra for $\Sigma 5$, 13, and 37 boundaries for Cu are shown in **Figure 9(c)**. The disconnection mode with the lowest formation energy corresponds to the dominant/ most favorable disconnection mode, although in reality deformation occurs by an average of multiple disconnection modes [114]. The boundary with the lowest CSL Σ value has a much higher number of permissible disconnection modes than the others and the spacing between energy levels is smaller. For low CSL Σ boundaries with closer spaced energy lines, it is more likely to have multiple disconnection modes activated for a given energy allowance. Each disconnection mode will have a different mobility and temperature dependency. This is because the activation energy of a disconnection mode depends on local bonding, GB structure, point defects, solute segregation, etc [114]. This energy spectrum also determines the disconnection nucleation dependence on temperature. At high temperatures, more energy is available to nucleate high-energy disconnection modes characterized with large \mathbf{b} but small h [97]. This means that at high temperature, GB sliding dominates over GBM.

In addition to the disconnection nucleation energy barrier, there is also a barrier to disconnection glide analogous to the Peierls barrier for lattice dislocation glide. However, once again under stress-assisted GBM, the driving force associated with disconnection glide is the Peach-Koehler force along the glide direction \mathbf{b} which provides the means to overcome the glide barrier. The driving force associated with the step height h is linked to

the jump in chemical potential (energy density) across the GB [114]. Stress-assisted GBM is characterized by the shear-coupling factor, which defines the relative ratio between GBM to sliding and is given by: $\beta = v_{\parallel}/v_n = \mathbf{b}/h$ where v_{\parallel} and v_n are the average velocities of GB sliding and migration, respectively [97]. If \mathbf{b} is not parallel to the GB (as it is for symmetric and twist GBs), motion of disconnection involves climb (diffusion). As a result, GB inclination does not affect the set of possible $\{\mathbf{b}_n, h_{nj}\}$ for a given boundary, but it does however affect the manner in which disconnection glide occurs by (conservatively or non-conservatively). GBM facilitated by disconnection glide has been observed both experimentally [115] and through atomic simulations [114].

1.5.4 Influence of Triple Junctions

GBM in polycrystals is inherently complicated due to the added restrictions imposed by TJs and the interaction of a complex GB network. TJs are 1-dimensional defects where three GBs meet (see **Figure 10**). It was initially assumed that TJs did not influence the motion of connected GBs but instead facilitated control of thermodynamic equilibrium dihedral angles (θ) at the junction during migration. It has since been shown both through experiments and simulations that TJs play an increasingly important role in deformation, particularly as the grain size decreases.

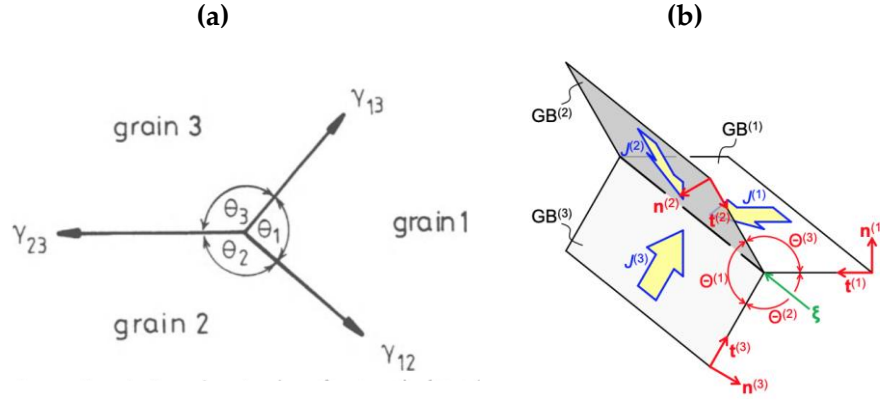


Figure 10 – (a) 1D representation of TJ structure where γ is the line tension for each GB and θ is the angle between GBs [104], (b) 3D geometry of a TJ where the three GBs (GB⁽¹⁾, GB⁽²⁾, and GB⁽³⁾) meet along line direction ξ . $J^{(1)-(3)}$ are disconnection fluxes from the three GBs to TJ [98].

The proposed mechanism of TJ migration is similar to that of GBs: the nucleation, glide, and accumulation of GB disconnections at the TJ [26,116]. Experiments have shown the amount of GB sliding decreases along the GB near immobile TJs [117,118], suggesting that TJs inhibit continued disconnection glide [97]. This occurs when the disconnections gliding in the GB cannot annihilate at the TJ and the \mathbf{b} of the disconnections accumulate. This accumulation creates back stress on the GB disconnections that either leads to TJ stagnation (by repelling subsequent disconnections) or some form of plasticity to dissolve the back stress, such as lattice dislocation emission, which has been observed both experimentally [116] and in simulation [117]. Within the disconnection model, TJs can serve as both sources and sinks for disconnections gliding along the GB. Since the ease of disconnection nucleation varies with GB structure, it is expected that TJs will show anisotropic mobility dependent on GB/TJ structure [117].

A discussion on GB kinetics in NC material would be incomplete without a similar discussion on TJ kinetics. The structure of TJs is even more complex than that of GBs with

11 DOFs (five to define first boundary, five to define a second boundary, and one to define orientation of third boundary) [118]. A simplified 1D and 3D construction of a TJ is shown in **Figure 10(a)** and (b), respectively. TJs are typically classified as one of the following: (1) R0 type with no random boundaries, (2) R1 type with two low- Σ CSL boundaries and one random boundary, (3) R2 type with one low- Σ CSL boundary and two random boundaries, and (4) R3 type with three random boundaries [119]. The addition of TJs increases the overall excess free energy of the system by imposing additional energy in the form of line tension (γ). It has been proposed that this excess energy is the driving force for TJ migration: TJs migrate in order to balance line tension imposed by constituent GBs. It is further predicted that below a certain grain size, the driving force for TJ migration outweighs that of GBM [120] and that grain growth is controlled by TJ drag [117,121]. MD simulations on TJ motion driven by capillarity has shown that TJs composed of certain CSL boundaries (particularly $\Sigma 7$ and $\Sigma 13$) exert substantial drag on GBM [122]. In any case, additional detailed investigations on NC/UFG metals is required in order to better clarify how TJ/GB structure affects TJ and GBM as well as how initial grain size plays a role in TJ/GBM. As the grain size decreases, the number of TJs increase and as such the behavior of TJs become increasingly more important.

The abovementioned disconnection-mediated GB and TJ migration model is best suited to describe behavior of CSL-type Σ boundaries, as disconnections are particularly well defined for these boundaries. It is possible to approximate non-CSL boundaries as a CSL-type GB with non-periodical distributed secondary GB dislocations [123], but there is evidence to suggest random HAGB migrate via atomic shuffling mechanisms instead [109]. Random HAGB have a more open core structure which allows for the room required

for atomic-scale rearrangement necessary to start the shuffling process. Experimental results have shown that GB motion of HAGB occurs in a ‘jerky’ step-wise fashion, with the stagnation periods occurring before required initiation of rapid atomic shuffles [109].

1.6 Radiation-Induced Changes

Material degradation resulting from irradiation is a challenge that plagues a variety of industries, including the nuclear energy sector [124,125] and the aerospace industry [126]. Notable material failure modes for structural materials include irradiation creep [127], swelling [128], and hardening and embrittlement [124,129]. These property changes originate from displacement cascades caused by energetic particles such as neutrons, protons, and ions that lead to nanometer-sized defect clusters in the form of vacancy and interstitial loops, stacking-fault tetrahedra (SFT), or voids. **Figure 11** illustrates the typical

changes in mechanical properties (increase in strength accompanied by a decrease in ductility) due to radiation damage [124,130].

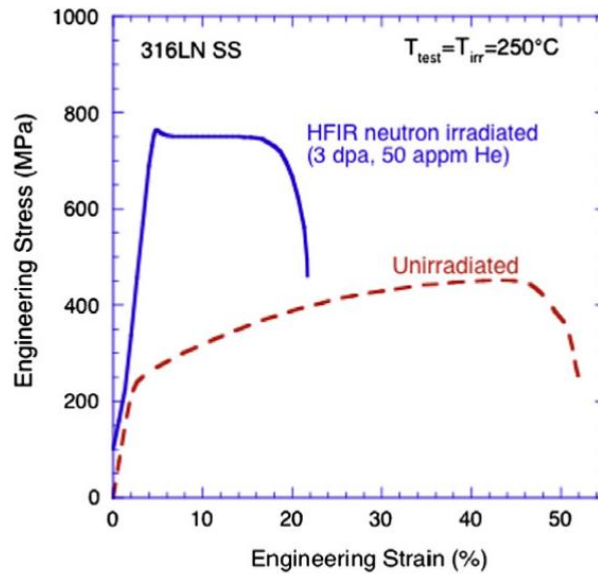


Figure 11 – Effect of neutron irradiation (3 dpa) on the engineering stress-strain curve for annealed 316LN austenitic steel [124,130].

To understand the change in mechanical properties after irradiation, numerous experimental [131–134] and computational techniques [135] have been employed. *In situ* TEM straining experiments [132,133] on irradiated material have been particularly useful in identifying interactions between dislocations and radiation defects. These studies show that radiation defects can impede dislocation glide (leading to an increase in strength) but that these defects can be eventually removed by a single dislocation or the passage of many dislocations thus leading to defect-free channels. This leads to deformation localization that has been well document during bulk-scale mechanical testing of coarse-grained materials [131,133,136] and can lead to premature failure (decreased ductility).

1.6.1 Radiation Tolerance in NC and UFG Metals

NC and UFG metals have emerged as promising radiation-tolerant materials [137–140] due to the high volume-fraction of GBs that serve as defect sinks and can lead to a drastic decrease in defect density [139,141–144]. MD simulations suggest that GBs annihilate nearby vacancies by re-emitting interstitials [145] or that regions of misfit within the boundary can be sites for interstitial and SFT absorption [144], both of which lead to the experimentally observed defect denuded zones on either side of a boundary [146]. Numerous reports have shown that irradiation also causes GBM/grain coarsening [147,148], with MD simulations proposing that migration is a response to the defect absorption [149,150]. Additional reports have shown that radiation-induced GBM can remove SFT [151], indicating that a migrating GB serves as an effective sink for defects.

In many radiation environments, materials are also subject to extreme temperatures which can lead to large thermal stresses [152]. It is well documented that stress can promote a variety of GB behaviors in non-irradiated materials, such as GBM. Therefore, it is possible that stress-assisted GB migration could facilitate additional defect removal in irradiated materials. In fact, MD simulations on bicrystals have highlighted that shear-coupled GB motion can remove intragrain SFT [153] and partially dissolve voids [154], leading to an interstitial-loaded GB that can remove defects in its path [152,155]. Stress-assisted GBM is a common deformation mechanism in non-irradiated NC and UFG metals [20,63,68,94] which suggests that these materials might have an additional ‘self-healing’ mechanism that could facilitate a further increase in radiation-tolerance when subject to mechanical stresses.

1.7 Motivation and Thesis Objectives

It is evident that NC and UFG metals are an important class of materials due to their unique mechanical properties that arise from the high volume fraction of GBs. It has been shown that NC/UFG metals exhibit an increase in strain-rate sensitivity and decrease in measured activation volume compared to their coarse-grained equivalents, both of which imply different atomistic mechanisms control the deformation. Years of research has provided evidence that alternative deformation mechanisms involving GBs are activated at decreasing grain sizes, such as dislocation nucleation/absorption at GBs, GBM, GB sliding, etc. However, there remains a lack of quantitative characterization for these deformation mechanisms and not fully understanding the plastic kinetics in NC and UFG metals is hindering material design towards exceptional mechanical properties. MD simulations provide useful information regarding the plastic kinetics of individual mechanisms; however, they suffer from time- and small-scale limitations that make comparing with experimental result nontrivial. *In situ* TEM straining techniques are required for characterizing the active deformation mechanism but most are limited in the ability to estimate the far-field applied stress and thus cannot accurately quantify the mechanical properties during straining. Therefore, new studies and techniques are required to characterize the microstructure evolution during straining of NC/UFG metals in detail while concurrently quantifying the mechanical properties.

This thesis aims to use an *in situ* quantitative MEMS-based nanomechanical testing technique to investigate how microstructure controls the deformation mechanisms and relate it to the measured mechanical properties. This includes both the qualitative identification and characterization of the active deformation mechanisms from TEM

images/videos, and also quantification of the mechanical properties through the measurement of activation volume, strain-rate sensitivity, yield strength, etc.

The specific objectives of this thesis are as follows:

- Determine the grain size effect on deformation mechanisms and measured activation volume by characterizing the plastic deformation in UFG and NC Al specimens with varying grain sizes.
- Determine the effect radiation damage has on the active deformation mechanism of UFG Au films.
- Interpret all experimentally measured (sample-level) activation volume values and relate to individual mechanisms through existing models and MD simulations.
- Investigate how local microstructure (grain size, GB character, Schmid factor, etc) influences stress-assisted GBM/grain growth in UFG Au films.

CHAPTER 2.

EXPERIMENTAL METHODS

2.1 Overview

The following chapter outlines the experimental methods used in this study. Section 2.2 describes the geometry and basics of operation of MEMS-device used to conduct the *in situ* TEM experiments, including details regarding a recently redesigned MEMS to improve experimental yield. Section 2.4 outlines the steps required to fabrication the tensile specimens. Section 2.5 discusses the irradiation parameters and Section 2.6 will briefly describe the characterization tools used to study the material microstructure.

2.2 *In Situ* MEMS-Based Technique

2.2.1 *MEMS Geometry and Capacitive Sensing*

The *in situ* TEM tensile testing is executed via a MEMS-based nanomechanical technique that has been previously used in Refs. [92,93,156–158]. The MEMS device consists of a thermal actuator (*TA*), two capacitive sensors (CS_1 and CS_2), load sensor (*LS*) beams and a specimen gap (*SG*) (see **Figure 12**(a) and (c)). The MEMS are fabricated by MEMSCAP using the SOIMUMPS process.

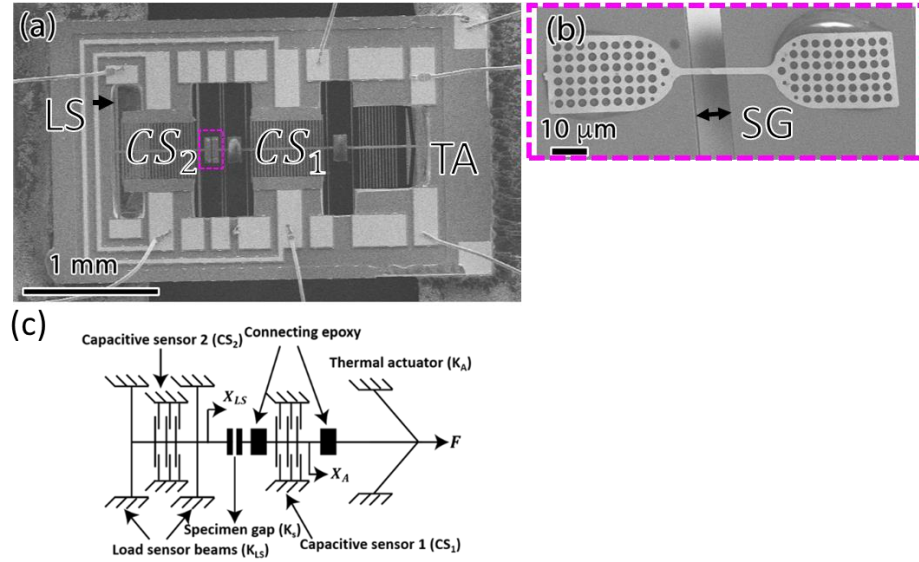


Figure 12 – MEMS device tensile testing operation. (a) SEM image of the MEMS device with the thermal actuator (TA), capacitive sensor one (CS₁), capacitive sensor two (CS₂), and the load sensor (LS) beams labeled. The specimen gap (SG) is outlined in magenta and shown at a higher magnification in (b). (b) SEM image of a specimen on MEMS device clamped with glue. (c) Schematic of the MEMS device showing the key components.

The thermal actuator is composed of ten inclined pairs of beams and provides the displacement. When a voltage is applied across the thermal actuator, resistive heating of the beams drives the displacement of the device's central shuttle. A large heat sink is provided between the thermal actuator and the nearest capacitive sensor to limit the temperature increase at the specimen gap to 0.07 °C/10 nm actuator displacement [159]. The load and displacement of the specimen are electronically measured using capacitive sensors. The capacitive sensors are composed of a set of fixed beams (attached to device) and a set of mobile beams (attached to the central shuttle). When a voltage is applied, the displacement of the actuator (X_a) causes a shift in the mobile beams which leads to a change in capacitance. The displacement of each capacitance sensor (X) can be related to the capacitance following:

$$C = \alpha \kappa \varepsilon_0 n A \left(\frac{1}{d_1 - X} + \frac{1}{d_2 + X} \right) \quad (19)$$

where α is the calibration constant, κ is the relative permittivity of air, $\varepsilon_0 = 8.854 \times 10^{-12} \text{ Fm}^{-1}$ is the permittivity of free space, n is the number of comb structures ($n = 42$), A is the overlapping area of the comb structure, and d_1 and d_2 are the nominal gaps in the comb structure. These are measured prior to starting an experiment using TEM images. Both capacitive sensors are calibrated individually for each test. The measured change in capacitance ΔC between the initial ($X = 0, V_{in} = 0$) and current state (X, V_{in}) is given by:

$$\Delta C = \alpha \kappa \varepsilon_0 n A \left[\left(\frac{1}{d_1 - X} + \frac{1}{d_2 + X} \right) - \left(\frac{1}{d_1} + \frac{1}{d_2} \right) \right] \quad (20)$$

The capacitance measurements are measured using a commercially available capacitive readout sensor MS3110 (Microsensors Inc.) For more details regarding the capacitance measurements and calculations, see Refs. [156,159].

2.2.2 Stress and Strain Calculation

The first capacitive sensor (CS_1) is rigidly connected to the thermal actuator and thus measures the displacement of the thermal actuator X_A . The second capacitive sensor (CS_2) is directly connected to the load sensor beams and measures the displacement of the load sensor (X_{LS}) which has a known load sensor stiffness (K_{LS}) of either 480 or 100 Nm^{-1} .¹ Since the specimen gap lies in-between the two capacitance sensors, the displacement of the specimen can be determined:

$$X_S = X_A - X_{LS} \quad (21)$$

The displacement of the load sensor X_{LS} is used to calculate the force on the specimen using the known stiffness of the load sensor beams.

$$F = K_{LS}X_{LS} \quad (22)$$

Stress and strain are then calculated by considering the specimen geometry. The gauge length (l) is estimated by measuring the free-standing portion from SEM images taken before or after the experiment and the gauge width (w) is estimated prior to the experiment from TEM images. The thickness (t) is pre-defined per the fabrication recipe. The (engineering) stress (σ) and strain (ε) are calculated following:

$$\sigma = \frac{F}{tw} \quad (23)$$

$$\varepsilon = \frac{X_S}{l} \quad (24)$$

As the freestanding gauge length varies depending on sample manipulation, the gauge length is measured in the SEM for each specimen. This definition of strain is based on the cross-head displacement which leads to inaccurate elastic strain measurements due to finite deformation of the specimen within the fillet region in contact with the glue [157]. As a result, the slope of the linear region of the stress-strain data is not an accurate measurement of the Young's modulus. Despite this, previous work has shown that the plastic strains (ε_p) are measured accurately with this technique and are determined using the following equation,

$$\varepsilon_p = \varepsilon - \sigma/E \quad (25)$$

here ε and σ are the total strain and stress measured by the MEMS device and E is the measured apparent Young's modulus.

2.2.2.1 Pre-Stress Measurement

The specimens are secured across the specimen gap using UV curable glue and upon curing, the glue shrinks which can lead to 'pre-stress' imparted on the specimen prior to the test beginning. This indicates that at the beginning of a test, the stress does not begin at 0 MPa, but rather at the pre-stress value. Pre-stress is measured by determining the displacement of the CS_2 beams due to the pre-stress (i.e. X_{LS}^{Pre}). This is done by comparing the distance between the comb structure in CS_2 before the test begins and after the specimen fails (and CS_2 returns to its original location before a specimen is placed and pre-stress causes a shift in the load sensor). The change in this distance is equal to X_{LS}^{Pre} . Pre-stress value typically ranges from 10 – 300 MPa.

2.2.3 *Experimentally Measuring Activation Volume*

When the total strain is held constant, a material undergoes stress-relaxation due to time-dependent deformation. Repeated stress-relaxation tests are done to differentiate the effect of mobile dislocation density and dislocation velocity on the strain rate. These experiments are conducted by performing successive short relaxation segments with a short reloading segment in between. The reloading segments must be quick (and elastic) to ensure frozen microstructure, and thus constant dislocation density. If this is the case, the

difference in strain rates for different relaxation segments can be attributed to a change in dislocation velocity only.

With this technique, a stress-relaxation segment is performed by keeping the actuator displacement X_A constant (i.e. holding a constant V_{in}). This implies that during a relaxation, the following condition is true:

$$X_A = X_S + X_{LS} = constant \quad (26)$$

As plastic deformation occurs during a relaxation segment, the plastic strain increases (X_S increases) which results in a decrease in X_{LS} and thus a measured decrease in stress. During a relaxation segment, the plastic strain rate can be determined following:

$$\dot{\epsilon}_p = -\dot{\sigma}/M \quad (27)$$

where $\dot{\sigma}$ is stress rate obtained by fitting the stress relaxation data with logarithmic fit and M is the machine-specimen stiffness [72,92,156,157]. The load sensor is assumed to undergo elastic deformation only and M is given by:

$$M = \left(\frac{K_{LS}K_S}{K_{LS} + K_S} \right) \left(\frac{l}{wt} \right) \quad (28)$$

The true activation volume V^* can then be calculated using the following equation.

$$V^* = \sqrt{3}kT \frac{\ln(\dot{\epsilon}_{i2}/\dot{\epsilon}_{f1})}{\Delta\sigma_{12}} \quad (29)$$

In the above equation, $\dot{\epsilon}_{f1}$ and $\dot{\epsilon}_{i2}$ are the final and initial strain rates for the first and second relaxation segment, respectively and $\Delta\sigma_{12}$ is the stress increase during reloading. The $\sqrt{3}$ term arises from converting the shear stress/strains to normal stress/strains following $\sigma = \sqrt{3}\tau$. Since dislocation density ρ_m is constant, the change in plastic strain rate is a direct result of a change in dislocation velocity, which is a thermally activated process (according to Eqn. (8)) and thus $\Delta\sigma_{12}$ represents a change in effective stress τ^* .

By combining Eqn. (29) and Eqn. (27), the true activation volume V^* can be calculated from:

$$V^* = \sqrt{3}kT \frac{\ln(\dot{\sigma}_{i2}/\dot{\sigma}_{f1})}{\Delta\sigma_{12}} \quad (30)$$

Using Eqn. (30) eliminates the dependency of V^* on the strain rate and instead implies that the accuracy of V^* depends on the stress rate, which is independent of gauge length and is more accurately determined using this technique. The accuracy of the determined stress rate depends on the signal-to-noise ratio (SNR) of the measurement. Previous work has shown that a $\text{SNR} > 5$ requires logarithmic fits with $R^2 > 0.9$, which is used as a criterion for accurate V^* measurements [92]. This technique is also capable of measuring apparent activation volume by fitting the relaxation with a logarithmic fit and using Eqn. (13).

2.2.4 MEMS-Device Limitations

The abovementioned MEMS device is a useful tool for performing *in situ* TEM straining experiments while simultaneously quantifying the mechanical properties, however, it does suffer from some limitations that decrease experiment yield. The most

significant and hardest to account for is parasitic capacitance and drift in the capacitive signals. This can take a variety of forms and can ultimately lead to data that is unrealistic (i.e. capacitance signals that indicate negative stresses even when specimen is under tension). It can also invalidate the assumption that the calibration constant α is constant through the full duration of an experiment.

Another limitation is the overall stability of the device during relaxation segments (V_{in} held constant). During a relaxation segment, it is assumed that X_A is held constant which indicates that any decrease in X_{LS} is due to an increase in X_S only (i.e. specimen elongation due to plastic deformation). However, by measuring X_A manually using TEM videoing, it has been shown that X_A actually increases slightly at a constant V_{in} (**Figure 13**). The individual paused segments are shown in more detail in **Figure 13**(b) and (c) for $V_{in} = 3V$ and $V_{in} = 6V$, respectively. Over the course of the 60-second pause, X_A increased by 60 nm when $V_{in} = 3V$ and by 115 nm when $V_{in} = 6V$. This suggests that the drift in X_A worsens as V_{in} increases. At higher V_{in} , the temperature of the TA is increased which could decrease the stability as the TA reaches thermal equilibrium. Overall, the drift in X_A means that the total amount of stress-relaxation (decrease in X_{LS}) might be underestimated since X_A continues to increase slightly during the relaxation segment, although this is expected to have minor effect on measurements made. In order to minimize the effect of this instability, MEMS with stiffer load sensors (higher K_{LS}) should be used because lower V_{in} will be required to achieve sufficient stress levels.

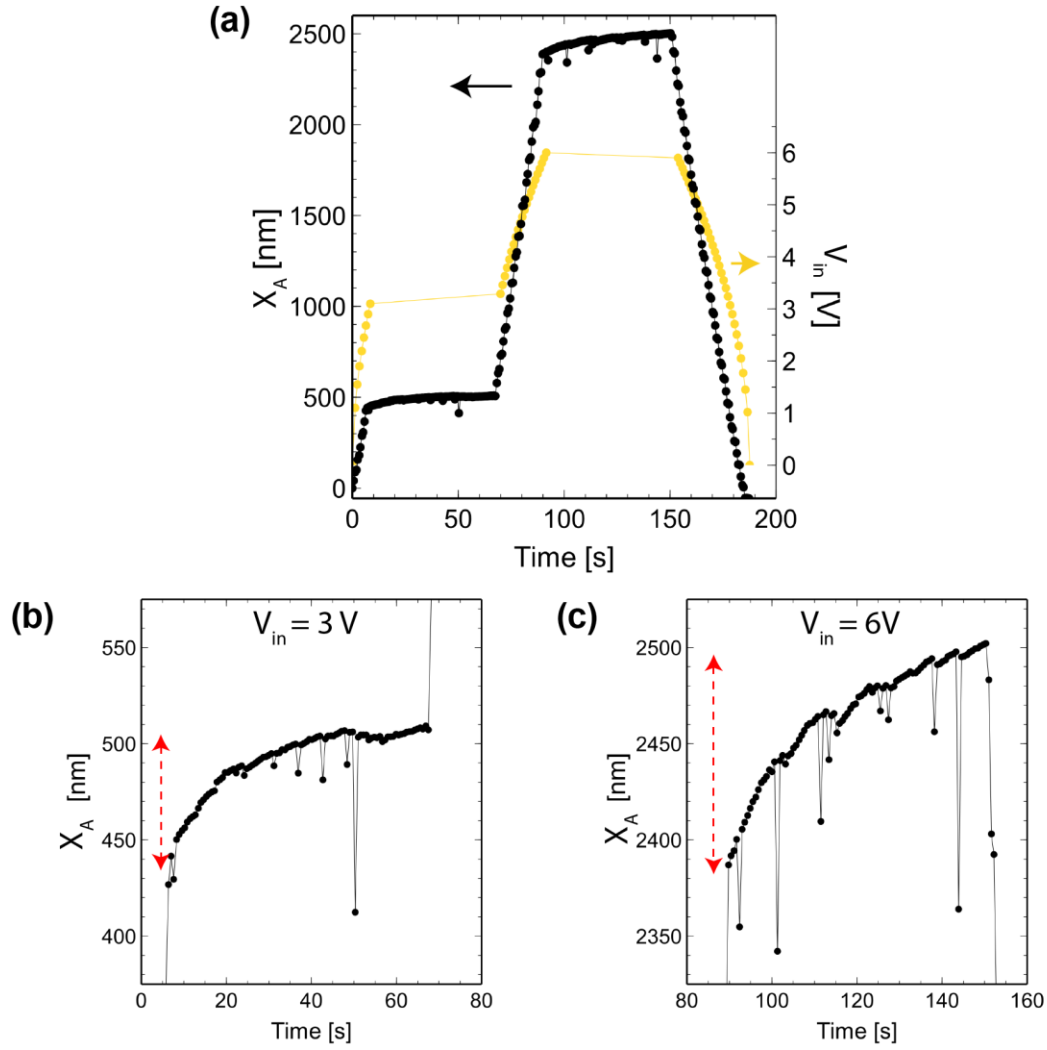


Figure 13 – Physical drift in X_A during a paused segment (constant V_{in}). (a) Full X_A data for the V_{in} loading scheme. The loading was paused at (b) $V_{in} = 3$ V and (c) $V_{in} = 6$ V. In both cases, X_A increases during the paused segment by the amount represented with the red double-arrow.

Because the technique was developed to measure stress (used to measure V^*), the technique does suffer from uncertainty in the strain measurement. This is due to the (1) deformation of the specimen/epoxy glue used to clamp the specimens and (2) uncertainty in the initial gauge length. 3D finite element modeling (FEM) of the specimen and epoxy clamps indicate that the compliance of the glue leads to finite deformation of the thin film

specimen along both the fillet region and the gauge section that is in contact with the glue [157]. These sections of the specimen are not included in the free-standing gauge length used to calculate strain and therefore contributes to errors in the strain measurements. This results in an underestimate of Young's modulus using this technique and stems from the approximate calculation of strain based on crosshead displacement values. While the measured value of Young's modulus is highly sensitive to the accuracy of small strain measurement, this issue does not affect the ability of the technique to measure relatively large plastic strains, as has been previously demonstrated [92,93,157]. Additional characterization has shown that the epoxy clamps do not deform plastically, so it is reasonable to assume most of the plastic deformation of the specimen only occurs within the free-standing gauge section and thus plastic strain measurements are reliable.

2.3 Updated MEMS-design: Imaged-Based Sensing

Given the occasional unreliable nature of the electrical-based sensing, the MEMS-device has recently been redesigned without capacitance sensors and instead utilizes a new 'image-based' technique. Instead of relying on capacitance measurements to determine the displacement of the thermal actuator X_A and load sensor beams X_{LS} , it uses the imaging capability of the TEM to manually measure each displacement separately and simultaneously. This also eliminates any uncertainty that was previously present due to errors in calibration constant or electrical drift. SEM images of the updated MEMS are shown in **Figure 14**.

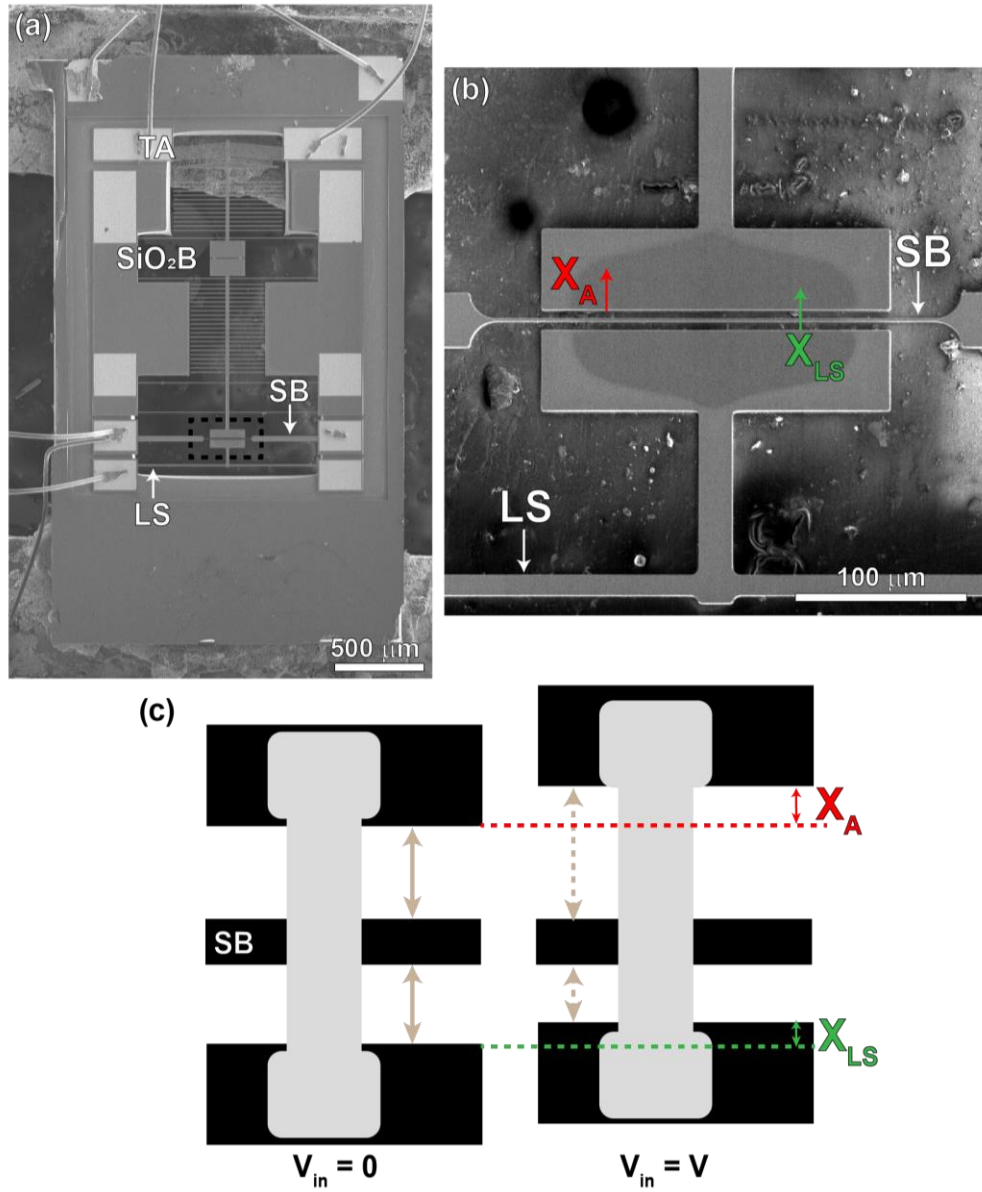


Figure 14 – SEM images of image-based MEMS device. (a) Full device with the thermal actuator (*TA*), SiO₂ bridge (*SiO₂ B*), stationary beam (*SB*), and load sensor (*LS*) labeled. The specimen gap is outlined and shown in more detail in (b). The displacement of the actuator X_A and load sensor X_{LS} are indicated. (c) schematic of the MEMS operation.

The basics of operation is similar to the previous MEMS design in that a voltage is applied across the thermal actuator to cause a displacement of the central shuttle. Now, there are no capacitive sensors and instead, there is a thin (2 μm) stationary beam (*SB*) that

lies in the middle of the specimen gap (the specimen gap is shown in more detail in **Figure 14(b)**). This beam serves as a reference point for the displacements (X_A and X_{LS}) to be measured. The schematic shown in **Figure 14(c)** illustrates how the measurements are determined. At the $V_{in} = 0$ state, there is no applied voltage and the initial distance between the *SB* and the top and bottom specimen pads are indicated by the brown arrows. After a voltage is applied ($V_{in} = V$), the central shuttle is shifted by X_A which shifts the specimen by X_S and the load sensor by X_{LS} . The top pad of the specimen gap is rigidly connected to the thermal actuator, so the movement of this pad is exactly the displacement of the actuator (X_A) whereas the bottom pad is rigidly connected to the load sensor so the movement of this is the displacement of the load sensor (X_{LS}). Measuring these simultaneously requires a fixed object to be able to separate the total increase in the specimen gap into the two components (X_A and X_{LS}). To do this, the gap sizes indicated by the dashed brown arrows are compared to the original gap sizes (solid brown arrows) to determine X_A and X_{LS} .

An example of how this is done during an *in situ* TEM experiment is shown in **Figure 15** which provides a series of images during a monotonic test. In all of the frames, the stationary beam is visible to serve as the reference point. As a voltage is applied, the top Si pad is displaced by X_A and by being connected via the specimen, the bottom Si pad is displaced by X_{LS} . The progression of these displacements is easily visualized by noting the distance between the position of either pad and the red and green dotted line. The displacements are shown in **Figure 15(d)**. The example shown also illustrates how local strain can be estimated and compared to the nominal strain. This was done by measuring the distance between the two points indicated by the arrowheads. Note that pre-stress is measured in a similar manner described in Section 2.2.2.1. Now, the difference in the

distance between the stationary beam and the lower specimen pad (the gap used to measure X_A) before the specimen is placed and after specimen failure is X_{LS}^{Pre} .

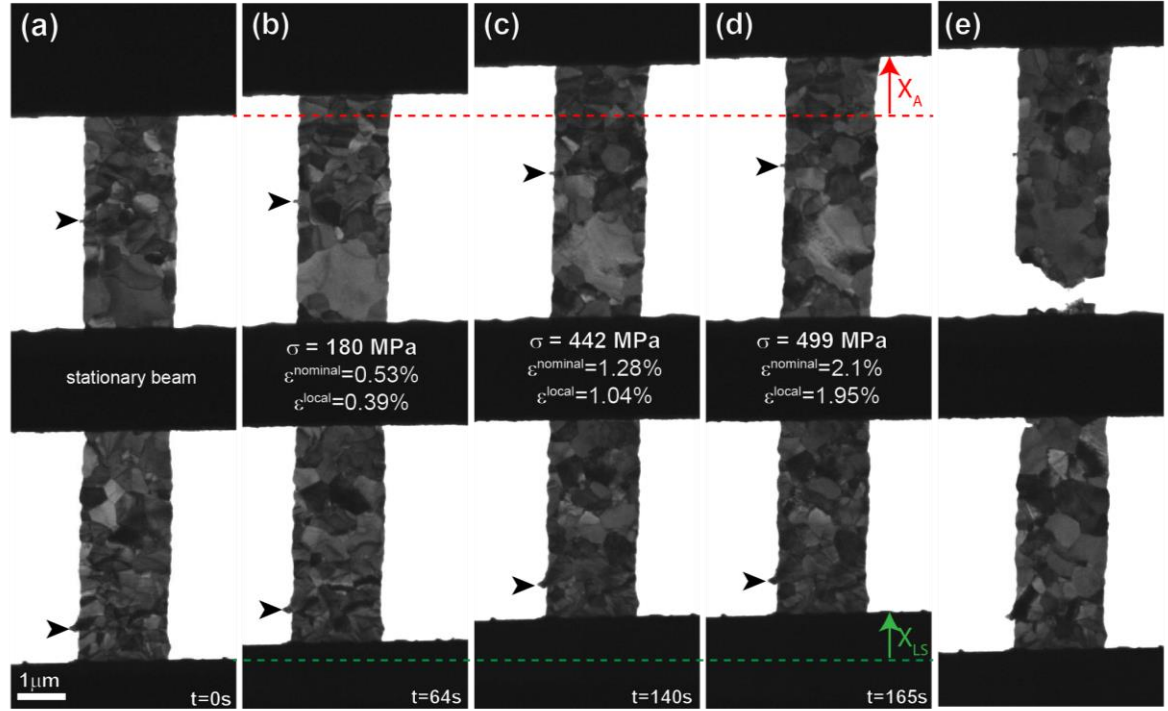


Figure 15 – *In situ* operation of image-based MEMS during monotonic tensile test. The stationary beam is labeled and remains in the same position. (b)-(d) images captured throughout the experiments. The time stamp, far-field stress levels, nominal and local strain are provided. The local strain is estimated by measuring the distance between the two indicated edge features. (d) X_A and X_{LS} are indicated.

The glued pads connecting the different components of the MEMS device have been replaced by an oxide bridge to eliminate any effect of the glue on the measurements. The oxide bridge (SiO_2 B) serves as both a physical connector but also provides electrical isolation between the thermal actuator and the specimen. The table below provides the nominal specifications of the MEMS devices compared to values that have been measured.

Table 2 – Measurements of MEMS features compared to the nominal dimensions.

MEMS Feature	Nominal Dimension	Measured
Structural Si thickness	25 μm	23.9 μm
Load sensor width: $K_{LS} = 125 \text{ N/m}$	12.5 μm	12.8 μm
Load sensor width: $K_{LS} = 600 \text{ N/m}$	21 μm	20.7 μm

2.3.1 Comparing Data from Electrical- and Imaged-based Sensing Techniques

Section 2.2.4 suggests that the electrical capacitive sensing was occasionally unreliable due to unknown reasons (presumably due to parasitic capacitance). It is important to stress, however, that when the electrical sensing worked it yielded reliable results comparable to image-based sensing results. This is shown in **Figure 16**. This monotonic experiment was conducted using the capacitive sensing MEMS (Section 2.2.1) while simultaneously using the TEM to video CS_2 throughout the experiment. This allows for the comparison of X_{LS} determined from capacitive sensing (using Eqn. (20)) with the X_{LS} determined manually from the CS_2 video. The results indicate almost a perfect match between the ‘Image-based’ and ‘Sensing-based’ data indicating that with correct calibration and minimal parasitic capacitance, the electrical sensing is reliable. There appears to be minor variation after specimen yielding occurs and during specimen failure, however, these variations do not significantly impact the overall curves. The image-based data is ‘cleaner’ than the electrical sensing-based (fewer outliers) which implies the advantage of implementing an image-based only MEMS.

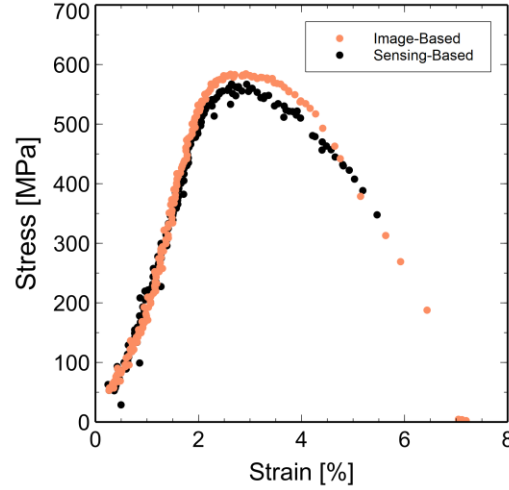


Figure 16 – Comparing electrical- and image-based sensing results under monotonic loading conditions for a UFG Au specimen.

The comparison of image- and sensing-based results during a stress-relaxation experiment is shown in **Figure 17**. **Figure 17(a)** is the full stress vs. time curve for the experiment. At the beginning of the experiment, the image-based (orange) and sensing-based (black) data match up well. However, after 400-seconds the data begins to deviate with the image-based results reaching slightly higher stress levels. This deviation between image-based and sensing-based results could indicate that the calibration constant α needs to be updated throughout the test to ensure X_{LS} from the capacitive sensing matches that of the image-based data. The relaxation behavior for three of the relaxations are shown in **Figure 17(b)-(d)**. For all of these relaxation segments, the image-based data achieves slightly larger relaxation levels ($\Delta\sigma$). The image-based data is ‘cleaner’ with higher R^2 values for all relaxation segments, indicating that the noise in the data is decreased by utilizing the image-based technique.

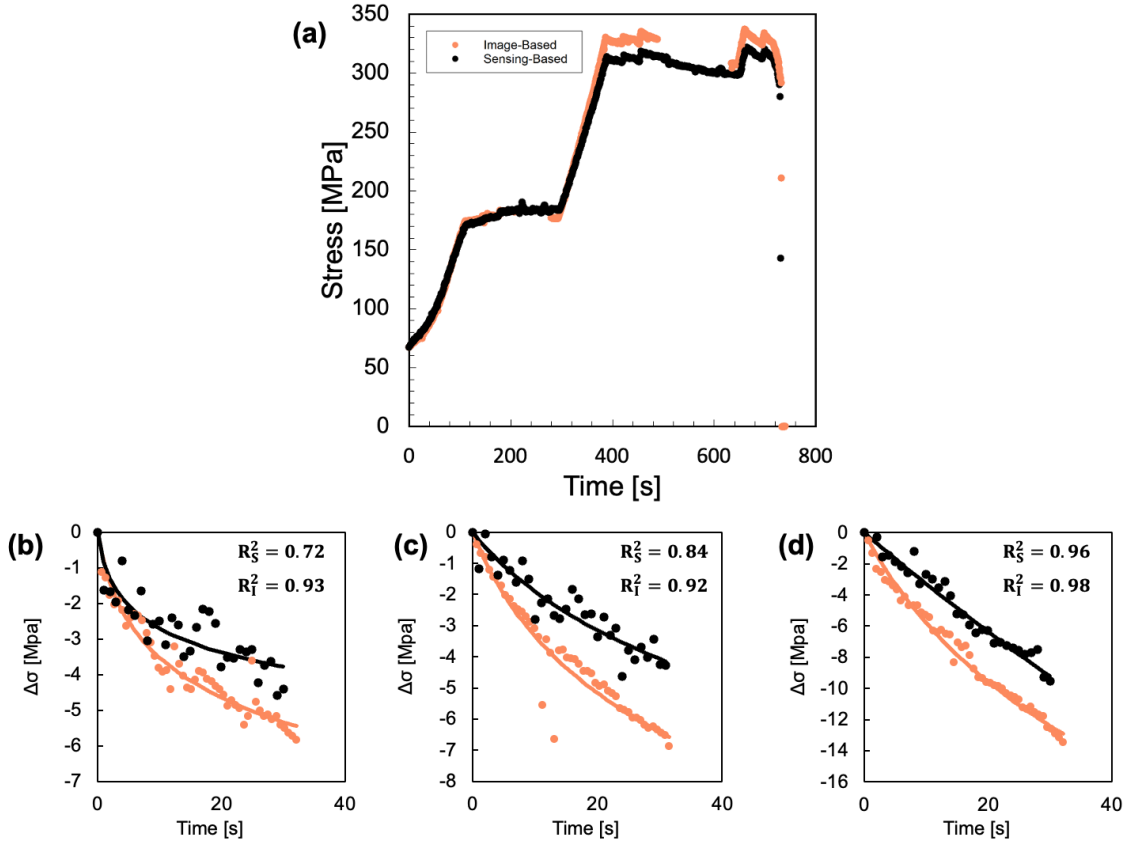


Figure 17 – Comparing electrical- and image-based sensing results during stress-relaxation experiment. (a) Stress vs. time data for full experiment until specimen failure, (b)-(d) individual relaxation segments. The solid lines are logarithmic fits of the corresponding datasets.

It is important to note that these examples are not a direct comparison of the electrical- and image-based sensing techniques since the image-based MEMS does not have the capacity for electrical capacitive sensing. These comparisons are done by comparing the electrical sensing results with a hybrid image-based sensing technique by videoing CS_2 during the experiment to measure X_{LS} directly and compare to the X_{LS} determined from electrical-sensing (using method described in Section 2.2.1). The method for measuring X_{LS} using the image-based MEMS is the same and as such these results are sufficient for comparing the two techniques. Comparing the techniques indicates that the

image-based method is more accurate and precise. The capacitive sensing has a typical noise level of 0.1-0.2 fF in capacitance which translates to a precision of 1-2 MPa in stress. The image-based sensing has improved noise levels of ~ 0.1 nm (< 0.1 MPa).

2.4 Specimen Fabrication and Manipulation

The specimens used in this study are fabricated in the Micro/Nano Fabrication Facility at the Georgia Institute of Technology. The specimens are fabricated independent of the MEMS device which allows each MEMS device to be used to test multiple specimens. The specimen fabrication process involves optical lithography to define the desired pattern followed by electron-beam evaporation of the metal thin film, a lift-off technique, and XeF_2 etching of Si substrate to ‘release’ the specimens. Detailed description of each of the processes steps is provided in **Table 3**. After the release, a portion of specimens were annealed to different temperatures and held for different time durations. This step is Step 10* and indicated by an asterisk because this step is not followed for every specimen.

Table 3 – Detailed description of the fabrication steps and specifications for the thin film fabrication.

Step #	Process	Equipment	Specifications
1	Spin coat Si wafer	SC8 G3P8 Spin Coater	Photoresist: NR9-1500PY (3000rpm, 40-seconds)
2	Soft-bake	Hot plate	150°C, 60-seconds
3	Optical lithograph	Heidelberg MLA 150	Dose: 860 mJ/cm ² ; Defocus: -2
4	Hard-bake	Hot plate	100°C, 60-seconds
5	Develop	Glassware	Developer: RD6; 12-seconds
6	Remove residual resist	Vision RIE	Recipe: Descum, 90-seconds
7	Metal deposition	Denton Explorer	Rate: 0.5 Å/s
8	Lift-off	Sonicate	Acetone solution, <5-seconds

9	Substrate etch	Xactix	40 cycles, 10-seconds each, 3T XeF ₂ , 9T N ₂
10*	Anneal	SSI RTP	A350 specimens: 350°C, 30-minutes A700 specimens: 700°C, 5-minutes

The fabrication process results in free-standing cantilevers with the nominal dimensions shown in **Figure 18(a)** (specimen pattern was drawn using AutoCAD). **Figure 18(b)** is an SEM image of the final specimens after they have been released. They can be manipulated onto the MEMS device using an approach that does not utilize a Focused Ion Beam (FIB). This ensures that minimal damage to the specimen is caused during manipulation. FIBs are notoriously known to cause ion implantation which can have a significant impact on the mechanical properties of specimens.

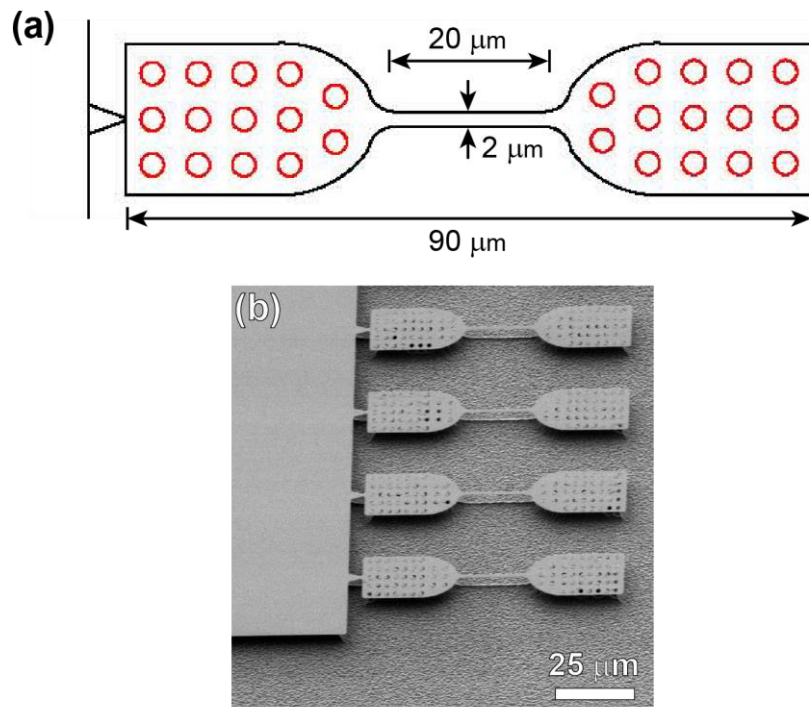


Figure 18 – Specimen geometry. (a) Schematic of the specimen with nominal dimensions labeled, (b) SEM image of the released specimens.

2.5 Specimen Irradiation

A subset of Au specimens were irradiated at the Ion Beam Laboratory (IBL) at Sandia National Labs. A 2.8 MeV Au⁴⁺ ion beam was used with a fluence of 5.5×10^{13} ions cm⁻². Based on the Stopping and Range of Ions in Matter (SRIM 2013) [160] (Kinchin-Pease Estimates) using a 40 eV displacement energy [161], **Figure 19**, shows the average dpa in the Au film is ~.65 dpa (displacement per atom), and there is minimal Au implantation in the film, with the peak implantation concentration of 30 appm.

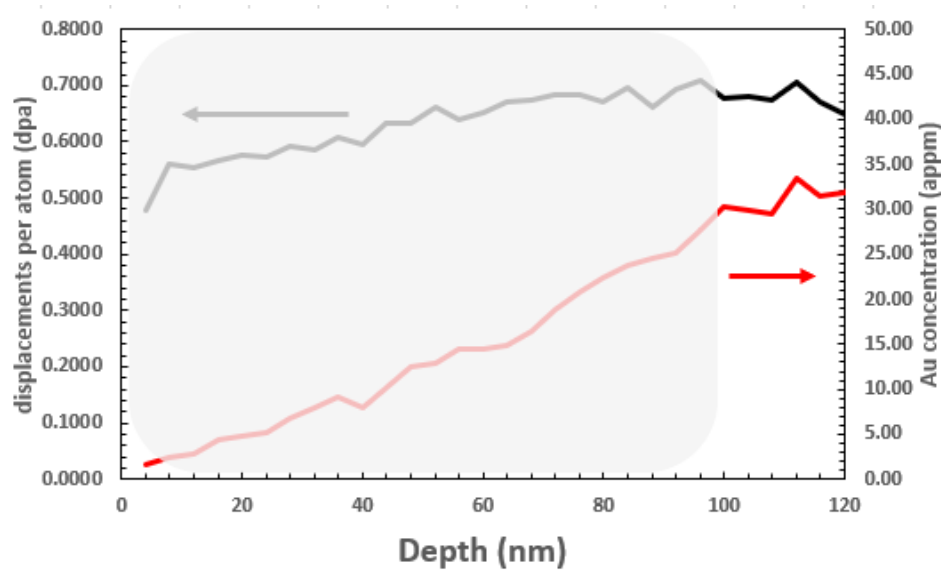


Figure 19 - SRIM-estimated damage profile (black) and Au implantation profile (red) for 100 nm-thick Au film irradiated with 2.8 MeV Au ions. Shaded area in the plot indicates the thickness of the Au film, offering a visual guide. Average dpa in the film is ~0.65 dpa and peak implantation level is 30 appm.

2.6 Characterization

2.6.1 Transmission Electron Microscopy

The *in situ* experiments were performed in a FEI Tecnai F30 TEM operating at 300 kV using a 7-lead Hummingbird Scientific electrical biasing TEM holder. Images and videos were collected using a Gatan OneView camera at various collection rates and pixel

resolutions. Both bright-field and dark-field imaging modes were utilized. Selected area diffraction (SAD) patterns were also collected.

2.6.1.1 Precession Electron Diffraction

Precession electron diffraction (PED) was performed on a FEI Technai F-20 TEM operating at 200 kV at the University of Alabama. The step sizes were 5-10 nm with 2-3 precessions, depending on grain size. The orientation map was analyzed using the OIM software. The data was cleaned using confidence index (CI) standardization (minimum grain size of 5 and 7° tolerance angle) followed by grain dilation restricted to points with CI less than 0.1.

2.6.2 *Scanning Electron Microscopy*

SEM was performed on a Hitachi SU8010 SEM operating at 5kV to image the specimen before or after the test. The sample stage was tilted to at least 30° to facilitate easier imaging of the free-standing portion of the gauge.

CHAPTER 3.

INVESTIGATING ELECTRON BEAM EFFECTS ON *IN SITU*

TEM EXPERIMENTS

3.1 Overview

This chapter aims to quantify the effect the TEM electron beam (e-beam) has on the deformation behavior of NC Al and UFG Au thin films. This is a crucial understanding as the nanomechanical testing platform relies on TEM imaging to document the deformation mechanisms during straining and it is important to understand how the e-beam may interact and change the observations or measurements. Section 3.2 outlines common material e-beam effects. Section 3.3 reports the influence the e-beam has on the mechanical properties and measured activation volume for both NC and UFG Au specimens. Section 3.4 offers a discussion as to the proposed mechanism of e-beam effect on deformation mechanism.

3.2 Common Electron Beam Effects

TEM imaging relies on high energy electrons for atomic scale resolution, however, the resolving power of the e-beam comes at a price, with the electrons themselves interacting with and possibly altering the material being imaged. The result of these interactions varies with material type, but common effects of electrons include radiolysis, e-beam induced specimen heating, or defect generation due to the displacement of either bulk atoms or sputtering of surface atoms [162,163].

Radiolysis and specimen heating are typically considered to have minimal impact on metal specimens due to the nature of the delocalized electrons in the atomic bonding and, at least for most metals, their high thermal conductivity [162]. This leaves knock-on damage and sputtering as the most likely primary sources of e-beam induced damage in metals. The severity of this type of damage is dependent on both the maximum transferable energy of the incident electrons and the threshold displacement energy of the specimen, both of which are related to the atomic bonding [162]. Additionally, the local bonding is disrupted at defects and GBs which leads to lower atomic bonding energies. As such, it is likely that atoms near dislocations and GBs are more easily displaced, although the exact displacement energies for these environments are not well-defined [163]. Similar sub-threshold displacement events have been reported for hydrogen impurities in copper and vanadium, with electron irradiation damage increasing with hydrogen content [164].

When incident electrons displace atoms in a material, this leads to the formation of defects (interstitials and vacancies) which can assist diffusional processes [163,165]. There have been a variety of e-beam-induced effects on defect behavior during *in situ* TEM testing reported in the literature. For example, Wang *et al.* reported that e-beam exposure led to the thickening of the native oxide layer on iron nanoparticles due to enhanced mass transport facilitated by e-beam induced defects [166]. Similarly, Muntiferling *et al.* demonstrated void formation in regions of e-beam exposure during *in situ* annealing of self-ion irradiated NC Ni [167]. They hypothesized that e-beam exposure stimulated oxide growth in localized regions which limited the ability of vacancies to escape through the free surface thus resulting in void formation. The e-beam has also been found to selectively suppress crack growth in NC copper (Cu) thin films on a polyimide (PI) substrate by

increasing the adhesion between the Cu and PI as a result of enhanced migration of Cu into the PI substrate [168]. This led to increased interfacial area between the Cu and PI as well as oxide formation of the migrated Cu atoms with oxygen atoms present in the PI substrate, both of which strengthened the adhesion and resulted in tensile strains surpassing 30%, whereas e-beam free regions formed cracks before strains of 10%.

3.3 Electron Beam Influence on Deformation of Metal Thin Films

The *in situ* tensile tests were conducted in an FEI Tecnai F30 TEM operating at an accelerating voltage of either 300 kV (current ~ 11 nA) or 80 kV (current ~ 4 nA) using a Hummingbird electrical biasing holder. During each experiment, the beam condition was controlled and defined as either ‘beam-on’ or ‘beam-off’. Under the beam-on condition, the e-beam was used to illuminate a portion of the specimen, while under the beam-off condition, the specimen was moved so the e-beam was exposed to vacuum only. For both the Al and Au specimens, monotonic tensile tests were conducted in which the beam condition was switched from beam-on to -off every 30 seconds for both 80 and 300 kV TEM accelerating voltages. Additional monotonic tensile tests were performed on the Al specimens with the beam condition constant throughout (either beam-on or beam-off). A stress-relaxation experiment was also completed on an Al specimen while changing beam-on/off condition for the loading and paused segments in order to measure the corresponding true activation volume.

3.3.1 Electron Beam Effects in NC Al

In order to study the potential impact of the e-beam on the deformation of NC Al thin films, monotonic tensile tests were first conducted in either a complete beam-on or

beam-off condition at different strain-rates. **Figure 20(a)** shows the influence of the e-beam on the mechanical properties of the Al thin films tested under varying beam condition and strain rates (strain rates for each test are given in **Figure 20** caption). For samples tested at similar strain rates of $1.2 - 2.6 \times 10^{-4} \text{ s}^{-1}$ (specimen #1, #3, and #5), the e-beam drastically increases the ductility of the samples, with the specimen #5 (beam-on condition) failing at 19% strain, while specimens #1 and #3 (beam-off condition) failed at strains of 3.7% and 6%, respectively. The specimens also showed variations in apparent yield stress, though this may have been due to early crack initiation during deformation leading to a stress decrease. For all the curves, the offset from the zero-point origin is to account for pre-stress caused by the shrinkage of the glue upon curing (see Section 2.2.2.1 and Ref. [92] for more details). Specimen #2 was tested under beam-on condition at a slightly faster strain rate of $6 \times 10^{-4} \text{ s}^{-1}$. The specimen deformed uniformly until failure quickly occurred, similar to that of specimen #1 and #3. Specimen #4 was deformed under beam-off condition with a strain rate ~ 10 times slower of $2 \times 10^{-5} \text{ s}^{-1}$. Under this condition, significant ductility was achieved with failure occurring at 12% strain.

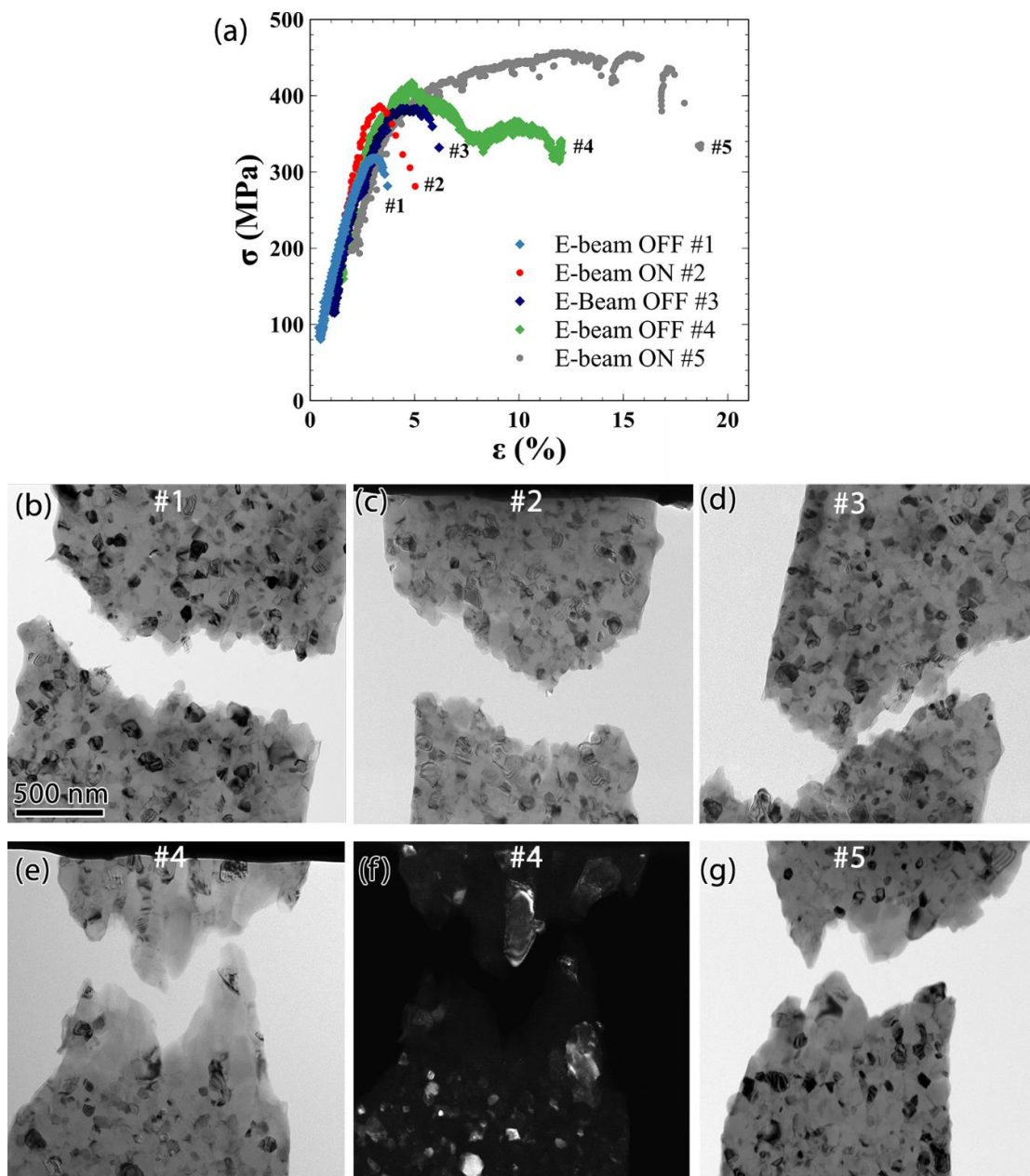


Figure 20 – Behavior of NC Al under monotonic testing for 5 different specimens tested under different beam condition and strain rates. (a) The strain rates for each specimen are: (#1) 1.2×10^{-4} s⁻¹, (#2) 6×10^{-4} s⁻¹, (#3) 1.8×10^{-4} s⁻¹, (#4) 1.5×10^{-5} s⁻¹, (#5) 2.7×10^{-4} s⁻¹. (b-g) Bright-field TEM micrographs of the fracture surfaces with the white numbers assigning the micrograph to the corresponding curve on (a). (e) Bright-field and (f) dark-field TEM micrographs of a fracture surface for a specimen tested in beam-off condition with a strain rate of 1.5×10^{-5} s⁻¹ which exhibit large grains within the necked region, closely resembling that of (g). (b-g) are all taken at the same magnification.

Post mortem analysis of the fracture surfaces revealed different types of microstructures at failure depending on e-beam exposure and strain rate (**Figure 20(b)-(g)**). In agreement with the mechanical testing data, the fracture surfaces of specimens #1 and #3 (beam-off, $\dot{\epsilon} \sim 1.2 - 1.8 \times 10^{-4} \text{ s}^{-1}$) showed features characteristic of brittle failure (**Figure 20(b)** and **(d)**). Specifically, there is no evidence of a necked region or grain growth in the surrounding area. In contrast, the fracture surfaces for specimen #5 (beam-on, $\dot{\epsilon} = 2.7 \times 10^{-4} \text{ s}^{-1}$) shows that a necked region developed alongside substantial grain growth within that region during the beam-on condition (**Figure 20(g)**). Grains in the necked region were measured to be upwards of 250 nm in size, almost three times larger than the initial average grain size. This grain size was determined by manually tracing the grains and calculating the diameter of a circle with area equivalent to that of the largest grains. This grain growth is consistent with other studies that reveal stress-assisted grain growth in NC metals [20,63,68,94,169]. Specimen #2, tested under beam-on condition with a slightly faster strain rate $\dot{\epsilon} = 6 \times 10^{-4} \text{ s}^{-1}$, shows only a slight neck with minimal grain growth near the fractured surface. Interestingly, the mechanical behavior and microstructure evolution for specimen #4 (beam-off, $\dot{\epsilon} = 2 \times 10^{-5} \text{ s}^{-1}$) closely resembled that of the sample deformed under the beam-on condition at $\dot{\epsilon} = 2.7 \times 10^{-4} \text{ s}^{-1}$ and exhibited extended plasticity with a failure strain of 12%. **Figure 20(e)** is a bright-field TEM micrograph of a fractured surface from such an experiment with **Figure 20(f)** highlighting certain large grains in dark-field mode. In agreement with the measured ductility, the TEM micrographs show necking behavior accompanied by significant grain growth. These results indicate that the e-beam may be promoting slow strain rate conditions, without changing the deformation mechanisms.

To understand the instantaneous e-beam effect on the mechanical behavior, monotonic tensile tests were conducted at similar strain rates ($\dot{\epsilon} = 1 - 2.7 \times 10^{-4} \text{ s}^{-1}$) on NC Al specimens while alternating between beam-on to beam-off conditions every 30 seconds for both TEM accelerating voltages (300 and 80 kV), as shown in **Figure 21**. The first beam-on (grey data) then -off (green data) segments correspond to the elastic loading of the specimen. The second beam-on segment deviates from the linearity of the previous two segments, indicating that yielding of the material has occurred under the beam-on condition. The apparent yield point for the 300 kV experiment smaller than that previously reported in **Figure 20(a)** (127 MPa versus 380 MPa), however this could be an artifact of the small-scale of the specimens, which tends to amplify minor variations in the material starting geometry, alignment, or clamping that may lead to different local stress states. Based off analysis by Kang *et al.*, given the specimen geometry and assuming a maximum misalignment of $\theta=5^\circ$, the majority of the specimen is expected to be under uniaxial tension [170]. During the next beam-off segment, the stress increases in the same linear manner as the first beam-off segment, likely indicating that the stress level is not sufficient to activate deformation mechanisms in this beam-off condition or that plastic deformation occurs at a slower rate. The next 30-seconds with the beam-on is marked by a decrease in stress during e-beam exposure, followed by an increase in stress when the e-beam is removed again. This trend is mirrored by the next six beam-on segments which all exhibit substantial stress decrease while exposed to the e-beam, resulting in the ‘saw-tooth’ like behavior seen in **Figure 21(a)**.

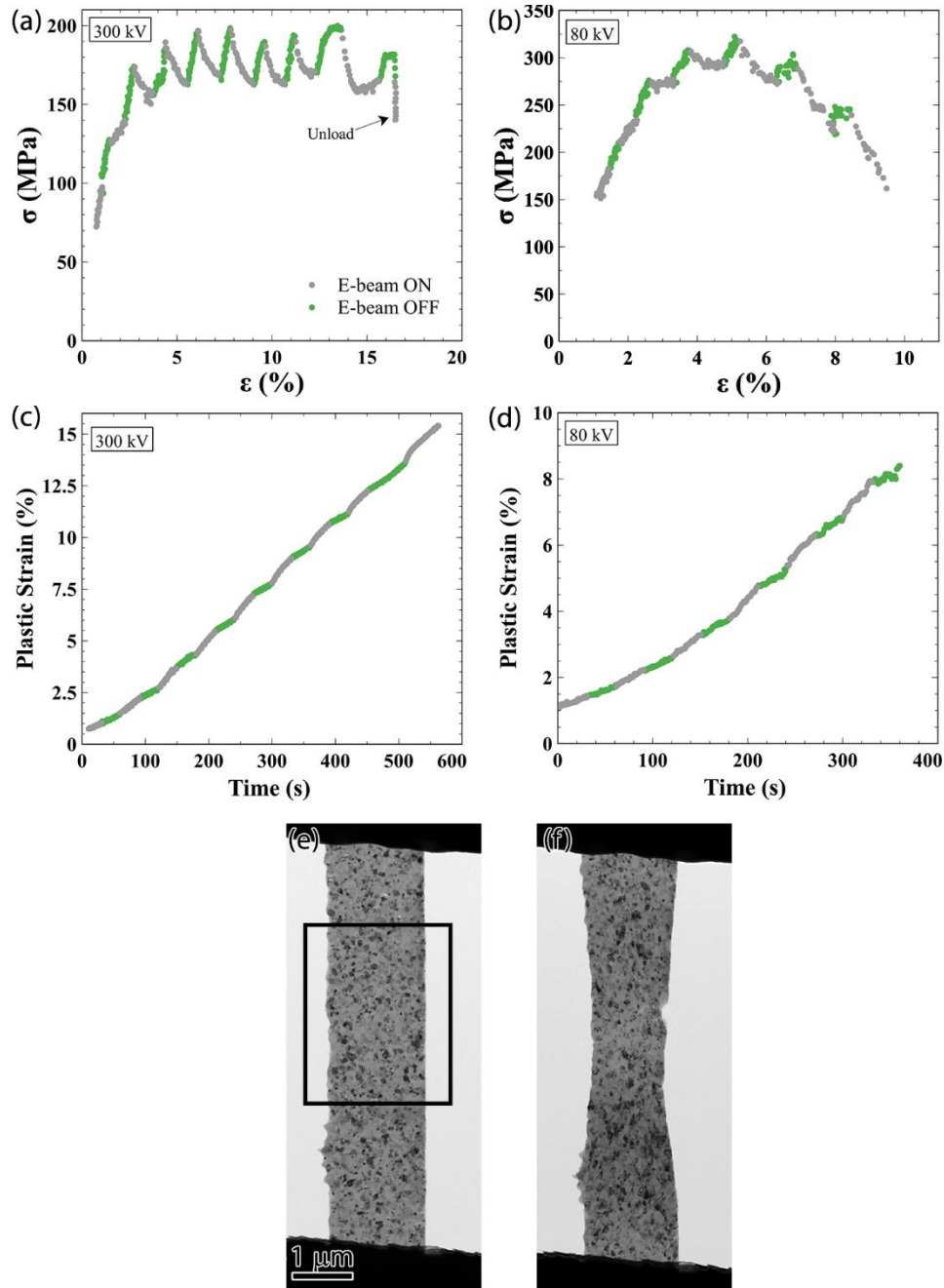


Figure 21 – Monotonic deformation of NC Al under alternating beam-off and -on conditions for TEM accelerating voltages of 300 and 80 kV. Stress-strain behavior during a monotonic test with alternating beam-on (grey) and -off (green) conditions every 30 seconds for experiments conducted during (a) 300 kV and (b) 80 kV TEM accelerating voltage. Accumulated plastic strain throughout the experiment showing an increase in plastic strain rate during beam-on conditions for (c) 300 kV and (d) 80 kV accelerating voltages. (e,f) Bright-field TEM images showing the (e) initial microstructure and (f) final microstructure of the specimen. The black box in (e) outlines the region of the specimen exposed to the e-beam during beam-on conditions.

It is important to note that this stress decrease is during monotonic loading (applied displacement from the MEMS thermal actuator, X_A , increases) and not during a stress-relaxation experiment (in which X_A is kept constant). A decrease in stress during monotonic loading indicates that thermally activated plasticity leads to specimen elongation at a faster rate than the applied displacement. This means that when the specimen is exposed to the e-beam, specimen elongation initially occurs at a faster rate than the applied displacement, leading to a decrease in stress even during monotonic loading.

Figure 21(c) displays the accumulation of plastic strain throughout the duration of the experiment, with the different beam-on/off segments colored accordingly. This figure reveals that the plastic strain rate is roughly 3 times higher during beam-on segments than when the beam is off. This experiment was completed at a TEM accelerating voltage of 300 kV, however, the same ‘saw-tooth’ trend was observed even when the voltage was lowered to 80 kV, as shown in **Figure 21(c)** and (d). This indicates that even at the much lower accelerating voltage of 80 kV, the e-beam effect is still observed through an increase in plastic strain rate (increased by a factor of 1.95). **Figure 21(e)** and (f) show the initial and final microstructure (after unloading) of the specimen, respectively. Since **Figure 21(f)** is taken after unloading has occurred, there is a certain amount of specimen buckling due to plastic elongation which causes some distortion in the specimen. Despite this, it is still clear that there is localized reduction in width (necking) near the center of the gauge, directly corresponding to the region exposed to the e-beam during the beam-on segments.

In addition to monitoring the e-beam effect on monotonic behavior, a multiple stress-relaxation experiment was completed to measure the change in activation volume V^* between beam-on and beam-off conditions. The results of this can be seen in **Figure**

22, which includes both the stress-strain response as well as specific relaxation segments highlighted to show more detail. The grey data points were collected when the specimen was exposed to the e-beam, while the green data corresponds to the beam-off condition. The specimen was deformed at a strain rate of $2 \times 10^{-4} \text{ s}^{-1}$. Elastic loading of the specimen occurred during the beam-on condition (**Figure 22(a)**) followed by two 60 second relaxations (with a short reloading in-between) shortly after yielding at 240 MPa. The loading scheme can be better understood in **Figure 22(b)** where the circle data points represent active loading and the diamond data points correspond to when the loading is paused. During the relaxation, the strain increases due to time-dependent plastic deformation of the specimen which results in stress-relaxation.

The first relaxation occurred at a starting stress of 242 MPa and decreased to 210 MPa in a manner shown in **Figure 22(d)**, which shows the stress-relaxation (stress decrease vs. time) data for the first four relaxation segments. This was followed by a quick reloading to 242 MPa and a second 60 relaxation resulting in similar relaxation behavior as the first relaxation. In **Figure 22(d)**, the black line represents the relaxation data fitted with the logarithmic fit, which is used to determine the stress rates. The true activation volume V^* was calculated as $24b^3$ for the second relaxation following Eqn. (30).

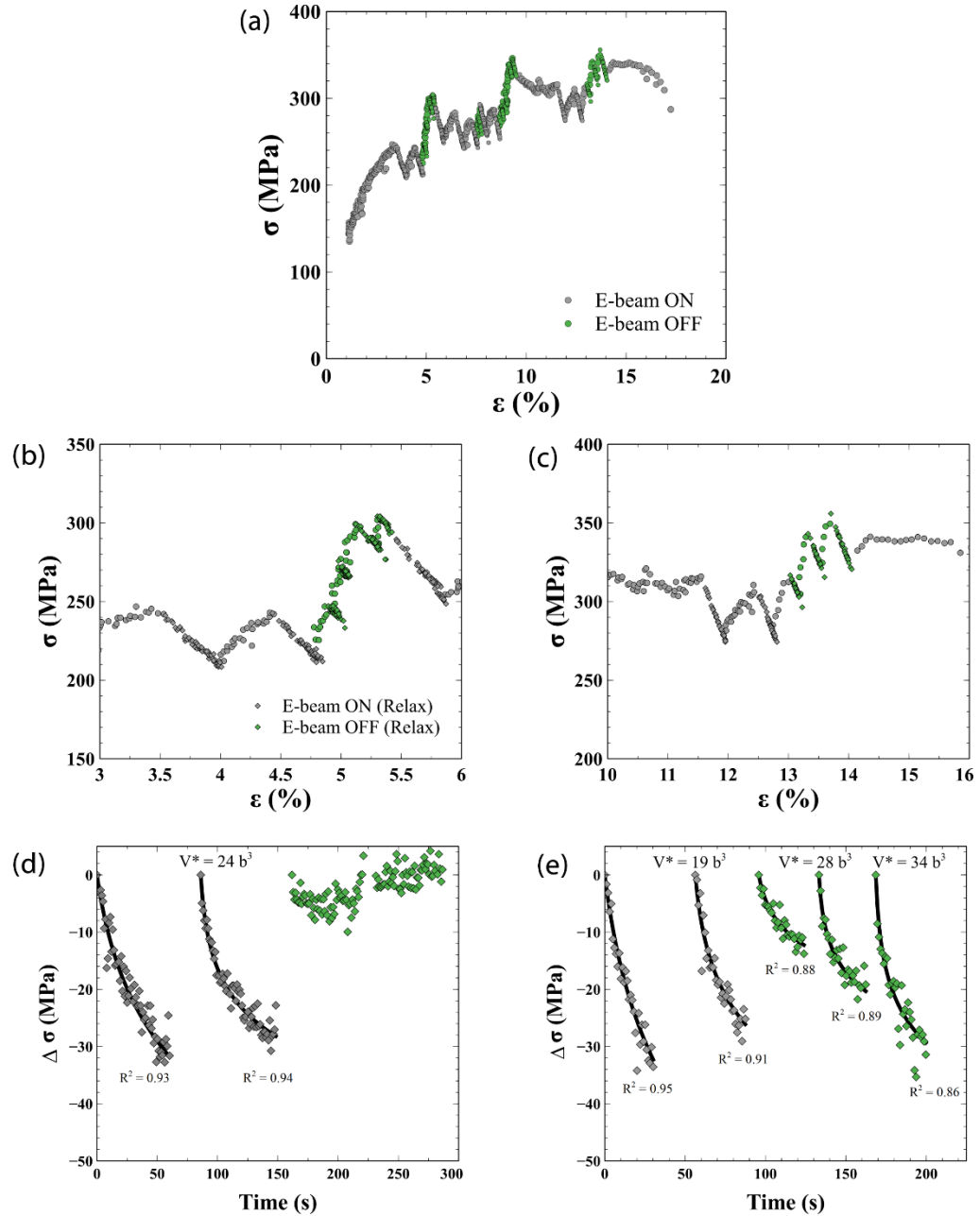


Figure 22 – Behavior of NC Al during a multiple stress-relaxation experiment with alternating beam on- and -off condition. (a) Stress-strain curve with 20 total segments of paused loading (for stress-relaxation) of length 30-60 seconds alternating between beam-on (grey) and beam-off (green) conditions until specimen failure. (b,c) Stress-strain data scaled to show (b) the first four and (c) the last five segments of paused loading in detail. Grey diamonds correspond to the beam-on relaxation data while green diamonds are the beam-off relaxation data. (d) The stress-relaxation data for the first four relaxation segments. The first two occur during beam-on condition with substantial stress-relaxation. The second two (green) segments occur during beam-off condition with negligible stress-relaxation. (e) Stress-relaxation data for the last five

relaxation segments where the first two occur during the beam-on condition and the last three occur during beam-off condition. All segments are fitted with a logarithmic fit with R^2 values shown.

The beam was then removed and the specimen was reloaded to 248 MPa in the beam-off condition, followed by a 60-second pause in loading. Unlike the previous two beam-on relaxations, there is essentially no stress-relaxation during this beam-off pause in loading, which can be seen in the first cluster of green data points in **Figure 22(d)**. Because there was no stress-relaxation in the first beam-off pause, the reloading segment started at a stress of 247 MPa until the second beam-off pause occurred at 268 MPa. There is once again no stress-relaxation during this segment, and neither beam-off relaxations could be fit with a logarithmic fit. The lack of stress-relaxation indicates that no plastic deformation occurred during the beam-off condition, even though it is clear that thermally activated plasticity was already active at similar stress and strain values during the previous two beam-on stress-relaxation segments. This could indicate that the deformation remains in the elastic regime during the beam-off condition in early stage deformation. These results are consistent with those previously shown in **Figure 21**, in which the e-beam induces stress-relaxation during monotonic loading.

These relaxation segments are followed by multiple relaxation segments alternating between beam-on and -off conditions. Minimal relaxation is observed for the beam-off pauses until the last three relaxations before failure, which are shown in **Figure 22(c)** and **(e)** along with the two beam-on relaxation segments just prior. The first two beam-on relaxation segments begin at plastic strain values of 7.4 and 8.4%. The true activation volume for the second beam-on relaxation was measured to be $19 b^3$. The beam was removed and the specimen was reloaded to 310 MPa ($\epsilon_p = 8.6\%$) at which loading was

paused and a 30 s relaxation was allowed. Unlike the previous beam-off paused segments (**Figure 22(d)**), measurable stress-relaxation occurs resulting in a stress drop of 14 MPa. The specimen was reloaded to 343 MPa, which is slightly larger than the initial stress of the previous relaxation, however, the plastic strain $\varepsilon_p = 8.7\%$ is essentially the same. A second beam-on relaxation occurs with a larger decrease in stress of 19 MPa followed by a reloading segment and the final relaxation starting at 355 MPa ($\varepsilon_p = 8.8\%$). True activation volume V^* was measured for the last two beam-off relaxation segments at 28 and 34 b^3 . A change in true activation volume from 19 to 28/34 b^3 when going from a beam-on to -off condition for relaxation segments at similar stress and plastic strain values likely indicates that the e-beam causes this change. The results of the experiment are summarized in **Table 4** which shows V^* measurements for three consecutive relaxations segments starting at the given plastic strain values. These results show that at similar deformation (plastic strain) levels, V^* increases from 19 to 28/34 b^3 when the condition is changed to beam-off. This is the first time a change in V^* due to e-beam presence has been reported.

Table 4 – True activation volume measurements V^* for three different relaxation segments with varying e-beam condition during repeated stress-relaxation experiment for NC Al.

	ε_p (%)	V^* (b^3)
Beam-on	8.4	19
Beam-off	8.6	28
	8.8	34

Figure 23 shows V^* measurements for relaxation segments of different Al specimens from beam-on and beam-off conditions. The solid green squares specifically correspond to tests done *ex situ*. Because the experiments were conducted *ex situ*, there is a certain amount of error in the V^* measurements because the device cannot be fully calibrated. This type of error is not present for *in situ* experiments as CS_2 can be exactly calibrated prior to the test [159]. The beam-on and -off V^* measurements from **Table 4** are indicated by the unfilled data points. The average V^* for all beam-on condition is $21.7 b^3$, which is consistent with the measured V^* of $19 b^3$ in **Table 4**. The average V^* for all beam-off conditions is $28.6 b^3$ is once again comparable to the values of 28 and $34 b^3$ measured for the last beam-off relaxations in **Table 4**. Overall, this figure shows that there is a consistent and repeatable decrease in measured true activation volume when the specimen is exposed to the e-beam.

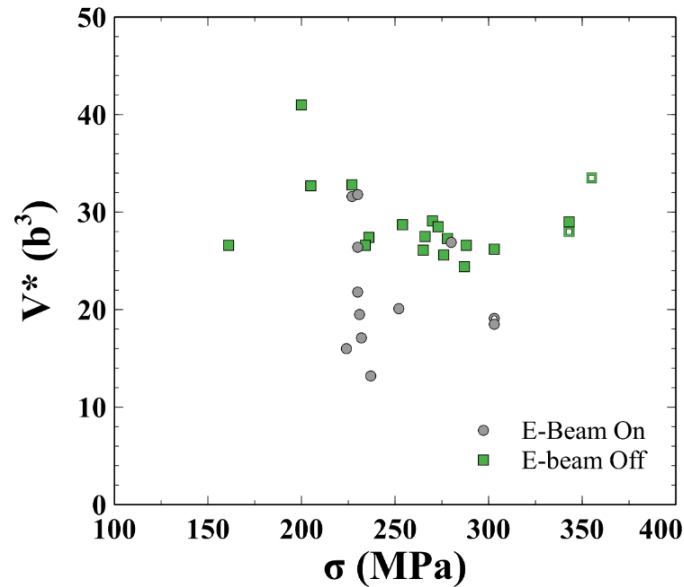


Figure 23 – True activation volume V^* measurements for NC Al specimens tested under beam-off (green squares) and beam-on (grey circles) conditions. The open

square data points correspond to the activation volume measurements shown in Table 4 and Figure 22(c) and (e).

3.3.2 *Electron Beam Effects in UFG Au*

Additional experiments were conducted on as-deposited UFG Au thin films to investigate how the e-beam effect varies across different materials. Specifically, the potential interaction between the e-beam and oxide layer (a possible e-beam effect for the NC Al films) can be directly investigated as Au films do not have a native oxide layer. **Figure 24** shows the response of two UFG Au specimens under monotonic loading with alternating beam-on and -off conditions every 30 seconds (similar to that done on Al in **Figure 21**). **Figure 24(a)** and (c) correspond to a specimen tested under a TEM accelerating voltage of 300 kV whereas **Figure 24 (b)** and (d) are from a specimen tested under a lower TEM accelerating voltage of 80 kV. An accelerating voltage of 80 kV was chosen as this beam energy is well below that required for knock-on and sputtering damage in Au. The strain rates for the experiments are 1.4×10^{-4} (300 kV) and $1.1 \times 10^{-4} \text{ s}^{-1}$ (80 kV). For both accelerating voltages, the stress-strain response resembles the ‘saw-tooth’ like behavior previously seen in Al (**Figure 21**), indicating that some stress decrease occurs during e-beam exposure for the Au specimens. For 300 kV, the average stress decrease during the beam-on segments is 18 MPa, with a maximum of 23 MPa. The average stress decrease for the 80 kV experiment was 16 MPa, although there were only two beam-on segments inducing stress-relaxation before specimen failure at $\varepsilon = 3.7\%$. When considering the accumulation of plastic strain (shown in **Figure 24(c)** and (d)), the plastic strain rate for beam-on is ~ 1.2 times larger than that of beam-off for 300 kV and ~ 1.1 times larger for 80 kV. This is a sizeable decrease in the effect seen in Al, where the e-beam

induced a three times increase in plastic strain rate. Although the effects discussed above are minimal and less drastic than those seen in Al, these results suggest that the effect of the e-beam cannot be ignored in Au, even at accelerating voltages as low as 80 kV.

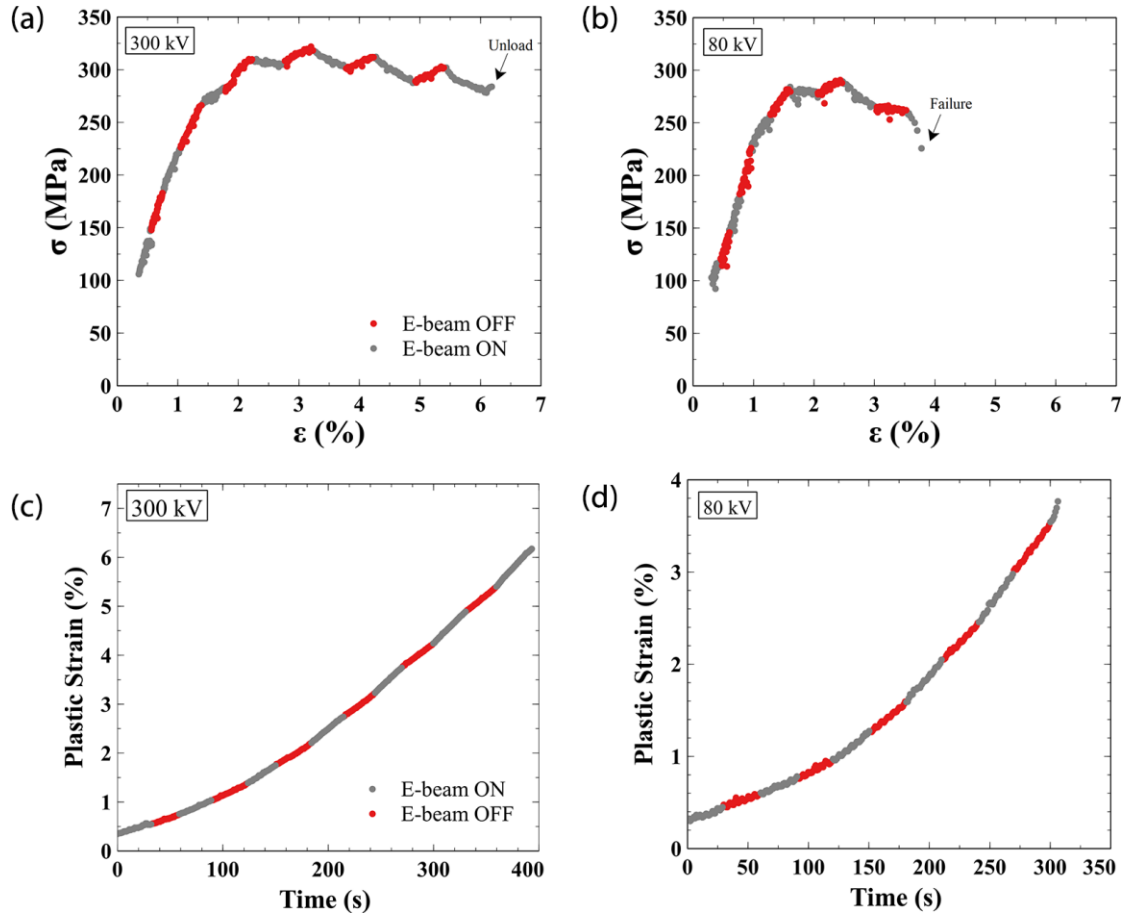


Figure 24 – Stress-strain response during monotonic testing of UFG Au specimen with alternative beam-on and beam-off conditions with a TEM e-beam accelerating voltage of (a) 300 kV and (b) 80 kV. Accumulated plastic strain during the experiments conducted at TEM accelerating voltages of (c) 300 kV and (d) 80 kV. The strain rates for (a) and (b) are 1.4×10^{-4} and $1.1 \times 10^{-4} \text{ s}^{-1}$, respectively.

Figure 25 shows the deformation during the *in situ* test conducted using the 300 kV accelerating voltage. **Figure 25(a)** and (b) are the initial and final microstructures, with the black box on both designating the region of the specimen that was repeatedly illuminated by the e-beam during the beam-on segments. Although failure of the specimen

occurred outside this region, **Figure 25(b)** does provide evidence that the region exposed to the e-beam experiences more necking in comparison to the regions not exposed to the e-beam (average local width within the box is $1.52\ \mu\text{m}$ compared to $1.65\ \mu\text{m}$ outside this region).

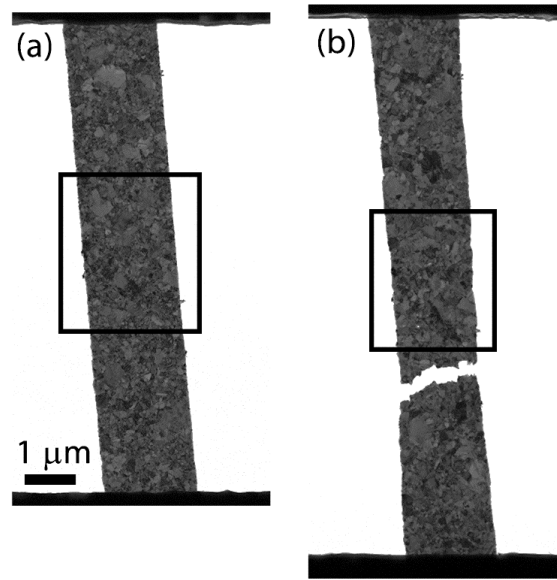


Figure 25 – TEM micrographs of the microstructural evolution of a UFG Au specimen tested under monotonic loading with alternating beam-on and beam-off conditions every 30 seconds. (a) Initial microstructure with black box indicating region of specimen that was repeatedly exposed to the e-beam. (b) Final microstructure after failure.

Similar to the Al specimens, V^* measurements were obtained for different Au specimens and relaxation segments for both beam-on (*in situ*) and beam-off (*ex situ*) conditions and are shown in **Figure 26**. Unlike the Al specimens, however, there is a minimal change in average activation volume V^* from beam-on ($10.9 \pm 5.5\ b^3$) to beam-off ($10.3 \pm 3\ b^3$) conditions. Given the scatter in the data points, these averages can be considered essentially the same. This indicates that the e-beam effect on true activation volume for Au may be negligible or too small to be measured with the precision of the

current technique. This is also in agreement with only a slight increase in plastic strain rate during e-beam exposure as shown in **Figure 24**.

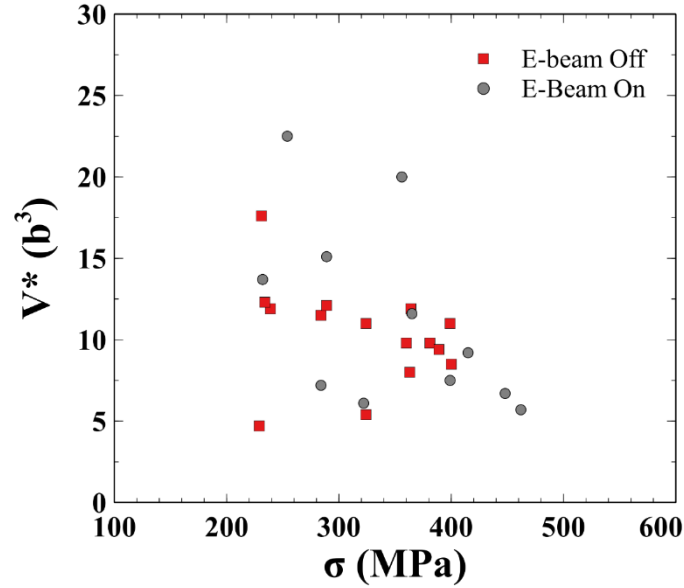


Figure 26 – True activation volume V^* measurements from different UFG Au specimens and relaxation segments for *ex situ*/beam-off (red squares) and *in situ*/beam-on (grey circles) conditions.

3.4 Discussion

The above experimental results show that the e-beam influences the behavior of both NC Al and UFG Au specimens during *in situ* TEM straining. The e-beam effect is more apparent in the NC Al specimens, with the beam accelerating the plastic strain rate by a factor of three and reducing the true activation volume V^* by 25%. For the UFG Au specimens, the e-beam increases the plastic strain rate by a factor of 1.2 and the true activation volume essentially remains unchanged. In both materials, necking was observed to occur in the region illuminated by the e-beam, indicating localized deformation.

Knock-on displacement is typically considered as the most prevalent form of e-beam damage in metals. However, the experiments completed at a TEM accelerating voltage of 80 kV show the same e-beam induced stress-relaxation during monotonic loading as the experiments completed at 300 kV in both NC Al and UFG Au. At a beam accelerating voltage of 80 kV, the maximum transferable energy to Al is less than 8.93 eV, which is lower than the energy required for knock-on damage (16 eV), however, larger than the energy required for sputtering (~4-8 eV) [162]. For Au, the maximum transferable energy of an 80 kV e-beam is less than 1.22 eV, which is much smaller than the required energy for bulk knock-on displacement (36 eV) or sputtering (~9-18 eV) [162]. Since an e-beam effect is observed for Au tested under an 80 kV accelerating voltage, the effect cannot be explained by either bulk knock-on displacement or sputtering of the surface atoms.

Specimen heating is another common effect of e-beam interactions. The heat transfer characteristics have been analyzed for the particular specimen geometry and experimental setup. One-dimension steady state heat transfer is given by the Fourier equation ($q = -\kappa A \frac{dT}{dx}$) where q is the energy entering the system, κ is the thermal conductivity, A is the area normal to the direction of heat flow, and dT/dx is the temperature gradient in the x direction [171]. This equation takes the following form in the context of a TEM sample,

$$(I/e)\Delta E = -\kappa A \frac{dT}{dx} \quad (31)$$

where I is the e-beam current, e is electron charge, and ΔE is the total energy loss per electron [172]. This equation can be further refined in the context of the specimens in this study, where the area of heat transfer is the cross-section area of the gauge length of width w and thickness d . At a given distance x from the center of the beam, the temperature profile must satisfy the following equations:

$$\frac{(I/e)\Delta E}{wd} = -\kappa \frac{dT}{dx} \quad (x \geq x_0) \quad (32)$$

$$\frac{(I/e)\Delta E(x/x_0)}{wd} = -\kappa \frac{dT}{dx} \quad (x < x_0) \quad (33)$$

where x_0 is the e-beam radius. Two equations are required depending on x since for $x < x_0$ only a portion of the energy is deposited. Using the boundary condition that at a certain distance b , the temperature will reach a fixed value T_0 (heat sink) and continuity requirements, Eqns. (32) and (33) can be solved:

$$T - T_0 = \begin{cases} \frac{I}{\kappa w e} \frac{\Delta E}{d} [b - x], & (x \geq x_0) \\ \frac{I}{2\kappa w e} \frac{\Delta E}{d} \left[-\frac{x^2}{x_0} + 2b - x_0 \right], & (x < x_0) \end{cases} \quad (34)$$

Considering that the largest temperature increase will occur at the center of the e-beam ($x = 0$), the maximum temperature increase due to e-beam heating is given by:

$$\Delta T = \frac{I}{2\kappa w e} \frac{\Delta E}{d} [2b - x_0] \quad (35)$$

The following values were used to determine the maximum temperature change: thermal conductivity $\kappa = 320$ (Au), 237 (Al) W/mK, $w = 1700$ nm, $b = 10$ μ m, $x_0 = 1200$ nm,

$\Delta E/d = 3.74$ (Au), 0.84 (Al) eV/nm at 80 kV and $\Delta E/d = 2.33$ (Au), 0.50 (Al) eV/nm at 300 kV. For Al, the maximum expected temperature increase is 0.08 K at 80 kV and 0.13 K at 300 kV. The temperature increase in the Au specimens is 0.25 K at 80 kV and 0.44 K at 300 kV. Considering that there is a thin native oxide layer on Al, the calculations were also completed for alumina ($\kappa = 30$ W/mK), which resulted in an expected temperature increase of 0.24 K at 80 kV and 0.39 K at 300 kV. For each material, the estimated temperature increase is higher at a higher accelerating voltage, which is counter to what is generally expected. In this case, the beam current I is different and large enough for the higher accelerating voltage (11 nA at 300 kV versus 4 nA at 80 kV) which leads to a higher estimated temperature increase using Eqn. (35). Based on these values, no significant heating is expected during e-beam exposure. This is also confirmed by considering that no e-beam effect is seen during the elastic portion of deformation (**Figure 21** and **Figure 24**). If the specimens were heating during e-beam exposure, the increase in thermal strain would be detected before yielding occurs, which is not currently the case. Any temperature rise due to the e-beam is considered negligible.

Another possible explanation for this phenomenon is that the e-beam induces additional fluctuations of atomic motion in the two metals which effectively accelerate the stress-driven, thermally-activated processes during their plastic deformation. As mentioned in Section 1.4.1, the plastic shear rate given by an underlying rate-controlling process is expressed as

$$\dot{\gamma}_p = \dot{\gamma}_0 \exp\left(-\frac{\Delta G}{kT}\right) \quad (9)$$

where $\dot{\gamma}_0$ is a pre-exponential factor and ΔG is the activation free energy of the rate-controlling process. Activation volume is given by the equation:

$$V^* = kT \frac{\ln(\dot{\gamma}_{p2}/\dot{\gamma}_{p1})}{\Delta\tau^*} \quad ()$$

Substituting Eqn. (6) into Eqn. (), we obtain the activation volume under the beam-off condition,

$$V_{OFF}^* = \sqrt{3} \frac{\Delta G_2 - \Delta G_1}{\sigma_1 - \sigma_2} = -\frac{\partial \Delta G}{\partial \tau} = V^* \quad (36)$$

where ΔG_2 is activation energy corresponding to the initial plastic strain rate $\dot{\gamma}_{p2}$ (at stress σ_2) of the second relaxation, and ΔG_1 is activation energy corresponding to the final plastic strain rate $\dot{\gamma}_{p1}$ (at stress σ_1) of the first relaxation segment. Under the beam-on condition, the thermal activation process is promoted by an additional effective thermal energy E_{beam} due to the beam effect and thus plastic strain rate during e-beam on can be written as:

$$\dot{\gamma}_p = \dot{\gamma}_0 \exp\left(-\frac{\Delta G}{kT + E_{beam}}\right) \quad (37)$$

Similar to the activation volume under the beam-off condition in Eqn. (36), we combine Eqns. () and (37) to obtain the activation volume under the beam-on condition,

$$V_{ON}^* = \frac{1}{1 + E_{beam}/kT} V^* \quad (38)$$

Eqn. (38) indicates that due to the presence of E_{beam} , the true activation volume during e-beam exposure V_{ON}^* is smaller than the activation volume V^* under no beam conditions,

which is consistent with the results reported in **Figure 23** for NC Al. Using the measured activation volume in **Figure 23**, we estimate the E_{beam} value for the Al specimens as $E_{beam} = 8.2 \text{ meV}$ under a 300kV e-beam. Activation volume measurements were also completed under the 80kV e-beam condition, but there was not a measurable change in the activation volume values. This is likely because any change in activation volume values due to a decrease in TEM accelerative voltage only is below the measurable limit of the testing platform. Hence, the accelerated plastic strain rate under the beam-on condition is equivalent to an effective temperature increase $\Delta T = 96 \text{ K}$ for NC Al. This is not an actual increase in temperature, but results in the same increase in plastic strain rate as a temperature increase would. Unlike a physical temperature increase of the whole specimen, the e-beam effect influences the highly localized regions around defects where the atomic bonds are weaker. For the UFG Au specimens, the true activation volume remains essentially unchanged depending on the beam condition, likely indicating that E_{beam} is very small, leading to a negligible change in V_{ON}^* versus V^* . Interpreting the beam effect in terms of additional thermal energy differs from previous interpretations of irradiation causing a decrease in activation energy for dislocation glide [173]. However, this new interpretation is necessary to explain the change in V^* measured during e-beam exposure, as a decrease in activation energy would leave V^* unchanged.

During e-beam exposure, the additional energy E_{beam} accelerates plastic deformation by introducing additional atomic fluctuations. This leads to the observed increase in ductility (**Figure 20**) and accelerated plastic strain rate (**Figure 21**). The effect is magnified in NC Al because the E_{beam} term, which is likely related to atomic number, is larger than that of UFG Au, although an exact E_{beam} term could not be determined for

Au since the effect on activation volume is too small to be measured. The results presented here are similar to previous reports of e-beam induced stress relaxation in Al and Au via increased dislocation activation and depinning [174]. It is possible that the additional atomic fluctuations provided by the beam can lead to dislocation activation and depinning, which underlie the apparent increase of plastic strain rate. It is unlikely the depinning occurs due to a displacement cascade effect (as previously reported for ion irradiation [175]) since electron irradiation does not cause a displacement cascade. Instead, the e-beam affects the highly localized regions around defects. It is also unlikely that the observed effect is due to the local climb of dislocations aided by absorption of point defects, as minimal point defects are expected in the Au specimens (with higher knock-on and sputtering energies) but the e-beam influence is still observed. However, it is possible that the atoms near dislocations and GBs experience sub-threshold displacements as the periodic lattice is disrupted and the energy required to displace these atoms is reduced [164]. This could contribute to the observed e-beam effect, as this could induce additional fluctuations in atomic motion and aid in dislocation glide and GBM.

There is no evidence in the present study that the deformation mechanisms themselves change due to e-beam exposure; rather the mechanisms are accelerated with e-beam exposure. The *post mortem* fracture surface and surrounding microstructure of the NC Al specimen tested at a slow strain rate (**Figure 20(e)** and (f)) beam-off condition resembles that of the beam-on condition at a faster strain rate (**Figure 20(d)**). Both specimens exhibit a necked region with prevalent grain growth, which suggests that the deformation mechanisms may not have changed due to the influence of the e-beam, however, this cannot be proved exactly as the deformation cannot be documented in the

beam-off condition. This indicates that the measured change in true activation volume, which is a parameter typically associated with a rate-controlling deformation mechanism, is not a result of a change in deformation mechanisms, but rather the addition of effective thermal energy. Other researchers have reported a similar decrease in apparent activation volume (12 to $4b^3$) under e-beam exposure for Al-4Cu alloys, however, they attributed the decrease to a change in deformation mechanisms from internal dislocation nucleation to surface dominated dislocation nucleation processes [82]. They claim that the e-beam causes local disorder between the native oxide layer and the Al-4Cu alloy which promotes dislocation nucleation at the surface. As the e-beam influence on mechanical properties was demonstrated in the Au thin films, oxide layer effect alone cannot explain the observed behavior. In addition, the slow strain rate experiment on the NC Al specimens suggests that the underlying deformation mechanisms do not change in response to the e-beam. Instead, the experiments conducted in this study suggest that the change in true activation volume is due to the increase in atomic fluctuations by an additional effective thermal energy. This accelerates the thermally-activated deformation mechanism present in these materials, such as grain boundary migration, dislocation glide, and dislocation nucleation/emission from grain boundaries.

3.5 Conclusion

This chapter investigates the effect of the e-beam on the deformation behavior of NC Al and UFG Au thin films using an *in situ* TEM nanomechanical testing technique that allows for stress-strain and true activation volume measurements. The effect of the e-beam was quantified as an increase in plastic strain rate in both materials, and a decrease in true activation volume from 28 to $21 b^3$ in Al and a negligible change of true activation volume

in Au. The e-beam effects were seen at TEM beam accelerating voltages of 80 and 300 kV, discounting knock-on damage as the source of e-beam influence. Instead, the experiments suggest that the e-beam causes additional thermal activation that accelerates the stress-driven, thermally-activation plastic deformation. The additional thermal activation eases the barrier to plastic deformation and leads to the change in the mechanical properties across the beam-on and -off conditions, but does not change the active deformation mechanisms themselves. These results show that there is non-negligible e-beam effect in different materials that must be considered for accurate interpretation of in situ experiment results. The reported e-beam effects should be broadly applicable to other NC/UFG face-centered cubic metals and warrant further in-depth study in the future.

CHAPTER 4.

PLASTIC DEFORMATION MECHANISMS IN ALUMINUM

4.1 Overview

The following chapter provides an overview of the active deformation mechanism in NC Al as well as quantification through the measurement of activation volume and mechanical properties. Section 4.2 provides microstructural characterization of the NC Al specimens and Section 4.3 summarizes the mechanical response in terms of monotonic tensile curves. This is followed by *in situ* TEM observations of the active deformation mechanisms and measurement of true and apparent activation volume.

4.2 Initial Microstructure

The initial microstructure of the NC Al specimens is shown below in **Figure 27**. There are specimens of two different thicknesses: 200 nm-thick (Al-200) and 100 nm-thick (Al-100). **Figure 27(a)** and **Figure 27(b)** are BF TEM images of the Al-200 and Al-100, respectively. PED was performed on an Al-200 specimen, resulting in the orientation map shown in **Figure 27(c)** [176]. This map indicates that the Al films exhibit random out-of-plane texturing and as a result, the majority of the GBs are random HAGBs. The grain size distribution for both is shown in **Figure 27(d)** (grain sizes were measured manually by tracing grains). Due to the reduction in film thickness, the Al-100 specimens have smaller grain sizes. The (weighted) average grain size for the Al-100 is 55 ± 14 nm which increases to 93 ± 29 nm for the Al-200 specimens.

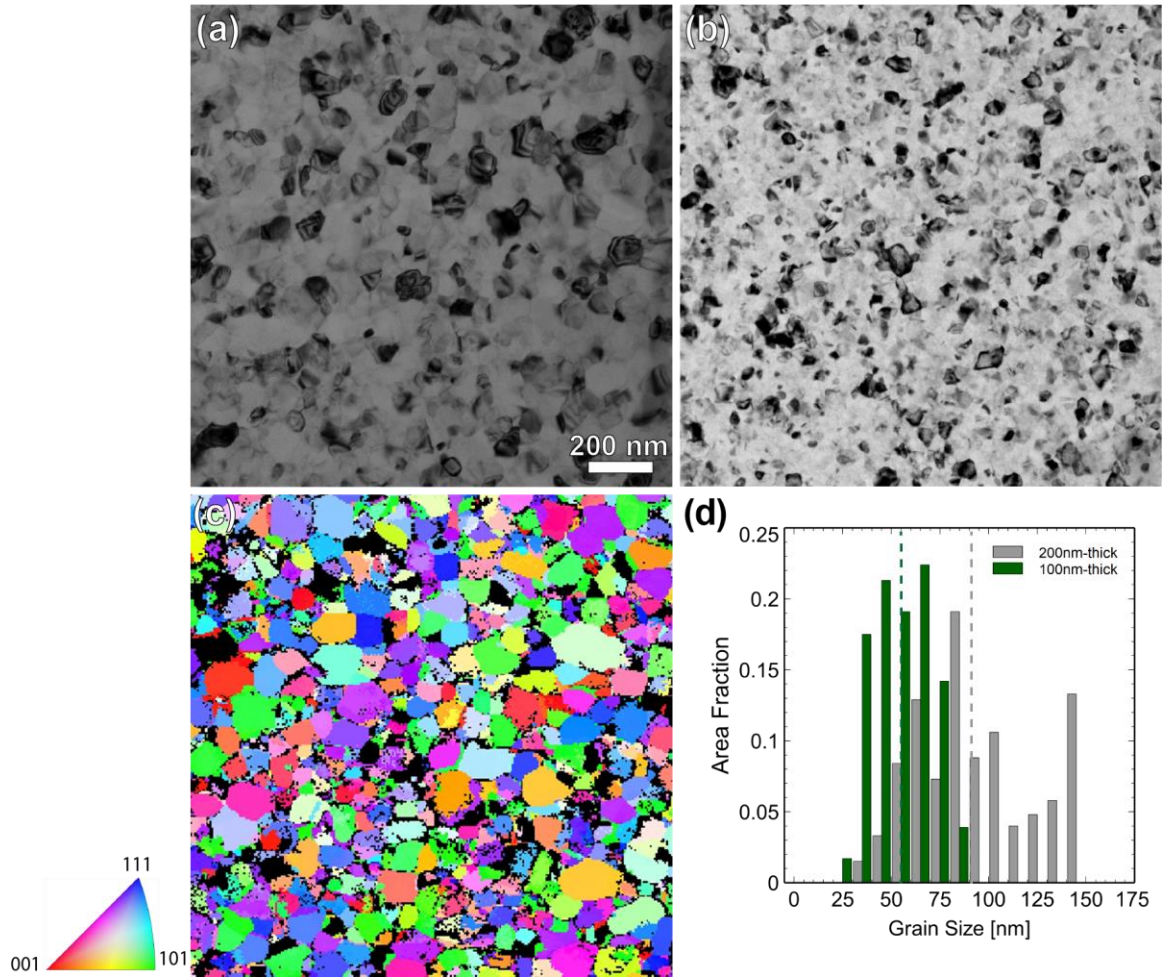


Figure 27 – Initial microstructure of the NC Al specimens. BF TEM images of (a) 200 and (b) 100-nm thick specimens. (c) PED map of a 200 nm-thick specimen indicating a random out-of-plane texture. (d) grain size distribution of the 200 nm-thick (gray) and 100 nm-thick (green) specimens with the weighted average indicated by dashed line.

4.3 Monotonic Response

The monotonic tensile response for the Al-100 and Al-200 specimens is shown in **Figure 28** with the tensile properties summarized in **Table 5**. The offset of the initial stresses on both curves from a zero value results from residual tensile stress developing when the glue shrinks after curing (more details provided in Section 2.2.2.1 and Ref. [92]). After the linear elastic region, the Al-100 specimen yielded at $\sigma_y \sim 405$ MPa, reached a

UTS of 426 MPa. After the UTS, the stress quickly declines until eventual failure at $\epsilon_f \sim 12.6\%$ ($\epsilon_f^p \sim 8.7\%$). The Al-200 specimen yielded at a slightly lower stress ($\sigma_y \sim 380$ MPa) but reached a higher UTS ($\sigma_{UTS} \sim 443$ MPa). After this, a crack formed which leads to the discontinuities in the stress-strain curve (the loading was paused to image/video the crack growth).

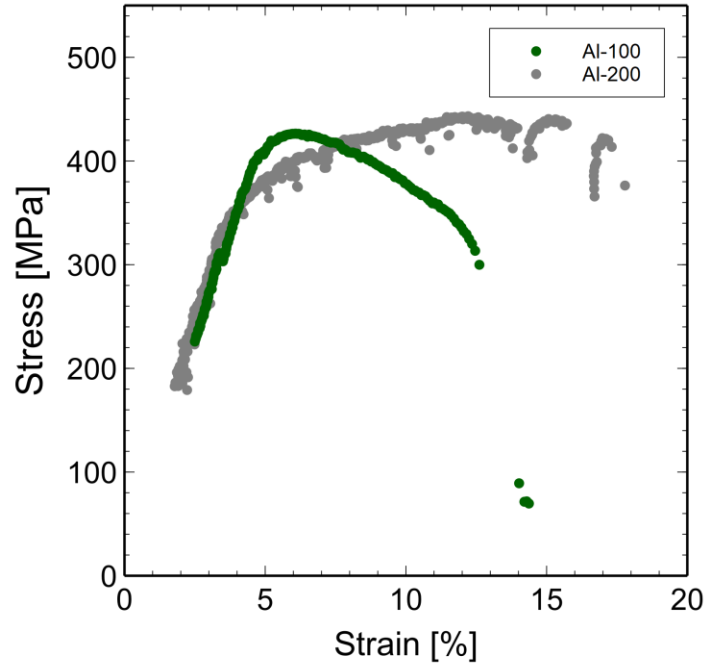


Figure 28 – *In situ* monotonic tensile curves for Al-100 (green) and Al-200 (gray) specimens tested at $\dot{\epsilon} \sim 1 - 3 \times 10^{-4} \text{ s}^{-1}$.

Table 5 – Summary of tensile properties determined by *in situ* monotonic experiments for Al-100 and Al-200.

Specimen	σ_y (MPa)	σ_{UTS} (MPa)	$\epsilon_f(\epsilon_f^p)$ (%)	$\dot{\epsilon}$ (s^{-1})
100-Al	405	426	12.6 (8.7)	1.6×10^{-4}
200-Al	380	443	18.7 (13.6)	3×10^{-4}

The largest difference between the two specimens is the extent of strain hardening and ductility. In the Al-100 specimen, the yield and UTS stress is essentially the same,

indicating no work hardening. In contrast, the Al-200 specimen yields at 380 MPa and the stress gradually increases until the UTS at 443 MPa. These differences are as expected since smaller grain sizes typically promote decreased ductility and work hardening ability.

4.4 In Situ TEM Observation of Deformation Mechanisms

4.4.1 200 nm-thick NC Al

An example of the typical deformation behavior of an Al-200 specimen is shown in **Figure 29**. This shows initial uniform deformation (**Figure 29(a)-(c)**) followed by localized necking (**Figure 29(d)-(e)**), with significant grain growth in the necked region before final fracture of the specimen. This sample was strained at the strain rate $\dot{\epsilon} \sim 1 - 2 \times 10^{-4} \text{ s}^{-1}$ until failure with roughly one third of the specimen gauge in the view frame. Once localized width reduction occurs (**Figure 29(d)-(e)**), increased grain growth is observed within that region, with grain sizes ranging up to 130 nm. This grain growth behavior accompanying neck formation was found to be general among all of the tested samples. That is, in cases where a neck developed, enhanced grain growth occurred within the necked region.

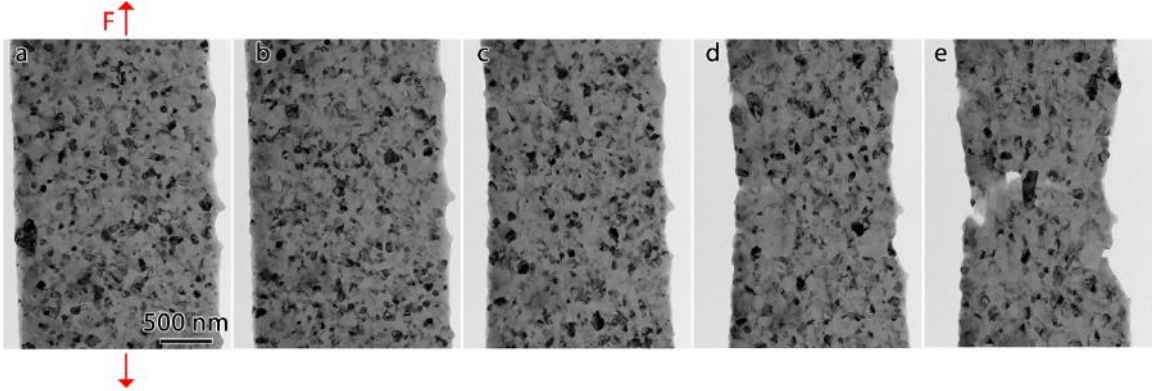


Figure 29 – Bright-field TEM images showing the microstructure evolution of a 200-nm-thick Al microspecimen under uniaxial load (direction of applied load indicated by red arrows). The frames taken at (a) 0%, (b) 4.7%, (c) 8.5%, (d) 12.1% and (e) 14.4% strain [176].

Additional *in situ* TEM straining experiments were performed to quantify the GBM behavior by documenting the migration throughout the entire duration of an experiment and measuring GBM velocities. One example is shown below in **Figure 30**. Data from this experiment is also shown in **Figure 31** to **Figure 33**. The specimen was strained at $\dot{\epsilon} \sim 3 \times 10^{-4} \text{ s}^{-1}$ until failure with roughly 45% of the specimen gauge in the view frame. **Figure 30(a)-(f)** are TEM micrographs that track the deformation and formation of a neck. The view frame is moved towards the end to capture the neck, with the arrowhead marking the same location in each figure (**Figure 30(d)-(f)**). The far-field engineering stress and strain values for each figure is marked in the accompanying stress-strain curve shown in **Figure 30(g)**. From the data, the yield point and apparent Young's modulus were determined to be 380 MPa and 8.9 GPa, respectively. The loading was paused twice in order to capture the neck formation in more detail, which resulted in the stress relaxation/drop seen prior to **Figure 30(d)** (purple square in **Figure 30(g)**) and after **Figure 30(e)** (orange square in **Figure 30(g)**). From the pre-test **Figure 30(a)** to (b), only minor contrast changes can be seen accompanied by a uniform reduction in width, with some

contrast variations attributed to eliminating any film bending that might be present due to specimen manipulation. Continued width reduction is seen in the progression from **Figure 30(b)** to (c), however slight localized width reduction can be seen near the top of the micrograph. As deformation unfolds to **Figure 30(d)**, localized reduction continues and leads to the development of a necked region. The neck further develops in **Figure 30(e)** and (f) where failure eventually occurs. Within this region, pronounced visible grain growth is observed with grain sizes exceeding 250 nm.

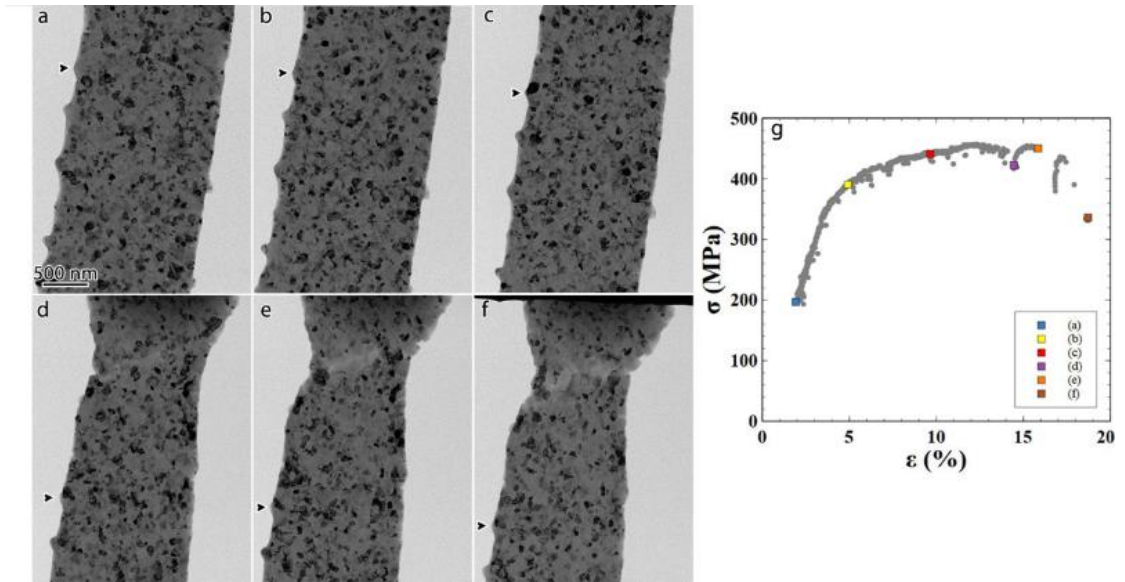


Figure 30 – Low magnification TEM images showing microstructure evolution at different strain values [120]. The frames are taken at (a) 1.9%, (b) 4.9%, (c) 10%, (d) 14.5%, (e) 16.5% and (f) 18.7% total strain. Arrowhead in each designating the same feature. (g) Engineering stress-strain curve with the total strain of (a-f) indicated by the colored squares [176].

In order to provide a further detailed view of the GBM process, TEM video captured during the *in situ* deformation was analyzed to monitor when the onset of grain coarsening occurred and details of the grain growth process. **Figure 31** shows snapshots taken from a continuous video during the highlighted portion (dark blue segment) on the

stress-strain curve (**Figure 31(d)**), beginning at a far field plastic strain of 1.5% and stress of 415 MPa. **Figure 31(a)** is a low magnification snapshot illustrating that the specimen has undergone uniform elongation without the development of a necked region, with the white circle indicating the location of the grain of interest shown in **Figure 31(b)-(c)**. At this point, the specimen is past yield but prior to reaching the UTS of 450 MPa and subsequent neck formation. The grain marked in **Figure 31(b)**, with an equivalent diameter of 63 nm, undergoes grain growth over the course of 34 seconds, resulting in the grain shape shown in **Figure 31(c)** and a final equivalent diameter of 75 nm. The two GBs indicated by arrowheads in **Figure 31(c)** migrated 17 nm at an average speed of 0.5 nm s^{-1} and a maximum ‘jump’ migration speed of 0.7 nm s^{-1} in direction normal to the respective GB. Contrast changes within the highlighted grain as well as in nearby grains could suggest that grain rotation accompanies the grain growth process. Interestingly, the highlighted region is where the neck eventually forms and appears to have increased amount of grain rotation compared to the remaining portion of the specimen, possibly indicating strain localization within this region occurs early in the deformation process and may be a required precursor to neck formation.

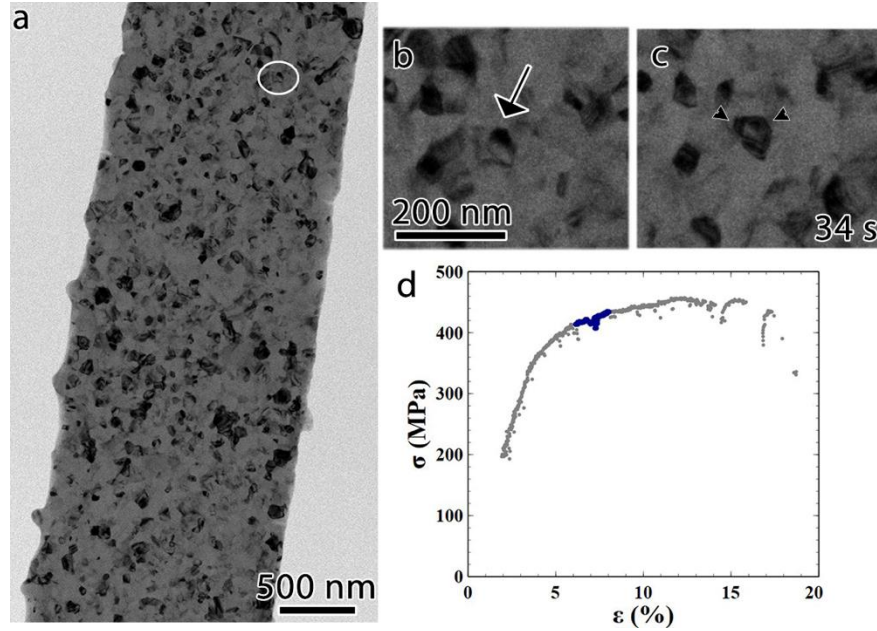


Figure 31 – GBM during uniform deformation. (a) Low magnification TEM image showing no neck developed. Circle indicates location of grain marked by arrow in (b-c). (b) and (c) are digitally magnified snapshots taken 34 seconds apart during the highlighted portion in the stress-strain curve (d).

As deformation progresses and a neck develops, fast GB motion was observed within the necked region, with an example shown in **Figure 32**. **Figure 32(a)** shows that a neck has developed, and the corresponding stress has dropped below the ultimate tensile strength in **Figure 32(e)**. Resetting the TEM time $t = 0$, the vertical dimension of the grain marked by an arrowhead in **Figure 32(b)** is measured at 115 nm. After 78 seconds, only a slight decrease to 112 nm occurs. However, from **Figure 32(c)** to (d), the bottom boundary migrates 12 nm in 5 seconds, resulting in a migration rate of 2.4 nm s^{-1} . This indicates that within the necked region where the stresses are higher, boundary migration occurs at an increased speed resulting in the rapid collapsing of grains and by geometrical necessity, the rapid growth of neighboring grains. Within this region, the local gauge width is decreased from 1700 nm to 1190 nm. For a simple lower-bound estimate, this indicates

that the local stress is increased by a factor of 1.4, resulting in a local stress of at least 630 MPa. This value is not accounting for any decrease in local film thickness that would also contribute to a further increase in stress. To better visualize the different migration rates, the grains tracked in **Figure 31** and **Figure 32(b)-(d)** have been isolated and shown in **Figure 32(f)-(g)** and (h)-(i), respectively. It is clear that the grain within the necked region experiences a larger change in grain size over the course of the 5 seconds separating **Figure 32(h)** and (i) due to the faster GBM speed of 2.4 nm s^{-1} . This is another example of ‘jerky’ type boundary motion, with limited motion for over a minute and then rapid boundary motion.

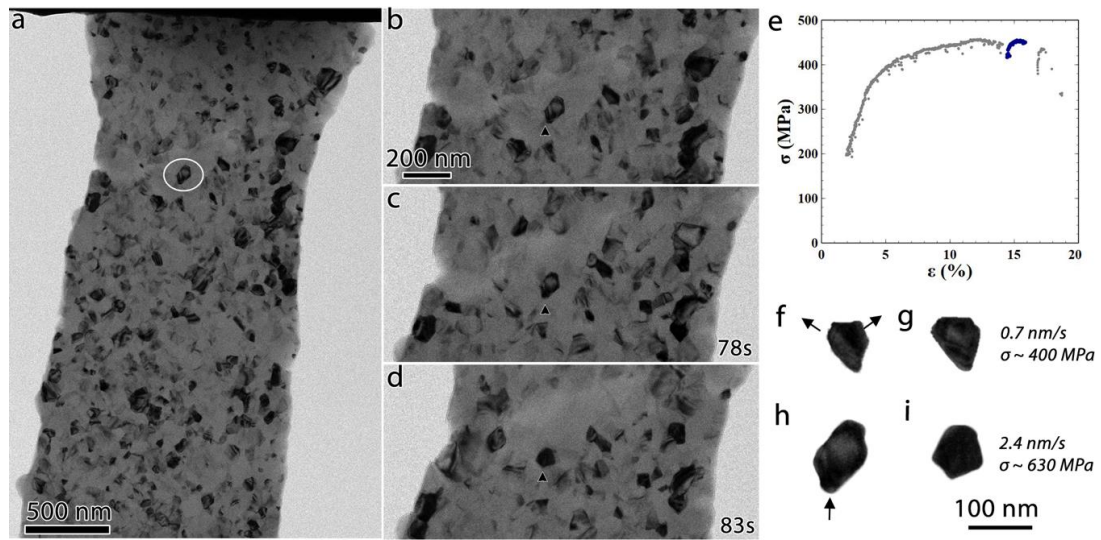


Figure 32 – Fast GBM after neck develops. (a) Low magnification TEM image showing developed neck near top of snapshot. White circle indicates location of highlighted grain in (b-d). (e) Stress-strain curve with highlighted region corresponding to when snapshots (a-d) were recorded. Change in grain size as a function of time for (f,g) a grain in uniform region and (h,i) necked region (from b-d).

In order to quantitatively track grain growth further, grain sizes were measured using frames taken from TEM videos during the *in situ* deformation. The results of this

analysis are shown in **Figure 33** by comparing measured grain size distributions within both the necked and uniform regions as the deformation progresses. Once a visible neck was formed, grain size was measured both within and outside the neck region and used to produce separate distributions. **Figure 33(b)** shows an example of how the *necked* vs. *uniform* regions were defined: the grains within the two white lines were considered within the 'necked' region and grains outside that region were marked as within the 'uniform' region. The cumulative area fraction plots illustrate that grains within the necked region, represented by triangle markers and dashed lines, experience enhanced grain growth when compared to the uniform region (circle markers and solid lines) for the same strain value. For each strain value, there is a measurable increase in grain size within the necked region when compared to the uniform region. For $\varepsilon = 14.1\%$ (green data), half of the measured grains are below 94 nm within the uniform region, however, this value increases to 115 nm within the necked region. Measurable grain size increase within the necked region suggest that grain coarsening is caused by the increased stress, which is consistent with previous reports of stress-driven grain growth [20,68]. Additionally, there is little variation in grain size as the strain progresses within the 'uniform' region of the specimen. Within this region, the local stress is less than that within the necked region and thus likely not high enough to promote extensive grain coarsening. These results also suggest that the formation of a necked region further promotes grain coarsening. For example, the maximum grain size within the necked region for $\varepsilon = 12.6\%$ is 192 nm while for $\varepsilon = 16.8\%$, the maximum is 280 nm. As deformation progresses and strain increases, the disparity between *uniform* versus *necked* region grain size increases as well. Each of the 'necked' data sets share a similar grain size minimum of ~50 nm while the maximum grain size increase with strain.

This is evidence of inhomogeneous grain growth as small grains remain, albeit with diminishing area fraction, while other grains grow resulting in increased maximum grain size.

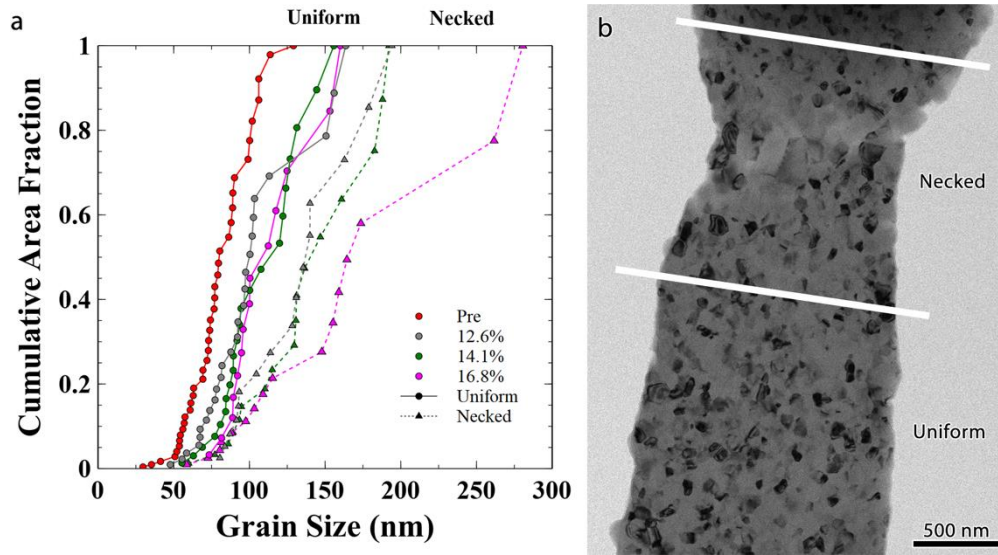


Figure 33 – (a) Cumulative area fraction grain size plots for different strain values post neck formation compared to the initial microstructure (red data). Data with circle markers and solid lines are taken from grains within the uniform region while data with triangle markers and dashed lines are from grains within the necked region. (b) Low magnification TEM micrograph designating regions defined as ‘Necked’ (in between white lines) and the remaining ‘Uniform’ region.

Evidence presented thus far has pointed to GBM promoted by increasing stress, and based on this, it would be expected that other sources of stress raisers would lead to a similar observation. **Figure 34** shows such an example, where rapid GBM is seen ahead of an extending crack tip during *in situ* TEM deformation. In **Figure 34(a)**, a relatively large grain with a vertical dimension of 268 nm in front of a crack tip is marked by an arrow. This dimension increases to 273.7 nm in **Figure 34(b)**. Contrast changes in the above neighboring grain (marked with a grey arrowhead) indicate grain rotation. This could be associated with dislocation emission and absorption at GBs as well as rapid dislocation

glide through the grain, although dislocations are not visible in the electron diffracting condition of the experiment. From **Figure 34**(b) to (c), the top boundary, marked by a black arrowhead, migrates upward 3.6 nm in 0.6 s, corresponding to a migration speed of 6 nm s⁻¹. The final grain microstructure, prior to complete failure, has a drastically increased vertical dimension of 336 nm, which is 1.25 times larger than the initial size as 268 nm. This is another example of the jerky, stop-and-go behavior of boundary migration, but with a GBM rate 3-30 times larger than those measured in grains away from a crack tip.

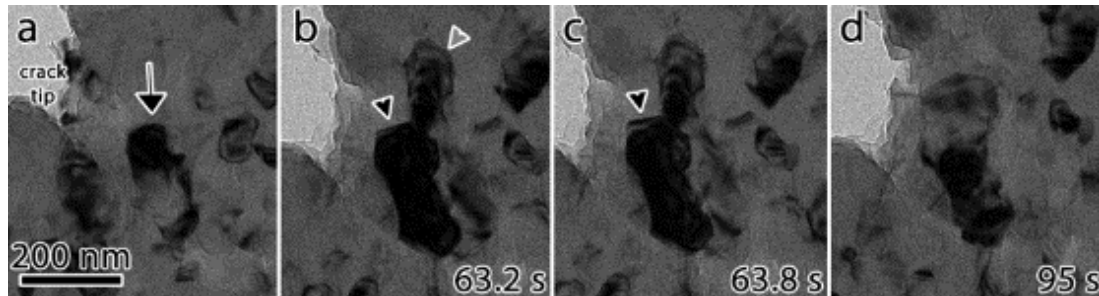


Figure 34 – Rapid GB motion ahead of crack tip. (a) the beginning of recorded segment. (b) $t = 63.2$ s, slight grain growth. (c) $t = 63.8$ s. Top boundary migrated 3.6 nm in the 0.6 s separating (b) and (c) resulting in migration speed of 6 nm s⁻¹. (d) $t = 95$ s, final grain structure prior to failure [176].

During each of the above *in situ* TEM experiments, no dislocation activity is observed. However, post-mortem TEM analysis shows dislocation structures present in the large grains near the fracture surfaces. One such example is seen in **Figure 35**. From **Figure 35**(a), it is clear that the fracture surface is intergranular and composed primarily of large grains, which is consistent with the previous analysis of pronounced grain growth within necked region. GB sliding is also seen to accompany the intergranular fracture. The fracture surface resembles a Wilsdorf-like tooth structure similar to previous reports [177,178]. An enlargement of the four highlighted grains (B, C, D and E) shows dark field

images with evidence of intragranular dislocations, suggesting that either dislocation activity accompanies the grain growth process or dislocation activity initiates once the grains reach a critical size. These results are similar to those reported by Hattar *et al.* which show that the density of both dislocations and deformation twins is much greater near the fractured surface than that of the gauge section in UFG Al thin films [179]. Similarly, they reported intergranular crack propagation.

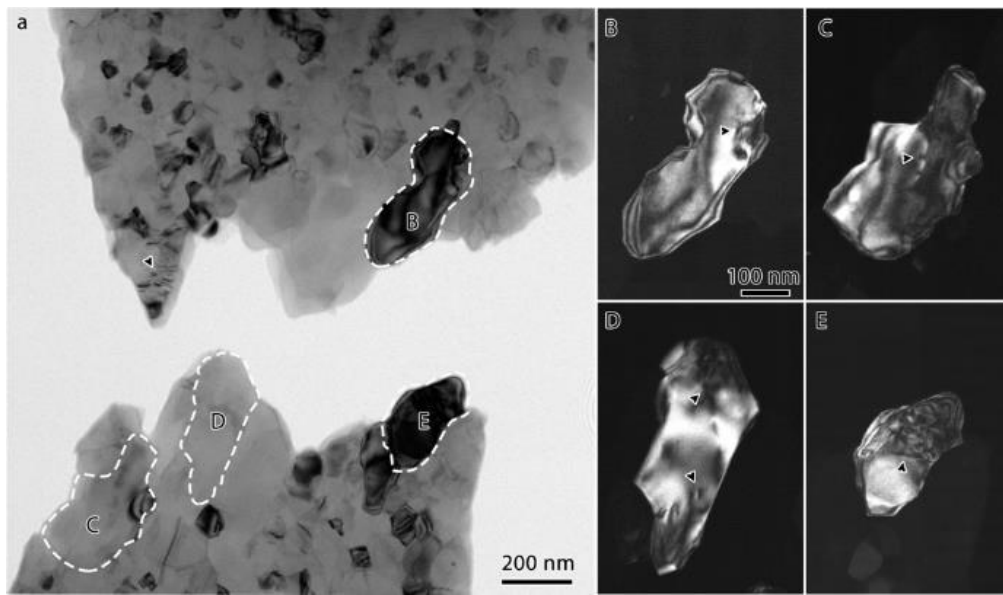


Figure 35 – Post-mortem TEM analysis of fracture surface (a) multiple large grains near fracture surface, (b-e) enlarged dark-field TEM images of highlighted grains with evidence of dislocation structures indicated by arrowheads [176].

4.4.2 100 nm-thick NC Al

The behavior of an Al-100 specimen during tensile loading is shown in **Figure 36**. Prior to any load being applied, the gauge width is roughly uniform, as seen in **Figure 36(a)**. However, during deformation a slight necked region formed in the bottom portion of the gauge length (arrowed in **Figure 36(b)**). This frame was recorded after a 56-minute repeated stress-relaxation experiment with a maximum stress of $\sigma \sim 457$ MPa (the data

from this experiment is shown in **Figure 38** and discussed later). The local width in this region is 2240 nm compared to the original 2735 nm (this is also the width near the top of the gauge far from the necked region). This decrease in the local gauge width will lead to an increase in local stress by a factor of 1.22 within the ‘necked’ region. The fact that failure eventually occurred in this region (**Figure 36(c)**) is likely attributed to this increase in local stress.

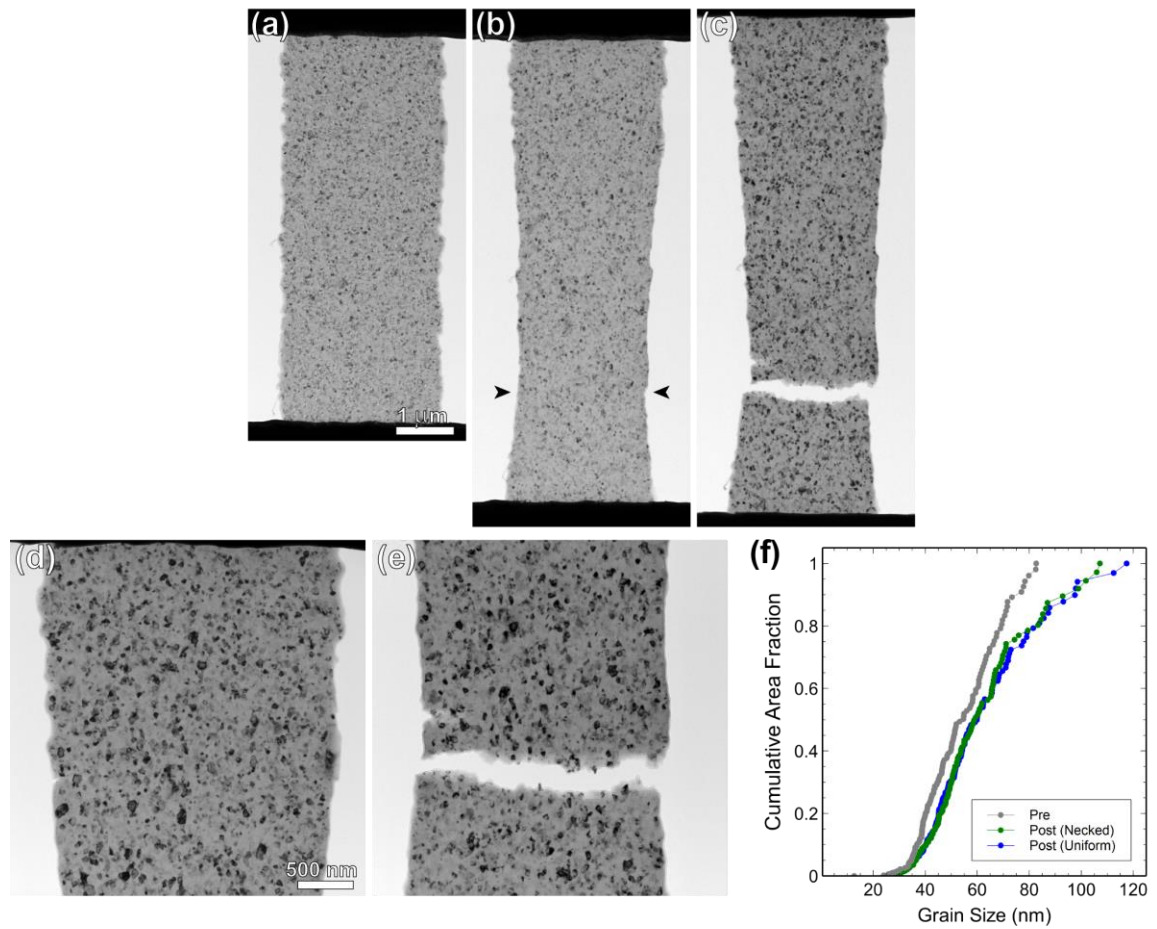


Figure 36 – *In situ* TEM observations of deformation of Al-100 during tensile loading. BF TEM images of the gauge length (a) prior to an applied load, (b) while straining, and (c) after failure. Microstructure after failure in the region of (d) ‘uniform’ (far from necked region) and (e) near the necked/fracture surface. (f) grain size distribution in terms of cumulative area fraction for the pre-strain state (gray), region far from neck (blue), and necked/fractured (green).

During this experiment (and others performed), it was difficult to identify individual examples of GBM/grain growth. This could be related to difficulties with imaging and analyzing small grains. Tracking grains in detail requires that the same grain remain in contrast long enough to observe the behavior of the GBs. Additionally, the contrast for these specimens is less than that of the Al-200 due to the reduced thickness. In any case, GBM/grain growth was characterized by comparing the grain size distribution of the pre-strained state versus grains within the ‘uniform’ (far from neck/fracture surface, **Figure 36(d)**) and grains within the necked/fractured region (**Figure 36(e)**). This data is presented in terms of a cumulative area fraction grain size distribution shown in **Figure 36(f)**. The grain size of the pre-strained state is shown in gray and has an average (weighted) grain size of 55 ± 14 nm. The post-strained grain size dataset is divided by proximity to the necked/fractured surface. Both of the post-strained datasets illustrate a shift towards larger grain sizes, indicating that stress-assisted GBM/grain growth does occur in these specimens, albeit by a small amount.

There is a negligible difference between the average grain sizes in the region far from the neck area (64 ± 13 nm) versus the grains within the necked region and close to the fracture surface (63 ± 20 nm). This is likely explained by the unstable crack growth that led to premature specimen failure (i.e. the specimen fails before there is chance for an extensive necked region to develop with enhanced stresses to promote grain growth). This is contrast to the behavior seen in for the Al-200 specimen in which a necked region gradually forms in addition to a relatively slow crack growth in a ductile manner. The fact that the fracture surface in **Figure 36(c,e)** is 90° with respect to the vertical loading axis is

indicative a brittle failure, which is different from the ‘saw-tooth’, ductile-type fracture surface of the Al-200 specimen (**Figure 35**).

4.5 *In Situ* TEM Activation Volume Measurements

4.5.1 200 nm-thick NC Al

In situ repeated stress-relaxation experiments have been conducted to characterize the deformation in terms of the measured activation volume. **Figure 37** shows the results from one of these experiments performed on a Al-200 specimen. The data was collected using electrical-based sensing. The test was conducted at $\dot{\epsilon} \sim 1.5 \times 10^{-4} \text{ s}^{-1}$. **Figure 37(a)** is the full stress-strain curve until the specimen was unloaded. The gaps in the data correspond to the stress transients which are shown in **Figure 37(b)**. This experiment consisted of 5 stress-relaxation segments with each having an initial $\sigma \sim 325 \text{ MPa}$. Each relaxation was roughly 30 seconds in length with the exception of the final relaxation. Even though the initial stress level does not change significantly, the amount of stress relaxation $|\Delta\sigma|$ increases with successive relaxations. The 5th and final relaxation had a stress decrease of 58 MPa after the first 15 seconds which is larger than the 15-second decrease in the 2nd relaxation (38 MPa). As shown in **Figure 37(c)** and (d), the true activation volume V^* varied from $7-16b^3$ and the apparent activation volume ranged from 3 to $15b^3$. The amount of stress-relaxation $|\Delta\sigma|$ influences the amount of stress increase required during the quick reloading between successive relaxation segments to reach the same initial stress value. For example, a reloading of 55 MPa was required after Relax #1 for the initial stress level for Relax #2 to reach that of initial level of #1. Since the amount of stress relaxation

increased with increasing relaxations, a reloading of 85 MPa was required after Relax #4 to ensure Relax #5 begins at a similar stress level.

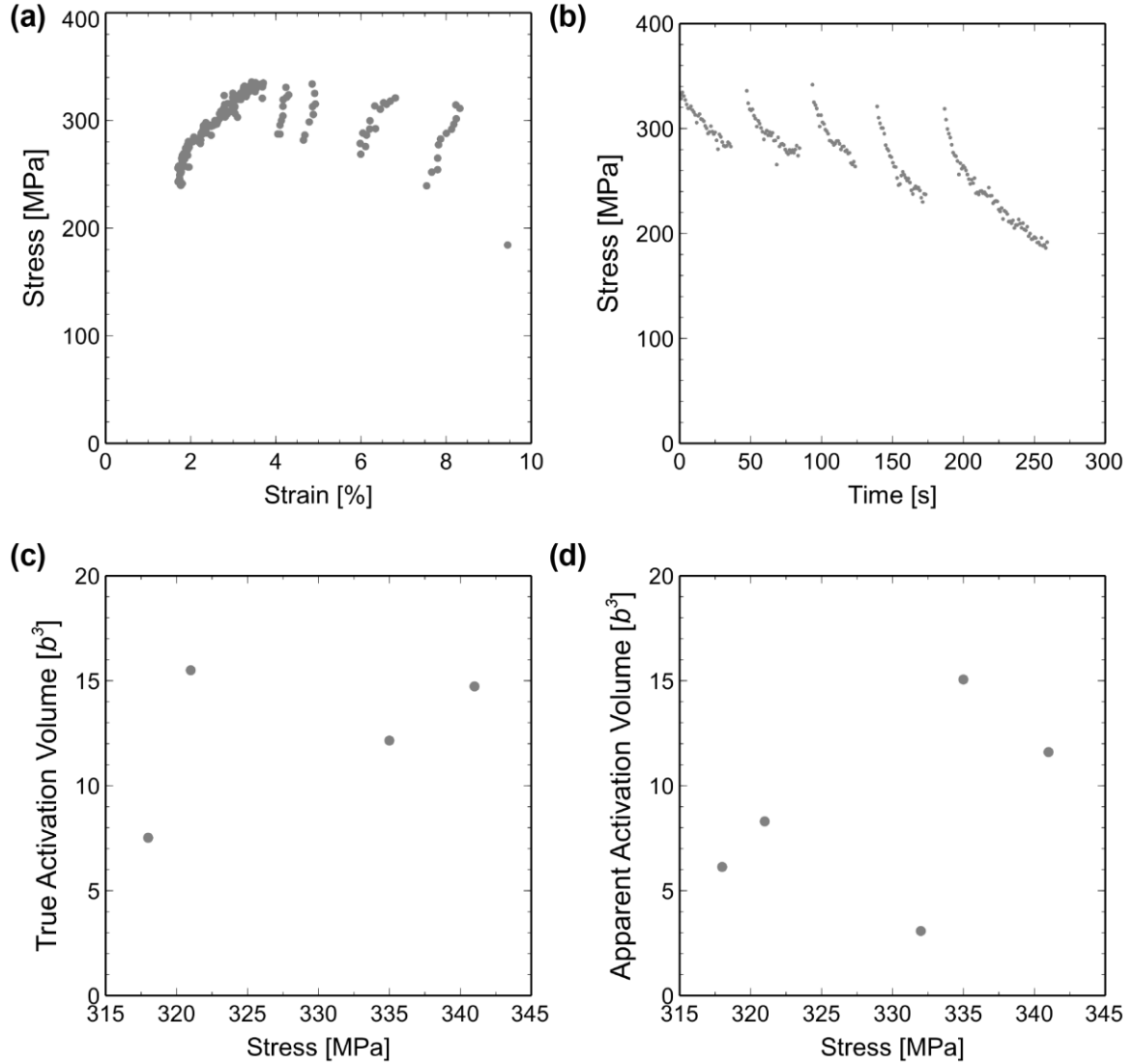


Figure 37 - *In situ* measurement of activation volume in Al-200 NC Al. (a) The full stress-strain curve until the specimen was unloaded. Gaps in the data correspond to stress-relaxation segments which are shown in (b). The measured (c) true and (d) apparent activation volumes values.

Since the amount of stress increase during reloading ($\Delta\sigma_{12}$) is a component of calculating V^* (Eqn. 29), it is likely that this will have an effect on the measured true

activation volume. Another component in Eqn. 29 is the ratio of strain rates ($\dot{\epsilon}_{i2} / \dot{\epsilon}_{f1}$). Since all of these relaxations occur at similar stress levels, this experiment is useful in evaluating the different factors that contribute to the measured values. These are summarized for three of the relaxations (Relax #2, #4, and #5) in **Table 6**. Relax #2 and #4 have similar reloading stress $\Delta\sigma_{12}$ but different $\dot{\epsilon}_{i2} / \dot{\epsilon}_{f1}$ and the V^* values only differ slightly (12 vs. $15b^3$). Relax #2 and #5 have very different $\Delta\sigma_{12}$ and essentially the same $\dot{\epsilon}_{i2} / \dot{\epsilon}_{f1}$ and their V^* values differ by almost a factor of two (12 vs. $7b^3$). This indicates that the amount of stress-relaxation $|\Delta\sigma|$ and stress reloading $\Delta\sigma_{12}$ have a larger impact on the calculated V^* values than $\dot{\epsilon}_{i2} / \dot{\epsilon}_{f1}$.

Table 6 – Summary of activation volume values and contributing components (strain rate ratio and reloading stress) for 3 of the relaxations in Figure 37.

Relax #	$V^* (b^3)$	ϵ_p (%)	$\dot{\epsilon}_{i2} / \dot{\epsilon}_{f1}$	$\Delta\sigma_{12}$ (MPa)
2	12	1.1	8.9	55
4	15	4.0	12.9	50
5	7	6.1	8.1	85

4.5.2 100 nm-thick NC Al

Results from a repeated stress-relaxation experiment on an Al-100 specimen are shown below in **Figure 38**. The data was collected using electrical-based sensing and the test was conducted at $\dot{\epsilon} \sim 6.2 \times 10^{-5} \text{ s}^{-1}$ with 14 total relaxation segments before the specimen was unloaded (specimen did not fail). **Figure 38(a)** is the full stress-strain curve and **Figure 38(b)** is all of the relaxation data. There were 11 relaxations that achieved $R^2 > 0.9$ and of those 6 of them met the assumptions required for V^* measurement (quick reloading to similar stress level as previous relaxation segment). These V^* values are shown

in **Figure 38(c)** and vary from $2-9b^3$ for the stress range $368 < \sigma < 454$ MPa. The apparent activation volume V_a measurements varied from $1-9b^3$.

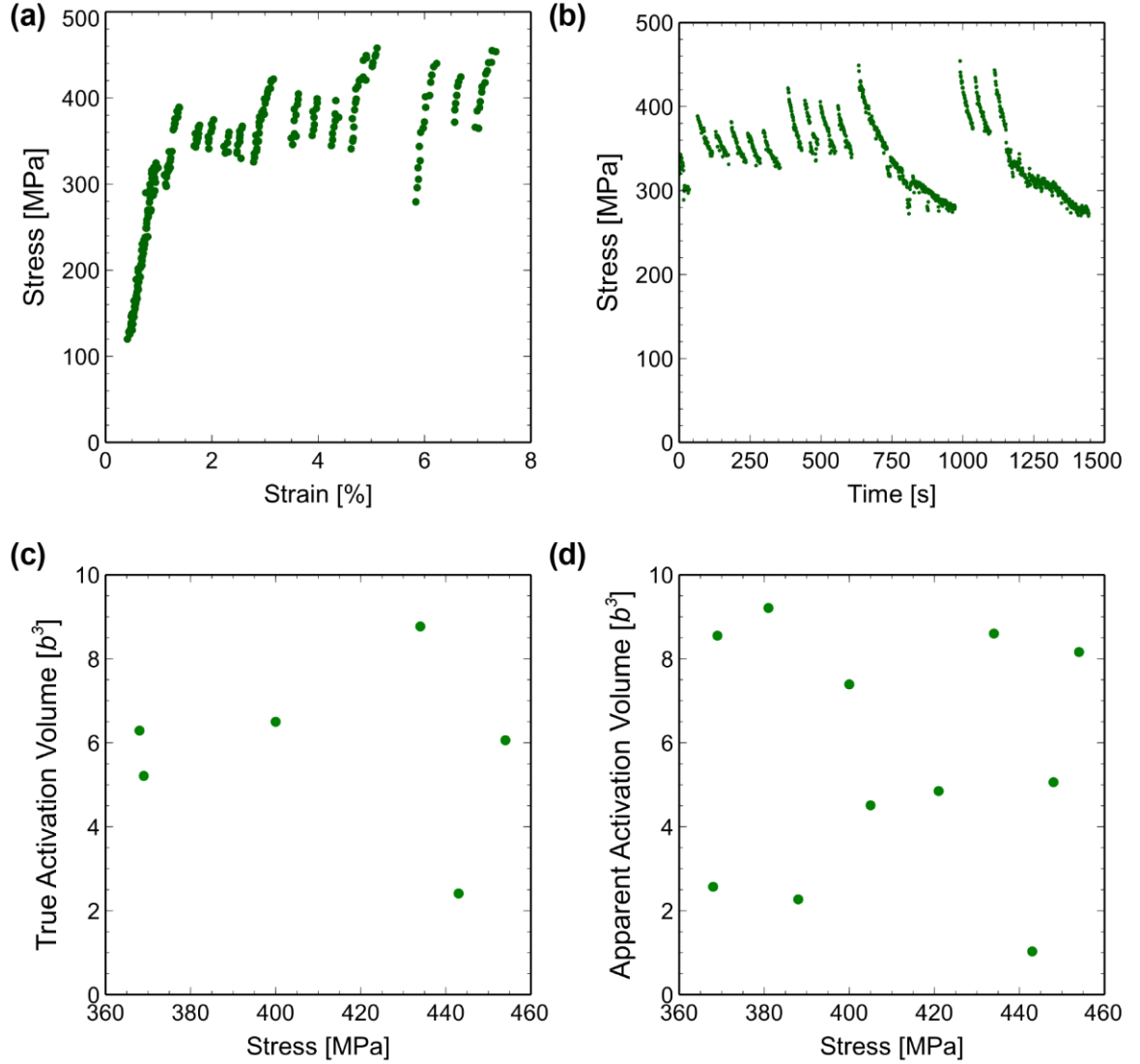


Figure 38 – *In situ* repeated stress-relaxation experiment and activation volume measurements for Al-100 specimen. Full (a) stress-strain and (b) stress-time (relaxation) data for the experiment, (c) true and (d) apparent activation volume values determined from the relaxations in (b) with $R^2 > 0.9$.

4.6 Discussion

Based on the Hall-Petch law (Eqn. 1), a reduction in grain size from ~90 nm to ~55 nm would be expected to cause an increase in the yield strength by a factor of 1.27. For the two monotonic curves shown in **Figure 28**, the yield strength increases from 380 MPa (Al-200) to 405 MPa (Al-100), which is a factor of 1.06. Qualitatively, the increase in yield strength is consistent to what is expected. Additionally, the curves indicate differences in the strain hardening ability. The Al-100 specimen exhibits almost no strain hardening as the strength does not increase after yielding (yield and UTS stress are essentially the same). This is likely attributed to the smaller grain sizes limiting dislocation generation, storage and entanglement which will lead to strain hardening. In the Al-200 specimen, there is evidence of strain hardening (an increase in strength with increasing strain post yielding) and there is evidence of dislocation storage (**Figure 35**). It is important to note that these curves are from two specimens only and additional monotonic curves should be collected to establish statistical differences between the two specimen types.

By utilizing *in situ* TEM straining techniques, the deformation mechanisms active in NC Al has been investigated. Direct evidence of GBM and grain growth is provided for the Al-200 specimens (**Figure 29-Figure 35**). Grain growth is also shown to occur in the Al-100 specimens (**Figure 36**), however, these specimens exhibit decreased ductility and premature failure prior to extensive grain growth. Deformation-induced grain growth has been observed in a multitude of studies, including tensile straining of NC Al [20,63,68], NC Ni [67], and NC Au [66] and under nanoindentation of NC Al [79,169] and NC Cu [180]. Some studies, however, report grain growth is preceded by grain rotation, suggesting that grain growth occurs by the coalescence of neighboring grains [66,67]. Direct evidence of GBM in this chapter eliminates this as the dominant mechanism for grain growth. There

is some evidence to suggest grain rotation may occur prior to and after neck formation. However, it could not be determined if the observed contrast changes were a direct result of crystallographic rotation due to dislocations passing through the grain or solely transgranular dislocation glide. In either case, the contrast changes are indicative of increased plastic deformation occurring within that region as it is not expected that global rotation of the specimen would result in bend contours within the local region.

The *in situ* observations in this chapter offer additional insight into the effect local stress has on GBM. In the *in situ* experiments on the Al-200 specimens, extensive grain growth was observed to occur preferentially within the necked region of the specimens. This is strong evidence to suggest that the GBM is driven by the local increase in stress within the necked region. In the Al-200 specimens, evidence that GBM occurs outside of the necked region suggests that neck formation is not a direct result of grain growth but that instead, the increased stress within the necked region is necessary for increased GB migration. This is consistent with the growing number of studies that report stress-assisted GBM leading to preferential grain growth in highly stressed regions [16,20,63,68,169,181,182]. Extensive grain growth is not seen in the Al-100 specimens. This is attributed to the fact that a significant neck does not form and unstable crack growth leads to specimen failure prior to grain growth.

For the Al-200 specimens, GBM speeds varied from $0.2 - 0.7 \text{ nm s}^{-1}$ for grains either outside or prior to neck formation (**Figure 31**) when the applied tensile stresses were close to the ultimate tensile strength of 450 MPa. The GBM speeds increased to 2.4 nm s^{-1} for grains within the necked region (**Figure 32**) where the local tensile stresses were elevated to around 630 MPa, and even advanced to 6 nm s^{-1} for a growing grain ahead of a

crack-tip (**Figure 34**). Other researchers have observed boundary migration speeds ranging of 5 - 10 nm s⁻¹ for grains near a crack tip in pure NC Al down to 0.7 - 1 nm s⁻¹ for boundaries doped with oxygen (impurities lead to a drag effect) [181]. Legros *et al.* has also reported speeds of 0.1 - 0.2 nm s⁻¹ up to 50 and 200 nm s⁻¹ for GB ‘jumps’ and suggested that these drastic speeds were a result of different mechanisms of migration [63]. The migration velocities reported in this study of 0.2 – 6 nm s⁻¹ seem to be comparable with those reported in other studies as well as the ‘jerky’ migration behavior. The order of magnitude difference between the migration speed of grains prior to or outside neck formation and the grains within highly stressed regions likely reflect the inhomogeneity of driving force (stress) that can be measured by the present MEMS-based platform. Stress-driven GBM is activated by stress and as such, areas of increased stress – such as within necked region or ahead of a growing crack – experience increased migration velocity. Other studies have suggested a similar trend by observing that grain size decreases with increasing distance from a crack tip and by geometrical necessity, GBM velocity follows the same trend [63].

4.7 Conclusion

This chapter presents characterization of the deformation mechanisms active in the Al-200 and Al-100 specimens by combining *in situ* TEM observations with measurement of activation volume. Extensive grain growth was observed in the Al-200 specimens with the results indicating that GBM is primarily stress-induced and that the local increase in stress (either due to necking or a crack tip) drives faster GBM. Measured GBM speeds ranged from 0.2 – 0.7 nm s⁻¹ when the applied tensile stresses were close to the ultimate tensile strength of 450 MPa, increased up to 2.5 nm s⁻¹ for grains within the necked region

where the local tensile stresses were elevated to around 630 MPa, and even rose to 6 nm s^{-1} for GBM that occurred ahead of crack tip. There was no direct TEM evidence of grain growth in the Al-100 specimens, however, measuring the grain size distribution before and after straining indicated an increase in average grain size from 55 to 64 nm. True and apparent activation volume was measured by performing repeated stress-relaxation experiments. True activation volume V^* values ranged from $7-16b^3$ for the Al-200 specimens and $2-9b^3$ for the Al-100 specimens.

CHAPTER 5.

PLASTIC DEFORMATION MECHANISMS IN GOLD

5.1 Overview

Experiments involving the UFG Au microspecimens have been completed to identify different deformation mechanisms (both dislocation- and GB-based) through repeated stress-relaxation tensile tests. Section 5.2 provides a detailed description of the initial microstructure of the as-deposited and annealed Au films, followed by the characterization of the mechanical properties in Section 5.3. Sections 5.4 and 5.5 provide *in situ* observation of the active deformation mechanisms and measurement of activation volume, respectively.

5.2 Initial Microstructure

Gold specimens with three different average grain sizes have been tested. The initial microstructure is shown below for each. **Figure 39(a)-(c)** are BF TEM images for the as-deposited, 350°C annealed (A350), and 700°C annealed (A700) specimens, respectively (see **Table 3** in Section 2.3.1 for annealing details). For the as-deposited and A350 specimens, orientation mapping has been performed and respectively shown in **Figure 39(d)** and **(e)**. The grain size distribution for each is shown in **Figure 39(f)** and illustrates the change in grain size that occurs during annealing. The as-deposited specimens have an average (weighted) grain size of 142 ± 68 nm whereas the A350 specimens have an average (weighted) grain size of 287 ± 150 nm. In constant, the A700 specimens have the largest average grain size of 768 ± 252 nm. These reported averages were done by manually

tracing grains for a section of each specimen type. Both the minimum grain size and maximum grain size increases with increasing annealing temperature and time. The minimum grain size increases from 22 to 57 and finally to 140 nm for the A700 specimens. Similarly, the maximum grain sizes are 265, 580, and 1353 nm. Specifically, 20% of the area of the as-deposited specimens is composed of grains sizes less than 50 nm or less, whereas only 2.5% of the area of the A350 specimen contains grains less than 50 nm in size and 0% of the area of A700 is composed of grains of this size.

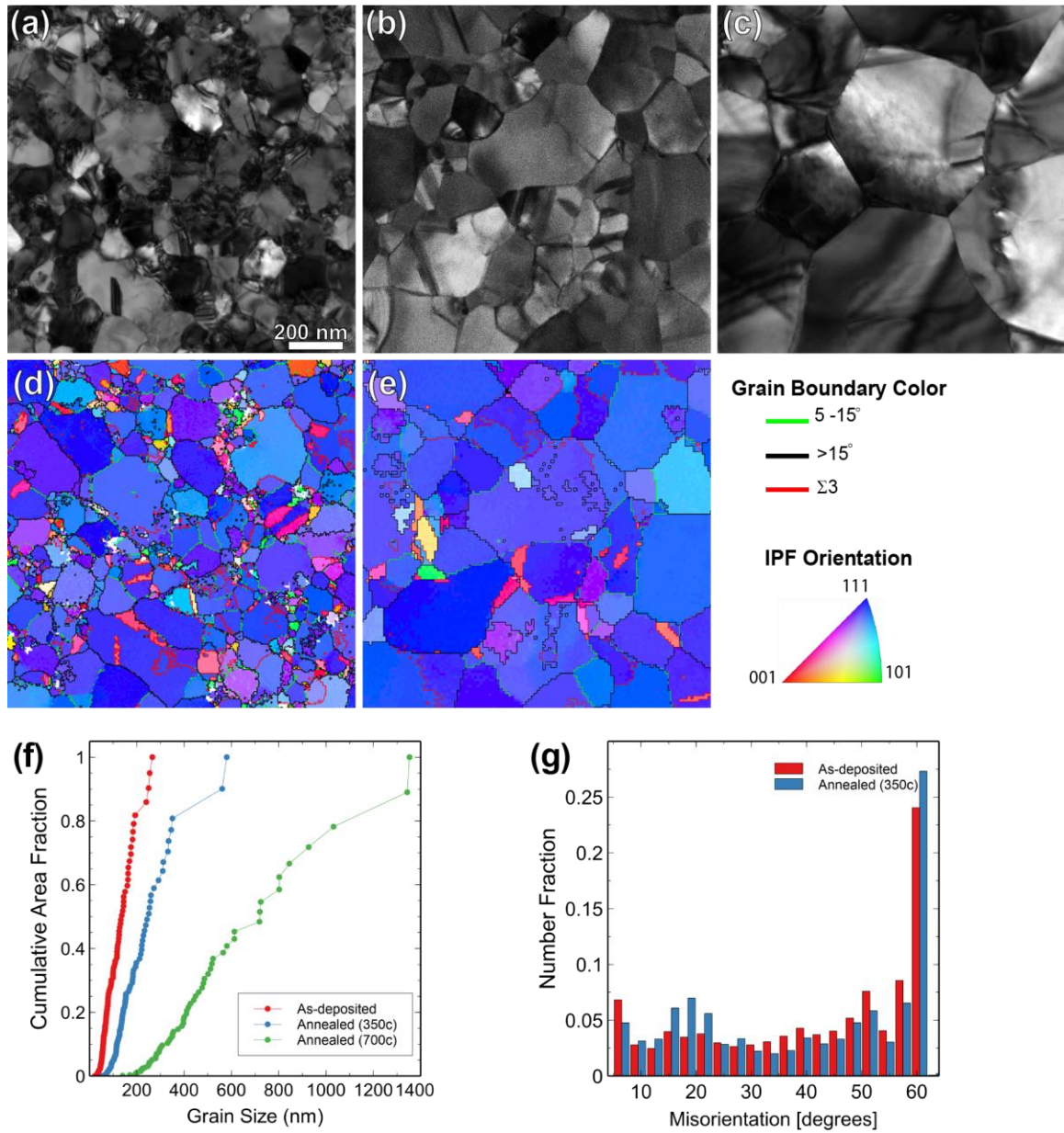


Figure 39 – Initial microstructure of UFG Au specimens. Bright-field TEM images of (a) as-deposited and specimens that have been annealed at (b) 350°C (30 minutes) and (c) 700°C (5 minutes) with corresponding orientation maps for (a) and (b) in (d) and (e), respectively. The legend for the orientation and GB orientation is provided to the right. (f) Grain size distribution for each shown in terms of cumulative area fraction and (g) GB misorientation distribution from (d) and (e).

Many of the grains within the as-deposited films contain pre-existing dislocations, whereas most of the A350 and A700 grains do not contain pre-existing dislocations as the

annealing process removes these. The orientation maps in **Figure 39**(d-e) show the films exhibit a dominant $\langle 111 \rangle$ out-of-plane texture. The GB misorientation angle distribution taken from the orientation maps is shown in **Figure 39**(g). Both as-deposited and A350 specimens show similar GB misorientation distribution. The number fraction of GBs with $9.5^\circ < \theta < 27.5^\circ$ increased after annealing and those with $\theta > 30^\circ$ decreased, with the exception of twin boundaries ($\theta = 60^\circ$). In both films, a large fraction of the boundaries are $\Sigma 3$ twin boundaries with the number fraction increasing slightly during annealing (0.24 to 0.27). An orientation map for the A700 specimen is not available, but based off the TEM imaging it appears to contain primarily HAGB (large contrast change across GBs) with a smaller number of LAGBs that resemble dislocation arrays.

5.3 Monotonic Response

Each specimen type has been monotonically tensile tested, resulting in the stress-strain curves shown below in **Figure 40** with the tensile properties summarized in **Table 7**. The different specimens have slightly different tensile properties, albeit not by a large margin. The tests were all conducted in a similar strain rate regime of $\sim 9 \times 10^{-5} - 1.5 \times 10^{-4} \text{ s}^{-1}$. The A350 specimen has the largest 0.2% yield stress σ_y of 550 MPa followed closed by A700 (544 MPa) while the as-deposited specimen yielded at 489 MPa. This trend is counterintuitive given that the as-deposited has the smallest grain sizes and would be expected to have the highest yield strength (Hall-Petch effect). This could be due to the fact that each of these curves are from one specimen only. Repeating for multiple specimens in each category would be required to make definitive comparisons as there can be significant sample to sample variation. The UTS σ_{UTS} was 520, 545, and 584 for the as-

deposited, A700, and A350, respectively. The most striking difference between the curves is the extent of ductility, which decreases with increasing grain size (failure strain ϵ_f^p decreases from 5.1 (as-deposited) to 3.7 (A350) to 1.6 (A700)). This is once again opposite from anticipated as larger grained materials are expected to be able to support more intragrain plasticity and thus achieve higher ductility. This could indicate that alternative mechanisms are active in the as-deposited specimens that accommodate the plastic deformation or that additional experiments are needed to investigate if the differences shown here are repeatable (more discussion on this will be provided in Section 5.6).

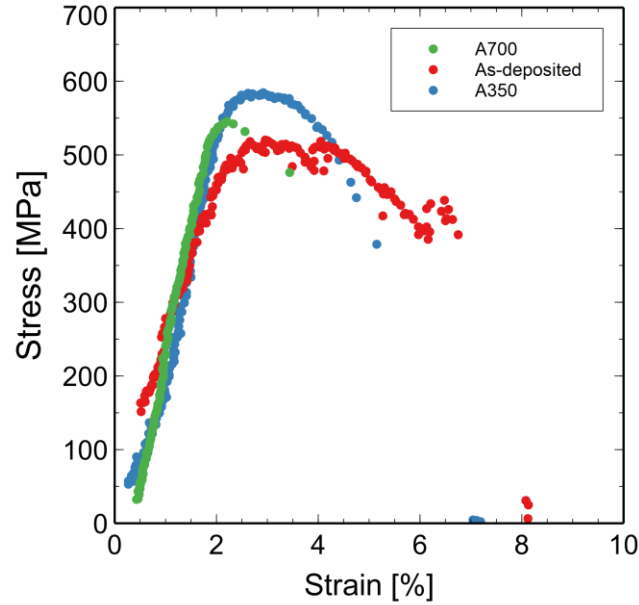


Figure 40 – *In situ* monotonic tensile curves for as-deposited (red), A350 (blue), and A700 (green) tested under similar strain rates.

Table 7 – *In situ* monotonic tensile properties for as-deposited, A350, and A700 UFG Au specimens.

Specimen	σ_y (MPa)	σ_{UTS} (MPa)	$\epsilon_f(\epsilon_f^p)$ (%)	$\dot{\epsilon}$ (s ⁻¹)
As-deposited	489	520	6.7 (5.1)	1.5×10^{-4}
A350	550	584	5.1 (3.7)	1.2×10^{-4}

5.4 In Situ TEM Observation of Deformation Mechanisms

5.4.1 As-deposited UFG Au

Both GB- and dislocation-based deformation mechanism are active during deformation in the as-deposited UFG Au specimens. Early in deformation (i.e. shortly after yielding), isolated dislocation nucleation and slip is observed, including the nucleation of both perfect and partial dislocations emitted from GBs, with an example of this shown in **Figure 41**. During this segment, a leading partial is emitted from the top GB and glides across the majority of the grain, leaving behind a stacking fault region in its wake (marked by arrowhead in **Figure 41(a)**). The trailing partial is emitted four seconds later (**Figure 41(b)**) to form a perfect dislocation that joins a dislocation pile-up at the bottom GB. Multiple perfect dislocations are also emitted and glide in the direction indicated by the arrow in **Figure 41(c)** where the dislocations pile-up against the GB. The snapshots were taken at $\sigma \sim 170$ MPa and $\varepsilon \sim 3.2\%$.

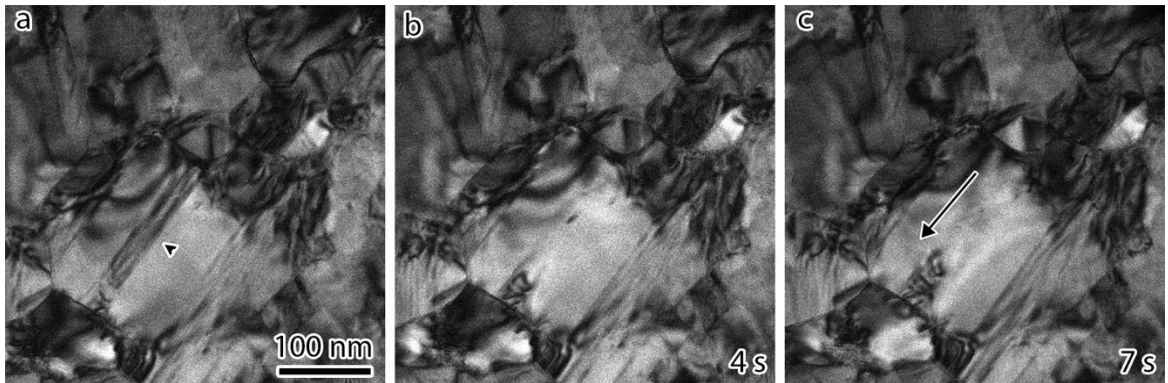


Figure 41 – Emission of leading and trailing partial dislocation from a GB during a stress relaxation segment. Arrowhead in (a) indicates the stacking fault region between leading and trailing partial dislocation. (b) Trailing partial is emitted and

perfect dislocation transverses the grain. (c) Arrow indicates direction of dislocation glide leading to pileup at the nearby GB [92].

Another observed mechanism is dislocation cross-slip resulting in a transition between intra- to intergranular glide. Shown in **Figure 42**, a single dislocation (marked by arrowhead) is emitted from a GB and glides in the interior of the grain (transgranular glide). Between **Figure 42**(c) and (d), the dislocation cross-slips onto a GB (marked by ‘GB’ in **Figure 42**(d)) and subsequently glides the boundary plane (intergranular glide). The boundary plane is presumably a coherent twin boundary, although this could not be directly confirmed.

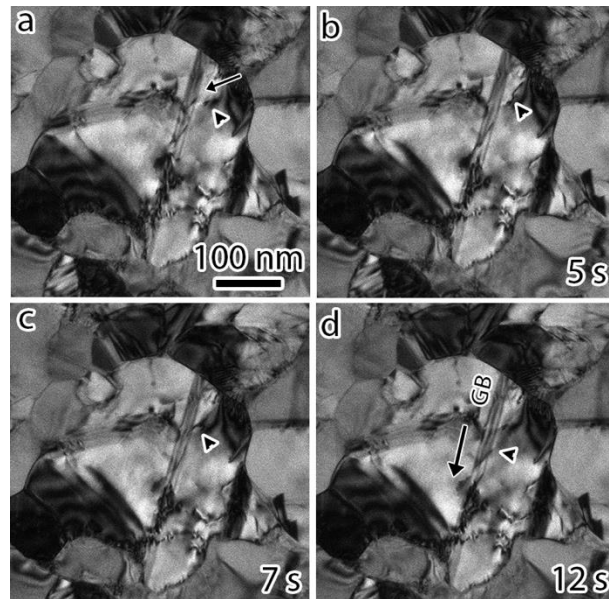


Figure 42 – Dislocation cross-slip resulting in a transition from transgranular to intergranular dislocation glide. Arrowhead in each frame tracks a single dislocation. (a) Dislocation is emitted from GB and glides transgranular in direction indicated by arrow. (b)-(c) transgranular dislocation glide. (d) dislocation cross-slips onto GB and subsequently glides on GB in direction indicated by arrow. Experimental time is given in each frame [92].

In the late stages of deformation, multiple slip systems are activated. An example showing this is presented in **Figure 43**, where many dislocations are seen within a single

grain. These snapshots occurred one minute into a relaxation segment, with $\sigma \sim 216$ MPa and $\varepsilon \sim 7.1\%$.

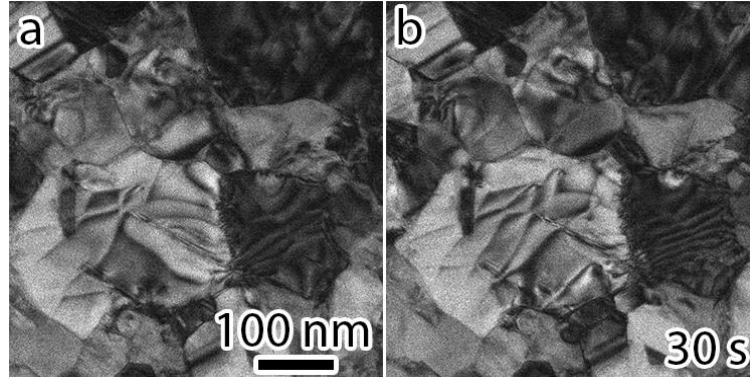


Figure 43 – TEM micrograph of dislocations on multiple slip systems during late stage deformation [92].

In the abovementioned dislocation interactions, there was no obvious evidence that GBM directly played a role in the observed deformation. However, stress-induced GBM is a very common deformation mechanism observed in the as-deposited specimen. GBM migration typically occurs throughout the specimen gauge, however, not all GBs migrate. A few examples are shown below, with a detailed analysis of GBM is provided later in CHAPTER 6.

Two examples in which GB and TJ migration occurred are shown in **Figure 44**. Both events (**Figure 44(a)-(e)**) and (f)-(j)) occurred nearly simultaneously during a relaxation segment with grain one (G1) being common to both sets. In **Figure 44(a)-(d)**, grain growth was observed for G1 to occur by the migration of the top-left boundary outwards 26 nm to eventually contact grain five (G5) in **Figure 44(d)**. The traces of G1 for each snapshots are shown in **Figure 44(e)**, making it clear the progression of the boundary migration. The average migration speed for this process is 2.7 nm s^{-1} . The second example

(**Figure 44**(f)-(j)) shows the migration of the boundaries of grain two (G2), particularly the boundaries between grain 3 (G3) and grain four (G4) and the corresponding TJs. The boundary between G2 and G3 migrated 15 nm over the course of 30 seconds, resulting in an average migration speed of 0.5 nm s^{-1} . Through this process, G2 grows while the already small G3 shrinks. The curvature of the boundary between G2 and G4 actually increases due to the migration of the TJ through this process, suggesting that boundary curvature is not the driving force for this migration. This also might imply that this TJ is more mobile than the boundary between G2 and G4 (GB2-4), as the TJ migration leads to larger curvature but the GB does not migrate in response to decrease this curvature.

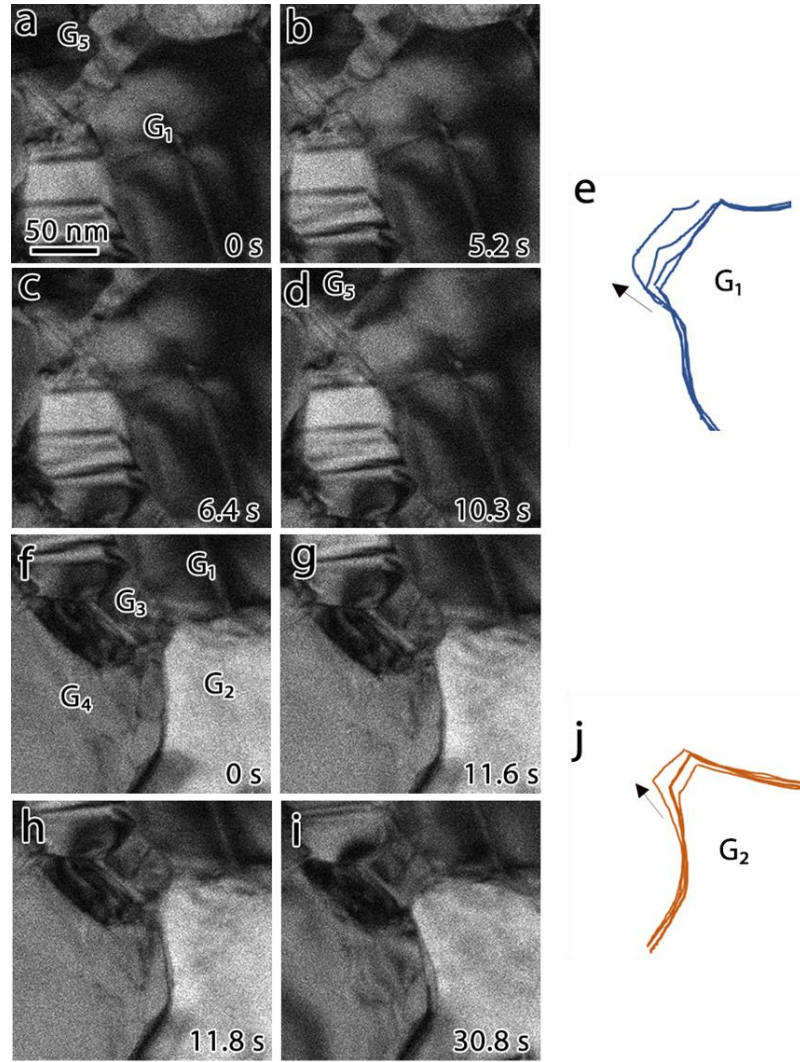


Figure 44 – Sequence of snapshots taken from a TEM video recording documenting separate instances of nearby GBM. (a) – (d) Grain G1 expands and makes contact with G5, (e) the progression of boundary migration in direction of the arrow from (a) to (d). (f) – (i) Grain G2 expands via progression shown in (j) while G3 shrinks. Time stamps are given on each snapshot.

5.4.2 Annealed UFG Au

The deformation mechanisms active in the annealed specimens are similar to the mechanisms previously discussed regarding the as-deposited specimens in that both dislocation and GB-based mechanisms are active. However, as the grain size increases, the GBs are less involved in the deformation via GBM but still serve as sites for dislocation

nucleation and absorption. At even larger grain sizes (A700), intragranular plasticity increases which is evident both by increased dislocation activity within the grains and longer dislocation pile-up at GBs. The following discussion is on both the A350 and A700 specimens as the TEM observation across these specimen types do not vary drastically.

Figure 45 provides an example of dislocation emission from a GB, transgranular glide, dislocation pile-up and absorption at a GB in an A350 specimen. These frames were captured during a repeated stress-relaxation experiment with 10 relaxation segments reaching a maximum $\sigma \sim 482$ MPa. In the first frame of this series (**Figure 45(a)**), a dislocation (black arrowhead) has been emitted from GB₁ in the direction of the white arrow. This dislocation is indicated by the black arrowhead in **Figure 45(a)-(d)** until it is absorbed by GB₂. In **Figure 45(b-d)**, the 2nd, 3rd, and 4th dislocations are emitted from GB₁ (each of these dislocations is indicated by a white arrowhead). The dislocations glide towards GB₂ but are not directly absorbed, leading to a dislocation pile-up. Eventually, the first dislocation (black arrowhead) is absorbed into GB₂ (**Figure 45(e)**). Additional dislocations are emitted from GB₁ and absorbed at GB₂. In total, 5 dislocations are emitted and 2 dislocations are absorbed with a maximum of 5 dislocations in the pile-up at one time and a pile-up length of 271 nm (distance between GB₁ and GB₂). The small grain marked by the white star in **Figure 45(a)** is completely removed, however, it occurs seemingly unrelated to the dislocation emission/absorption process.

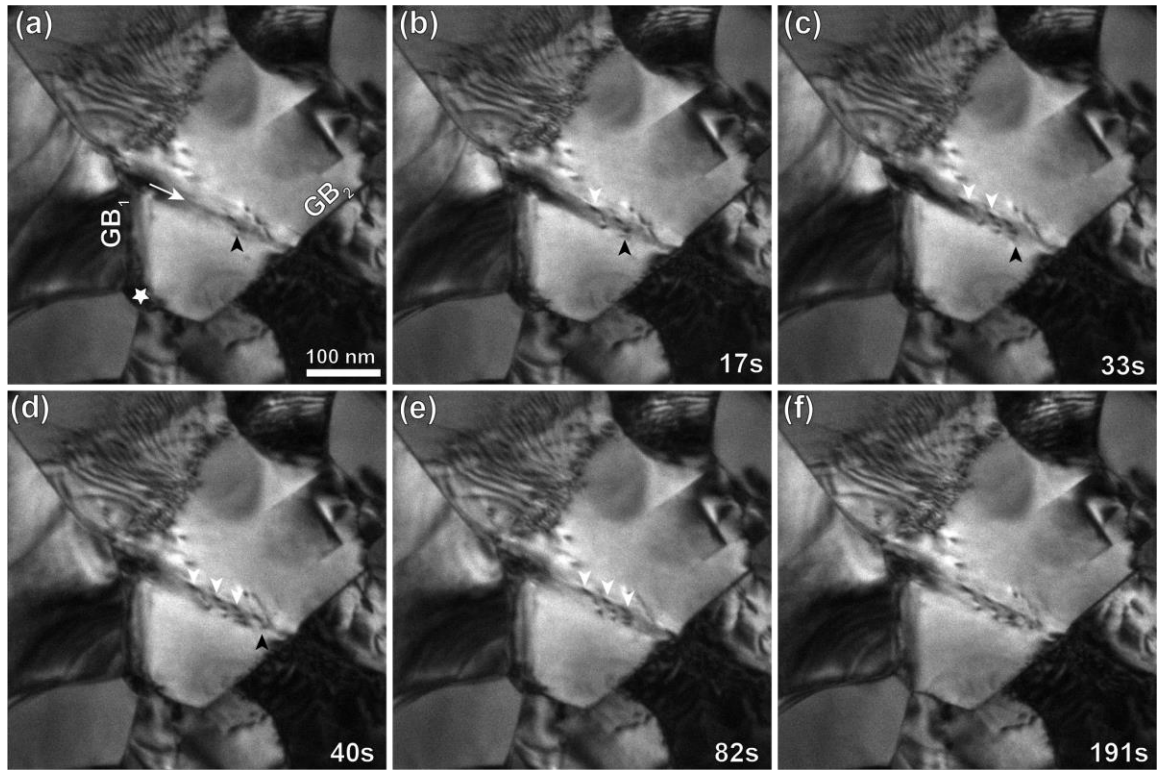


Figure 45 – Dislocation emission, pile-up, and absorption in A350 UFG Au specimen. Dislocations are emitted from GB₁ and glide in the direction of white arrow. Black arrowhead tracks the same dislocation until it is absorbed by GB₂. Progression of the dislocation emission/absorption after (b) 17s, (c) 33s, (d) 40s, and (e) 82s. Given time is in terms of elapsed time since first frame of the video (a). The grain marked by the star in (a) is removed during this process.

In both A350 and A700 specimens, the extent of stress-induced GBM is decreased compared to the as-deposited specimens. GBM in the A350 specimens is discussed in detail in CHAPTER 6. In the A700 specimens, there is still evidence of stress-induced GBM, however, it appears to be primarily limited to LAGBs. An example of this can be seen in **Figure 46**. **Figure 46(a)** is a TEM image taken of a region of the specimen 7 minutes after the initial load is applied. There is very little evidence of plastic deformation with only a few lattice dislocations within the large center grain. The GB of focus is identified using the white arrowhead. For the remaining frames, the white arrow remains in the same

location to indicate the initial location of this GB. This GB has a unique ‘stitch-like’ appearance, which is indicative of an array of dislocations resulting in a LAGB. The GB does not move for the first 17s, however there is a dislocation that has been further extended into the grain (black arrowhead in **Figure 46(b)**). Five seconds later (after the load has been increased slightly), the GB migrates 34 nm at a rate of 5.4 nm/s resulting in the position seen in **Figure 46(c)**. Between **Figure 46(c)** and (d), the GB continues to migrate 38 nm (6.8 nm/s)) and an additional dislocation is emitted as indicated by the black arrowhead. At this point, the migration slows to 1 nm/s to migrate a distance of 14 nm (**Figure 46(e)**) and then an additional 2 nm to result in the final location seen in **Figure 46(f)**. This is the only GB to experience GBM in this region.

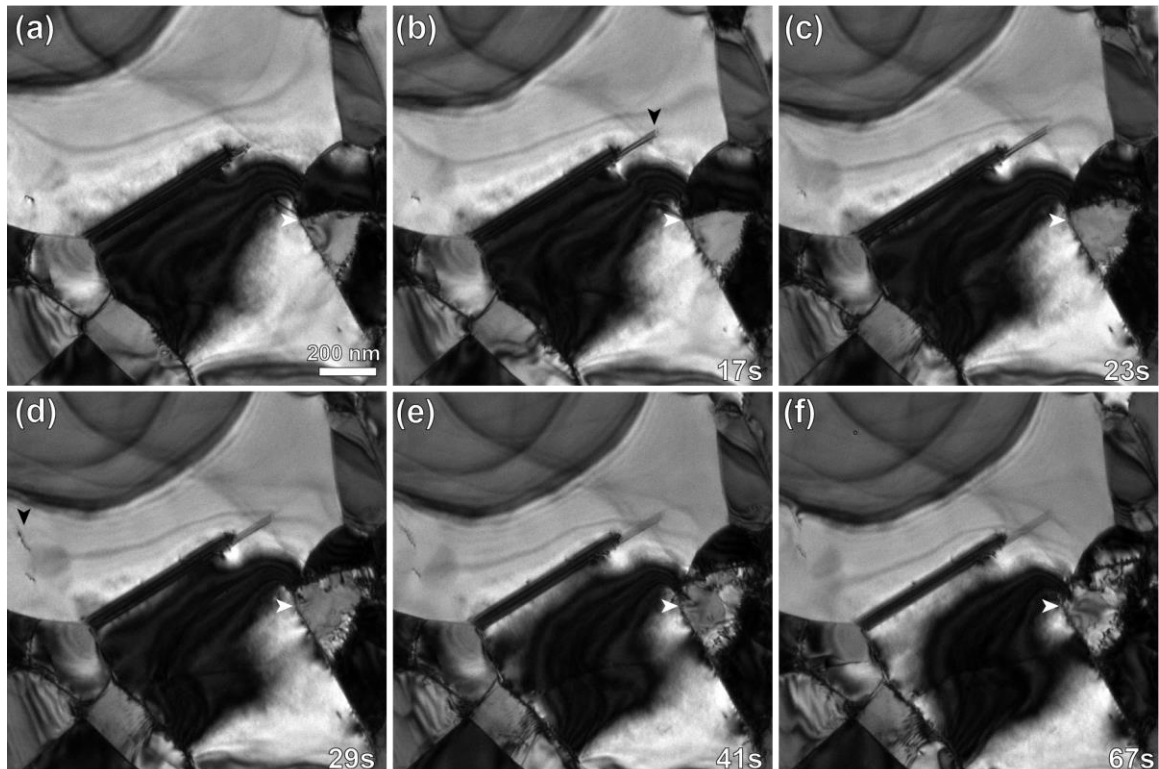


Figure 46 – GBM and dislocation glide active during *in situ* TEM straining of A700 Au specimens. The GB marked by the white arrowhead in (a) undergoes stress-induced GBM through the progression of images. The white arrow marks the initial

location of the GB in each frame. Dislocations glide is denoted by black arrowheads in (b) and (d). Time is provided in terms of seconds since first frame of the sequence.

5.5 *In Situ* TEM Activation Volume Measurements

5.5.1 *As-deposited UFG Au*

In addition to capturing the active deformation mechanism during *in situ* straining, this technique allows for the measurement of activation volume V^* , which is done by performing repeated stress-relaxation experiments (see Section 2.2.3 for experimental methods). Typically, 2-3 short (30 second) relaxation segments are done to measure V^* , followed by a longer relaxation (>10 minutes) to allow for TEM observations.

Results for an as-deposited UFG Au specimen are shown below in **Figure 47**. Electrical sensing was used to determine both stress and strain values for the full test duration. **Figure 47(a)** is the stress-strain curve collected under a strain rate of $\dot{\epsilon} \sim 1.5 \times 10^{-4} \text{ s}^{-1}$. Unlike the monotonic curves shown in **Figure 40**, this curve is discontinuous due to the stress-relaxation segments performed, which are shown in **Figure 47(b)**. Ten relaxation segments were performed spanning stress levels 298-352 MPa. Fitting the stress-relaxation data for the first 5 relaxations ($\sigma \sim 300$ MPa) lead to $R^2 < 0.9$ and are omitted from this discussion. This could be a result of the resolution limit of the electrical sensing technique for small relaxations that occur at lower stress levels ($|\Delta\sigma| < 2$ MPa). The next 5 relaxations ($\sigma \sim 350$ MPa) all achieve an $R^2 > 0.9$ as the amount of stress-relaxation has increased to $|\Delta\sigma| \sim 10$ MPa. The first 4 relaxations for this segment are individually shown in **Figure 47(c)-(f)**. The x-axis is the time duration of that particular relaxation segment and the y-axis is the amount of stress decrease during the pause. **Figure**

47(c) relaxation occurs after reloading to 340 MPa (a higher value than the previous relaxation occurring at 310 MPa) and only apparent activation volume V_a is measured. After this 40 second relaxation ($\Delta X_{LS} = -14.8$ nm, $\Delta\sigma = -6$ MPa), the stress was quickly reloaded back to 340 MPa and paused again. The stress relaxes by $\Delta\sigma = -6.6$ MPa in the behavior shown in **Figure 47(d)** and the apparent and true activation volumes were determined to be 8 and $10 b^3$, respectively. A similar process was followed for the next two relaxation segments shown in **Figure 47(e)-(f)** resulting in apparent activation volume values of 8 and $6 b^3$ and true activation volume V^* of 6 and $21 b^3$, respectively.

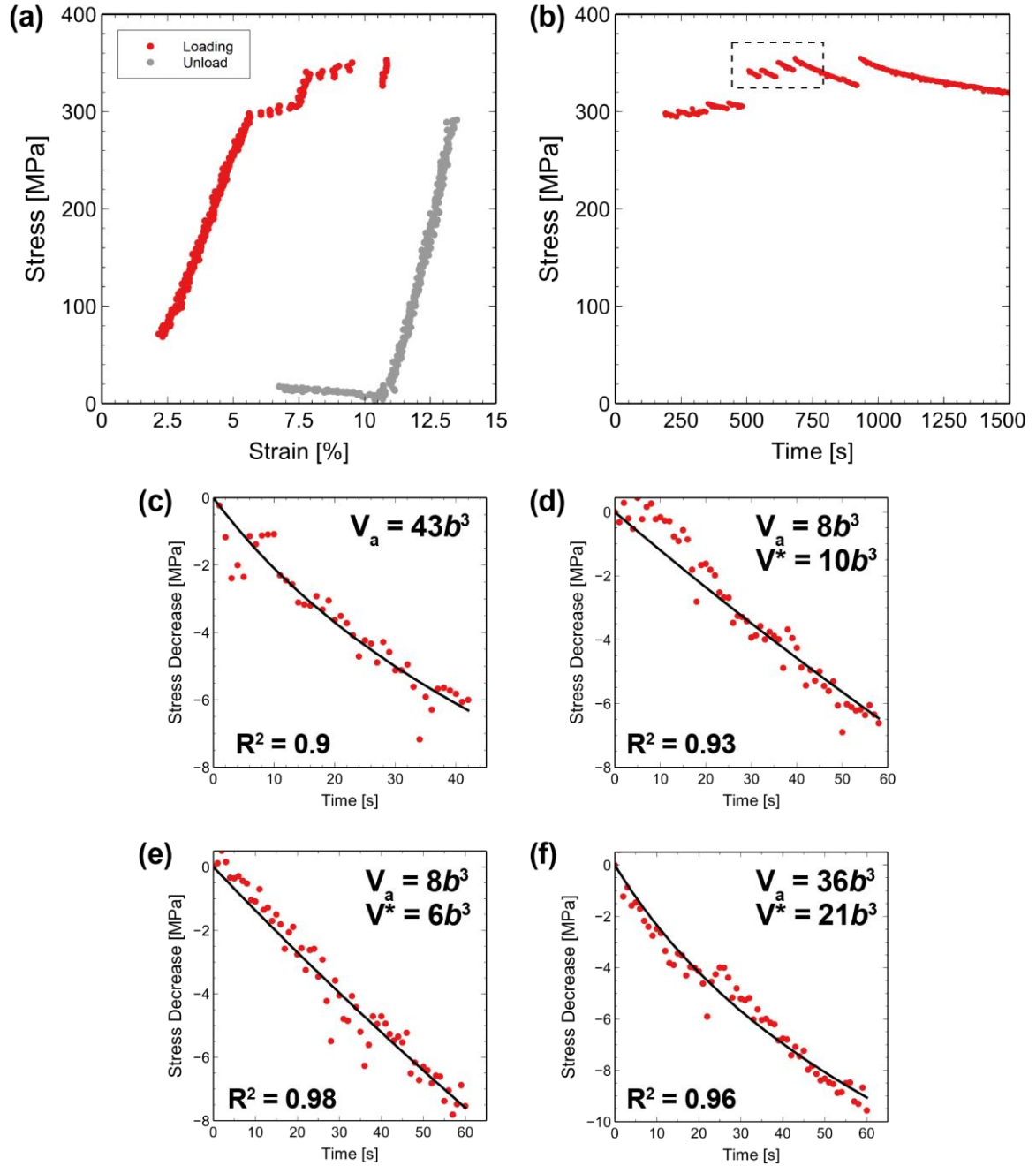


Figure 47 - *In situ* measurement of activation volume in as-deposited UFG Au. (a) stress-strain curve with both loading (red) and unloading (grey) data. Gaps in the data correspond to stress-relaxation segments which are shown in (b). The dashed box identifies the region in which the relaxations shown in (c)-(f) occur. The apparent and true activation volume values are printed on each relaxation segment.

The previous experiment relied on electrical sensing only for stress and strain measurement. The sensitivity in the measurements can be improved by implementing the

updated ‘image-based sensing’ technique (description of MEMS geometry and operation can be found in Section 2.3 with details on the sensitivity improvement in Section 2.3.1). The following experiment was conducted in a hybrid fashion combining both electrical-based and image-based sensing. CS_1 was connected as normal to collect the electrical signal required to measure X_A , however, no capacitance measurement were collected from CS_2 . Instead, the TEM was used to manually measure the gap in CS_2 beams during the experiment. The vidoes were then analyzed to determine X_{LS} directly following the process described in Section 2.3. The stress-strain and stress-time data for this experiment is shown below in **Figure 48**. Because the data was collected using a hybrid technique, only a portion of the stress-strain curve in **Figure 48(a)** has been constructed by linking the electrical- and image-based sensing. Namly, **Figure 48(a)** displays the first loading segment and one point at the beginning of every stress-relaxation segment. The 24 relaxation segments are shown in **Figure 48(b)**.

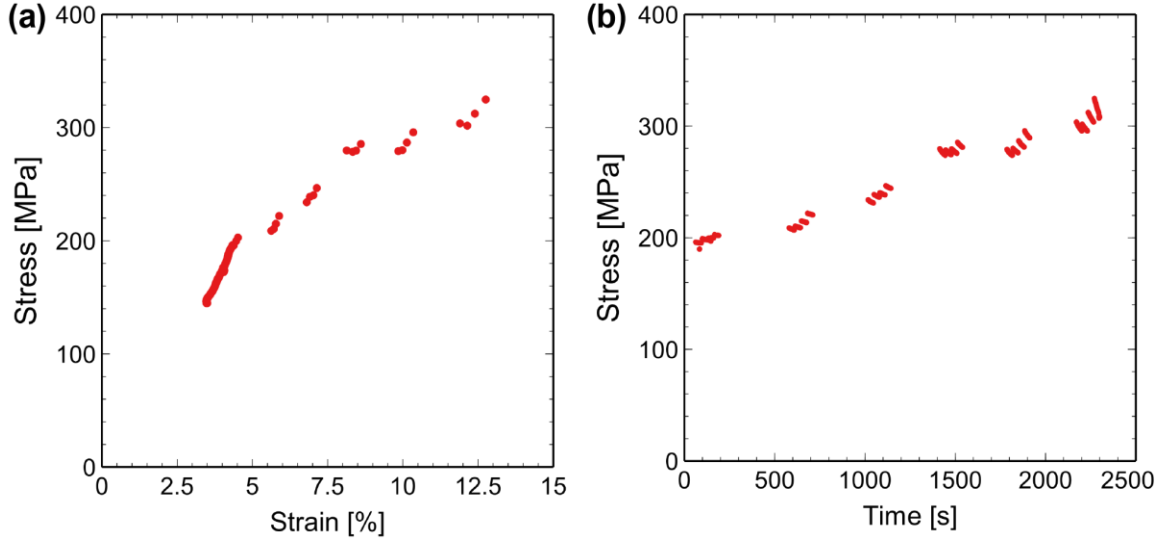


Figure 48 – *In situ* measurement of activation volume in as-deposited UFG Au using image-based technique for stress measurements. (a) stress-strain curve constructed from points throughout the experiment and (b) stress-time data for all the relaxations.

The relaxations were performed in clusters at various stress levels in order to measure activation volume as the stress evolves. The stress range for each relaxation cluster are as follows: Relax # 1 – 4 (196 – 203 MPa), 5 – 8 (209 – 222 MPa), 9 – 12 (234 – 247 MPa), 13 – 16 (280 – 286 MPa), 17 – 20 (279 – 295 MPa), and 21 – 24 (304–324 MPa). Six of the 24 total relaxation segments are shown in **Figure 49**. **Figure 49(a)** and (b) are from Relax #1 and #2, respectively, and illustrate the increased sensitivity that is achieved from the image-based sensing technique. These relaxations occurred at relatively low stress levels ($\sigma \sim 196 - 199$ MPa) but the image-based technique is sensitive enough to measure the amount of stress-relaxation that occurred ($|\Delta\sigma| < 1$ MPa). This is contrast to the relaxations at lower stress levels using the electrical-based sensing technique that cannot accurately capture these small stress changes. Thus, the image-based technique is required to measure activation volume values for small stress-relaxations that occur at small stress or plastic deformation levels.

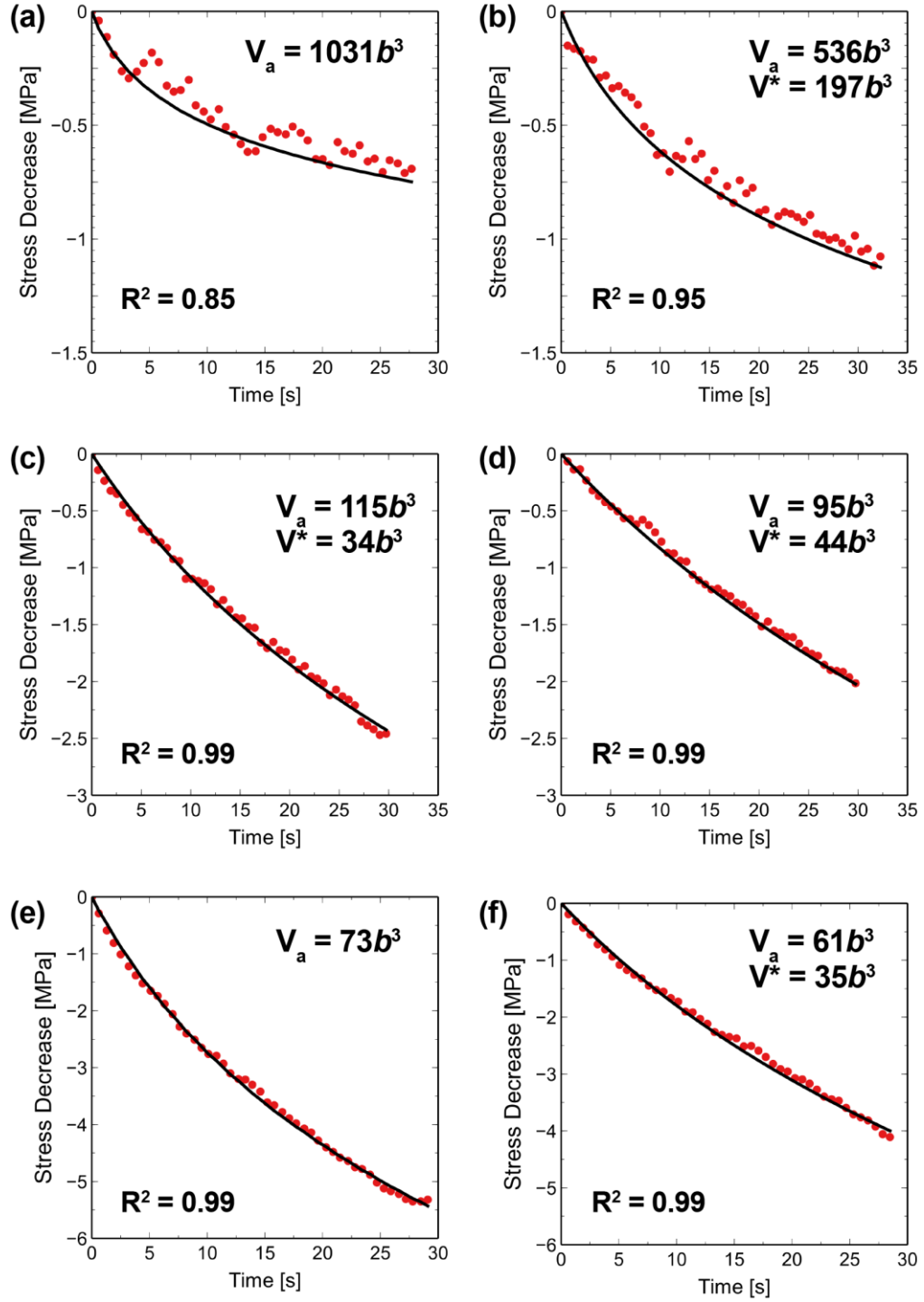


Figure 49 – *In situ* activation volume measurements for as-deposited UFG Au measured using image-based sensing technique. Results are displayed for relaxation number (a) 1, (b), 2, (c) 10, (d) 11, (e) 17, and (f) 18. The displayed apparent and true activation volume values have units of b^3 .

The next set of displayed relaxations (**Figure 49(c), (d)**) are Relax #10 and #11 and occur at an initial stress level of 239 and 241 MPa, respectively. The higher stress and plastic strain level promotes more plastic deformation during the relaxation segment and the amount of stress decrease over the 30 seconds has increased to $|\Delta\sigma| \sim 3$ MPa. Fitting the stress-time relaxation curves results in remarkably high R^2 values. As shown, the true activation volume V^* for these relaxations are $34b^3$ and $44b^3$ with apparent activation volume values V_a of $115b^3$ and $95b^3$. The next set of relaxations shown in **Figure 49(e)** and (f) are Relax #17 and #18 which occur at $\sigma \sim 279$ MPa. The amount of stress-relaxation has once again increased, now reaching $|\Delta\sigma| \sim 6$ MPa. The apparent activation volume V_a range $61-73b^3$ with Relax #18 having a true activation volume V^* of $35b^3$. Relax #17 is the first relaxation in this cluster of relaxations after the stress was reloaded slowly and to a higher level. This voids the assumption of a frozen microstructure which is required for V^* measurement.

A summary of the measured apparent and true activation volume values for the previous two experiments (**Figure 47 – Figure 49**) is shown in **Figure 50**. Activation volume values are graphed against the initial stress level for the corresponding stress-relaxation segment. Both image- and electrical-based measurements result in similar values that obey the general trend of decreasing V^* , V_a with increasing stress. The interpretation of these values as well as additional trends will be discussed in detail in CHAPTER 8.

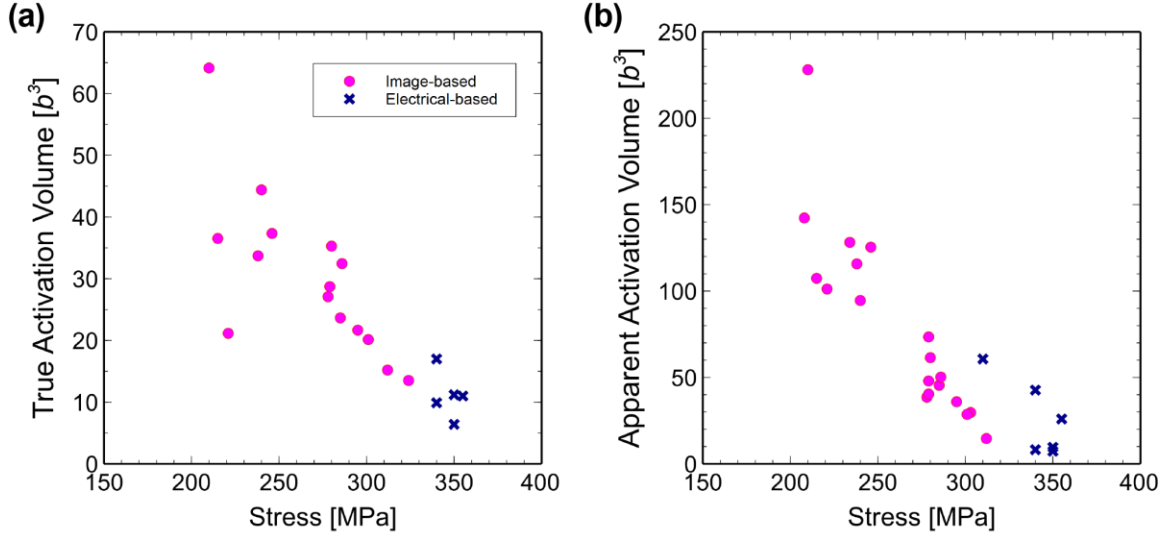


Figure 50 – A summary of *in situ* values of (a) true and (b) apparent activation volume vs. stress for as-deposited UFG Au

5.5.2 Annealed UFG Au

Results from an *in situ* repeated stress-relaxation experiments on an A350 specimen is shown below in **Figure 51**. This experiment was performed in a similar hybrid fashion as that in **Figure 49** (X_A data is generated from the electrical signal of CS_1 and X_{LS} is manually measured by measuring the displacement of the CS_2 beams). **Figure 51(a)** is the stress-strain curve (constructed using same method described for **Figure 49(a)**) and the 25 relaxations are shown in **Figure 51(b)**. Four of these relaxations indicated by the dashed outline are shown in more detail in **Figure 51(c-f)**. Relax #15 (**Figure 51(c)**) occurs at an initial $\sigma \sim 290$ MPa and undergoes $|\Delta\sigma| \sim 1.8$ MPa. A short and quick reloading segment occurred and the next relaxation (**Figure 51(d)**) begins at $\sigma \sim 295$ MPa ($|\Delta\sigma| \sim 1.5$ MPa). For these, the apparent activation volume V_a varies from 200 to 900 b^3 with a true activation volume V^* measurement of 35 b^3 . The next set of shown relaxation segments occur after the stress has been reloaded to a significantly higher value ($\sigma \sim 370$ MPa). Due the increase

in stress, these segments undergo a larger stress decrease over the 30 second relaxations ($|\Delta\sigma| \sim 9$ MPa). The measured activation volume values for these relaxations are 15 and $16b^3$ (apparent) and 15 and $19b^3$ (true).

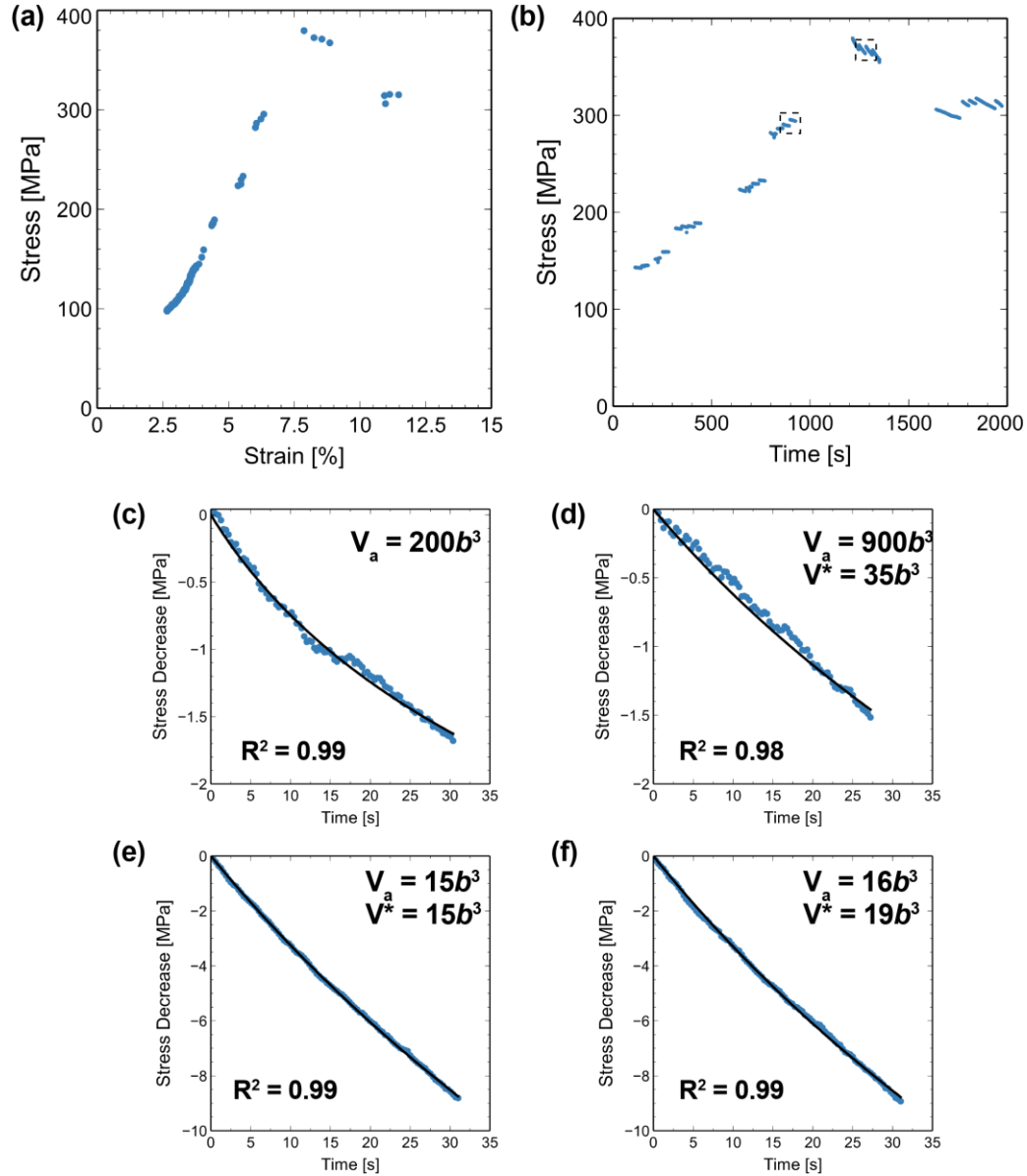


Figure 51 – *In situ* repeated stress-relaxation experiment on A350 Au specimen. (a) stress-strain curve, (b) stress-time data displaying all the relaxation segments. Relaxation number (c) 15, (d) 16, (e) 18, and (f) 19. Apparent V_a and true V^* activation volume values are shown for each relaxation along with the R^2 values corresponding to the fit (solid black line).

True and apparent activation volume measurement for all of the relaxations in **Figure 51(b)** with $R^2 > 0.9$ are shown in blue ‘image-based’ data in **Figure 52**. This figure also includes data (grey) from a separate A350 specimen tested under electrical-sensing conditions. Across the full stress range of $295 < \sigma < 506$ MPa, V^* varies from 4 to $35b^3$. There is a larger spread in the apparent activation volume values ($2 - 238b^3$).

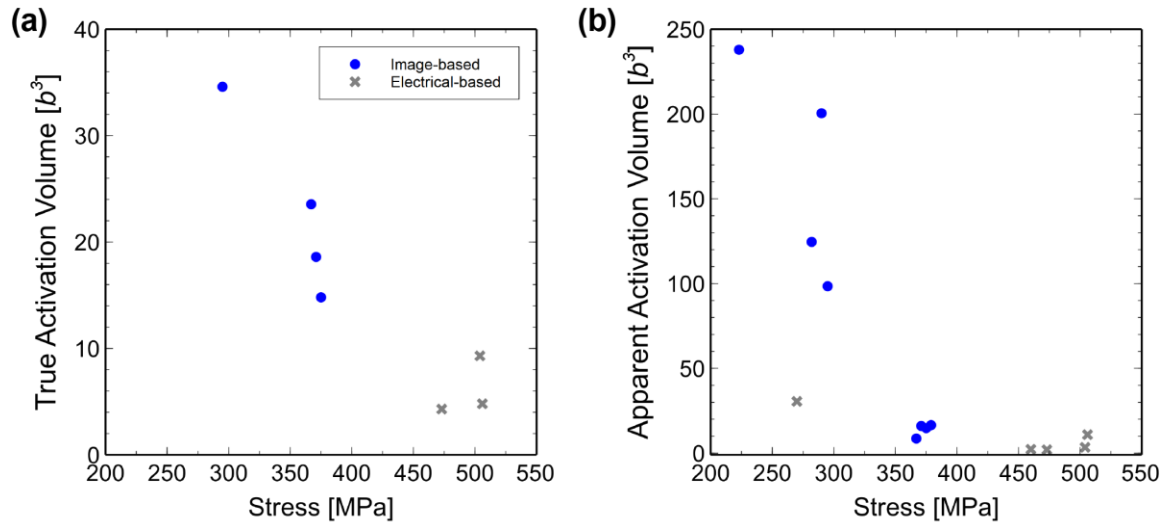


Figure 52 – *In situ* (a) true and (b) apparent activation volume measurements for A350 specimens. The blue data is all the values from the experiment shown in Figure 51 and the gray data is from a purely electrical-based sensing experiment on a separate specimen (stress-strain data not shown).

Finally, an *in situ* repeated stress-relaxation experiment has been completed on a A700 specimen with the results shown in **Figure 53**. The stress-strain and relaxation data are shown in **Figure 53(a)** and (b), respectively. This experiment consisted of 8 relaxation segments prior to specimen failure. Four relaxations (Relax #4, #5, #7, and #8) are shown in more detail in **Figure 53(c-f)**. The successive relaxations shown in **Figure 53(c-d)** occurred at an initial stress $\sigma \sim 330$ MPa and have slightly different extent of stress decrease during the 25 second relaxation ($|\Delta\sigma| \sim 6$ MPa versus $|\Delta\sigma| \sim 3$ MPa). This could be due to

the fact that Relax #4 (**Figure 53(c)**) is the first relaxation performed after a significant stress increase from the first set of relaxations that occurred at $\sigma \sim 175$ MPa. The apparent activation volume V_a increases from 166 to $193b^3$ and the true activation volume V^* for Relax #5 was measured as $91b^3$. The next set of displayed relaxations (**Figure 53(e-f)**) occurred at a similar starting stress level ($\sigma \sim 337$ MPa), however, a larger amount of stress-relaxation occurs with $|\Delta\sigma|$ reaching 15 MPa. The specimen started fracturing during the final relaxation, which is why **Figure 53(f)** only displays the first 15 seconds prior a crack forming. The apparent activation volume V_a increases from 27 to $41b^3$ and the final measured true activation volume V^* was $104b^3$. All of the true and apparent activation volume values for this experiment are shown in **Figure 54** (note that only one experiment has been performed on these specimen). The measurements were made over the small stress range of $330 < \sigma < 337$ MPa, with true activation volume V^* values ranging from 91 to $104b^3$ and the apparent V_a ranging from 27 to $194b^3$.

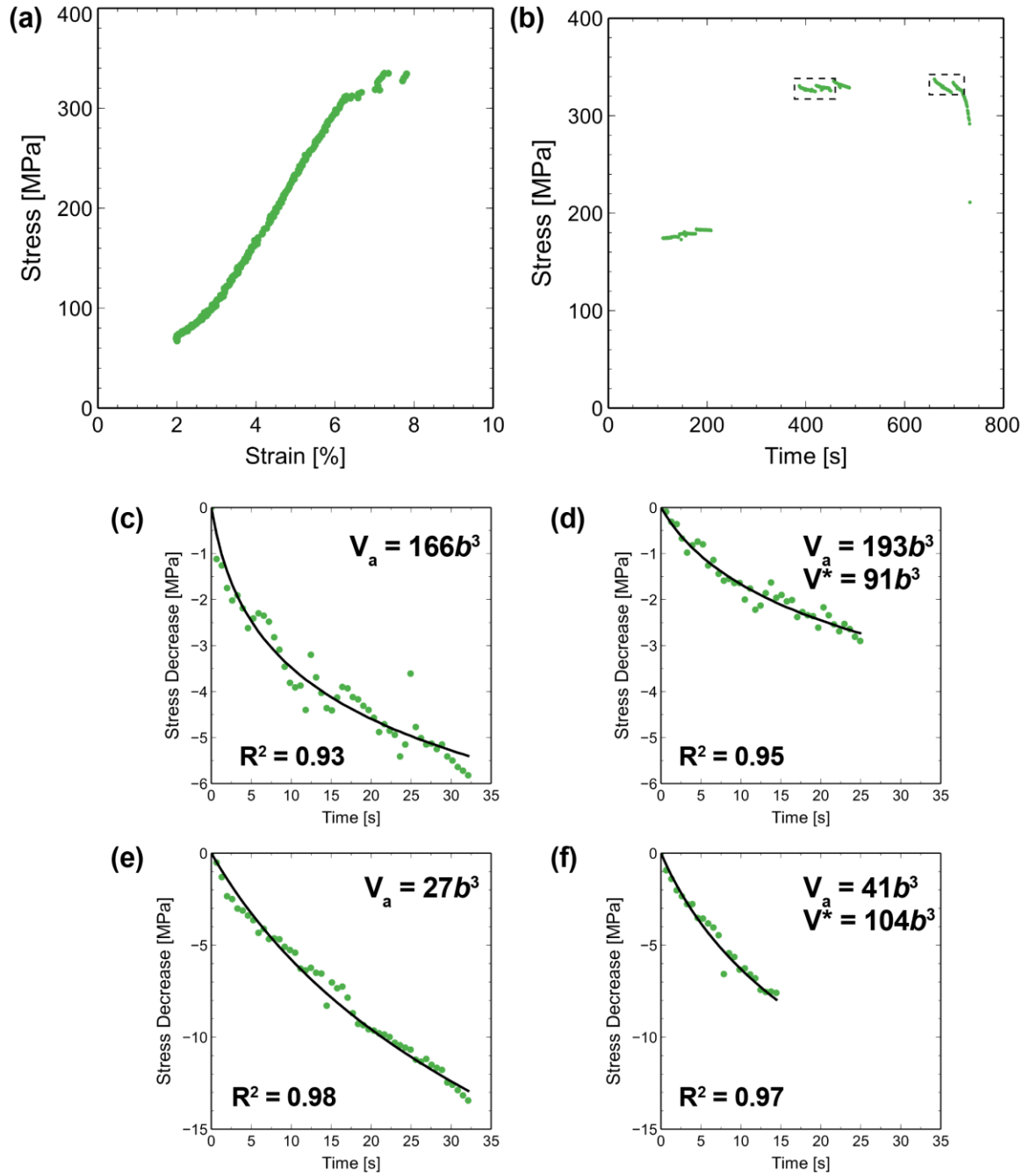


Figure 53 – *In situ* repeated stress-relaxation experiment on an A700 specimen. (a) full stress-strain curve, (b) stress-time data for the relaxation segments. Relax # (c) 4, (d) 5, (d) 7, and (f) 8 shown in more detail with the measured apparent and true activation volume values displayed.

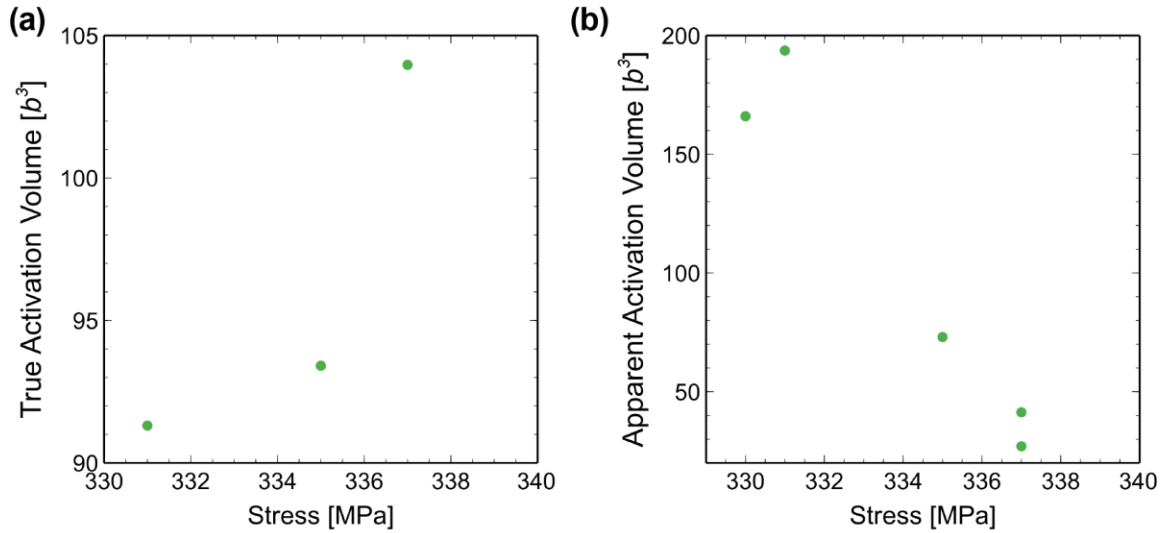


Figure 54 – *In situ* (a) true and (b) apparent activation volume values for A700 Au.

5.6 Discussion

Gold specimens of three different average grain sizes have been studied using the *in situ* TEM technique. According to the Hall-Petch law (Eqn. (1)), yield strength is expected to decrease with increasing grain size. However, the yield points determined from monotonic tests (**Figure 40, Table 7**) do not qualitatively fit the expected size-dependent yielding. The yield point increases from 489 MPa to 544 MPa as the grain size increases from 142 to 768 nm. One possible explanation for the reduced strength measured in the as-deposited Au specimens (with the smallest average grain size) could be related to the quick removal of the smallest grains upon applying a load. The smallest grains are unstable and are quickly removed (this will be discussed in further detail in CHAPTER 6) which results in a grain size distribution not all that dissimilar from the A350 specimens (larger grains only). The ductility also decreases with increasing grain size. It is likely that the annealing causes significant GB grooving that lead to local stress concentrations on the surface which promote premature failure [9]. This leads to the observed decrease in ductility in the A700

specimens. These observations could also be related to uncertainty with the measurements, including the measurements of the pre-stress which can have a large effect on the reported stress levels. Additional monotonic tests need to be completed to investigate this further.

Both dislocation- and GB-based mechanisms are active in all the Au specimens tested. This is consistent with previous reports that a unique mixture of conventional dislocation-based mechanisms are active in addition to GB-based within the UFG grain size regime [16,33,65,69]. Although not specifically characterized, GBM occurs for a wide range of GBs in the as-deposited specimens whereas it appears that in the A700 specimens, only the LAGB (described as array of dislocations) are susceptible to stress-assisted GBM. This is likely related to the general ease of the collective motion of the individual dislocation in the boundary compared to the high stresses required to activate mechanisms required for HAGB migration, such as disconnection glide or climb [183,184].

In situ TEM nanomechanical experiments are required to identify the active deformation mechanisms while concurrently quantifying the plastic flow characteristics through V^* and strain rate sensitivity m . For $\sigma < 350$ MPa, V^* was found to vary from $25b^3$ to $96b^3$ as the grain size increased from 142 to 798 nm. For higher stresses ($\sigma > 350$ MPa), V^* varies from $9b^3$ ($d = 142$ nm) to $13b^3$ ($d = 287$ nm). Interpretation of the measured V^* will be provided in CHAPTER 8, however, the measured values are consistent with the low V^* values shown in **Table 1** for a wide range of NC and UFG metals. The experiments conducted here are unique in the sense that V^* is measured throughout a single experiment as the plastic deformation and stress levels evolve. This is unlike most experiments in which one or two V^* measurements are made at a single stress level. Since

the results shown here indicate a strong stress-dependence (**Figure 50**), it makes it difficult to compare with literature results.

5.7 Conclusion

An *in situ* TEM nanomechanical testing technique has been used to characterize the active deformation mechanisms and mechanical properties of as-deposited and annealed UFG Au specimens. Identified deformation mechanisms include dislocation nucleation/absorption at GBs, transgranular dislocation glide, dislocation pile-up, and GBM. Although not specifically characterized, it is suggested that the propensity for GBM decreases as the grain size increases. True and apparent activation volume calculations were performed on each specimen type. It was observed that for the as-deposited specimens, V^* ranged from $6\text{--}64\ b^3$ ($208 < \sigma < 355$ MPa), $4\text{--}35\ b^3$ ($222 < \sigma < 506$ MPa) for the A350 specimens, and $91\text{--}103\ b^3$ ($330 < \sigma < 337$ MPa) for the A700 specimens.

CHAPTER 6.

STRESS-INDUCED GRAIN BOUNDARY MIGRATION

6.1 Introduction

The following chapter provides a comprehensive review of stress-assisted GBM occurring in UFG Au. The first section briefly describes how GBM is tracked during an experiment, followed by a review of the initial microstructure of the as-deposited and A350 specimens in Section 6.2. Sections 6.4 and 6.5 discuss GBM that occurs in the as-deposited and A350 films, respectively. Section 6.5.1 discusses stress-assisted GBM in terms of the possible influencing microstructural features (grain size, Schmid factor, etc).

6.2 Documenting Grain Boundary Migration

GBM has been observed to occur in all specimen types tested in this thesis, including NC Al (CHAPTER 4) and UFG Au (CHAPTER 5). The following results will be focused on as-deposited and A350 Au only. For each experiment, low magnification TEM images have been taken while the specimen is under tension at different time intervals. The chosen magnification is typically such that only one third of the specimen is in view at one time. The micrographs for each of the specimen sections are put in series and combined to form a video (using ImageJ) and stabilized (using MATLAB). The videos are analyzed to determine which GBs are mobile or immobile throughout the test. Once the behavior of the GBs have been identified, information regarding the GB character is recorded by comparing to the PED orientation map that was obtained prior to testing.

6.3 Comparing Initial Microstructure

Since the results in this chapter involve the as-deposited and A350 specimens only, a comparison of their initial microstructures is shown in detail in **Figure 55(a)** and **(b)**, respectively. The accompanying orientation map of each region is shown in **Figure 55(c)** and **(d)**. Upon annealing, the average grain size increased from 142 ± 36 nm to 360 ± 83 nm as a large portion of the small grains were removed (grain sizes determined from TEM PED dataset). The average grain sizes for both are indicated by the vertical dashed lines in the grain size distribution shown in **Figure 55(e)**. Specifically, 20% of the area of the as-deposited specimens is composed of grains sizes less than 50 nm or less, whereas only 2.5% of the area of the annealed specimen contains grains less than 50 nm is size. Comparing the PED maps indicates that both the films maintain the $\langle 111 \rangle$ dominant out-of-plane texture. **Figure 55(f)** compares the GB misorientation angle θ distribution before and after annealing and shows that number fraction of GBs with $9.5^\circ < \theta < 27.5^\circ$ misorientation angle increased after annealing and those with $\theta > 30^\circ$ decreased, with the exception of twin boundaries ($\theta = 60^\circ$). In both films, a large fraction of the boundaries are $\Sigma 3$ twin boundaries with the number fraction increasing slightly during annealing (0.24 to 0.27).

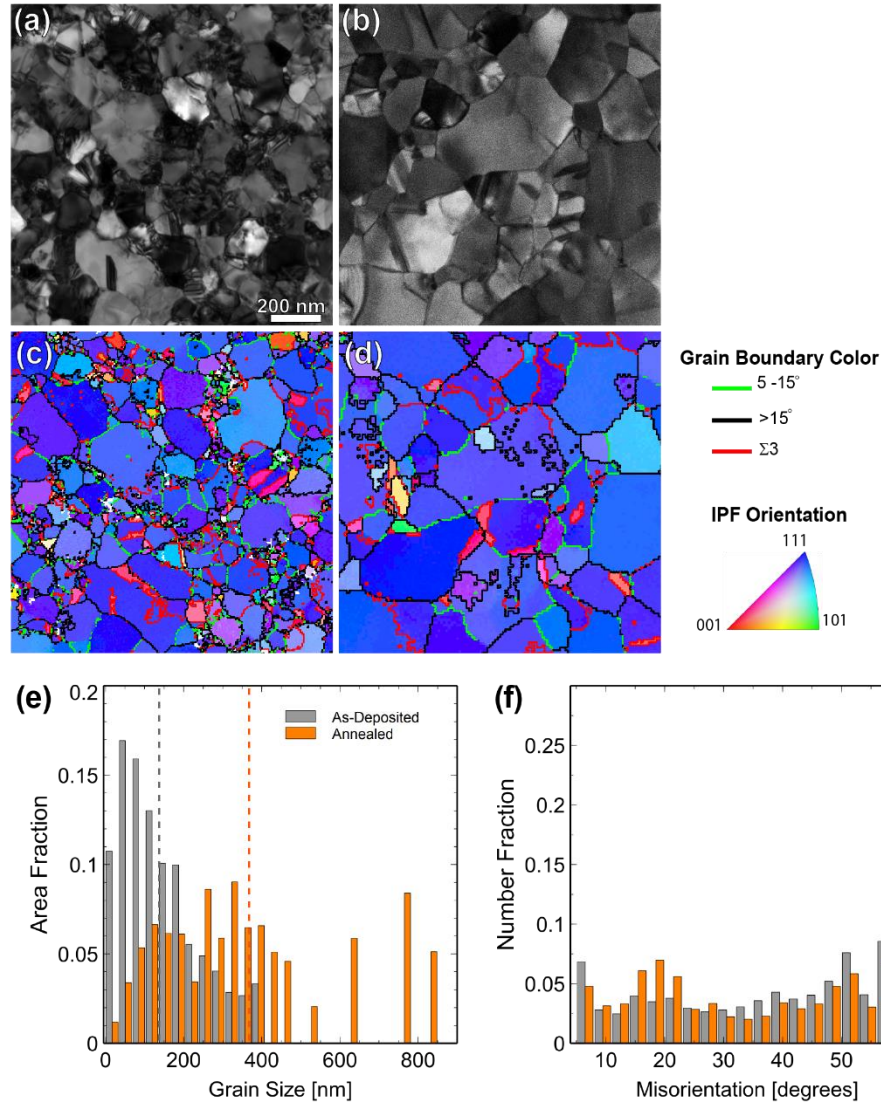


Figure 55 – TEM images of initial microstructure of (a) as-deposited and (b) annealed Au thin films with corresponding orientation map for each region in (c) and (d), respectively. (e) Area fraction grain size and (f) GB misorientation distribution for the as-deposited (grey) and annealed (orange) films. The average grain size is indicated by the vertical dashed lines and highlights the change in grain size after annealing.

6.4 Grain Boundary Migration in As-deposited Gold

An example of typical GBM/grain growth behavior in an as-deposited film is shown in **Figure 56**. This experiment consisted of four stress-relaxation segments at 240,

382, 481, and 420 MPa for a total of 63 minutes under tension. **Figure 56(a)** and (d) show BF TEM images of two different regions prior to straining and in both cases, the grain outlined by the bolded white line undergoes stress-assisted grain growth in the direction of the red arrows. This resulted in the outlined grains shown in **Figure 56(b)** and (e) which were taken at the end of the 3rd relaxation segment after the stress reached a maximum of 481 MPa. The initial (bolded) and final (dashed) grain outlines are overlaid on the initial orientation maps in **Figure 56(c)** and (f), which facilitates easy view of the region of the microstructure that is removed during straining. In both cases, the grains expanded to absorb/remove the highly disordered regions composed of small grains in the vicinity.

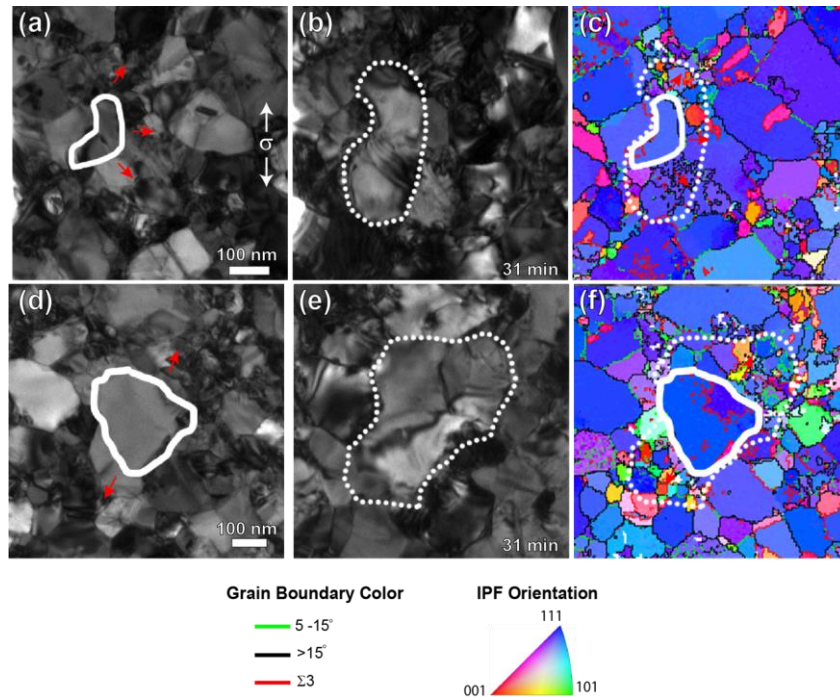


Figure 56 – Stress-induced grain growth and the removal of small grains. BF TEM images of (a) initial microstructure with grain traces outlined. The outlined grain undergoes extensive grain growth in the direction of the red arrows (stress is applied in the vertical direction as indicated). (b) microstructure after 31 minutes under a tensile load. The outline represents the final grain size/shape. (c) corresponding orientation map of the region with the initial and final grain outline overlaid. (d)-(f) similar analysis of a second region.

A detailed analysis of the evolution of a cluster of grains throughout the experiment is shown in **Figure 57**. This is shown to illustrate how grains are rearranged due to the disappearance and growth of certain grains. **Figure 57(a)** is a BF TEM image of the initial GB network outlined with 6 grains identified by lettering (roughly $1\text{ }\mu\text{m} \times 1\text{ }\mu\text{m}$ area). **Figure 57(b)** is the same region 16 minutes after an applied load at the beginning of the 3rd relaxation segment ($\sigma \sim 448\text{ MPa}$). The traced GB networks have been overlaid in **Figure 57(e)** to illustrate how the microstructure has changed as a response to the applied load. The solid lines are the ‘updated’ microstructure from **Figure 57(b)** whereas the dashed lines are the original arrangement shown in **Figure 57(a)**. This makes it clear that during this time, GBM has occurred and resulted in grain growth of certain grains due to the removal of nearby small grains. The red highlighted grains are the grains that have been removed/absorbed by neighboring grains which leads to the growth of grain ‘C’ and ‘D’. Although difficult to quantify and illustrate, GB sliding likely occurs simultaneously and aids in the rearrangement of the grains. Limited GBM was observed up until this point (relaxation 3), indicating that the stress may not have been high enough to promote extensive GBM/sliding.

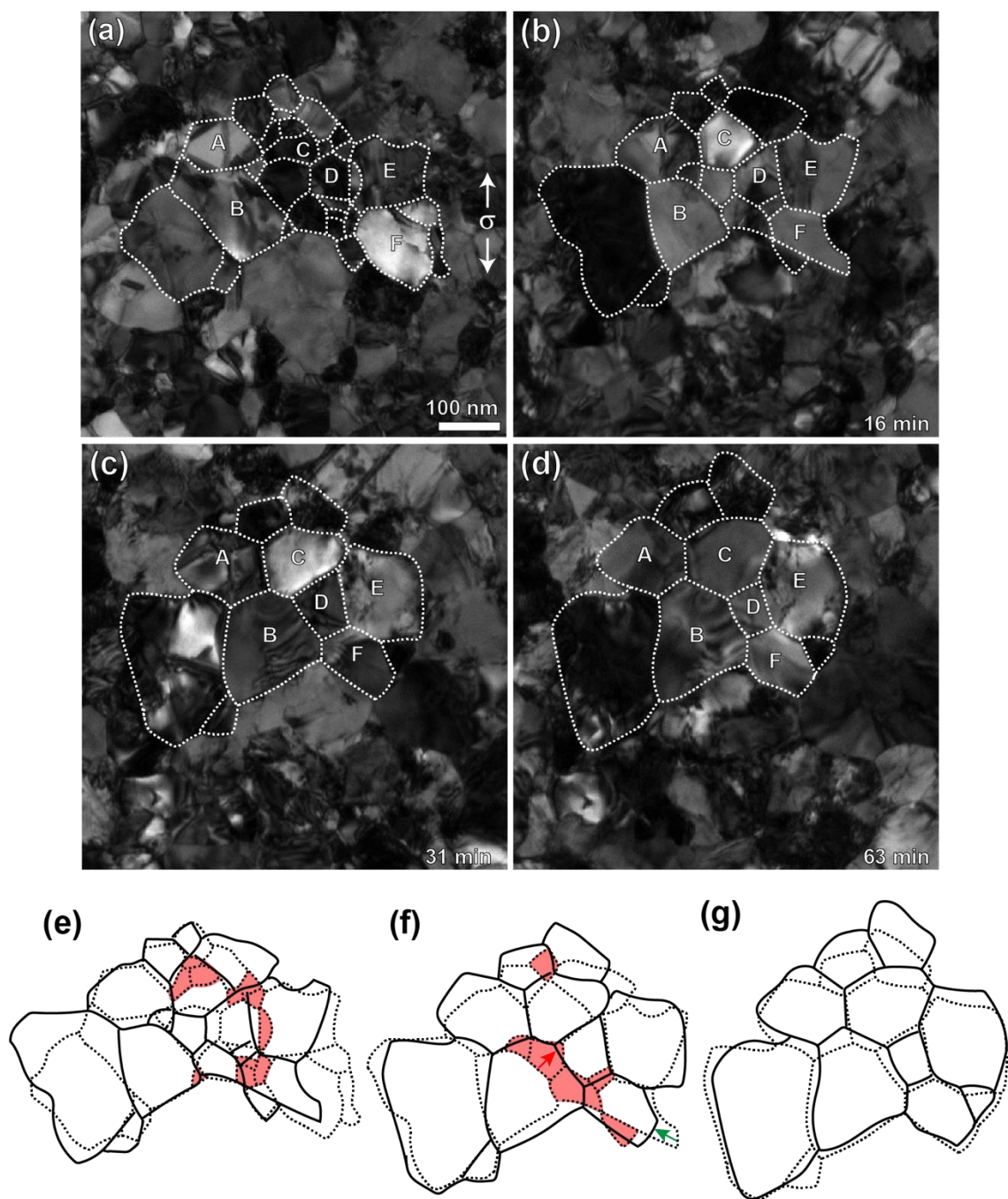


Figure 57 – Analysis of the grain growth and shrinkage of a cluster of grains. (a) initial microstructure with GB cluster outlined with certain grains that are constant throughout the transformation identified by letters. Same region with the GB network outlined (b) 16, (c) 31, and (d) 63 minutes after an applied load. The grains are labeled to help identify how the grains have been rearranged. (e) Overlays of the GB network between (a) (dashed) and (b) (solid) with the grains that are removed during the transition highlighted in red. (f) overlay of (b) (dashed) and (c) (solid). (g)

overlay of (c) (dashed) and (d) (solid) showing minimal changes for the last 32 minutes of the experiment.

The microstructure evolution during relaxation 3 is shown in **Figure 57(b)-(c)**. Over the course of the next 15 minutes of the relaxation segment, the microstructure evolves by the additional removal of small grains (highlighted in red in **Figure 57(f)**). The best example of small grain removal is indicated by the red arrow. These three smaller grains are removed as the larger grain 'B' to the left expands. This GB migrates ~ 62 nm until those grains are completely removed at an average velocity of 0.07 nm/s. During this time period, the far field stress level decreases from 448 MPa to 338 MPa (110 MPa decrease) and at this point, the majority of small grains have been removed within this region. GBM not directly linked to the collapsing of small grains is also documented and indicated by the green arrow in **Figure 57(g)**. After relaxation 3, the stress is reloaded to 420 MPa for the final relaxation segment. Documentation of the microstructure during this relaxation segment is shown in **Figure 57(c)-(d)**. During this time, there is minimal microstructural rearrangement compared to the previous examples and there is no evidence of complete grain removal during this segment. However, there is still evidence of GBM/sliding as the GB network traces do not match 100%.

In order to obtain statistical information regarding the GBM/grain growth, 1/3rd of the specimen gauge was analyzed in detail to identify common characteristics of the grains that grow, shrink, or completely disappear throughout the 63-minute stress-relaxation experiment. In total, 189 grains were identified and of those, 93 grains disappeared, 39 grew, 9 shrunk, and 48 grains experienced minimal changes. The initial GB network outline is shown in **Figure 58(a)**, where the grains are color-coded based on if the grain

disappears (red), shrinks (blue), grows (green) or experiences minimal changes (grey). The white grains could not be confidently identified throughout the experiment and are omitted from the analysis. Based off this visual representation, it is clear that it is common for larger grains to grow at the expense of disappearing smaller grains as there are plenty of instances of larger green grains surrounded by smaller red grains. To further quantify this, the initial grain size for each tracked grain was recorded and used to develop a grain size distribution for the grains that disappeared versus shrunk (**Figure 58(b)**). This grain size distribution unambiguously demonstrates that there is a strong grain size dependence on the growth/removal behavior. The number average grain size for the grains that disappeared was 60 ± 25 nm compared to 162 ± 52 nm for the grains that grew. The local strain within this portion of the gauge length was estimated by measuring the distance between the same edge features on the gauge which resulted in a local strain estimation of 11.7%.

The orientation of each grain was also recorded to explore any potential orientation dependence on the grain growth/shrinkage behavior. This is shown in **Figure 58(c)-(e)** where the orientation for the grains that disappeared, grew, or experienced minimal changes are plotted on the inverse pole figures (IPF), respectively. A variety of grain orientations were documented for the grains that disappeared (**Figure 58(c)**), including grains with orientations differing from the $\langle 111 \rangle$ film texture. There is less orientation variation for the grains that grew (**Figure 58(d)**) with the majority of grains exhibiting close to the $\langle 111 \rangle$ orientation. Finally, the orientation for the grains that experienced minimal changes is shown in **Figure 58(e)** and shows slight variation from the preferred $\langle 111 \rangle$ orientation. The variation in the in-plane orientation along the loading direction was also investigated and shown in **Figure 58(f)-(h)** for the grains that (f) grew, (g) shrunk and

(h) experienced minimal changes. These results indicate that there is not a strong dependency on in-plane orientation with respect to the loading axis. It is important to note that in general, there is a larger variation in orientation within the smaller grains ($d < 50$ nm) compared to grains with $d > 50$ nm that tend to exhibit the dominant $\langle 111 \rangle$ orientation (**Figure 59**).

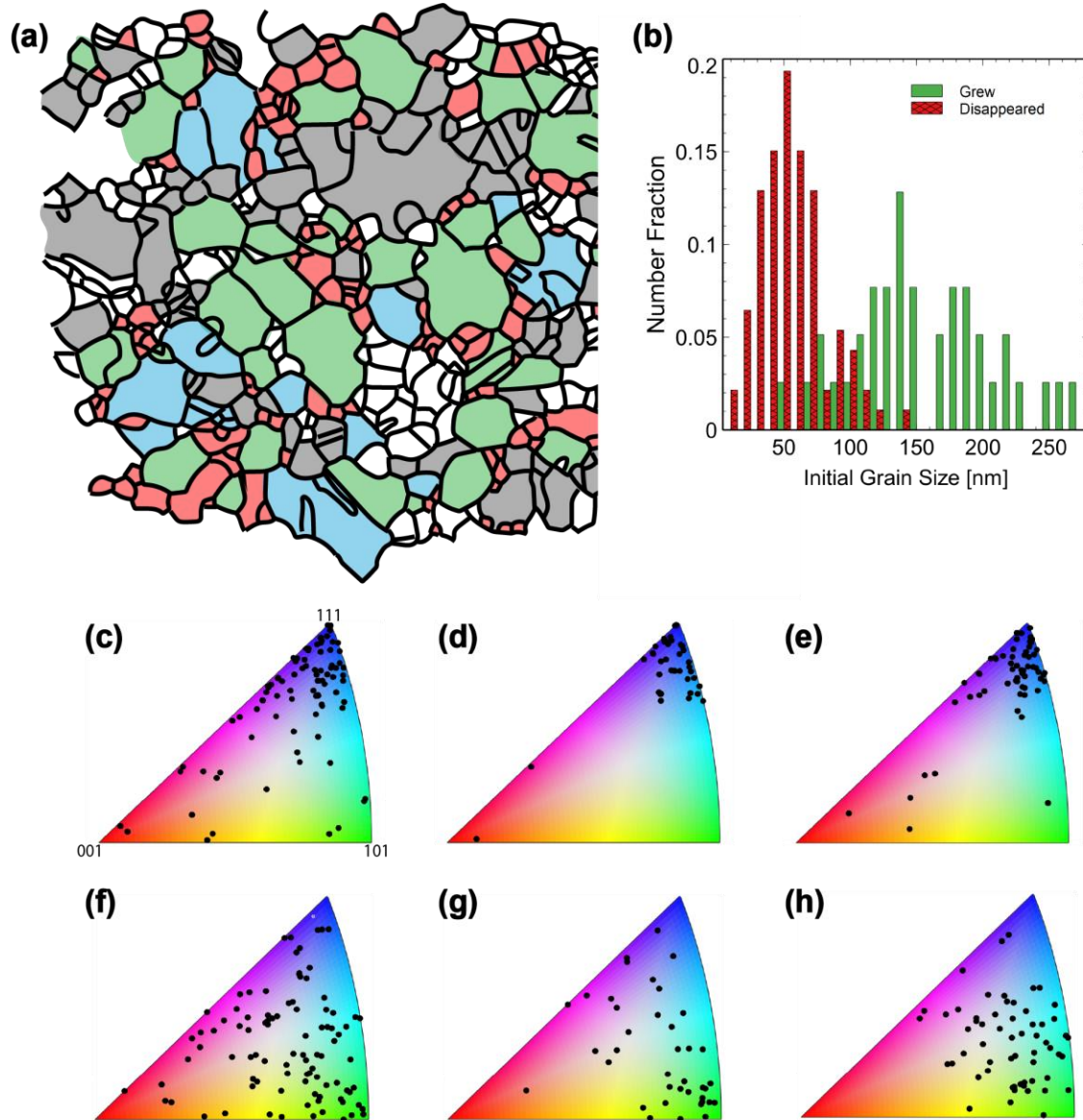


Figure 58 – Detailed analysis of grain growth and shrinkage due to mechanical loading. (a) Outlined GB network with grains color coded based on if the grain

disappears (red), shrinks (blue), grows (green), or undergoes minimal change (grey) throughout the 63-minute experiment. Grains colored white could not be tracked with confidence so are omitted from the analysis. (b) Distribution of grain sizes that grew (green) vs. disappeared (red-thatched), showing a strong grain size dependence. Out-of-plane orientation for the grains that (c) disappeared, (d) grew, and (e) experienced minimal change are plotted on IPFs, in addition to the in-plane orientation along the vertical loading direction for the grains that (f) disappeared, (g) grew, and (h) experienced minimal changes. The crystal direction for each color is shown in (c).

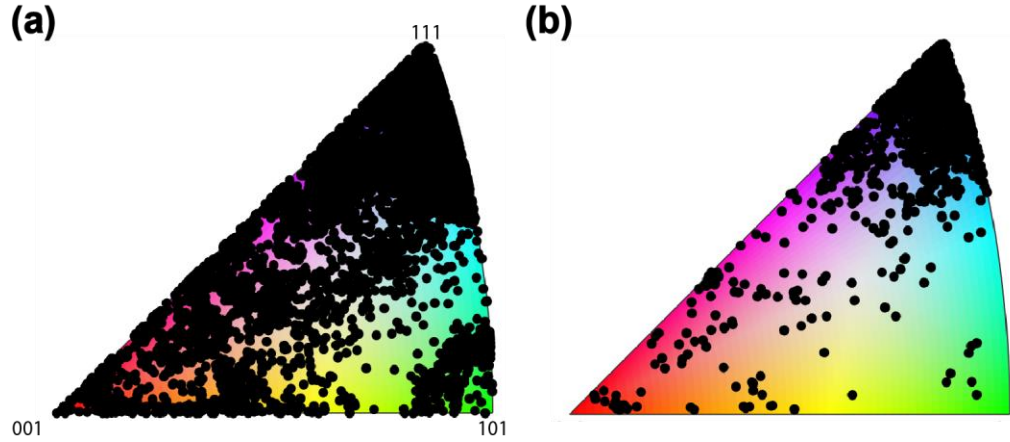


Figure 59 – IPF orientation of all grains in the specimen with grain sizes (a) less than 50 nm and (b) greater than 50 nm.

The crystallographic orientations were used to investigate the influence of Schmid Factor m on grain growth behavior. However, there was no significant difference in the average Schmid Factor m for the grains that disappeared ($m_{avg} = 0.458 \pm 0.03$) compared to the grains that grew ($m_{avg} = 0.459 \pm 0.04$), indicating that the grain orientation with respect to favorable slip does not have a large effect on the grain growth behavior.

6.5 Grain Boundary Migration in Annealed Gold

The A350 Au films are ideally suited to study migration behavior of the GB network in terms of characteristics of the GB, since there are in general fewer GBs to track

and the smallest grains ($d < 50$ nm) are absent. Unlike the as-deposited films previously analyzed, the GBM is not dominated by the removal of the smaller grains since many of these grains are removed during the prior heat treatment process. An experiment was completed in which two consecutive stress-relaxation segments were done on an A350 Au specimen as TEM images were captured every minute. The first test consisted of 5 relaxation segments for a total time under tension of 35 mins and the second test had one relaxation for 12 minutes total until the specimen failed with the stress ranging from 260 – 350 MPa.

Two examples of characteristic migration behavior in the annealed film is shown below in **Figure 60**. The initial microstructure, shown in **Figure 60(a)**, undergoes minimal changes throughout the 47-minute under tension resulting in the microstructure shown in **Figure 60(b)**. The orientation map of the region (**Figure 60(c)**) indicates that the large grain in **Figure 60(a)** contains $\Sigma 3$ twin boundaries (red) that are not directly obvious based only on the TEM images. During this process, three small grains are removed and two GBs migrate as identified by the black and red arrows in **Figure 60(c)**, respectively. This is further shown in **Figure 60(d)** which displays the initial outline (dashed) and the final outline (solid) with the removed grains highlighted red. The GB labeled ‘1’ migrated a total distance of 28 nm and GB ‘2’ migrated a distance varying from 8 to 28 nm with the migration distance of the boundary increasing near the regions where the small grains were removed.

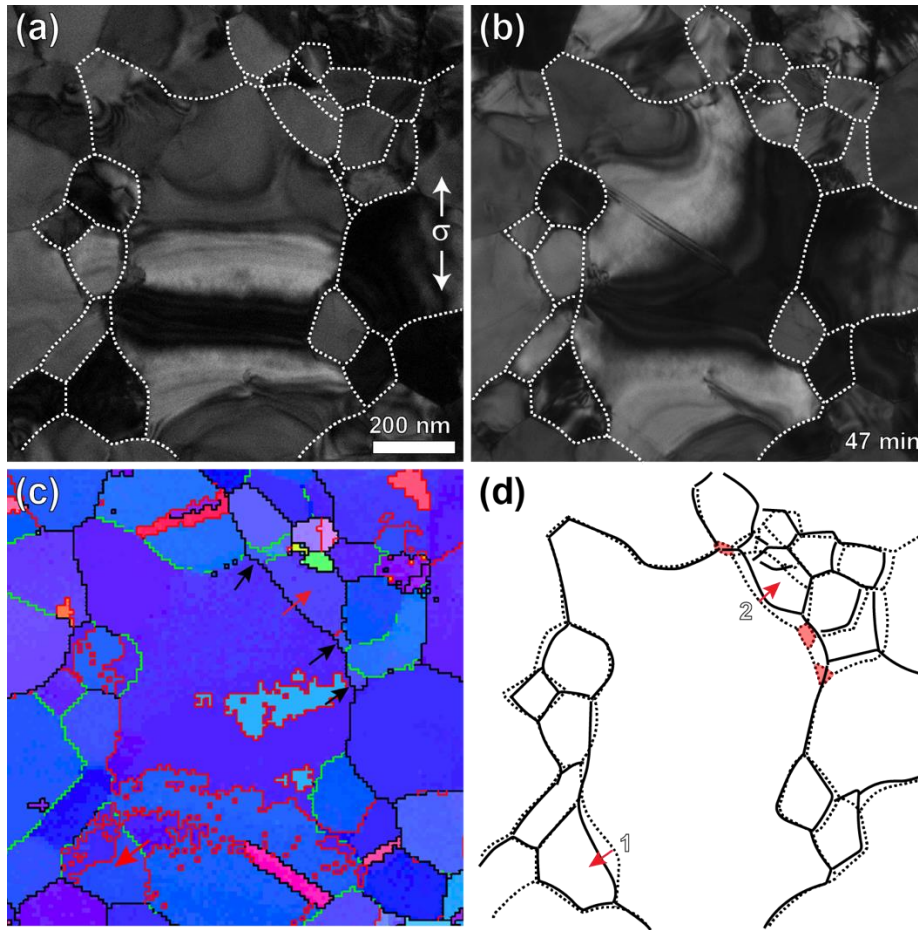


Figure 60 – GBM in A350 Au film. (a) BF TEM image of the initial microstructure with the GB network outlined, (b) same region after 47 minutes under load and specimen failure. The current GB network is outlined. (c) orientation map of the same region. Red arrows indicate direction of GBM and black arrows point to small grains that disappear. (d) overlaid outline from (a) (dashed) and (b) (solid) to show the instances of GBM (red arrows) and grain removal (red highlighted grains).

The above analysis was completed for 1/3rd of the specimen gauge length of the same specimen to identify the migration distance for every GB possible. The results of this can be seen in **Figure 61** where the initial GB network for this section has been outlined and color-coded based off of the migration distance for each boundary. For example, the dark blue boundaries undergo minimal migration of less than 10 nm. The light blue, green, and yellow boundaries experience migration distances within the ranges of 10-19, 20-29, and 30-39 nms, respectively. The red boundaries migrate the most with distances greater

than 40 nm, or the complete removal of a grain in cases where a full grain is outlined in red. The white boundaries undergo minimal or unmeasurable migration whereas the black boundaries cannot be confidentially identified throughout the experiment and are omitted from the analysis. The dashed GBs are $\Sigma 3$ twin boundaries as identified by the orientation map of this section. One of the obvious trends from this analysis is that there tends to be clusters of larger migrations (i.e. clusters of red, yellow, and green colored boundaries). Two examples are identified by arrows on **Figure 61**. This indicates that there is likely a GB connectivity effect, possibly due to the successive glide of disconnections through the GB network. Only three grains were completely removed in this gauge section during this experiment, all of which have an initial grain size $d < 75$ nm. Similarly, there is not a significant amount of grain growth as the average grain size remains unchanged. The local strain within this section of the gauge length during the experiment was estimated to be 3.8% (black arrowheads represent edge features used for strain estimation).

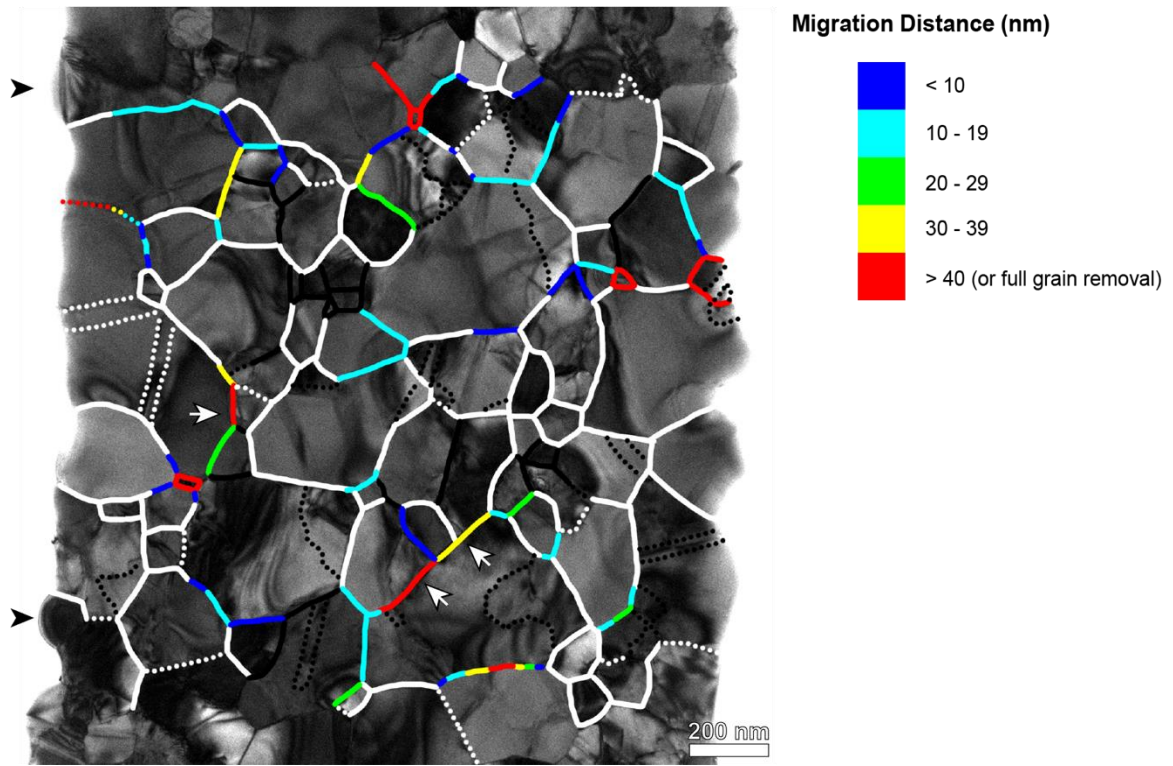


Figure 61 – GBM distances in an annealed specimen during stress-relaxation. The initial GB network is outlined and color coded based off of the migration distance. Color legend is provided on the figure. The white boundaries did not experience measurable migration and the black boundaries could not be confidently identified so are omitted from the analysis. The dashed boundaries are identified as $\Sigma 3$ twin boundaries using the orientation map. Examples of clusters of large migration distances are indicated by arrows.

6.5.1 Microstructural Features

For each of the above colored GBs (**Figure 61**), additional information regarding the GB structure and the local microstructure has been recorded. Specifically, for every GB the following has been identified and recorded: GB misorientation angle, GB trace angle, neighboring grain sizes and Schmid factor. This was done to investigate the common features for mobile or immobile GBs and the corresponding migration distances. In total, 132 boundaries have been tracked (66 mobile and 66 immobile).

6.5.1.1 Grain Boundary Character

The results for the GB misorientation angle are shown below for the mobile and immobile boundaries (**Figure 62(a)** and (b), respectively). Results are presented in terms of the number of mobile (or immobile) GBs for a given misorientation angle divided by the total number of GBs that were manually tracked (i.e. 132). The GB misorientation distribution for all the GBs in the specimen is shown (dashed bars) to provide context on the relative number of GBs present in the specimen for each misorientation angle (the same distribution is shown in the orange data in **Figure 55(f)**). The manually tracked twin boundaries are omitted from **Figure 62(a)** and (b) and shown in **Figure 62(c)** for both mobile (gray) and immobile (orange) twin boundaries. These results indicate that there is a wide range of GB misorientation angles for both mobile and immobile GBs and that there is no strong correlation between misorientation angle and GBM. For the immobile GBs (orange), the misorientation range $32^\circ < \theta < 35^\circ$ has the largest frequency and there are three local maximums for the mobile GBs (grey) occurring at misorientation ranges of $8^\circ < \theta < 11^\circ$, $26^\circ < \theta < 29^\circ$, and $44^\circ < \theta < 47^\circ$. For the GBs that were identified to have a $\Sigma 3$ twin structure, there is no strong difference in the migration behavior (**Figure 62(c)**). There is also no correlation between misorientation angle and the migration distance (data not shown). It is important to note that GB misorientation angle alone does not describe the full GB structure but only defines three of the five macroscopic DOFs associated GB structure [97]. The remaining 2 DOFs describing the GB plane cannot be extracted from the PED orientation maps. This factor could contribute to the fact that no trends are observed in relation to GB misorientation angle.

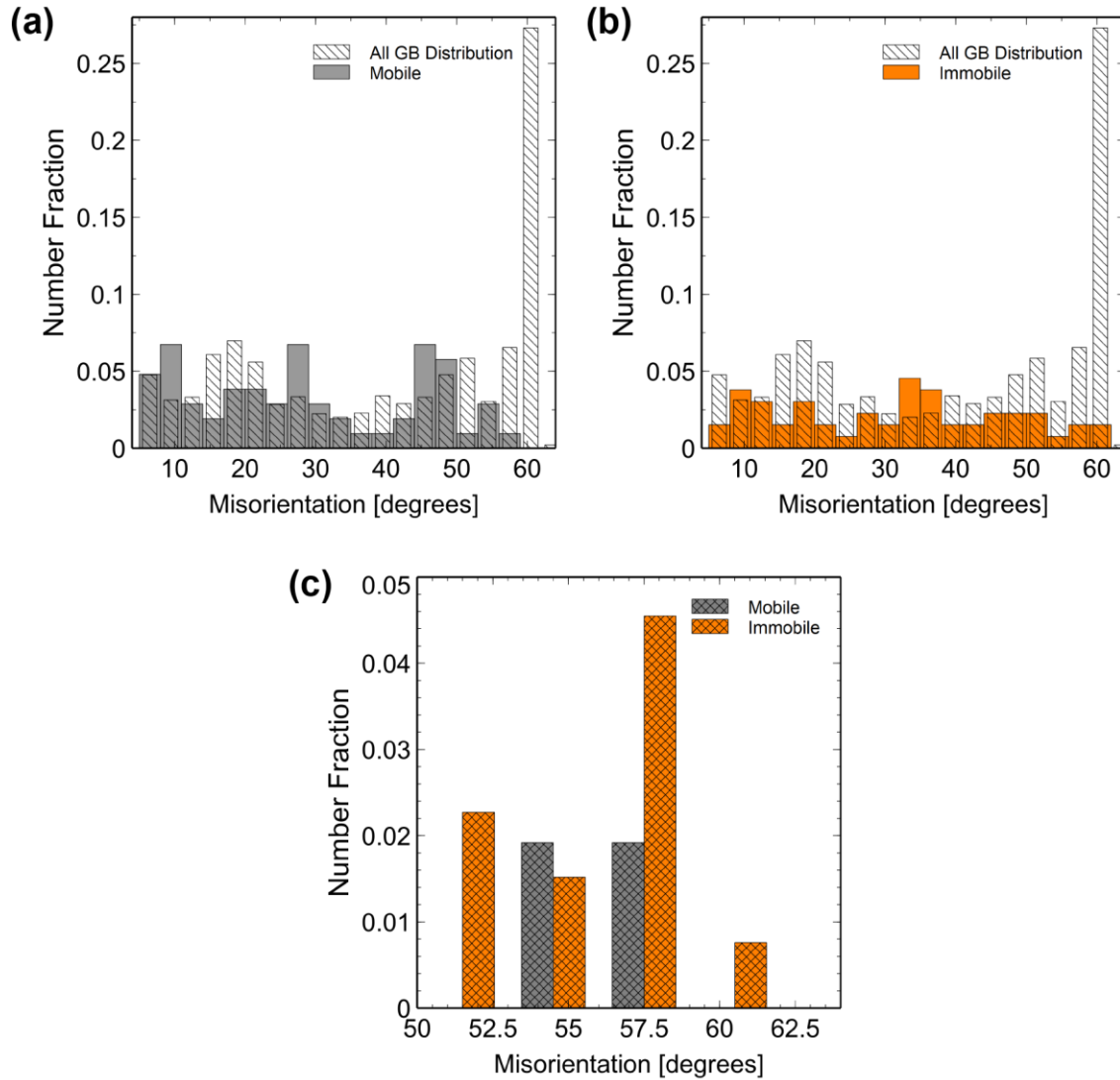


Figure 62 – GB misorientation angle distribution for (a) mobile and (b) immobile GBs during the stress-relaxation experiment. Number fraction is given in terms of the fraction of GBs for a given misorientation angle that are mobile or immobile compared to the total number of GBs that were manually tracked during the experiment. The GB distribution for the full specimen is shown on each with the dashed bars (same distribution is shown in Fig. 1(f)). (c) Distribution of the tracked twin boundaries for both mobile (gray) and immobile (orange) twin boundaries.

6.5.1.2 Grain Boundary Trace Angle

The GB trace angle (defined with respect to the vertical loading axis) was documented for each GB. These results are shown in the stacked distribution (**Figure 63**).

The largest variation between mobile and immobile GBs occurs for trace angles less than 10° of which 3.9% are mobile and 7.8% are immobile.

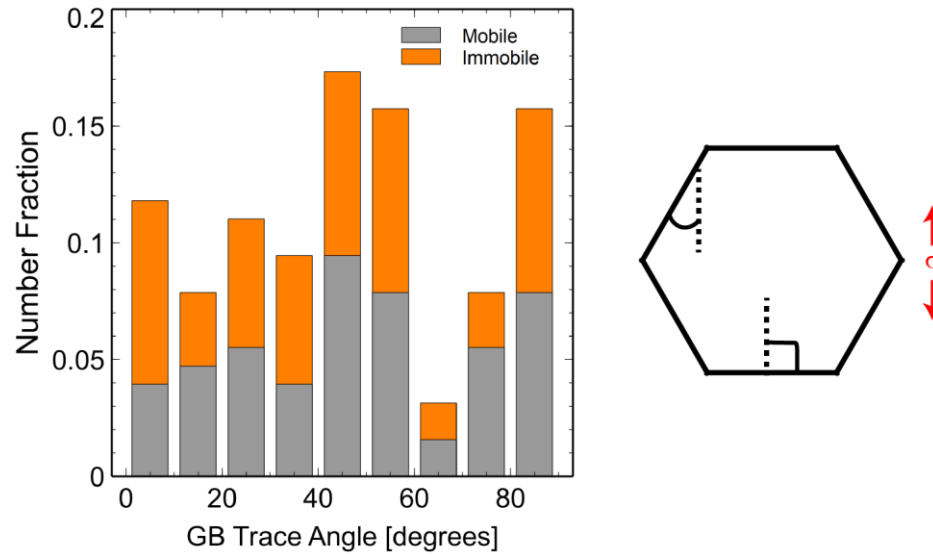


Figure 63 – GB migration distribution in terms of the GB trace angle for mobile (gray) and immobile (orange) tracked boundaries. The schematic to the right indicates how the GB trace angle is defined with respect to the vertical loading axis for a model grain.

6.5.1.3 Schmid Factor

The Schmid factor for each grain was documented to investigate how a favorable (or unfavorable) orientation for slip may influence GBM or grain growth. Previous groups have suggested that grains with a favorable orientation for slip (high Schmid factor) tend to grow at the expense of ‘hard’ grains that are less favorably oriented for dislocation activity [185]. Since these films are highly textured there is not a large variation in Schmid factors and no trend was observed when analyzing the extent of grain coarsening or shrinkage ($\Delta d/d_0$) versus Schmid factor (Δd is the change in grain size and d_0 is the initial grain size) (**Figure 64**).

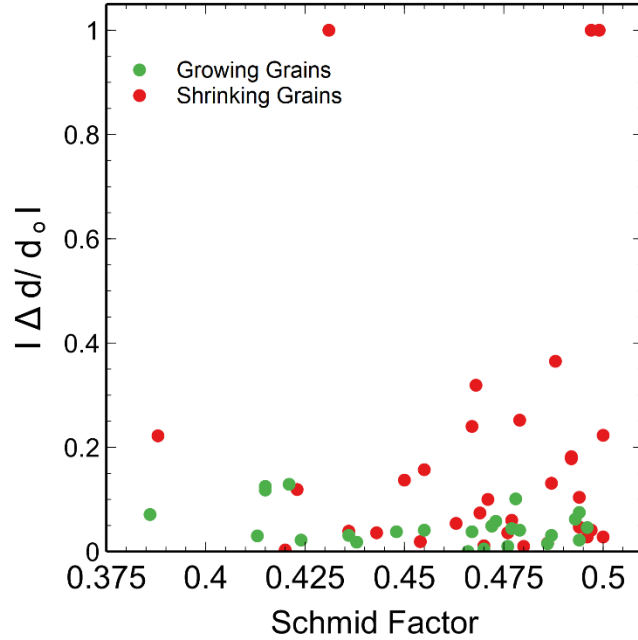


Figure 64 – Grain coarsening ability with respect to the initial grain Schmid factor for the grains that grew (green) and shrunk (red). The coarsening ability is defined as the absolute value of the total change in grain size (Δd) divided by the initial grain size (d_0).

6.5.1.4 Grain Size

The effect of grain size has been investigated in terms of the difference in grain size across a given boundary and displayed as a grain size ratio distribution for both mobile and immobile boundaries (**Figure 65**). The grain size ratio is defined as the ratio of grain sizes (max/min) on either side of each tracked GB. For example, a large ratio indicates that there is a large grain size difference across a particular boundary. Although there are more instances of mobile GBs with larger grain size ratios (24% of the mobile GBs have grain size ratios >2 versus 16% of immobile GBs), the results are not significant enough to claim a strong correlation.

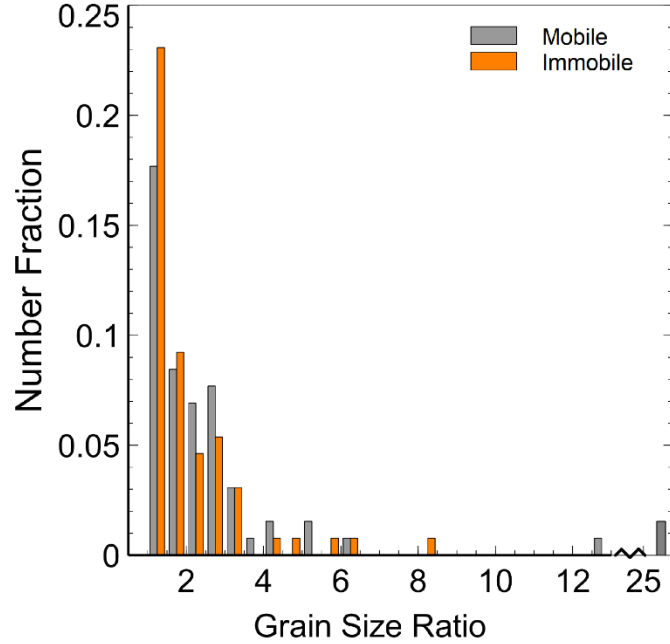


Figure 65 – GBM behavior in terms of grain size ratio across a given boundary. Grain size ratio defined as the maximum grain size divided by the minimum grain size on either side of a given boundary.

6.6 Discussion

This chapter provides a comprehensive investigation into different microstructural features that may influence the behavior and extent of stress-assisted GBM. This has been done by obtaining orientation maps followed by detailed analysis of *in situ* TEM observations during straining for both as-deposited and A350 UFG Au thin films.

In the as-deposited films, GBM appears to be largely dominated by the removal of the small grains ($d < 50$ nm). This is clearly seen through the TEM documentation of the microstructural changes while a stress is applied (**Figure 56** and **Figure 57**). Quantitative support for this is shown in the grain size distribution in **Figure 58(b)** and unambiguously highlights the propensity for small grain removal. These observations are consistent with

other experimental [102,186] and computational studies [187] that report similar preferential removal of small grains under mechanical loading. Small grain removal is still present in the annealed films (**Figure 60**). However, there are only a few occurrences due to the fact that the small grains are removed during the heat treatment prior to straining.

The fact that small grains are consistently removed upon straining indicates that there is a driving force acting on the small grains simultaneous to the driving force provided by the applied stress. GB energy, or capillary forces, are known to be high for small grains since the GB area and curvature increase as the grain size decreases. The removal of small grains could indicate that a reduction in GB energy is a significant driving force. However, this driving force is typically only active at elevated temperatures [188]. Because of this and the fact that grain growth is not observed without an applied stress, it is not likely that capillary-driven GBM is the dominant driving-force for these observations while under an applied stress.

An alternative driving force is related to elastic anisotropy that evolves under an applied stress. Stored elastic strain energy density, given by Eqn. (39), varies across different grains at the same applied load [98,189],

$$W = \frac{1}{2} \sigma_{ij} \varepsilon_{ij} \quad (39)$$

where σ_{ij} and ε_{ij} are stress and strain within a grain, respectively. Under this driving force, GBM will occur towards the grain with the larger strain energy density in attempt to decrease the overall energy of the system. This driving force has two contributing factors: grain orientation and grain size. Since elastic modulus is dependent on the grain orientation,

grains will have different stored elastic energy density based solely on their orientation. If this was a primary factor in controlling GBM/grain growth in these films, one would expect to see grains of certain preferred orientations grow or shrink. For example, a recent study has reported that a [100] texture develops in fatigue-tested UFG Ni due to the preferential growth of [100] grains during high cycle loading. Despite the low driving forces for grain growth at the low strain amplitude level ($<0.3\%$), the high number of load cycles led to a cumulative effect of grain growth. The authors attributed the texture development due to the [100] orientation having the smallest effective elastic constants and thus the smallest strain energy density [100]. This is also consistent with other studies that report texture development from mechanical loading [101,185]. Analyzing the orientation of the individual grains that grew/shrunk (**Figure 58(c)-(e)**) illustrates that this is not the case in this study. Although there is a larger variation in the orientations for the grains that were removed in **Figure 58(c)**, there does not appear to be a strong preferred orientation for grains that disappear versus grains that grow. In addition, there was not relationship between the in-plane grain orientation along the loading axis which further suggest that elastic anisotropy is not a contributing factor to the observed grain growth/shrinkage. However, collecting an orientation map after straining would be necessary to confirm this definitively.

Another grain-to-grain variation in strain energy density arises from grain size dependent yielding (Hall-Petch effect) [14]. Under an applied stress, each grain deforms elastically until the larger grains will yield through dislocation generation and slip. This yielding occurs at a lower stress level than the yield stress required in the smaller grains and as a result, the elastic strain energy density within the larger grains is smaller than that

of the smaller grains. This results in a difference in strain energy density across a GB and can promote GBM towards the small grain and eventually lead to the complete removal of small grains. This can explain the rapid and extensive small grain removal observed in the as-deposited films after a stress is applied. This has been previously proposed as a dominant driving force for small grain removal under cyclic loading [102], but these results indicate that this is likely a strong driving force under monotonic and stress-relaxation loading conditions as well.

The A350 Au specimens in this study are perfectly primed to study the behavior of stress-assisted GBM that is not associated with small grain removal (since most of these grains were removed upon annealing). Local microstructure factors such as GB misorientation angle, GB trace angle, grain size, and Schmid factor were investigated with no single component appearing to have a clear correlation with stress-induced GBM. For example, GBs of a wide variety of GB misorientation angles are mobile or immobile (**Figure 62**), which is consistent with previous reports that there is no general correlation between mobility and GB misorientation angle in polycrystals [186,190]. There is also not a clear trend related to the angle of the GB trace angle with respect to the loading axis (**Figure 63**), indicating that the direction of maximum shear does not have a large influence on GBM. This analysis does assume that the boundaries are perfectly edge-on and, although this is true for most of the boundaries, it may be an over simplification that can influence the apparent results. Unlike the as-deposited films, there is minimal impact of grain size on the GBM (**Figure 65**). As mentioned previously, this is likely due to the fact that the grains are on average larger and have a more uniform strain energy density due to limited grain-size yielding. Finally, there appears to be no effect of Schmid factor on stress-

induced GBM in this study as there is no clear correlation between coarsening ability ($\Delta d/d_0$) and the Schmid factor for a given grain (**Figure 64**). This could indicate that intragranular plastic deformation does not have an impact on intergranular mechanisms or that dislocation slip has less of an effect at the low levels of plastic deformation achieved in these experiments. Other studies have reported the growth of ‘soft’ grains (high Schmid factor) at the expense of ‘hard’ grains at large levels of deformation, however, this study was for randomly-textured Cu with smaller grains ($d \sim 60$ nm) [185]. The Au films in this chapter are highly textured and have minimal variation in Schmid factor across grains. Another distinction is that the grain growth in this study occurs while the specimen deforms plastically at a very low strain rate (i.e. during the relaxation experiment).

The results presented here indicate that there are no observed trends in relationship to the local microstructural features. This could be due to the fact that these observations are made under low driving forces (slow plastic strain rate during stress relaxation) whereas the other studies that report trends achieve larger driving forces (faster strain rate and/or stress levels). At lower driving forces, it is likely that restrictions imposed by TJs can have a large impact on GB mobility since GBM is intimately connected to the behavior of the TJ network. The motion of TJs can be viewed to be a result of the reaction between the disconnection glide within the three GBs that join to form the TJ [97]. If TJs inhibit disconnection glide through the network (leading to accumulation), this can result in back stress on GB disconnections and lead to GBM stagnation. If the GB disconnections are compatible with one or more of the connecting GBs, disconnections can flow through and lead to the connectivity effects observed in **Figure 66**. **Figure 66(a)** shows the initial microstructure of the grains/GB network with the GB labels provided in **Figure 66(e)**.

Disconnections are emitted from the TJ (marked by arrowhead) and glide in the direction of the red arrow along the boundary planes GB₁₋₃. There is also evidence that dislocations glide along GB₁₋₄ following the red arrow direction. This continues and dislocation glide is visible in the location indicated by the arrowhead in **Figure 66(b)**. PED orientation mapping of this region indicates that these dislocations are gliding along a twin boundary (GB₁₋₄). Through this process the TJ migrates upward 20 nm at a rate of $\sim 1 \text{ \AA/s}$ to result in the microstructure shown in **Figure 66(d)**. The schematic in **Figure 66(e)** shows the GB network geometry before (in black) and after (in red) over the course of the 311 seconds separating **Figure 66(a)** and (d), making it clear that the location of the TJ and GB₁₋₂ has migrated. This is a case where the GBs effectively serve as superhighways for disconnection and dislocation glide leading to the migration of both GB₁₋₂ and a TJ.

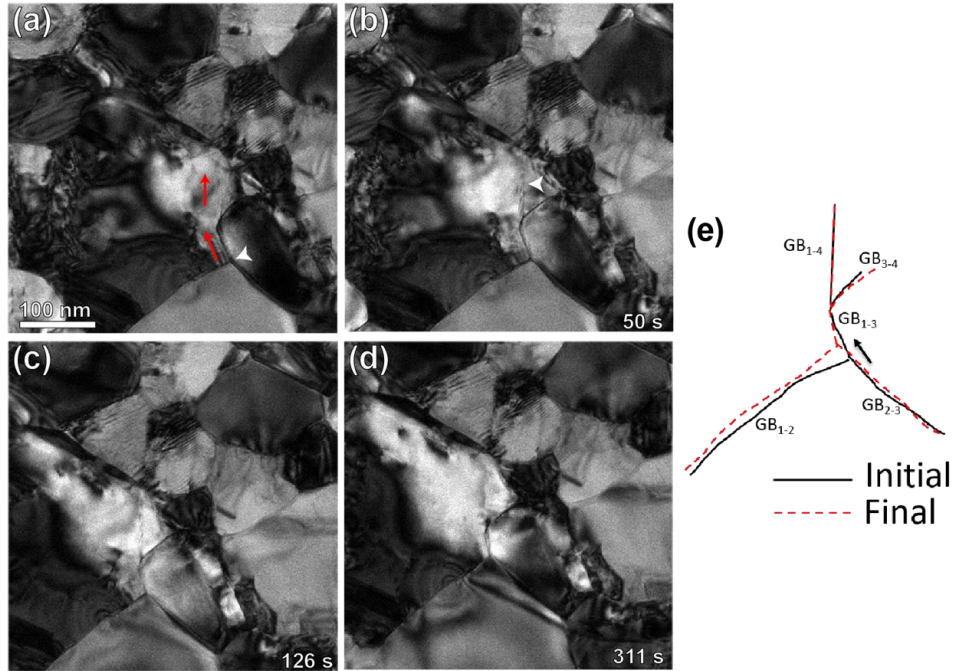


Figure 66 – An example of GB network effects where intergranular dislocation glide leads to triple junction migration during stress-relaxation. (a) intergranular dislocation glide on two GBs (direction of both indicated by red arrows). The white arrowhead marks the triple point that undergoes migration throughout the series of TEM images. (b)-(d) continued intergranular dislocation glide resulting in migration of TJ. White arrowhead in (b) marks visible dislocations. (e) schematic of the initial (black) and final (red dashed) trace of the GBs with arrow indicating TJ migration.

The difference in GBM behavior between the as-deposited and A350 specimens indicates that there are likely two competing driving forces for the observed stress-induced GBM/grain growth: 1) the strain energy difference that eliminates small grains and 2) GBM via disconnection motion. The former can be predicted based off of differences in grain size but appears to only be active when there are small grains ($d < 50\text{nm}$). The latter driving force leads to network TJ and GBM effects and does not have a direct correlation to local microstructure condition at the low applied driving forces in this study.

The mechanism facilitating the stress-induced GBM is the nucleation and successive motion of disconnections along the GBs. It is possible that the small grain

removal is facilitated by similar mechanisms, such as a rapid burst of disconnections, or it also possible that the disappearance of small grains involves alternative mechanisms. Such mechanisms could include grain rotation followed by absorption, which has been recently proposed using MD simulations [187]. Future work should include studying immobile and mobile TJs to investigate the influence of TJs on the evolving GB network.

6.7 Conclusion

Freestanding UFG Au specimens were characterized using orientation mapping and *in situ* TEM straining and features such as grain size, GB character, Schmid factor, and GB trace angle were analyzed in context of GBM and grain growth behavior. For the as-deposited specimens, grain size has a clear effect on GBM/grain growth with smaller grains tending to disappear at the expense of larger grains. This was discussed in terms of a driving force associated with small grain removal related to grain size-dependent yielding and stored strain energy density. There are no clear trends regarding GBM behavior and GB character, Schmid factor, or GB trace angle (with respect to the loading axis) which further suggests that a complicated interplay between GBM driving forces that are active during mechanical loading.

CHAPTER 7.

STRESS-ASSISTED SELF-HEALING OF RADIATION DAMAGE IN ULTRAFINE-GRAINED METAL THIN FILMS

7.1 Overview

NC and UFG metals are considered as an important class of radiation tolerant materials. The large volume fraction of GBs effectively serves as sinks for radiation damage, and understanding the mechanisms by which these 2D interfaces remove radiation-induced point and line defects is key to developing more effective radiation tolerant nanomaterials. This chapter characterizes the effect that radiation damage has on the active deformation mechanisms and mechanical property of UFG Au thin films. Section 7.2 and Section 7.3 respectively provide characterization of the microstructure after irradiation and the effect it has on the monotonic properties. This is followed by a detailed description of the active deformation mechanism in Section 7.4, including the first experimental observation of a radiation damage healing mechanism through stress-assisted GBM. Measured activation volume values are shown in Section 7.5 and a discussion is provided in terms of the effect radiation damage has on stress-assisted GBM and the potential impact of this new healing mechanism.

7.2 Initial Microstructure

A portion of the as-deposited Au specimens were irradiated with 2.8 MeV Au⁴⁺ at room temperature using a 6 MV Tandem accelerator at Sandia National Laboratories to ~ 0.7 displacement per atom (dpa) [161] (see Section 2.5 for irradiation details). The initial

microstructure of the non-irradiated specimens (**Figure 67(a)**) is provided again for easy comparison and shows that the majority of grains are defect free, with a few of the largest grains containing lattice dislocations and/or twin boundaries. The initial microstructure of the irradiated specimens is shown in **Figure 67(b)**, where there is ‘black-spot’ radiation damage within all the grains. The damage can be seen in more detail at higher magnification in **Figure 67(c)**. Although not specifically characterized, the radiation damage is likely to be small dislocation loops or small SFT [191]. Grain size (*d*) distributions show that radiation-induced grain growth results in a 33% increase in the average grain size from 142 nm to 189 nm, due to the near-total removal of grains smaller than 50 nm after irradiation (**Figure 67(d)**). This is consistent with *in situ* TEM irradiation studies that show that larger grains grow at the expense of smaller grains under irradiation alone [148]. An indexed diffraction pattern for the irradiated Au is provided in **Figure 67(e)** to show that the films maintain the FCC structure.

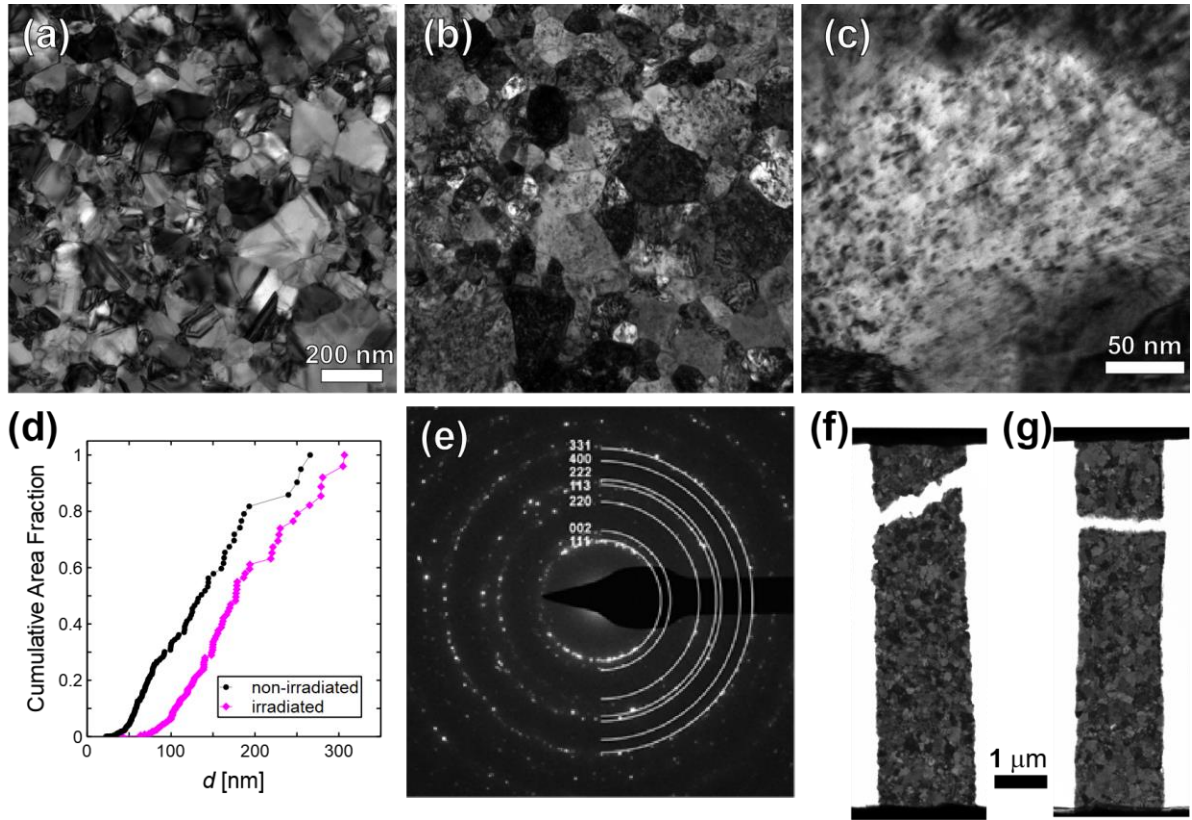


Figure 67 - Initial microstructure of irradiated UFG Au specimens. TEM micrographs of (a) non-irradiated Au film and (b) irradiated Au film. Most grain interiors contain ‘black-spot’ radiation damage. Scale bar is the same as in (a). (c) BF TEM micrograph of a grain interior of irradiated film to exhibit radiation damage. (d) Cumulative grain size distribution of non-irradiated (black circles) and irradiated (magenta diamonds) films prior to straining. (e) Indexed diffraction pattern of irradiated Au film exhibiting characteristic ring structure for NC and UFG FCC metals.

7.2.1 Defect Spacing Measurement

The defect spacing between radiation defects was estimated using the following approach. Weak-beam dark field (WBDF) TEM images were taken of the initial irradiated microstructure. From the WBDF image, defects were individually identified and counted. For the grain shown in **Figure 67(c)**, the parameters in calculating the defect spacing are

shown in **Table 8**. An invisibility criterion of 1.9 was used to estimate the defects that are invisible at any the particular diffraction condition [191].

Table 8 – Parameters used in estimating defect spacing.

# of counted defects	Total # of defects	Grain area (nm ²)	Defect density (nm ⁻³)
614	1166	42732	2.73×10^{-4}

The final defect spacing l was estimated as ~15 nm from the defect density ρ using the following equation:

$$l = \frac{1}{\sqrt[3]{\rho}} \quad (40)$$

The above equation assumes evenly spaced defects and does not consider the small portion (~5nm) of the thickness that is denuded of defects near either free-surface. However, if we assume the radiation defects are SFT, then there are minimal diffraction conditions in which the defects are completely invisible. If this assumption is correct, no invisibility criterion is used and the defect spacing only increases to ~19 nm.

7.3 Mechanical Properties

Figure 68(a) shows the monotonic tensile stress-strain curves for a non-irradiated and irradiated specimen at a strain rate of $\sim 10^{-4} \text{ s}^{-1}$. The monotonic response of the irradiated specimen shows evidence of brittle behavior with a linear elastic stress increase followed by failure after reaching the UTS of 663 MPa. In contrast, the non-irradiated counterpart yields at ~480 MPa (0.2% offset), reaches an UTS of 520 MPa, which is followed by a gradual decrease in stress and eventual failure at plastic strain $\varepsilon_p = 4.9\%$.

The post mortem fracture surface of the non-irradiated specimen, **Figure 68(b)**, indicates that the stress decrease after UTS is likely due to slight necking and stable crack growth promoted by the maximum shear stress along the 45° direction with respect to the vertical loading axis. Similarly, **Figure 68(c)** confirms the brittle-type unstable crack growth that occurred in the irradiated film, with the fracture surface at 90° from the vertical loading axis.

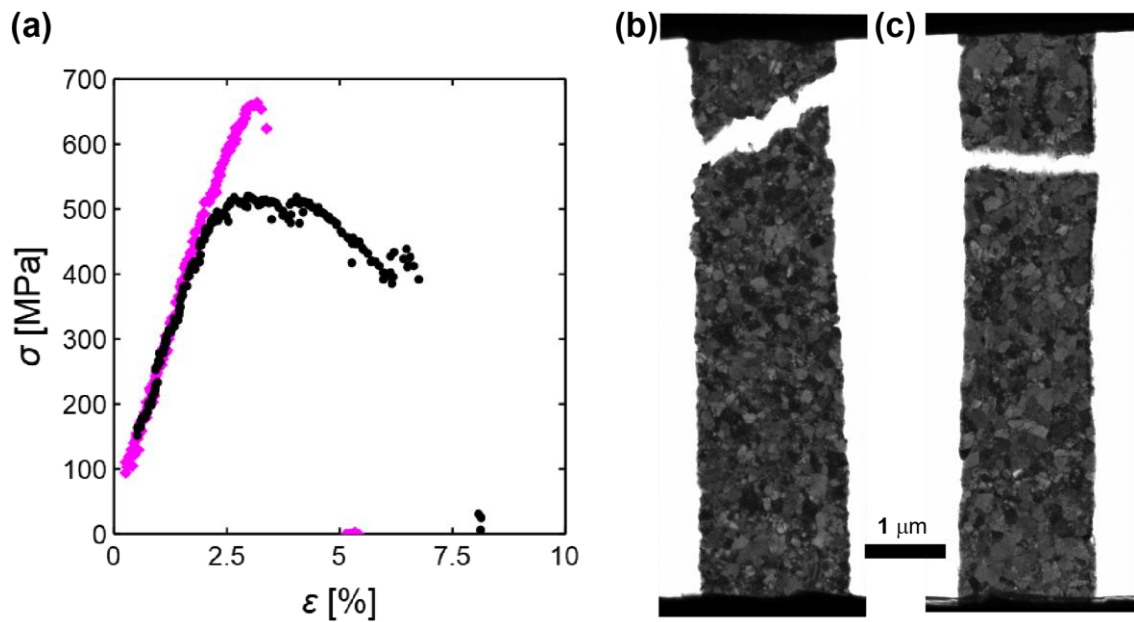


Figure 68 – Monotonic tensile curve for irradiated UFG Au specimen. (a) Stress-strain curves from *in situ* TEM tensile tests of non-irradiated and irradiated specimens. Both were conducted at a strain rate of $\sim 10^{-4} \text{ s}^{-1}$. TEM micrographs of (b) non-irradiated and (c) irradiated specimen tested under tension to show the differences in fracture surface.

7.4 Deformation Mechanisms

7.4.1 Dislocation-Based

The observed strengthening effect of the irradiated specimens is consistent with the *in situ* TEM observations of dislocation / radiation defect interactions, with the radiation defects serving as obstacles to dislocation glide [134]. A detailed description and TEM based characterization of dislocation pinning is provided in **Figure 69**. **Figure 69(a)** was captured 55 seconds into a stress-relaxation segment and shows a grain containing multiple ‘black-spot’ radiation defects in the grain interior with one indicated by the white arrowhead. After three seconds, multiple dislocations are emitted from the right GB (indicated in **Figure 69(a)**) and partially transverse the grain until pinned by defects. The dislocation indicated by the black arrowhead is pinned by the white arrowed defect and the neighboring GB to the left. The dislocation remains partially pinned at the defect in **Figure 69(c)** while a portion of it glides freely in the direction of the black arrowhead. After a short reloading segment, the dislocation continues to glide and becomes pinned on a second defect (second white arrowhead in **Figure 69(d)**).

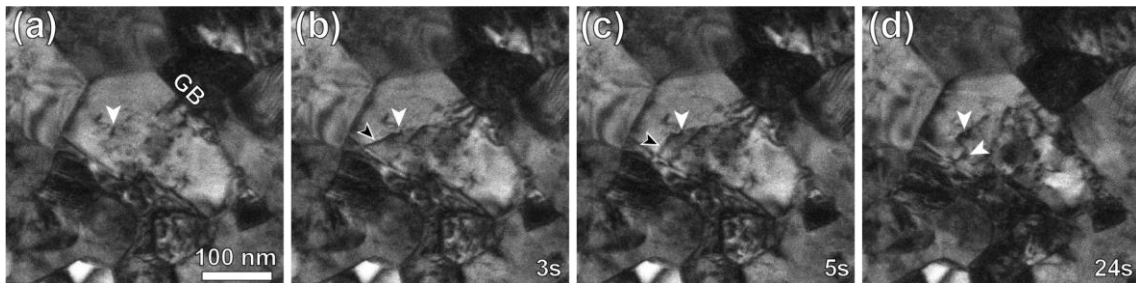


Figure 69 – Radiation defects serving as obstacles to dislocation glide. (a) Grain containing multiple radiation-induced defects with one specific defect indicated by white arrowhead. (b) After 3 seconds, dislocations are emitted from the indicated GB and partially transverse the grain until being pinned by defects. One pinned dislocation (indicated by black arrowhead) is pinned by the defect that is indicated by white arrowhead in both (a) and (b) and the leftmost GB. (c) After two additional seconds, the left end of the dislocation (black arrowhead) glides while a portion remains pinned by a defect (white arrowhead). (d) a portion of the dislocation continues to glide until being pinned by an additional defect indicated by the second white arrowhead.

In all of the irradiated specimens tested, there is no indication that defect-free channels form from repeated intragranular dislocation glide, which is a variation from what is typically observed in irradiated coarse-grained metals [133,192]. This likely indicates that there is an insufficient number of passing dislocations to facilitate complete removal of radiation defects within localized regions.

7.4.2 Grain Boundary-Based

In addition to restricted dislocation glide, stress-assisted GBM is another active deformation mechanism in the irradiated specimens. Clear evidence of radiation damage removal via GBM is illustrated by the TEM images in **Figure 70** where the outlined grain undergoes substantial grain growth while under a stress relaxation test with a series of relaxation segments. As the GB migrated, it absorbed the radiation defects in the neighboring grains, creating defect-free regions. This is clearly seen in **Figure 70(b)** where there is a region with radiation defects (where the original grain was) in addition to a region without any radiation damage as the GBs have migrated outwards in the direction indicated by arrows. This image was taken after a 28-minute-long series of stress-relaxation segments in which a maximum stress of 530 MPa was achieved. Additional *in situ* TEM observations of this growing grain were made throughout the duration of another series of stress-relaxation segments, during which the GBs continued to migrate (**Figure 70(c-f)**). The outlined GB migrates at an average velocity of 0.03 nm/s (for $\sigma < 530$ MPa), not including the one instance of a rapid jump in GB migration occurring at a maximum velocity of 34 nm/s during the transition from **Figure 70(b)** to (c). This maximum velocity did not occur simultaneous to an applied stress increase, indicating that a different factor contributed to the accelerated migration. In **Figure 70(c)**, a dislocation pinned on a

radiation defect is indicated by the arrowhead and 30 seconds later is de-pinned and glides unrestricted through the defect-free region (**Figure 70(d)**).

For the transition in **Figure 70(c-e)**, migration velocities for each GB were determined by measuring the change in GB location in 30 second intervals (data shown in **Figure 70(g)**). At an applied stress level of 550 MPa, the average GBM velocities range from 0.03 to 0.07 nm/s. Upon increase of the applied stress to 650 MPa (nearing the UTS of irradiated specimens), some average GBM velocities increase by more than one order of magnitude (to values ranging from 0.32 to 0.95 nm/s), suggesting that the local stresses may be significantly larger (similar to what has been observed in NC Al films [176]). After 51-minutes of total time under tension, extensive GBM has led to a large defect free region that can support unrestricted dislocation glide and dislocation-dislocation interactions. This is clearly seen in **Figure 70(f)** where there are multiple dislocations interacting with a partial dislocation within the defect-free region of the grain. The majority of the radiation defects remain within the original grain outline. This type of behavior is similar to grains distributed throughout the specimen gauge length; and in total, 14% of the specimen area was cleared of defects after this particular experiment.

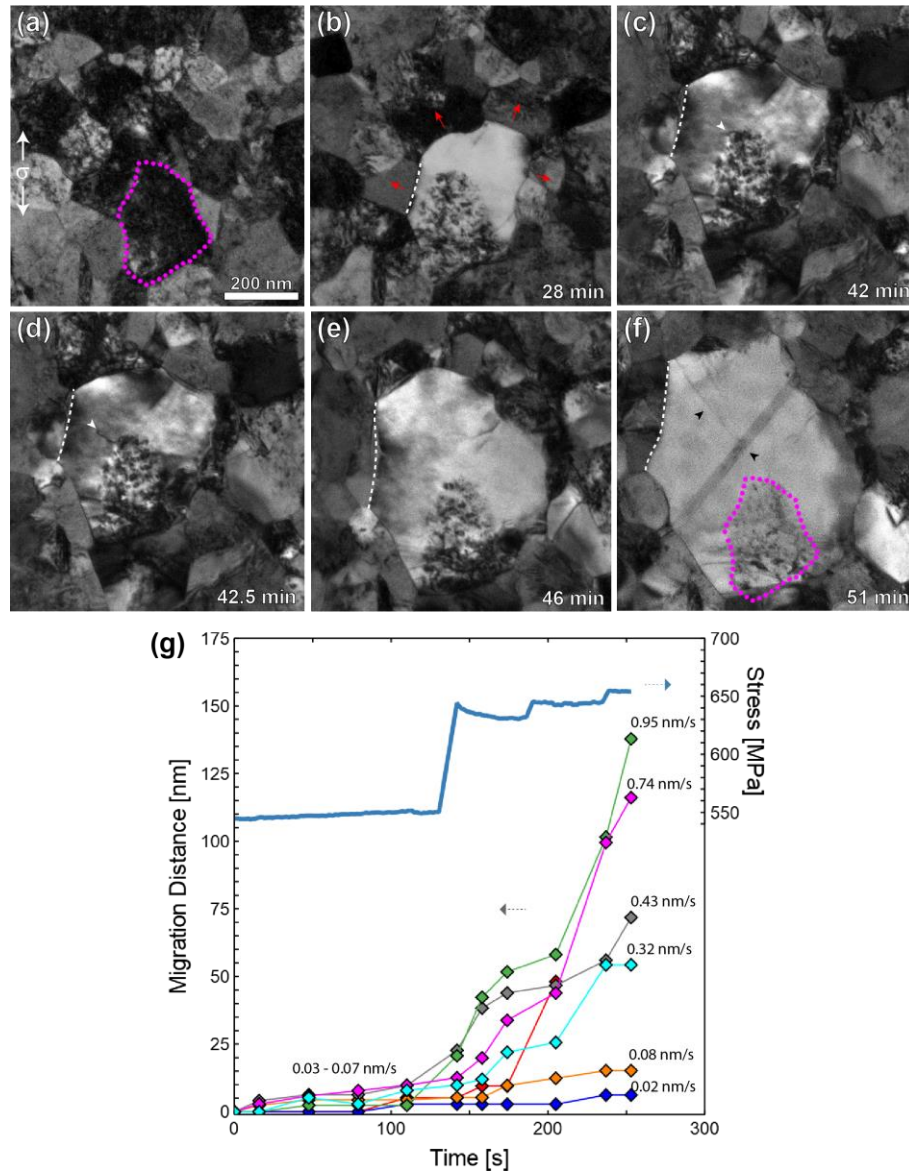


Figure 70 – Stress-assisted GB migration leading to radiation damage healing and defect-free regions capable of supporting extensive dislocation glide. (a) Microstructure prior to an applied load with a single grain outlined. (b) GBM has led to grain growth of the outlined grain resulting in defect-free regions where GB migration occurred. The radiation defects remain where the original grain was (no migrating GB passed through this region). Arrows indicate direction of continued GB migration. (c) GB migration continues and leads to a further increase in grain size and defect-free region. Arrow indicates a dislocation pinned on radiation defects. (d) The indicated dislocation becomes de-pinned and glides unrestricted in the radiation-free region until being absorbed by a nearby GB. (e) Continued GB migration leading to an increasing defect-free area. (f) The defect-free region can now support

dislocation-dislocation interactions, indicated by both arrowheads. Time stamp in each indicate the total time (in minutes) under a tensile stress (both during loading and stress-relaxation). (g) GB migration distance data for all the involved boundaries during the transition from (c) to (f). The far-field stress values are provided on the secondary axis to demonstrate how migration behavior varies with stress.

The effect of irradiation on GBM was further studied by tracking the same collection of grains. **Figure 71** is an example of such *in situ* TEM experiment consisting of successive stress-relaxation segments for an irradiated film where the outlined grain was tracked until specimen failure. The GBs marked 1 and 2 gradually migrate (red arrows indicate migration direction) while absorbing the radiation defects within the grain. This is clearly seen in **Figure 71(e)** where the original grain outline is overlaid on the final microstructure to show the change in grain shape due to GBM. The majority of GB 1 migrates at a steady velocity of 0.04-0.06 nm/s to a total migration distance of 83 nm (the right-most portion of this GB migrates an additional 31 nm at a maximum rate of 0.25 nm/s to result in the curved boundary seen in **Figure 71(e)**). The progression of GBs 1 and 2 migration, along with 4 other boundaries recorded simultaneously, can be seen in **Figure 71(f)** (curves for GB 1 and 2 are the grey and green curves, respectively). The average migration velocity (nm/s) for each tracked boundary is documented to the right of each curve. The instantaneous stress levels were measured and are displayed on the secondary axis. The stress ranged from 309 to 570 MPa with 22 instances of stress increase due to reloading in between relaxation segments (full stress-strain curve shown later in **Figure 74(a)**). For the majority of the boundaries, migration occurs at a relatively steady pace with average velocities ranging from 0.007 to 0.06 nm/s, which is consistent with the measured velocities for in **Figure 70(g)** at an applied stress of around 550 MPa. There is only one instance in which a GB jumped 16 nm at a maximum ‘jump’ velocity of 8.1 nm/s. This is

visualized by the large jump in migration distance in the brown data around 500 seconds and was associated with the collapsing of a smaller grain ($d \sim 47$ nm).

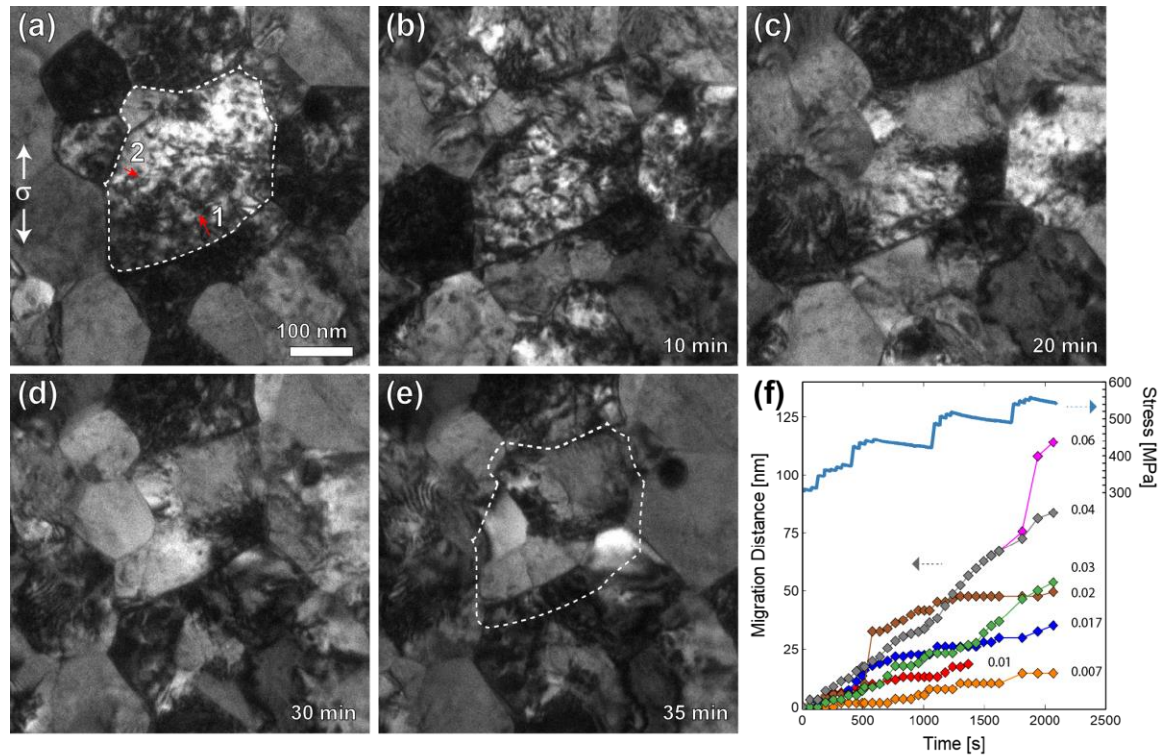


Figure 71 – “Steady” grain boundary migration documented in irradiated film during repeated stress-relaxation experiment. (a) Microstructure prior to an applied load. The outlined grain is one of the grains tracked throughout the experiment with two migrating boundaries labeled 1 and 2. The red arrows indicate direction of GBM. (b)-(d) the same grain shown in 10-minute increments, (e) final microstructure with the original grain outline from (a) overlaid to show the change in grain size and shape due to GB migration. The scale bar in (a) is the same for all frames. (f) GBM distance data throughout the experiment from six boundaries recorded simultaneously. The instantaneous far-field stress levels are shown with the stress scale on the right y axis. Average velocity (nm/s) is recorded to the right of each curve. Time is given in terms of time since initial recording of the grains, which began 3 minutes after initial load was applied.

7.4.2.1 Comparing Migration Behavior with As-Deposited

A similar experiment was conducted on a non-irradiated specimen to identify the main differences in GBM for irradiated versus non-irradiated films. In general, the GBM occurs at a faster rate in the non-irradiated films which facilitates the GBs reaching a stable position within the time frame of an experiment. This is shown in **Figure 72**, where the outlined grain undergoes significant stress-induced GBM in the direction of the red arrows to result in the larger grain seen in **Figure 72(b),(c)** with the final microstructure shown in **Figure 72(d)**. Migration data on these particular GBs as well as four additional migrating GBs is shown in **Figure 72(e)**. The total migration distances for the GBs associated with the growing grain in **Figure 72(a-d)** varied from 153 nm to a maximum migration of 270 nm over 25 minutes, with a maximum jump velocity of 85 nm/s corresponding to the first large jump in migration distance in the red line around 170 seconds. The four additional migrating GBs that were tracked simultaneously migrate quickly within the first few minutes and then stagnate, with migration velocities ranging from 0.03-0.12 nm/s (before stagnation). The instantaneous stress levels were not documented in this experiment, but the stress levels at different times were determined by measuring the displacement of the load sensor beams manually using TEM imaging and are indicated by the data points on the secondary stress axis in **Figure 72(e)**. The initial migration occurs at a far-field stress level of 340 MPa, with the stress recorded to vary between 197 to 367 MPa. The vertical grey dashed lines represent instances in which the stress is increased during a reloading segment. Half of the recorded GBs are sensitive to the loading and show an increase in migration speed directly after a reloading segment (vertical dashed line) which is followed by stagnation until the stress is increased again. The velocity of one of the GBs (red data) after the final three reloading segments until stagnation is 0.60, 0.22, 0.43 nm/s.

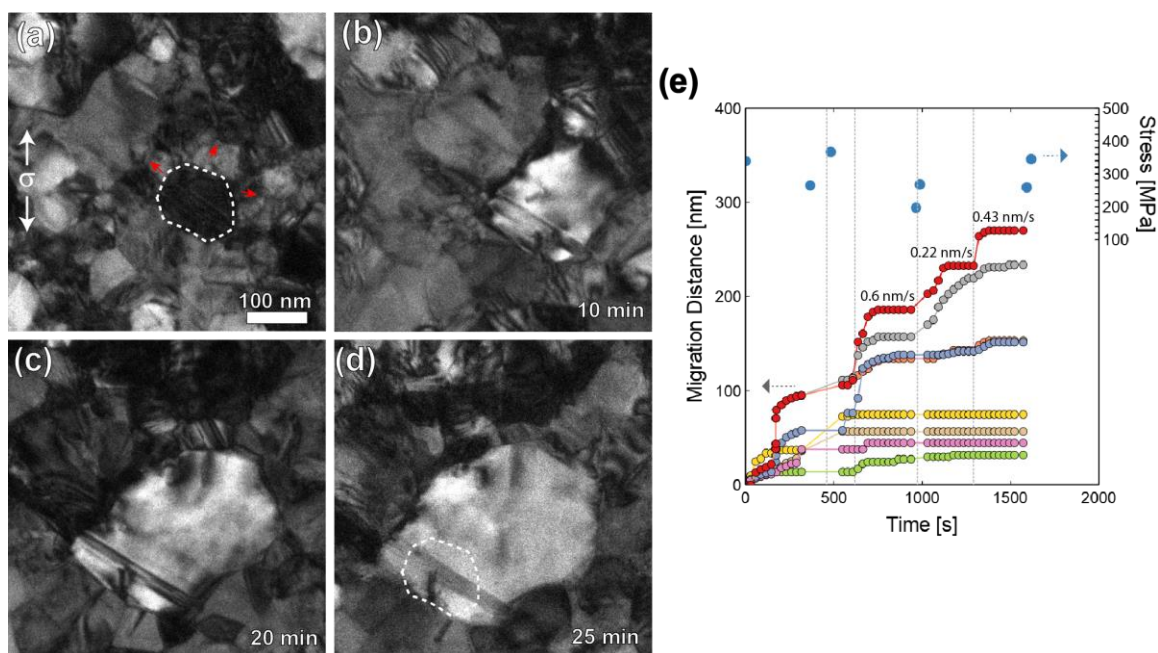


Figure 72 – “Rapid” stress-induced grain boundary migration in non-irradiated films during a stress-relaxation experiment. (a) Initial microstructure of a collection of grains. The outlined grain undergoes significant grain growth due to GBM in the direction indicated by red arrows. (b)-(c) the same grain in 10-minute increments. (d) Final grain microstructure with original grain outline from (a) overlaid to show the significant stress-induced grain growth. (e) GBM distance for different boundaries tracked simultaneously. The manually measured stress levels are plotted on the secondary axis. Vertical grey lines represent reload instances in which the stress was increased. Time is given in terms of seconds since first recording of given set of grains which occurred 2.5 minutes after load was first applied. The velocity of the GB represented by the red data points is shown for the final three reloading segments (i.e. velocity of the GB as it migrates after promoted by an increase in stress until stagnation again).

Comparing the migration data (**Figure 71(f)** and **Figure 72(e)**) indicates that the majority of boundaries in the non-irradiated film migrate at faster velocities than the boundaries in the irradiated film. Analyzing the first 5 minutes only (**Figure 73(a)**) clearly shows that all of the tracked boundaries in the non-irradiated film experience faster migration leading to larger migration distances compared to the boundaries in the irradiated films. For example, the maximum migration velocity within the first 5 minutes in the irradiated film was 0.03 nm/s (grey data) whereas the migration velocities in the non-

irradiated film varied from 0.04-0.30 nm/s despite the initial stress levels being comparable for both specimens. **Figure 73(b)** displays the “instantaneous” velocity for three GBs throughout the experiments shown in **Figure 71** and **Figure 72**. Representative GBs were chosen to show the characteristic migration behavior for each specimen type (i.e. non-irradiated GBs, with one that stagnates after some time and one that does not completely stagnate, and one irradiated GB that not does stagnate). Comparing the velocity throughout the experiment clearly illustrates that the non-irradiated GBs (dashed) experience higher velocities before reaching stable equilibrium positions (i.e. velocity is zero). In contrast, the irradiated boundary (solid) continues to migrate at a relatively consistent velocity. The instances of large velocity increase in the non-irradiated film occurring around 600, 970, and 1300 seconds corresponds to moments when the applied stress was reloaded to a higher value. The schematics shown in **Figure 73(c)** and (d) provide a visual comparison of the difference in GBM behavior in the grains analyzed in **Figure 72** and **Figure 71**, respectively. The schematics show the original GB trace (solid) and subsequent GB trace outlines (dashed) in 10-minute increments at the same length scale. The far-field applied stress ranges for the 20-minute intervals are displayed below the schematics and indicates that the non-irradiated grains undergo stress-assisted GBM at larger velocities despite the fact that the applied stresses are on average lower than that in the irradiated films.

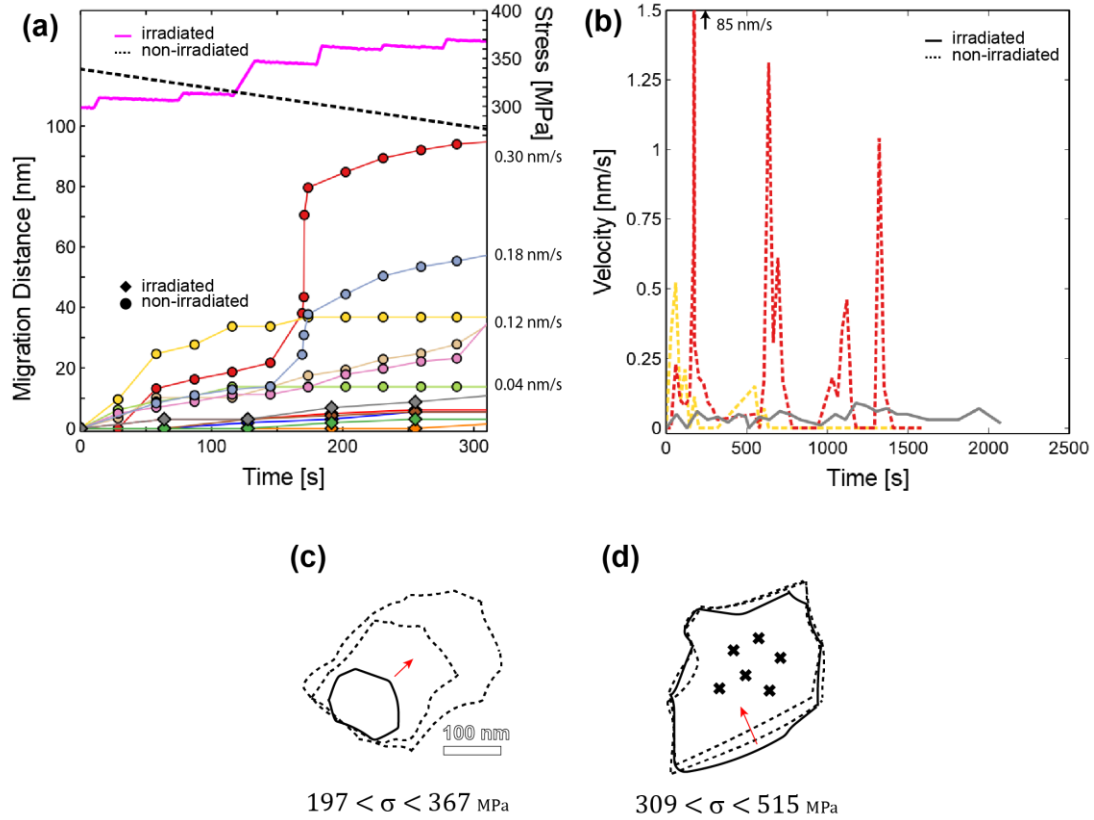


Figure 73 - Comparison of stress-assisted grain boundary migration distances and velocity in irradiated and non-irradiated Au films. (a) GB migration distance data from the irradiated film in Figure 71(diamonds) and non-irradiated specimen in Figure 72(circles) scaled to show first 5 minutes only. The stress levels for both are shown with the stress scale on the right y axis to show that the initial stress levels are similar followed by an increase in stress in the irradiated film and decrease in stress in non-irradiated. The average velocity is provided for each non-irradiated GB showing a range of 0.04 – 0.30 nm/s. (b) “Instantaneous” velocity for one GB in irradiated specimen and two GBs in non-irradiated specimen. “Instantaneous” velocity is defined as the velocity for a 30-60 second interval. The schematic of the grain shape change outline of (c) non-irradiated grain in Figure 72 and (d) irradiated Figure 71 to compare migration behavior at the same length scale (scale bar the same for both). The solid outline represents the initial grain size with the two dashed outlines representing the grain shape after 10 and 20 minutes. The red arrow indicates direction of migration. The black ‘x’ represents radiation damage. The stress ranges during migration are provided underneath the schematics.

7.5 *In Situ* TEM Measurements of Activation Volume

In situ repeated stress-relaxation experiments have been completed to measure true V^* and apparent V_a activation volume values for the irradiated Au specimens. An example of one experiment is shown in **Figure 74**. This experiment was conducted using electrical-sensing only. In total, 22 relaxation segments were conducted with a stress range of 309 to 570 MPa (this is the same experiment shown previously in **Figure 71**). Four of the relaxations are shown in more detail in **Figure 74(c)-(f)** and occur at an applied stress of 437, 443, 514, and 518 MPa, respectively. The true activation volume V^* values for all the relaxation segments varied minimally ($V^* \sim 26 - 29b^3$) with more variation with the apparent activation volume V_a values ($V_a \sim 35 - 101b^3$). These values are consistent with the V^* and V_a values measured across all experiments conducted on irradiated specimens (**Figure 75**).

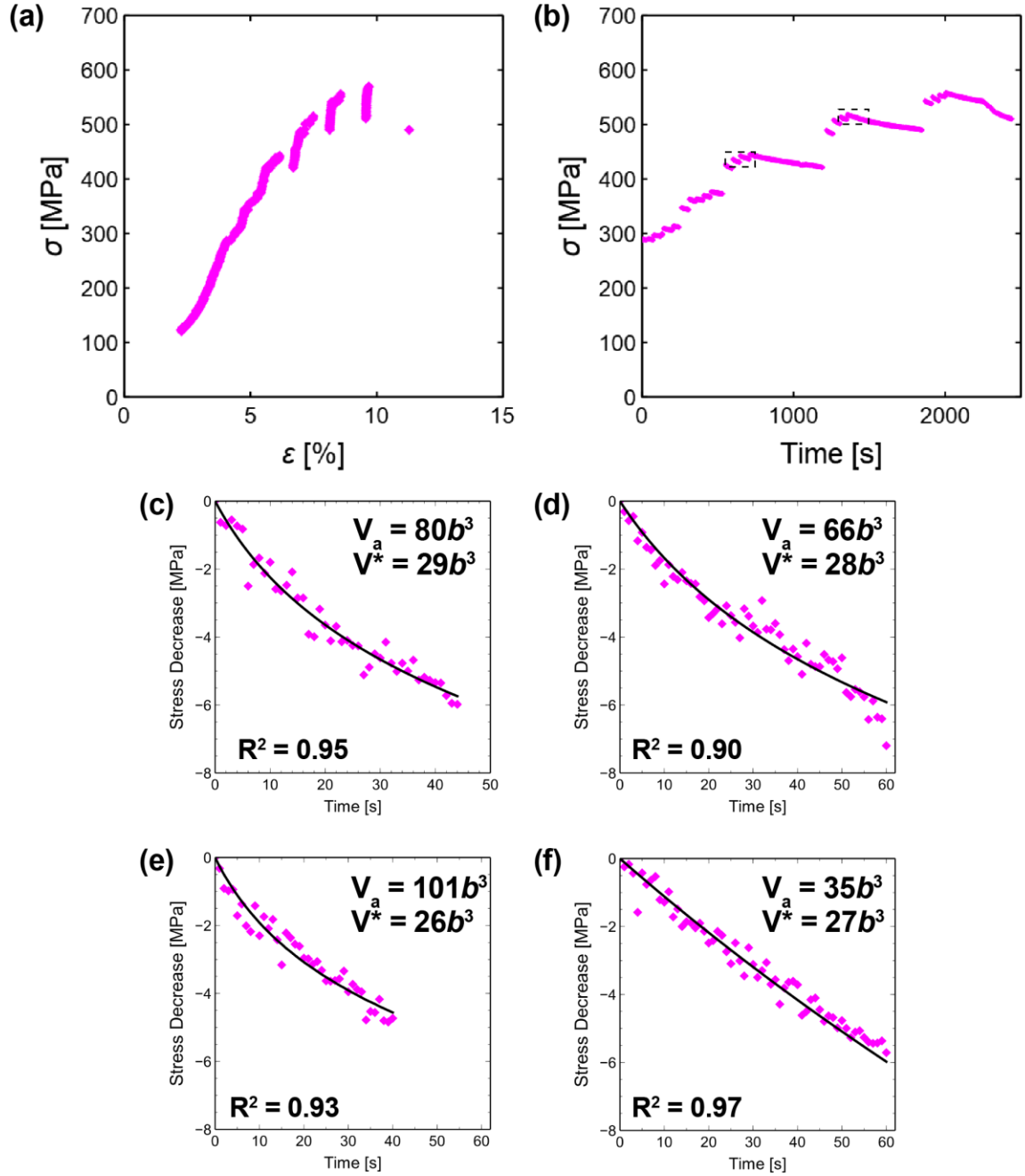


Figure 74 – *In situ* repeated stress-relaxation experiment and activation volume measurements for an irradiated Au specimen. (a) full stress-strain curve with stress-relaxation segments shown in (b). The four relaxations within the dashed boxes correspond to (c) Relax 12, (d) 13, (e) 17, and (f) 18.

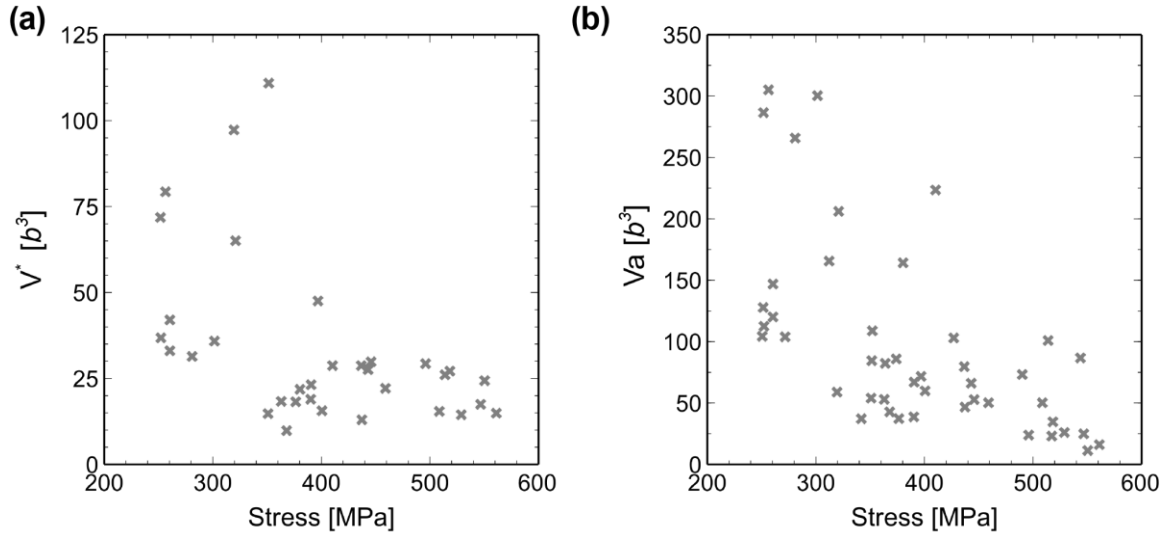


Figure 75 – All *in situ* true V^* and apparent V_a activation volume measurements on irradiated UFG Au specimens.

It is clear from **Figure 75** that both V^* and V_a vary across the stress range. Since the microstructure also evolves with applied stress due to GBM leading to defect removal, additional experiments were conducted to investigate if the observed trends in activation volume are a stress effect or an effect of the evolving microstructure. To do this, a stress-relaxation experiment was conducted to measure V^* and promote stress-assisted GBM to ‘clean’ the microstructure before unloading to prevent specimen failure. This experiment (Test 1) is shown in **Figure 76(a)** and was done with image-based sensing for CS2 (stress) only, so the data is presented in terms of stress-time. The specimen was unloaded and the microstructure was analyzed for evidence of GBM by identifying defect-free regions. After the 20-minute Test 1, ~1.62% of the specimen gauge volume has been removed of radiation damage. The specimen was then loaded again (Test 2, **Figure 76(b)**) to conduct additional relaxation segments until specimen failed after 16-minutes. The *post-mortem* gauge was analyzed and ~5.56% of the volume was cleaned of radiation damage due to stress-assisted

GBM. The V^* measurements from Test 1 and Test 2 are displayed on **Figure 76(c)**. The values for Test 1 range from $71-79b^3$ for $\sigma \sim 250$ MPa, decrease slightly to $42b^3$ (260 MPa) and further decrease to $21-28b^3$ as the stress increases to 380-410 MPa. If the decrease from ~ 70 to $\sim 20b^3$ was due to the evolving microstructure, one would expect that the V^* would be $\sim 20b^3$ for all the Test 2 measurements since the microstructure does not revert to the initial condition during unloading. However, the V^* for Test 2 are $\sim 60b^3$ (148 MPa) which decrease to $\sim 30b^3$ (300 MPa). This experiment confirms that the variation in V^* for a given specimen is likely a stress effect and not the effect of the evolving microstructure. Additional discussion on V^* interpretation is provided in CHAPTER 8.

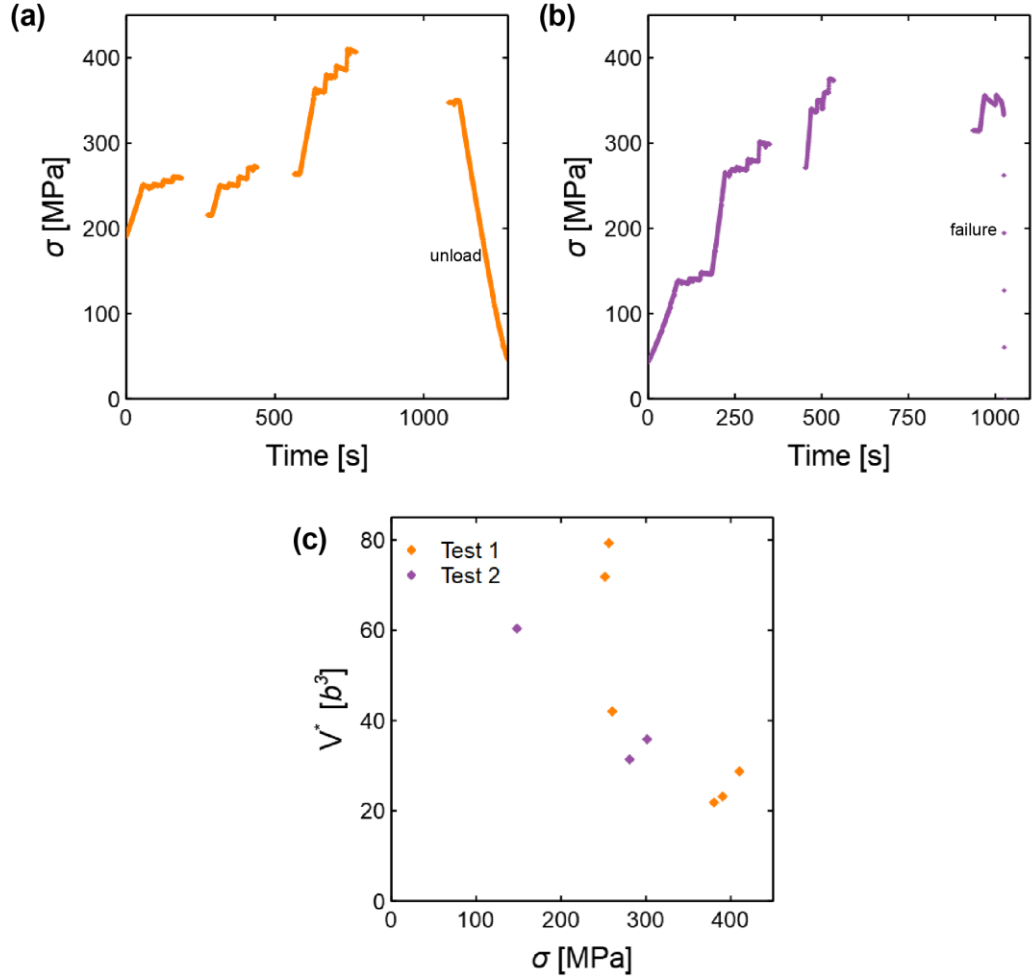


Figure 76 – Successive *in situ* stress-relaxation experiments to investigate how true activation volume V^* varies with evolving microstructure. Stress-time data for (a) Test 1 and (b) Test 2 for the same specimen. The measured V^* values for both tests are shown in (c).

7.6 Discussion

The above results provide experimental evidence that a boundary migrating under an applied stress can effectively remove radiation damage, confirming previous models that proposed stress-assisted GB migration can lead to SFT absorption [152–154]. It has been well documented that GBs absorb radiation defects under static conditions (owing to the increased radiation tolerance in NC/UFG metals), but the above results unambiguously

highlight that a mechanical stress can activate an additional mechanism for damage removal. The percentage of the area that is cleared of defects depends on the time under tension and stress levels, with the cleaned area percentage typically ranging between 2-15%. For example, 2.6% of the gauge area is cleared of black-spot damage during the monotonic test shown in **Figure 68(a)** (total time under tension was 2.5 minutes) compared to the 14% that was cleaned after 51 minutes under tension in **Figure 70**. This indicates that pausing the loading prior to failure is necessary to allow for more time to promote and observe the stress-assisted GBM and defect clearing. In this study, defect-free regions are always observed in the wake of a migrating GB, indicating that a wide range of GB types can absorb radiation defects during migration. This newly documented mechanism implies that the deleterious effects of irradiation on the mechanical properties of NC and UFG metals can be further reduced thanks to an evolving network of migrating GBs when subject to mechanical loading. It is therefore crucial to quantify the effects of this healing mechanism on the evolving microstructure and resulting mechanical properties. To that end, our quantitative *in situ* TEM technique is ideally suited, as it allows for direct quantification of microstructure evolution as a result of stress-assisted GB migration with and without irradiation damage.

Using the GB velocity information shown in **Figure 71-Figure 73** to conclude on the effect of irradiation on GB mobility would require knowledge of the driving force for GBM (since velocity is the product of mobility and driving force), which is challenging to quantify accurately [97,193,194]. Qualitatively, we believe that the increased GB velocities for the as-deposited, unirradiated Au films are related to an increased driving force associated with the smaller grains that are present in the unirradiated as-deposited films.

As stress is applied, small grains deform elastically whereas larger grains deform plastically and can achieve lower stresses. The size-dependent yield stress has been proposed as a size-dependent driving force for grain coarsening and can explain the specific observation that large grains (with lower strain energy density) grow while small grains (higher strain energy density) shrink and disappear [102,195]. This explanation is consistent with our *in situ* TEM observations of “rapid” grain growth for the unirradiated Au films that is associated with the disappearance of the smaller grains. In addition, “rapid” grain growth is not observed for unirradiated, annealed Au specimens (350°C for 30 minutes) that do not have small grains (<50 nm) initially present (see **Figure 77(a)** and (c) and discussed in detail in CHAPTER 6), which is also consistent with the notion that small grains are associated with larger driving force for GBM (and therefore increased velocities). Given the absence of small (<50 nm) grains in irradiated samples and non-irradiated annealed samples, comparing the average GBM velocities (see **Figure 77(b)**) suggests that the irradiated GBs have lower mobilities (similar velocities, larger applied stresses for the irradiated specimen). Lower GB mobilities could be attributed to increased disorder of the GB plane as the GB absorbs the radiation defects that could make disconnection motion more “sluggish”, or that the GBs are being temporarily pinned by the radiation defects. Additional experiments, particularly on irradiated annealed specimens, are required to further investigate the effect of irradiation on GB mobility.

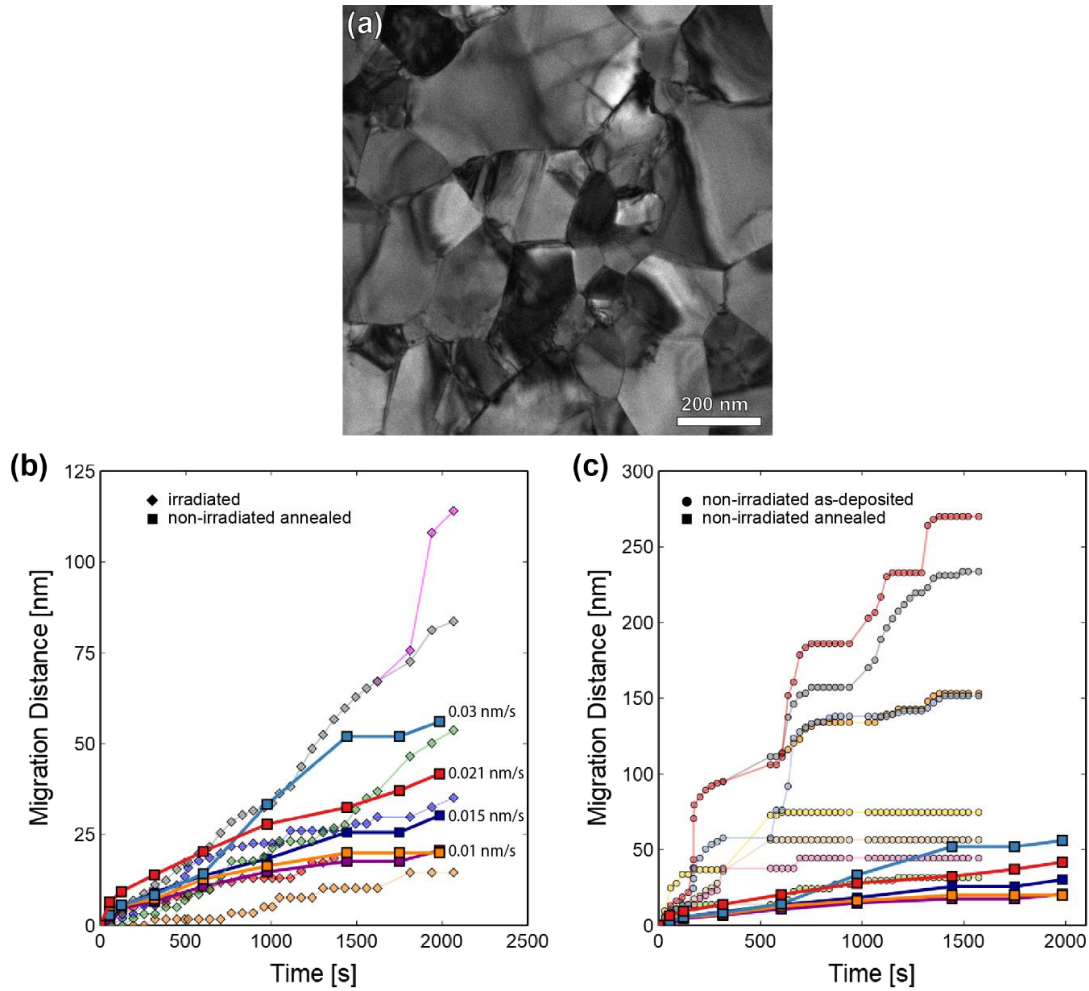


Figure 77 – GB migration data for migrating boundaries in a UFG annealed Au specimen. (a) TEM image of initial microstructure of UFG annealed Au. Migration behavior of annealed Au compared with the migrating boundaries in (b) irradiated specimen and (c) non-irradiated as-deposited.

It is important to note that the observed GBM behavior in the irradiated films exhibit similarities with dynamic recrystallization, which is typically observed in terms of newly nucleated (defect-free) grains growing and absorbing the neighboring grains that have a high number of defects [196]. However, we observe stress-assisted GBM with the unirradiated films, indicating that migration occurs without the additional defect-removal driving force and therefore it is likely that stress can also trigger GBM in irradiated films,

as suggested in [153]. Furthermore, in **Figure 71**, the grain that grew was not a small defect-free embryo, but instead had a high density of defects similar to the surrounding grains, which is inconsistent with recrystallization (nucleation of new grains).

7.7 Conclusion

This chapter provides striking evidence that stress-assisted GBM serves as an effective mechanism of defect removal in irradiated NC and UFG metals. This indicates that applying a small amount of stress sufficient enough to promote GBM could be implemented to facilitate ‘self-healing’ of irradiated materials. Future studies will involve characterizing the stress-assisted GBM in detail with particular interest in understanding how the irradiation-induced defects influence the GB structure and the GBM behavior in order to optimize the defect clearing capacity of NC and UFG metals.

CHAPTER 8.

INTERPRETATION OF MEASURED ACTIVATION VOLUME

8.1 Overview

The following chapter summarizes all the true V^* activation volume measurements made on the Au and Al specimens in this thesis. Then, Section 8.3.1 discusses computational techniques used by collaborators to relate the experimentally determined V^* values to individual deformation mechanisms. This is followed by a discussion on the observed trends in the measured V^* values and interpretation in terms of the effect of stress, grain size and irradiation.

8.2 Summary of All Activation Volume Values

8.2.1 Gold

Figure 78 provides a complete summary of all the true activation volume V^* measurements that have been made on the as-deposited, annealed (A350 and A700) and irradiated Au specimens. Across all specimen types, the true activation volume decreases with increasing stress (**Figure 78(a)**). This is true both for measurements made on an individual specimen and for the measurements across all specimens and stress levels. For the most part, the stress dependence appears to be minimized for measurements made for stress levels greater than 350 MPa. It is important to note that the measurements made with far-field $\sigma < 350$ MPa are prior to the specimen-level yielding (**Table 7, Figure 68**), however, the local stress is likely large enough to promote plastic deformation. At larger

stresses, it is likely that most or all of the grains have locally yielded and as such a further increase in stress will not have a significant impact on the stress-relaxation, which could explain the observed decrease in stress dependence at higher stresses. Additional experiments need to be completed on the A700 specimens in order to investigate a stress-dependence, since the current measurements were made at the same stress levels.

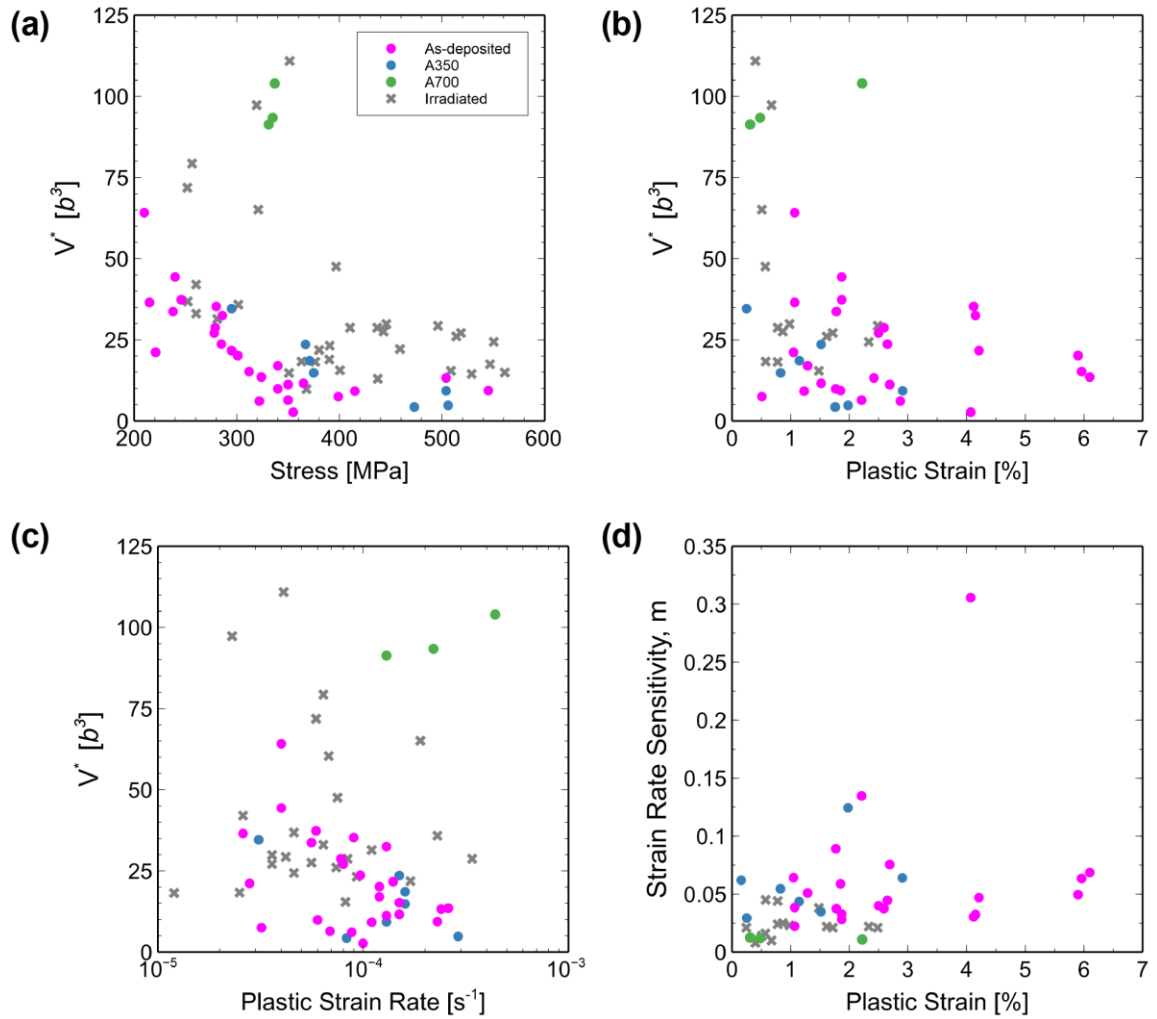


Figure 78 – All *in situ* true activation volume measurements made on UFG Au specimens (as-deposited, A350, A700, and irradiated). True activation volume V^* versus (a) the initial stress level, (b) plastic strain (%), and (c) plastic strain rate (s⁻¹) for each given relaxation segment. (d) strain rate sensitivity m calculated using V^* for each relaxation segment.

Due to the stress-dependence previously discussed, the averages have been separated into measurements made for stress levels either below or greater than 350 MPa. For $\sigma > 350$ MPa, the average V^* for the unirradiated specimens are as follows: $25 \pm 14b^3$ (as-deposited), $35b^3$ (A350), and $96 \pm 5b^3$ (A700). For the irradiated, the average $V^* \sim 57 \pm 28b^3$. The standard deviations for each are large due to the aforementioned stress dependence. For $\sigma > 350$ MPa, average V^* decreases to $9 \pm 3b^3$ (as-deposited), $13 \pm 7b^3$ (A350), and $22 \pm 8b^3$ (irradiated) (there are no available V^* measurements for A700 for this stress range).

V^* values decrease with increasing plastic strain level (**Figure 78(b)**). The reported strain value is defined as the initial plastic strain level at the beginning of each relaxation segment. It is likely that the observed stress- and plastic strain-dependence on V^* are related as in general the plastic strain increases with increasing stress. However, it is useful to look at the stress and plastic strain separately as different specimens can be at different plastic deformation (plastic strain) levels at the same stress level. For example, the irradiated specimens are stronger and will yield at higher stresses, so the plastic strain for the irradiated specimens will be lower than that of the as-deposited for the same stress level. In fact, all of the irradiated measurements are below $\varepsilon_p = 3\%$ even though the majority of the measurements were done at larger stresses ($\sigma > 350$ MPa) compared to the other Au specimen microstructures.

There is a slight decrease in V^* with increasing plastic strain rate for the as-deposited, A350 and irradiated specimens (**Figure 78(c)**), however, the trend is not as significant as with stress and plastic strain. Once again, the reported plastic strain rate

values are the initial plastic strain rate for a given relaxation segment. The A700 measurements do not follow this trend but more data points should be collected to confirm this.

The physical activation volume values can be directly related to the strain rate sensitivity m using the equation below:

$$m = \frac{\sqrt{3}kT}{\sigma V^*} \quad (41)$$

The strain rate sensitivity values are shown in **Figure 78(d)**. The average m values across all stress levels for each specimen types are summarized in **Table 9**. Although there is scatter in the data leading to large standard deviations, qualitatively the strain rate sensitivity increases going from A700 > irradiated > A350 > as-deposited specimens. This confirms that strain rate sensitivity increases with decreasing grains size. It also appears that m increases with increasing plastic strain level.

Table 9 – Average strain rate sensitivity values determined using V^* for all UFG Au specimens.

Specimen-type	m
As-deposited (Au)	0.067 ± 0.059
A350 (Au)	0.059 ± 0.029
A700 (Au)	0.012 ± 0.001
Irradiated (Au)	0.033 ± 0.018

In summary, there is minimal difference when comparing V^* values of the as-deposited and A350 specimens. However, V^* is consistently larger for the irradiated specimens and even larger for the A700 specimens, indicating that both radiation damage and grain size have an effect on V^* . Strain rate sensitivity m is also observed to increase

from 0.012 (A700), 0.033 (irradiated), 0.059 (A350) to 0.067 (as-deposited) indicating a variation in the strain rate sensitivity of the different microstructures.

8.2.2 Aluminium

All of the *in situ* true activation volume V^* measurements for the Al specimens (Al-100 and Al-200) are shown in **Figure 79**. Similar to the Au specimens, the measurements show a strong stress dependence of decreasing V^* with increasing stress (**Figure 79(a)**). This is particularly true for the Al-200 specimens where V^* decrease from $\sim 50b^3$ to $\sim 12b^3$ as the stress increases from 190 to 340 MPa. Commenting on the stress-dependence of the Al-100 specimens is more difficult as the available measurements are only made at higher stress ($\sigma > 350$ MPa) which could indicate that the stress-dependence is already minimized (similar to as discussed for the Au specimens in Section 8.2.1). Average V^* for the Al-200 specimens is $22 \pm 11b^3$ for the stress range $193 < \sigma < 341$ MPa. This decreases to an average $V^* \sim 6 \pm 2b^3$ for the Al-100 specimens ($368 < \sigma < 454$ MPa).

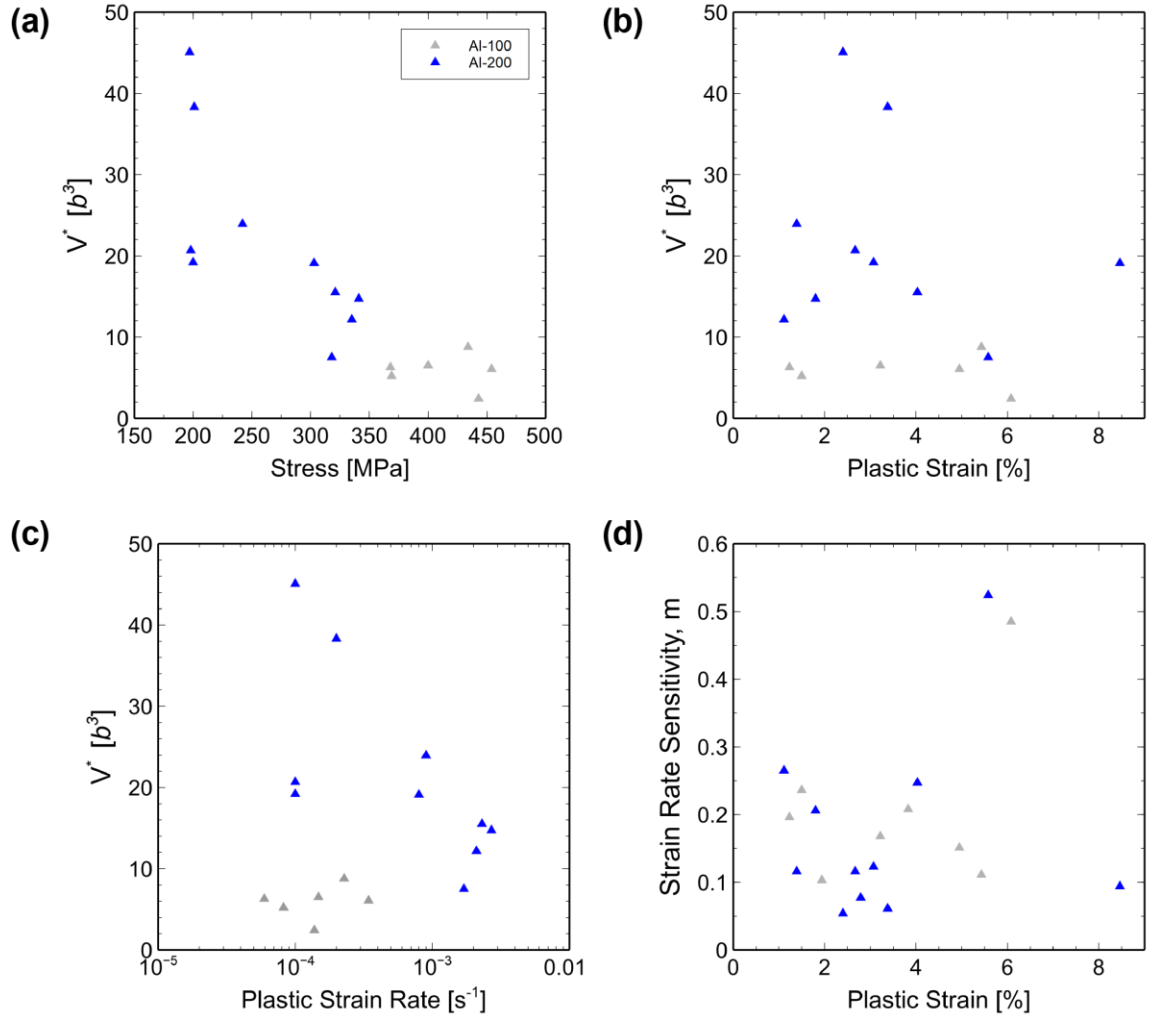


Figure 79 – All *in situ* V^* measurements made on NC Al specimens (Al-100 and Al-200). True activation volume V^* versus (a) the initial stress level, (b) plastic strain (%), and (c) plastic strain rate (s^{-1}) for each given relaxation segment. (d) strain rate sensitivity m calculated using V^* for each relaxation segment.

Figure 79(b) show V^* plotted against the initial plastic strain level for each relaxation segment. Since there is overlap between Al-100 and Al-200 plastic strain levels, comparing the activation volume values indicate that V^* tends to be larger for Al-200 for the same deformation (plastic strain) level. The V^* values versus initial plastic strain rate are shown in **Figure 79(c)**. For the Al-200 specimens, the activation volume values decrease with increasing plastic strain rate. This could be related to the stress dependence

as increasing stress will promote faster plastic deformation. The activation volume values for the Al-100 specimens are consistent across all plastic strain rate levels. The strain rate sensitivity m related to V^* (using Eqn. (41)) is shown in **Figure 79(d)**. Values range from 0.10 -0.48 for Al-100 and 0.05-0.52 for Al-200.

Table 10 provides a summary of V^* values for all UFG Au (as-deposited, A350, A700, and irradiated) and NC Al (Al-100 and Al-200) specimen types. This table illustrates that the physical activation volume values are found to vary across metal, microstructure (grain size or radiation damage) and stress level.

Table 10 – Summary of all True V^* values for the as-deposited, annealed (A350 and A700), and irradiated UFG Au and NC Al specimens.

Specimen-type	d_{avg} (nm)	Average $V^*(b^3)$	
		$\sigma < 350$ MPa	$\sigma > 350$ MPa
As-deposited (Au)	142	25 ± 14	9 ± 3
A350 (Au)	287	35	13 ± 7
A700 (Au)	768	96 ± 5	–
Irradiated (Au)	189	57 ± 28	22 ± 8
Al-100 (Al)	55	–	6 ± 2
Al-200 (Al)	93	22 ± 11	–

8.3 Relating Experimentally Measured V^* to Deformation Mechanisms

Activation volume is a signature parameter associated with a deformation mechanism and the ultimate goal is to relate the experimentally measured (sample-level) V^* values to the rate-controlling deformation mechanisms. This requires additional approaches, such as computational techniques. Atomistic models benefit from the ability to analyze an individual mechanism at one time to determine the expected V^* for that given

mechanisms. These values can be compared to the experimentally measured V^* to predict the active rate-controlling deformation mechanisms. The following section outlines modeling work done by collaborators to help correlate the experimentally measured V^* to deformation mechanisms (see Ref [95] for more details).

8.3.1 Atomistic Modeling

Activation volume is the derivative of activation energy with respect to stress ($V^* = dQ/d\sigma$) and characterizes rate-sensitivity. The stress dependence of activation energy can be calculated from the nudge elastic band (NEB) method, which is a chain-of-states approach to find the minimum energy path (MEP) on the potential energy surface (PES) [197,198]. For each mechanism, there are configurations that are a local minimum, local maximum, or saddle point on the PES and the MEP is the lowest energy path connecting two neighboring local minimum configurations. The activation energy barrier (ΔG) is given by the maximum on the MEP which occurs at the saddle point. This method works well for highly localized activation processes, however it is inefficient for defect nucleation processes in which the local minimum is far away from the initial state. A modified free-end NEB (FENEB) method is used to reduce the MEP length by removing the constraint of the final state and instead allow it to move freely on an energy iso-surface close to the initial state [199]. For more details on the computational methods see Refs. [95,198].

This approach has been performed for candidate rate-controlling dislocation process at different stress levels in order to calculate the activation energy stress dependence and V^* . This has been done for two mechanisms: dislocation nucleation from the free-surface and from a GB. These mechanisms were chosen since dislocation

nucleation is widely seen experimentally. The simulation setup for GB dislocation nucleation is shown in **Figure 80**. The bicrystal contains a symmetric tilt GB (similar to the GBs observed in the UFG Au specimens in CHAPTER 5) with the dimensions of $16.3 \times 32.8 \times 0.6$ nm and contains 226,260 atoms. A periodic boundary condition is imposed along the loading direct of $[\bar{4}\bar{1}5]$ and the two side surfaces of (111) and $(2\bar{3}1)$ are traction free. **Figure 80(b)** shows a typical “free-end” configuration in an FENEB calculation. The MEPs of GB dislocation nucleation are determined by FENEB calculations at different applied tensile stresses.

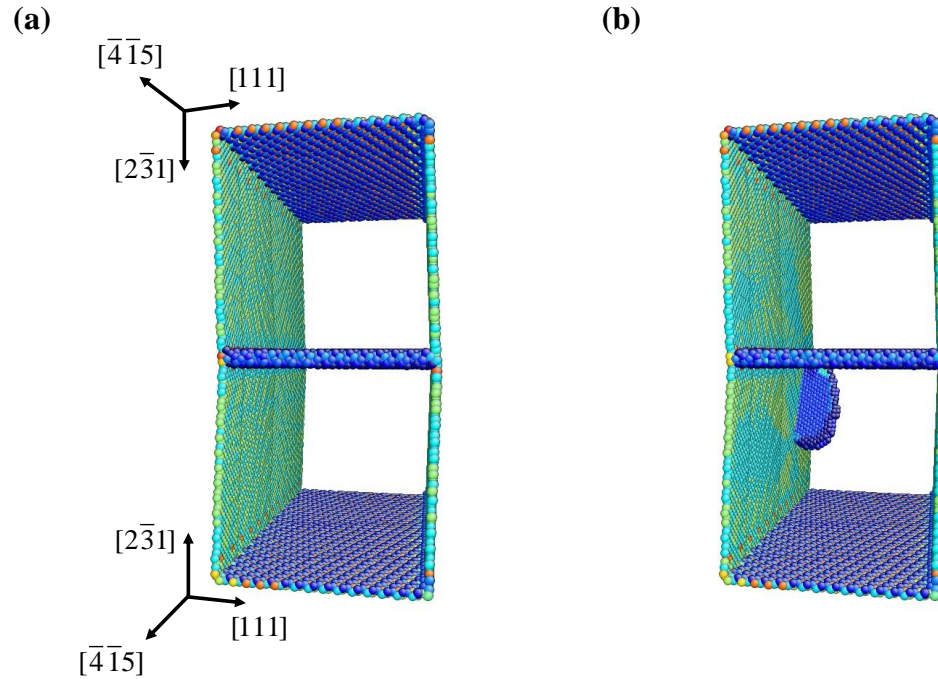


Figure 80 – Atomistic FENEB simulation setup for GB dislocation nucleation in an Au bicrystal. (a) An initial defect-free configuration containing a symmetric tilt GB. The tensile load is applied on $[\bar{4}\bar{1}5]$ direction. (b) A typical free-end state with an embryonic partial dislocation loop at the intersection between the GB and surface (from Ref. [95]).

The FENEB results for the GB dislocation nucleation in a bi-crystal Au nanowire is shown in **Figure 81**. The MEPs at different resolved shear stresses are shown in **Figure 81(a)** and illustrate how the energy barrier decreases with increasing stress. The atomistic configurations for point 1, 2, and 3 on the 827 MPa MEP are shown in **Figure 81(b)**. The maximum energy (saddle-point) state corresponds to dislocation nucleation (b3). The elongated structure seen in (b4) is due to different glide resistance to the loop intersection points at the GB and grain surface. The stress-dependent activation energy is shown in **Figure 81(c)**. For laboratory strain rates such as 10^{-2}s^{-1} , the activation energy is about 0.7 eV ($\sim 30k_B T$). At this activation energy, the stress required for dislocation nucleation is $\tau = 0.93$ GPa. **Figure 81(d)** shows the derivative of the curve in **Figure 81(c)**, which results in the activation volume vs. τ curve. At $\tau = 0.93$ GPa (0.7eV), $V^* \sim 50b^3$ for GB dislocation nucleation. This simulation was also completed for an Al bi-crystal which yielded $V^* \sim 16b^3$ for GB dislocation nucleation.

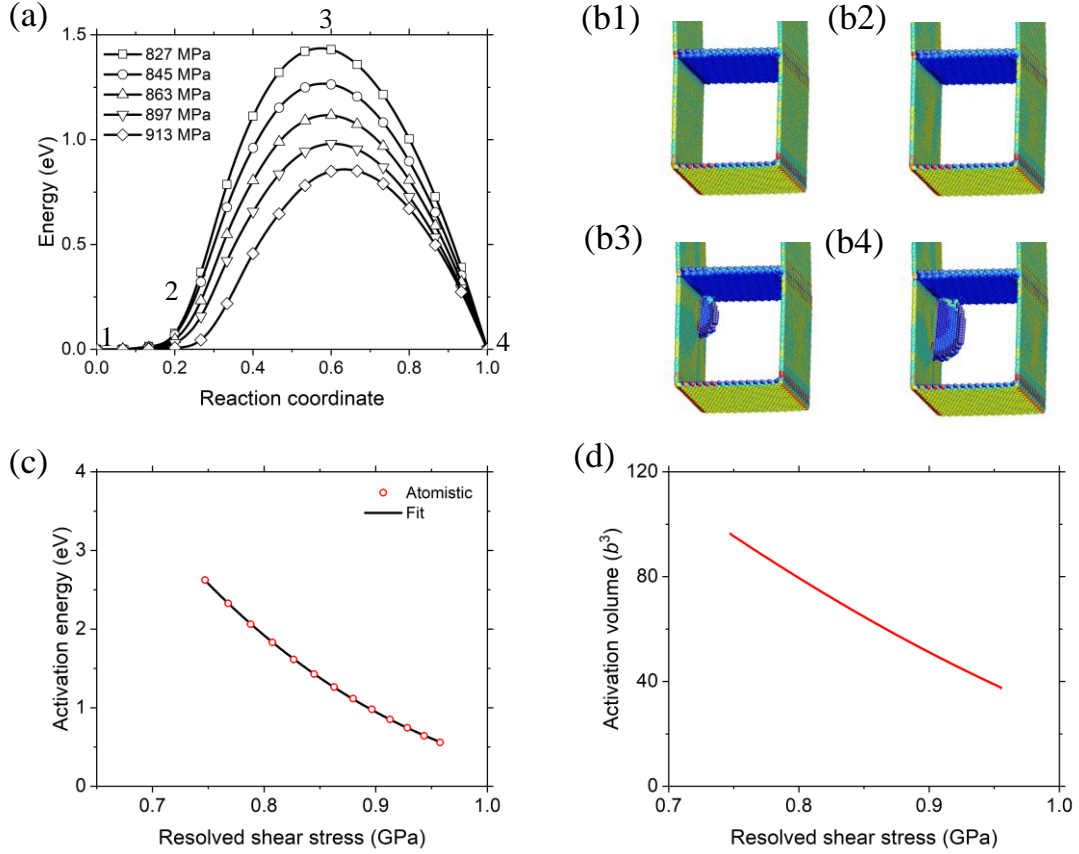


Figure 81 – FENEb results for GB dislocation nucleation in an Au bi-crystal. (a) MEPs at different applied resolved shear stresses, (b1-b4) Atomic configurations (marked in (a)), (c) Activation energy as a function of resolved shear stress. (d) Activation volume as a function of resolved shear stress.

In addition to GB dislocation nucleation, the simulations were completed for surface dislocation nucleation which resulted in estimated activation values of $V^* \sim 20b^3$ for both Au ($\tau = 0.97$ GPa) and Al ($\tau = 1.7$ GPa). Partial dislocation nucleation was also studied and resulted in $V^* \sim 31b^3$ for free-surface nucleation and $V^* \sim 52b^3$ for nucleation from GB in Au [198]. This value decreased to $V^* \sim 16b^3$ (free-surface nucleation) in Al. The high stacking fault energy of Al further increases the stress needed to nucleate a partial dislocation which contributes to the smaller V^* values compared to Au. In addition to displacive-type mechanisms, diffusive-type mechanisms have been investigated.

Additional GB processes could include shearing of a patch of GB atoms or atomic diffusion [26,88,92]. The FENEB calculations indicate that these mechanisms would have $V^* \sim 20b^3$ and $\sim 0.1b^3$, respectively. Additional simulations have been completed on the non-conservative motion of GB dislocations/disconnections, such as through a process involving climb. This is required if a GB dislocation/disconnection has a Burgers vector component perpendicular to the GB. A recent *in situ* HRTEM study has suggested that such mechanisms are active under a high applied stress [184]. These calculations resulted in $V^* \sim 1.5b^3$ for the climb of GB dislocations. All of the calculated V^* values for the studied mechanisms are summarized in **Table 11**.

Table 11 – A summary of V^* values calculated from the FENEB models for different deformation mechanism.

Deformation Mechanism	$V(b^3)$
Surface dislocation nucleation	20
Dislocation nucleation at GB	16-50
Surface partial dislocation nucleation	16-31
Partial dislocation nucleation at GB	52
Shearing of GB atoms	20
Atomic diffusion	0.1
Disconnection climb	1.5

8.4 Discussion

In order to relate the experimental sample-level V^* measurements to V^* determined from the atomistic models, the differences between both approaches must be considered. First, the experimental specimens have larger grain sizes (55-768 nm) compared to the cell size in the atomistic models (<10 nm). One can evoke the Conrad model to understand the grain size effect on V^* (Section 1.4.3 and shown below) [26,86].

$$\frac{1}{V^*} = \frac{1}{V_i^*} + \frac{M^2 \mu b}{K_{H-P} \sqrt{d}} \frac{1}{V_c^*} \quad (14)$$

This model is useful in comparing the experimentally measured V^* with the V_c determined for individual mechanisms using the atomistic models. The key component of this model is connecting the applied far-field stress to an amplified local stress at the GB where the mechanism is activated.

In general, the model states that the sample-level V^* will increase with increasing grain size d . Since the atomistic models are completed for the lower limit of grain size and the applied stress is roughly equal to the local stress (i.e. no dislocation pile-up), the activation volume values shown in **Table 11** are the lower limit values. If we extrapolate these to account for larger grains, these values would be expected to scale to larger values. For example, the values in **Table 11** for displacive-type mechanisms ($V_c \sim 16 - 51b^3$) are the lower limit values for these mechanisms and would be extrapolated to larger values for a more accurate comparison to the experimentally measured sample-level V^* . This indicates that the measured sample-level V^* values for as-deposited Au, A350, Al-100 and Al-200 cannot be attributed to displacive mechanisms since the experimental values ($V^* = 22 - 35b^3$) are within the range of $V_c \sim 16 - 51b^3$, keeping in mind the atomistic values are the lower limit and will only increase if the grain size is increased to match that of the experimental condition. However, it is possible that the larger experimentally measured V^* for the A700 ($95b^3$) and irradiated Au ($57b^3$) could be attributed to displacive type mechanisms at the GB.

Since displacive-type mechanisms at the GB cannot account for the low sample-level V^* measured for all the specimens, this indicates that there are alternative mechanisms active. This would lead to a modified Conrad's model to account for additional competing rate-controlling processes at the GB:

$$\frac{1}{V^*} = \frac{1}{V_i^*} + \frac{M^2 \mu b}{K_{GB-I} \sqrt{d}} \frac{1}{V_{GB-I}^*} + \frac{M^2 \mu b}{K_{GB-II} \sqrt{d}} \frac{1}{V_{GB-II}^*} \quad (42)$$

In the above equation, the V_c^* term from Eqn.(14) has been divided into two components (V_{GB-I}^* , V_{GB-II}^*) corresponding to different types of intergranular processes. Each of these components has their respective Hall-Petch coefficient (K_{GB-I} , K_{GB-II}) that depends on the critical local stress at the GB that is responsible for triggering the rate-controlling process. Competing rate-controlling mechanisms could include diffusive-type mechanisms such as disconnection climb. These mechanisms would be expected to have lower $V_{GB-II}^* \sim 1b^3$ that even when extrapolated to larger grain sizes, could help account for the lower V^* experimentally measured.

In summary, it is not likely that displacive-type mechanism at the GB (i.e. dislocation nucleation) can be the sole contributor to sample-level experimentally determined V^* values for all of the specimen types. Instead, other diffusive-type mechanisms are also likely active and important in controlling the rate-sensitivity.

8.4.1 General Trends in Activation Volume

8.4.1.1 Stress

A consistent trend seen throughout all specimens tested is that the measured activation volume V^* decreases with increasing applied stress. This is true both for measurements made on the same specimen and for different specimens tested at different stress levels. In all specimens, the stress dependence is minimized once the stress reaches higher values ($\sigma > 350$ MPa).

Each deformation mechanism has a unique stress-dependent activation energy curve and for a given mechanisms, the slope of these curves (V^*) decreases with increasing stress (**Figure 82**). Increasing the applied stress will increase the thermodynamic driving force, reduce the energy barrier, and result in an increased rate of a thermally activated process [200]. This can be rationalized in terms of the applied stress providing more mechanical work which results in a lower activation energy ΔG required to overcoming the local barrier. It is true that V^* generally decreases with increasing stress, however, in most cases V^* is usually treated as a constant when the rate or stress change is not large. The fact that there is a strong V^* stress dependence indicates that in NC and UFG metals, increasing the stress by 100-300 MPa is significant enough to result in a change in V^* . Another possible explanation for the observed stress effect could be that the higher stresses promote alternative deformation mechanisms that have different V^* values. In **Figure 82**, there is a ‘cross-over’ point in which the curves for the two mechanisms intersect. To the left of the cross-over, mechanism #1 (with V_1^*) will have a lower energy barrier than mechanism #2. However, at higher stresses the energy barrier for mechanisms #2 is less than #1. This results in the switching of the rate-controlling mechanism at different stress levels.

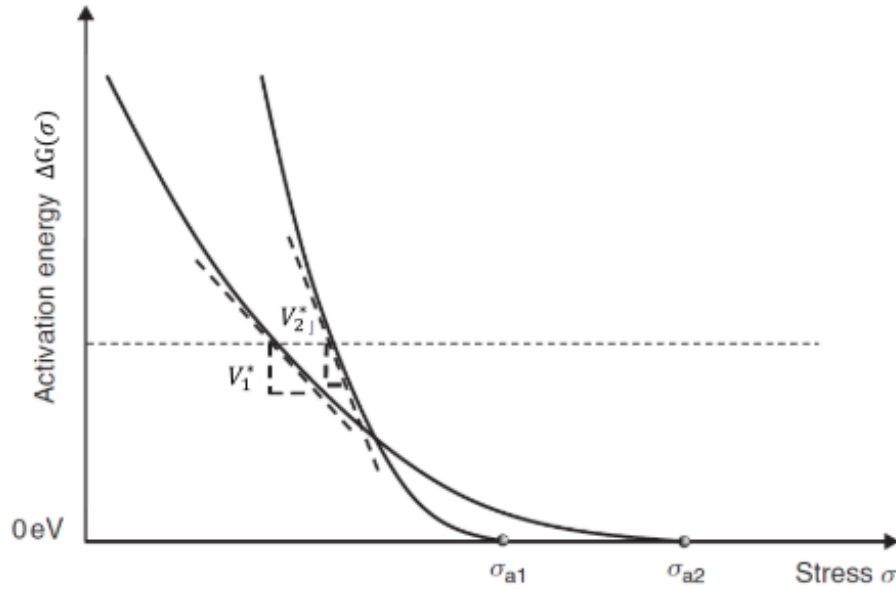


Figure 82 – Schematic of the stress-dependent activation energy for two competing thermally activated processes [200].

Along similar lines, it could be possible that plastic deformation transforms the microstructure to promote alternative deformation mechanisms. For example, stress-assisted grain growth could lead to grains that are larger enough to promote intragranular dislocation glide at a later stage in the deformation. Theoretically, this could cause a switch in rate-controlling deformation mechanisms from intergranular-based to transgranular. A similar phenomenon could occur in the irradiated Au since the microstructure is cleaned of radiation damage from stress-assisted GB migration. However, in both cases it is unlikely that a large enough proportion of the specimen gauge is transformed to an extreme enough degree to lead to a measurable difference in V^* . In fact, this is confirmed by the data shown in **Figure 76** in which successive experiments were completed on an irradiated Au specimen to investigate if the evolving microstructure leads to the decrease in V^* . The results show that in both Test 1 and Test 2 V^* values are higher at lower stresses and

proceed to decrease at higher stresses, indicating that the decrease is a stress effect and not an effect of the evolving microstructure.

A final proposed explanation for the observed V^* stress-dependence is related to the grain size distribution. At lower stress levels, larger grains dominate plastic deformation and therefore the stress-relaxation. These intragranular mechanism have large V^* due to the Conrad's model. At larger applied stresses, smaller grains will contribute more to the plastic deformation, for which V^* is lower since the grain size is smaller. This indicates that a weighted average between the V^* for large and small grains could explain the trend, even if the same mechanism dictates plastic deformation.

8.4.1.2 Grain size

Another consistent trend observed in the V^* values is that V^* decreases with decreasing grain size for the same metal. For example, the average V^* increases from $25b^3$ to $96b^3$ as the grain size increases from 142 to 768 nm in the Au specimens within the same stress range. Similarly, V^* decreases from $22b^3$ to $6b^3$ as the grain size in Al decreases from 93 to 55 nm. There are a few proposed explanations for this trend. The first follows the Conrad model, which is shown here again:

$$\frac{1}{V^*} = \frac{1}{V_i^*} + \frac{M^2 \mu b}{K_{H-P} \sqrt{d}} \frac{1}{V_c^*} \quad (14)$$

First, as grain size decreases the V_i^* term is negligible since intragranular mechanisms such as dislocation forest interactions do not occur in small grains. Second, as d decreases

further, V^* decreases due to the increasing $\frac{M^2 \mu b}{K_H - P \sqrt{d}}$ term. This means that for the same mechanism (with V_c^*), decreasing the grain size will lead to a smaller sample-level V^* .

A change in grain size could also signify a change in deformation mechanisms. For example, the transition from $V^* \sim 25b^3$ for a grain size of 142 nm to $V^* \sim 96b^3$ for the average grain size of 768 nm could indicate that a switch from a V_c^* to V_i^* dominated mechanisms. For the A700 specimens, it is possible that the grains are now large enough to support conventional transgranular dislocation mechanisms that have $V_i^* \sim 1000b^3$, leading to an overall increase in the sample-level V^* .

8.4.1.3 Irradiation

The sample-level physical activation volume V^* has been measured for both non-irradiated and irradiated specimens in order to investigate the effect of radiation damage on the rate-controlling deformation mechanisms. Although GBM clears grains of defects, the amount of “cleaned” microstructure (< 15%) is not enough to obtain unchanged activation volume after irradiation. In fact, V^* is consistently larger for the irradiated films compared to the non-irradiated films. For example, for stresses $\sigma > 400$ MPa, the average V^* increases from $9 \pm 3 b^3$ (non-irradiated) to an average of $22 \pm 6 b^3$ in the irradiated films. These results provide evidence that the radiation defects have an influence on the rate-controlling deformation mechanisms. The atomistic study provided in Section 8.3.1 and use of an existing model to account for the grain size dependence of activation volume have suggested that the measured low activation volume for the non-irradiated Au films is mainly attributed to GB mechanisms that involve diffusive processes driven by local high stresses, such as disconnection climb within the GBs [95]. As such, an increase in V^* could

indicate a change in rate-controlling mechanism from GB mechanisms (intergranular) to mechanisms within the grain (intragrain), or a change in the relative contributions of these two mechanisms. The activation volume within grains can be estimated using the following scaling equation,

$$V_i^* = lb^2 \quad (43)$$

where l is the spacing between obstacles and b is the Burgers vector length [201]. For non-irradiated Au films, V_i is expected to be large ($\sim 500 b^3$) and to not significantly affect the measured sample-level activation volume. This is not the case for irradiated Au films. Using the estimated defect-spacing in these films (15 nm) and the Burgers vector of Au, V_i^* is $\sim 52 b^3$. This is larger than the measured sample-level V^* of $21 \pm 6 b^3$, which is qualitatively consistent with changing the rate-controlling mechanism from GB-based (with activation volume $< 10 b^3$) to intragrain mechanism ($V_i^* \sim 52 b^3$). This implies that the rate-controlling mechanism in the irradiated film is likely dislocation pinning/depinning within grains.

8.4.1.4 Strain rate sensitivity

The physical activation volume V^* can be related to the strain rate sensitivity and both help provide a link between experimentally measurable parameters describing plastic flow characteristics and the underlying deformation mechanisms. For all Au and Al specimens, the strain rate sensitivity was found to decrease with increasing grain size. For example, m increased from 0.012 to 0.067 as the grain size in Au decreased from 768 to 142 nm. This implies that the strain rate sensitivity increases with decreasing grain size,

which is consistent with previous reports [34–37]. The full range of values determined for the Au specimens are 0.013-0.067, which are similar to other studies that have been conducted with values typically ranging from 0.015-0.103 [35,37,39,40,42,43]. The strain rate sensitivity for the Al specimens range from 0.05-0.52 (Al-200) and 0.10-0.48 (Al-100). These are larger than those in Au, possibility indicated the NC Al is more strain rate sensitive due to the smaller grain sizes.

8.4.1.5 Metal type

There is not a drastic difference in measured V^* values across Au and Al specimens, excluding the results from the irradiated and A700 Au specimens. For the as-deposited Au, $V^* \sim 25b^3$ which is similar to the values for the Al-200 specimens ($V^* \sim 22b^3$) for the same stress range ($\sigma < 350$ MPa). The averages are similar ($9b^3$ and $6b^3$) for $\sigma > 350$ MPa. Based solely on the grain size argument (decreasing V^* for smaller grain size), one would expect V^* would be smaller for the Al specimens since the grain size is smaller than all of the Au specimens. This trend is not observed which indicates that comparing V^* values across different metal type is not a 1-to-1 comparison. There are additional differences between the Au and Al specimens, including the film texture, stacking fault energy, shear modulus, etc. The Au specimens are $\langle 111 \rangle$ textured which results in a large proportion of the GBs being tilt boundaries and $\Sigma 3$ twin boundaries. The Al specimens are randomly textured and as a result the GBs are all random HAGB. The GB structure undoubtedly has an impact on the behavior of deformation mechanism at the GB, however, comparing Au and Al is not an optimal way to investigate the texture/GB structure effect.

8.5 Conclusion

Results from the *in situ* TEM activation volume V^* measurements have been summarized and discussed in terms of candidate rate-controlling active deformation mechanisms. Atomistic models have been performed to predict the expected V^* for individual mechanisms. By invoking the Conrad model, it is postulated that the experimentally measured V^* for both Au and Al is likely a result of a competition between displacive- and diffusive-type deformation mechanisms. The strongest trends observed in the measured sample-level V^* values are a decrease in V^* with increasing stress and decreasing grain size. Alternative interpretations for the trends were discussed. *In situ* TEM observations with quantification of plastic flow characteristics through V^* combined with atomistic modeling is necessary to fully understand the active plastic deformation mechanisms that control mechanical properties in NC and UFG metal thin films.

CHAPTER 9. CONCLUSIONS

The plastic deformation mechanisms of UFG Au and NC Al thin films were investigated using an *in situ* TEM MEMS-based nanomechanical testing technique. These investigations revealed multiple active deformation mechanisms including both dislocation- and GB-based. The true activation volume V^* was measured for all specimens and ranged from $9 - 95b^3$ (UFG Au) and $6 - 22b^3$ (NC Al) across all stress levels. A specific mechanisms (stress-assisted GBM) was analyzed in detail for the UFG Au, including irradiated specimens. Below presents a list of the major conclusions and significant contributions.

1. **Improved the existing *in situ* TEM MEMS-based nanomechanical technique by implementing image-based sensing to replace the capacitive electrical-based sensing.** This significantly increases the yield of successful experiments and improves the sensitivity of the technique. This allows for more reliable and precise stress and strain measurements and with a real-time output, allows for experiments to be conducted in intentional manner (i.e. stress-relaxation/ V^* measurements can be performed at pre-determined stress levels). The increased sensitivity allows for small stress-relaxation levels to be measured which expands the limits of the current electrical-based technique.
2. **Determined that the electron beam increases local atomic fluctuation during *in situ* TEM straining and leads to increased plastic deformation and a decrease in measured activation volume V^* .** *In situ* TEM straining experiments were conducted in either beam-off and beam-on conditions and it was found that

increased plastic deformation occurred under beam-on condition. For NC Al, this resulted in increased failure strain, a 3x increase in plastic strain rate, and a decrease in true activation volume V^* from 28 to $21b^3$. Similar results (yet to a lesser extent) were seen for the experiments conducted on UFG Au, including a 1.2x increase in plastic strain rate with e-beam exposure. The e-beam effects were seen at TEM beam accelerating voltages of 80 and 300kV which suggests that knock-on damage is not the source for the observed e-beam effect (since 80kV is below the knock-on threshold for both Al and Au). Instead, the experiments suggest that the e-beam causes additional thermal activation that accelerates the stress-driven, thermally-activation plastic deformation. The additional thermal activation reduces the barrier to plastic deformation and leads to the change in the mechanical properties across the beam-on and -off conditions, but does not change the active deformation mechanisms themselves. These results show that there is non-negligible e-beam effect in different materials that must be considered for accurate interpretation of *in situ* experiment results.

3. **Measured activation volume V^* across many specimens of different microstructures and stress levels and interpreted values in context of atomistic simulations and existing models.** True activation volume V^* calculations were performed for all of the UFG Au and NC Al specimen variations. For Au, it was found that V^* increases from $25 \pm 14b^3$ (as-deposited), to $35b^3$ (A350), and finally to $96 \pm 5b^3$ (A700) as the grain size increases from 142, 287, and 768 nm respectively. Average V^* for the Al-200 specimens was $22 \pm 11b^3$ which decreased to $V^* \sim 6 \pm 2b^3$ for the Al-100 specimens. These were compared with

MD simulations of displacive-type mechanisms (i.e. dislocation nucleation) which indicated that the measured sample-level V^* values for as-deposited Au, A350, Al-100 and Al-200 cannot be attributed to displacive mechanisms only. By invoking the Conrad model, it is proposed that the experimentally measured V^* for both Au and Al is likely a result of a competition between displacive- and diffusive-type deformation mechanisms. For all of the specimens, there was a strong stress-dependence of decreasing V^* with increasing stress. Multiple explanations for this trend were discussed, including the possibility that the active deformation mechanisms change at larger stress levels resulting in a change in V^* .

4. **Demonstrated that stress-assisted GBM is an active healing mechanism in irradiated UFG gold thin films through direct observation of migrating GBs absorbing irradiation-induced defects under stress.** In many cases, the defect-free regions can support prolonged dislocation glide and dislocation-dislocation interactions. Such mechanisms have only been predicted by MD simulations and as such the results in this Thesis are the first ever confirmation of this healing mechanism. Results also show a clear difference in GBM behavior with irradiated specimens exhibiting slower, but steady GBM whereas non-irradiated specimens experience rapid bursts in migration followed by stagnation. The difference in observed GBM across irradiated and unirradiated films was attributed to an increased driving force for small grain removal due to size-dependent yielding leading to variations in strain energy density across different grains (i.e. small grains do not yield and thus have larger strain energy and are removed). Comparing the GBM behavior of irradiated films with unirradiated, annealed Au (with no small

grains remaining after annealing) suggests that irradiated GBs have lower mobilities due to the similar measured velocities at larger applied stress. Activation volume V^* was also measured to increase from $9 \pm 3 b^3$ to an average of $22 \pm 6 b^3$ after irradiation ($\sigma > 400$ MPa). This provides evidence that the radiation defects have an influence on the rate-controlling deformation mechanisms and could indicate a change in rate-controlling mechanism from GB mechanisms (intergranular) to mechanisms within the grain (intragrain), or a change in the relative contributions of these two mechanisms.

5. **Illustrated that local grain size is a dominant factor dictating stress-assisted GBM and grain growth in UFG Au specimens.** *In situ* TEM straining experiments have been conducted in conjunction with orientation mapping for detailed analysis of stress-assisted GBM/grain growth for as-deposited and A350 Au specimens. In the as-deposited films, GBM appears to be largely dominated by the removal of the small grains ($d < 50$ nm) and is clearly illustrated using the initial orientation map to identify the microstructure that is removed upon straining. In the annealed films, most of the small grains are removed during the heat treatment and are not present to participate in the deformation. The few remaining small grains are removed upon straining but there are also many occurrences of stress-assisted GBM not specifically related to small grain removal. This GBM was analyzed in context of microstructural features such as GB character, grain orientation, Schmid factor, and GB trace angle with respect to the loading direction. There are no trends observed for any of the aforementioned features, suggesting a complicated interplay between driving forces and microstructures. It is postulated

that the consistent small grain removal is due to an increase in GBM driving force related to a reduction in strain energy density. Grain size-dependent yielding leads to yielded large grains and elastically-deformed small grains and as a result, the large grains (low strain energy density) will grow at the expense of the small grains (with high strain energy density).

9.1 Recommendation for Future Work

Although the technique used in this thesis provided a wealth of meaningful results, there are always avenues for improvement and the follow section provides a few examples. For the technique itself, additional characterization of the image-based MEMS design is required to understand the behavior during a stress-relaxation segment. Preliminary results have suggested that the thermal actuator is not perfectly stable during a relaxation and that X_A is not constant but actually slightly increases (**Figure 13**). This compromises the assumption made during a relaxation segment that the applied displacement is constant ($X_A = X_S + X_{LS} = \text{constant}$). This implies that it is likely the stress-relaxation that is currently measured is actually underestimating the true amount of plastic deformation in the specimen leading to stress-relaxation. To minimize this, stress-relaxation segments should be performed at lower input voltage V_{in} levels as the drift may increase with increasing voltage. It would be preferred if a feedback loop could be implemented to micro-adjust the V_{in} as need to ensure X_A remains constant during a pause segment.

For some of the results presented in this thesis, an orientation map was collected only prior to the experiment. It would significantly improve the stress-assisted GBM analysis (both accuracy and time efficiency) if an orientation map was collected post-straining. This

would eliminate ambiguity related to contrast in the TEM required to identify GBs and/or dislocations (i.e. some GBs are invisible in the TEM at a given stage tilt). It would also provide additional information on microstructure evolution such as a potential texture development during straining. Along the same lines, more focus should be placed on studying the migration behavior of TJs in addition to GBs. It is possible that in NC and UFG metals the behavior of the TJs dominate the evolution of the GB network and could explain why no trends were seen in Section 6.5.1.

There are also additional experimental approaches that could be utilized to address some of the remaining open questions related to the project. First, it remains unclear how stress-assisted GBM contributes to plastic deformation and activation volume V^* . Does GBM contribute to plastic strain and accommodate plastic deformation? Or is it a by-product of other mechanisms? The activation volume V^* results and discussion presented in CHAPTER 8 suggest that there is a competition between intragranular and intergranular mechanisms. To investigate this competition specifically, it would be helpful to engineer the GBs to be more stable under mechanical loading to effectively shut down their involvement in the deformation (and V^* measurement). This could be done by studying the large-grained Au specimens, since as grain size increases it is likely that GBs will have decreasing involvement in deformation. Another approach could be to dope the specimens with impurities to effectively pin the GBs [181,202]. This would require altering the fabrication deposition steps and ideally, this would occur without other significant microstructural changes (grain size, texture). However, introducing a different material would likely lead to additional factors to consider when measuring V^* that would make the comparison difficult.

Second, many of the V^* measurements made on a given specimen were done successively throughout the same experiment as plastic strain accumulates and it remains unclear how the loading history influences the measured V^* . To investigate this, it is recommended that multiple experiments are conducted such that the initial stress-relaxation segment for each specimen is performed at a different pre-determined stress level. This would ensure that there are V^* measurements at different stress levels with minimized plastic strain accumulation. These experiments would also help investigate the V^* stress-dependence as well. Along similar lines, additional experiments should be conducted on the A700 Au specimens for a wider stress range to determine if there is a similar stress-dependence on V^* measurements.

REFERENCES

- [1] K. Liu, W. Zhang, W. Chen, Revolution of Sensors in Micro-Electromechanical Systems Related content Topical Review, *Jpn. J. Appl. Phys.* 51 (2012). <http://dx.doi.org/10.1143/JJAP.51.080001> (accessed May 4, 2020).
- [2] S.A. Wilson, R.P.J. Jourdain, Q. Zhang, R.A. Dorey, C.R. Bowen, M. Willander, Q.U. Wahab, M. Willander, S.M. Al-hilli, O. Nur, E. Quandt, C. Johansson, E. Pagounis, M. Kohl, J. Matovic, B. Samel, W. van der Wijngaart, E.W.H. Jager, D. Carlsson, Z. Djinovic, M. Wegener, C. Moldovan, E. Abad, M. Wendlandt, C. Rusu, K. Persson, New materials for micro-scale sensors and actuators. An engineering review, *Mater. Sci. Eng. R Reports*. 56 (2007) 1–129.
- [3] J. Ponmozhi, C. Frias, T. Marques, O. Frazão, Smart sensors/actuators for biomedical applications: Review, *Meas. J. Int. Meas. Confed.* 45 (2012) 1675–1688.
- [4] L. Weiss, Power production from phase change in MEMS and micro devices, a review, *Int. J. Therm. Sci.* 50 (2011) 639–647.
- [5] J.A. Krogstad, C. Keimel, K.J. Hemker, Emerging materials for microelectromechanical systems at elevated temperatures, *J. Mater. Res.* 29 (2014) 1597–1608.
- [6] R.A. Coutu, P.E. Kladitis, K.D. Leedy, R.L. Crane, Selecting metal alloy electric contact materials for MEMS switches, *J. Micromechanics Microengineering*. 14 (2004) 11116457-.
- [7] H.D. Espinosa, B.C. Prorok, M. Fischer, A methodology for determining mechanical properties of freestanding thin films and MEMS materials, *J. Mech. Phys. Solids*. 51 (2003) 47–67.
- [8] G.Z. Voyiadjis, M. Yaghoobi, *Size Effects in Plasticity: From Macro to Nano*, Elsevier, 2020. <https://doi.org/10.1016/C2016-0-03366-1>.
- [9] W.W. Mullins, The effect of thermal grooving on grain boundary motion, *Acta Metall.* 6 (1958) 414–427. [https://doi.org/10.1016/0001-6160\(58\)90020-8](https://doi.org/10.1016/0001-6160(58)90020-8).
- [10] M.A. Meyers, A. Mishra, D.J. Benson, Mechanical properties of nanocrystalline materials, *Prog. Mater. Sci.* 51 (2006) 427–556.
- [11] F. Ebrahimi, G.R. Bourne, M.S. Kelly, T.E. Matthews, Mechanical properties of nanocrystalline nickel produced by electrodeposition, *Nanostructured Mater.* 11 (1999) 343–350.
- [12] P.G. Sanders, J.A. Eastman, J.R. Weertman, Elastic and tensile behavior of nanocrystalline copper and palladium, *Acta Mater.* 45 (1997) 4019–4025.

- [13] G.W. Nieman, J.R. Weertman, R.W. Siegel, Mechanical behavior of nanocrystalline Cu and Pd, *J. Mater. Res.* 6 (1991) 1012–1027.
- [14] E.O. Hall, The deformation and ageing of mild steel: II Characteristics of the Lüders deformation, *Proc. Phys. Soc. Sect. B.* 64 (1951) 747–753.
- [15] N.J. Petch, The cleavage strength of polycrystals, *J. Iron Steel Inst.* 174 (1953) 25–28.
- [16] F. Momprou, M. Legros, A. Boé, M. Coulombier, J.P. Raskin, T. Pardoen, Inter- and intragranular plasticity mechanisms in ultrafine-grained Al thin films: An in situ TEM study, *Acta Mater.* 61 (2013) 205–216.
- [17] J.C.M. Li, Y.T. Chou, The role of dislocations in the flow stress grain size relationships, *Metall. Mater. Trans. B* 1970 15. 1 (1970) 1145–1159. <https://doi.org/10.1007/BF02900225>.
- [18] A.H. Cottrell, B.A. Bilby, Dislocation Theory of Yielding and Strain Ageing of Iron The Steady Non-Uniform State for a Liquid, *Proc. Phys. Soc. Sect. A.* 62 (1949) 49.
- [19] J.D. Eshelby, F.C. Frank, F.R.N. Nabarro, The equilibrium of linear arrays of dislocations., *Philos. Mag.* 42 (1951) 351–364. <https://doi.org/10.1080/14786445108561060>.
- [20] D.S. Gianola, S. Van Petegem, M. Legros, S. Brandstetter, H. Van Swygenhoven, K.J. Hemker, Stress-assisted discontinuous grain growth and its effect on the deformation behavior of nanocrystalline aluminum thin films, *Acta Mater.* 54 (2006) 2253–2263.
- [21] C.J. Youngdahl, P.G. Sanders, J.A. Eastman, J.R. Weertman, Compressive yield strengths of nanocrystalline Cu and Pd, *Scr. Mater.* 37 (1997) 809–813. [https://doi.org/10.1016/S1359-6462\(97\)00157-7](https://doi.org/10.1016/S1359-6462(97)00157-7).
- [22] J.R. Davis, *ASM specialty handbook: aluminum and aluminum alloys*, ASM International, Metals Park (OH), 1993.
- [23] A.H. Chokshi, A. Rosen, J. Karch, H. Gleiter, On the validity of the hall-petch relationship in nanocrystalline materials, *Scr. Metall.* 23 (1989) 1679–1683. [https://doi.org/10.1016/0036-9748\(89\)90342-6](https://doi.org/10.1016/0036-9748(89)90342-6).
- [24] T.G. Nieh, J. Wadsworth, Hall-Petch Relation in Nanocrystalline Solids, *Scr. Mater.* 25 (1991) 955–958.
- [25] M. Ke, S.A. Hackney, W.W. Milligan, E.C. Aifantis, Observation and measurement of grain rotation and plastic strain in nanostructured metal thin films, *Nanostructured Mater.* 5 (1995) 689–697. [https://doi.org/10.1016/0965-9773\(95\)00281-I](https://doi.org/10.1016/0965-9773(95)00281-I).
- [26] H. Conrad, Plastic deformation kinetics in nanocrystalline FCC metals based on the

pile-up of dislocations, *Nanotechnology*. 18 (2007) 325701.

- [27] H. Van Swygenhoven, P.M. Derlet, Grain-boundary sliding in nanocrystalline fcc metals, *Phys. Rev. B*. 64 (2001) 224105.
- [28] H. Van Swygenhoven, M. Spaczer, A. Caro, D. Farkas, Competing plastic deformation mechanisms in nanophase metals, *Phys. Rev. B*. 60 (1999) 22–25.
- [29] C.C. Koch, Optimization of strength and ductility in nanocrystalline and ultrafine grained metals, *Scr. Mater.* 49 (2003) 657–662. [https://doi.org/10.1016/S1359-6462\(03\)00394-4](https://doi.org/10.1016/S1359-6462(03)00394-4).
- [30] Y.M. Wang, E. Ma, Three strategies to achieve uniform tensile deformation in a nanostructured metal, *Acta Mater.* 52 (2004) 1699–1709.
- [31] A. Hasnaoui, H. Van Swygenhoven, P.M. Derlet, On non-equilibrium grain boundaries and their effect on thermal and mechanical behaviour: A molecular dynamics computer simulation, *Acta Mater.* 50 (2002) 3927–3939.
- [32] M.G. Stout, P.S. Follansbee, Strain Rate Sensitivity, Strain Hardening, and Yield Behavior of 304L Stainless Steel, *J. Eng. Mater. Technol.* 108 (1986) 344–353. http://asmedigitalcollection.asme.org/materialstechnology/article-pdf/108/4/344/5788775/344_1.pdf (accessed October 15, 2022).
- [33] J. May, H.W. Höppel, M. Göken, Strain rate sensitivity of ultrafine-grained aluminium processed by severe plastic deformation, *Scr. Mater.* 53 (2005) 189–194. <https://doi.org/10.1016/J.SCRIPTAMAT.2005.03.043>.
- [34] R.P. Carreker, W.R. Hibbard, Tensile deformation of high-purity copper as a function of temperature, strain rate, and grain size, *Acta Metall.* 1 (1953) 654–655. [https://doi.org/10.1016/0001-6160\(53\)90022-4](https://doi.org/10.1016/0001-6160(53)90022-4).
- [35] Q. Wei, S. Cheng, K.T. Ramesh, E. Ma, Effect of nanocrystalline and ultrafine grain sizes on the strain rate sensitivity and activation volume: fcc versus bcc metals, *Mater. Sci. Eng. A*. 381 (2004) 71–79. <https://doi.org/10.1016/J.MSEA.2004.03.064>.
- [36] G.T. Gray, T.C. Lowe, C.M. Cady, R.Z. Valiev, I. V. Aleksandrov, Influence of strain rate & temperature on the mechanical response of ultrafine-grained Cu, Ni, and Al-4Cu-0.5Zr, *Nanostructured Mater.* 9 (1997) 477–480. [https://doi.org/10.1016/S0965-9773\(97\)00104-9](https://doi.org/10.1016/S0965-9773(97)00104-9).
- [37] L. Lu, S.X. Li, K. Lu, An abnormal strain rate effect on tensile behavior in nanocrystalline copper, *Scr. Mater.* 45 (2001) 1163–1169. [https://doi.org/10.1016/S1359-6462\(01\)01138-1](https://doi.org/10.1016/S1359-6462(01)01138-1).
- [38] R. Schwaiger, B. Moser, M. Dao, N. Chollacoop, S. Suresh, Some critical experiments on the strain-rate sensitivity of nanocrystalline nickel, *Acta Mater.* 51

- (2003) 5159–5172. [https://doi.org/10.1016/S1359-6454\(03\)00365-3](https://doi.org/10.1016/S1359-6454(03)00365-3).
- [39] F.D. Torre, P. Spätig, R. Schäublin, M. Victoria, Deformation behaviour and microstructure of nanocrystalline electrodeposited and high pressure torsioned nickel, *Acta Mater.* 53 (2005) 2337–2349. <https://doi.org/10.1016/J.ACTAMAT.2005.01.041>.
 - [40] Y.M. Wang, A. V. Hamza, E. Ma, Temperature-dependent strain rate sensitivity and activation volume of nanocrystalline Ni, *Acta Mater.* 54 (2006) 2715–2726.
 - [41] H. Miyamoto, K. Ota, T. Mimaki, Viscous nature of deformation of ultra-fine grain aluminum processed by equal-channel angular pressing, *Scr. Mater.* 54 (2006) 1721–1725. <https://doi.org/10.1016/J.SCRIPTAMAT.2006.02.016>.
 - [42] E. Izadi, J. Rajagopalan, Texture dependent strain rate sensitivity of ultrafine-grained aluminum films, *Scr. Mater.* 114 (2016) 65–69. <https://doi.org/10.1016/J.SCRIPTAMAT.2015.12.003>.
 - [43] I. suk Choi, R. Schwaiger, L. Kurmanaeva, O. Kraft, On the effect of Ag content on the deformation behavior of ultrafine-grained Pd–Ag alloys, *Scr. Mater.* 61 (2009) 64–67. <https://doi.org/10.1016/J.SCRIPTAMAT.2009.03.007>.
 - [44] C. Duhamel, Y. Brechet, Y. Champion, Activation volume and deviation from Cottrell-Stokes law at small grain size, *Int. J. Plast.* 26 (2010) 747–757.
 - [45] E.W. Hart, Theory of the tensile test, *Acta Metall.* 15 (1967) 351–355. [https://doi.org/10.1016/0001-6160\(67\)90211-8](https://doi.org/10.1016/0001-6160(67)90211-8).
 - [46] J.W. Hutchinson, K.W. Neale, Influence of strain-rate sensitivity on necking under uniaxial tension, *Acta Metall.* 25 (1977) 839–846. [https://doi.org/10.1016/0001-6160\(77\)90168-7](https://doi.org/10.1016/0001-6160(77)90168-7).
 - [47] A.K. Ghosh, Tensile instability and necking in materials with strain hardening and strain-rate hardening, *Acta Metall.* 25 (1977) 1413–1424. [https://doi.org/10.1016/0001-6160\(77\)90072-4](https://doi.org/10.1016/0001-6160(77)90072-4).
 - [48] U.F. Kocks, H. Mecking, Physics and phenomenology of strain hardening: the FCC case, *Prog. Mater. Sci.* 48 (2003) 171–273. www.elsevier.com/locate/pmatsci (accessed October 22, 2022).
 - [49] F. Ebrahimi, Q. Zhai, D. Kong, Deformation and fracture of electrodeposited copper, *Scr. Mater.* 39 (1998) 315–321.
 - [50] N. Wang, Z. Wang, K.T. Aust, U. Erb, Room temperature creep behavior of nanocrystalline nickel produced by an electrodeposition technique, *Mater. Sci. Eng. A.* 237 (1997) 150–158. [https://doi.org/10.1016/S0921-5093\(97\)00124-X](https://doi.org/10.1016/S0921-5093(97)00124-X).
 - [51] R.Z. Valiev, I. V. Alexandrov, Y.T. Zhu, T.C. Lowe, Paradox of strength and

- ductility in metals processed by severe plastic deformation, *J. Mater. Res.* 17 (2002) 5–8. <https://doi.org/10.1557/JMR.2002.0002>.
- [52] Y.M. Wang, E. Ma, M.W. Chen, Enhanced tensile ductility and toughness in nanostructured Cu, *Appl. Phys. Lett.* 80 (2002) 2395.
 - [53] O. V. Mishin, V.Y. Gertsman, R.Z. Valiev, G. Gottstein, Grain boundary distributions, texture and mechanical properties of ultrafine-grained copper produced by severe plastic deformation, *Mater. Sci. Forum.* 235–238 (1997) 887–892.
 - [54] J.R. Weertman, D. Farkas, K. Hemker, H. Kung, M. Mayo, R. Mitra, H. Van Swygenhoven, Structure and Mechanical Behavior of Bulk Nanocrystalline Materials, *MRS Bull.* 1999 242. 24 (2013) 44–53. <https://link.springer.com/article/10.1557/S088376940005154X> (accessed October 22, 2022).
 - [55] N. Tsuji, Y. Ito, Y. Saito, Y. Minamino, Strength and ductility of ultrafine grained aluminum and iron produced by ARB and annealing, *Scr. Mater.* 47 (2002) 893–899.
 - [56] E. Bruder, Formability of Ultrafine Grained Metals Produced by Severe Plastic Deformation—An Overview, *Adv. Eng. Mater.* 21 (2019) 1800316.
 - [57] Y. Wang, M. Chen, F. Zhou, E. Ma, High tensile ductility in a nanostructured metal, *Nature.* 419 (2002) 912–915. <https://doi.org/10.1038/nature01133>.
 - [58] Y. Zhao, T. Topping, J.F. Bingert, J.J. Thornton, A.M. Dangelewicz, Y. Li, W. Liu, Y. Zhu, Y. Zhou, E.J. Lavernia, High tensile ductility and strength in bulk nanostructured nickel, *Adv. Mater.* 20 (2008) 3028–3033.
 - [59] G.J. Fan, H. Choo, P.K. Liaw, E.J. Lavernia, Plastic deformation and fracture of ultrafine-grained Al–Mg alloys with a bimodal grain size distribution, *Acta Mater.* 54 (2006) 1759–1766.
 - [60] M. Kawasaki, T.G. Langdon, Principles of superplasticity in ultrafine-grained materials, *J. Mater. Sci.* 42 (2007) 1782–1796.
 - [61] T. Watanabe, Grain boundary design and control for high temperature materials, *Mater. Sci. Eng. A.* 166 (1993) 11–28.
 - [62] T.G. Langdon, Grain boundary sliding revisited: Developments in sliding over four decades, *J. Mater. Sci.* 41 (2006) 597–609.
 - [63] M. Legros, D.S. Gianola, K.J. Hemker, In situ TEM observations of fast grain-boundary motion in stressed nanocrystalline aluminum films, *Acta Mater.* 56 (2008) 3380–3393.

- [64] E. Izadi, A. Darbal, R. Sarkar, J. Rajagopalan, Grain rotations in ultrafine-grained aluminum films studied using in situ TEM straining with automated crystal orientation mapping, *Mater. Des.* 113 (2017) 186–194.
- [65] H. Idrissi, A. Kobler, B. Amin-Ahmadi, M. Coulombier, M. Galceran, J.P. Raskin, S. Godet, C. Kübel, T. Pardoen, D. Schryvers, Plasticity mechanisms in ultrafine grained freestanding aluminum thin films revealed by in-situ transmission electron microscopy nanomechanical testing, *Appl. Phys. Lett.* 104 (2014) 081906.
- [66] A. Kobler, A. Kashiwar, H. Hahn, C. Kübel, Combination of in situ straining and ACOM TEM: A novel method for analysis of plastic deformation of nanocrystalline metals, *Ultramicroscopy*. 128 (2013) 68–81.
- [67] Y.B. Wang, B.Q. Li, M.L. Sui, S.X. Mao, Deformation-induced grain rotation and growth in nanocrystalline Ni, *Appl. Phys. Lett.* 92 (2008) 061921.
- [68] T.J. Rupert, D.S. Gianola, Y. Gan, K.J. Hemker, Experimental Observations of Stress-Driven Grain Boundary Migration, *Science*. 326 (2009) 1686–1690.
- [69] S. Cheng, J.A. Spencer, W.W. Milligan, Strength and tension/compression asymmetry in nanostructured and ultrafine-grain metals, *Acta Mater.* 51 (2003) 4505–4518.
- [70] K.S. Kumar, S. Suresh, M.F. Chisholm, J.A. Horton, P. Wang, Deformation of electrodeposited nanocrystalline nickel, *Acta Mater.* 51 (2003) 387–405.
- [71] V. Yamakov, D. Wolf, S.R. Phillpot, H. Gleiter, Deformation twinning in nanocrystalline Al by molecular-dynamics simulation, *Acta Mater.* 50 (2002) 5005–5020.
- [72] E. Hosseini, M. Legros, O.N. Pierron, Quantifying and observing viscoplasticity at the nanoscale: highly localized deformation mechanisms in ultrathin nanocrystalline gold films, *Nanoscale*. 8 (2016) 9234–9244.
- [73] L. Capolungo, D.E. Spearot, M. Cherkaoui, D.L. McDowell, J. Qu, K.I. Jacob, Dislocation nucleation from bicrystal interfaces and grain boundary ledges: Relationship to nanocrystalline deformation, *J. Mech. Phys. Solids*. 55 (2007) 2300–2327.
- [74] K. V. Ivanov, E. V. Naydenkin, Grain boundary sliding in ultrafine grained aluminum under tension at room temperature, *Scr. Mater.* 66 (2012) 511–514.
- [75] P. Kumar, M. Kawasaki, T.G. Langdon, Review: Overcoming the paradox of strength and ductility in ultrafine-grained materials at low temperatures, *J. Mater. Sci.* 51 (2016) 7–18.
- [76] R.J. Asaro, P. Krys, B. Kad, Deformation mechanism transitions in nanoscale fcc metals, *Philos. Mag. Lett.* 83 (2003) 733–743.

- [77] I.A. Ovid'ko, R.Z. Valiev, Y.T. Zhu, Review on superior strength and enhanced ductility of metallic nanomaterials, *Prog. Mater. Sci.* 94 (2018) 462–540.
- [78] M.Y. Gutkin, I.A. Ovid'ko, N. V. Skiba, Crossover from grain boundary sliding to rotational deformation in nanocrystalline materials, *Acta Mater.* 51 (2003) 4059–4071.
- [79] M. Jin, A.M. Minor, J.W. Morris, Strain-induced coarsening in nano-grained films, *Thin Solid Films.* 515 (2007) 3202–3207.
- [80] D. Caillard, J.L. Martin, *Thermally Activated Mechanisms in Crystal Plasticity*, Pergamon, 2003. [https://doi.org/10.1016/s1470-1804\(13\)60016-4](https://doi.org/10.1016/s1470-1804(13)60016-4).
- [81] D. Hull, D.J. Bacon, *Introduction to Dislocations*, 5th ed., Elsevier Ltd, 2001. <https://doi.org/10.1016/b978-0-08-096672-4.00001-3>.
- [82] S.H. Li, W.Z. Han, Z.W. Shan, Deformation of small-volume Al-4Cu alloy under electron beam irradiation, *Acta Mater.* 141 (2017) 183–192.
- [83] P. Spätig, J. Bonneville, J.L. Martin, A new method for activation volume measurements: application to Ni₃(Al,Hf), *Mater. Sci. Eng. A.* 167 (1993) 73–79.
- [84] Y.M. Wang, A. V Hamza, E. Ma, Activation volume and density of mobile dislocations in plastically deforming nanocrystalline Ni, *Appl. Phys. Lett.* 86 (2005). <https://doi.org/10.1063/1.1946899> (accessed May 12, 2020).
- [85] Y.M. Wang, E. Ma, On the origin of ultrahigh cryogenic strength of nanocrystalline metals, *Appl. Phys. Lett.* 85 (2004).
- [86] H. Conrad, Grain size dependence of the plastic deformation kinetics in Cu, *Mater. Sci. Eng. A.* 341 (2003) 216–228. [https://doi.org/10.1016/S0921-5093\(02\)00238-1](https://doi.org/10.1016/S0921-5093(02)00238-1).
- [87] R. Fritz, D. Wimler, A. Leitner, V. Maier-Kiener, D. Kiener, Dominating deformation mechanisms in ultrafine-grained chromium across length scales and temperatures, *Acta Mater.* 140 (2017) 176–187. <https://doi.org/10.1016/j.actamat.2017.08.043>.
- [88] N.J. Karanjgaokar, C.S. Oh, J. Lambros, I. Chasiotis, Inelastic deformation of nanocrystalline Au thin films as a function of temperature and strain rate, *Acta Mater.* 60 (2012) 5352–5361. <https://doi.org/10.1016/j.actamat.2012.06.018>.
- [89] K. Jonnalagadda, N. Karanjgaokar, I. Chasiotis, J. Chee, D. Peroulis, Strain rate sensitivity of nanocrystalline Au films at room temperature, *Acta Mater.* 58 (2010) 4674–4684. <https://doi.org/10.1016/j.actamat.2010.04.048>.
- [90] L. Lu, T. Zhu, Y. Shen, M. Dao, K. Lu, S. Suresh, Stress relaxation and the structure size-dependence of plastic deformation in nanotwinned copper, *Acta Mater.* 57 (2009) 5165–5173. <https://doi.org/10.1016/j.actamat.2009.07.018>.

- [91] K. Lu, L. Lu, S. Suresh, Strengthening materials by engineering coherent internal boundaries at the nanoscale, *Science* (80-.). 324 (2009) 349–352. <https://doi.org/10.1126/science.1159610>.
- [92] S. Gupta, S. Stangebye, K. Jungjohann, B. Boyce, T. Zhu, J. Kacher, O.N. Pierron, In situ TEM measurement of activation volume in ultrafine grained gold, *Nanoscale*. 12 (2020) 7146–7158.
- [93] S. Gupta, S. Stangebye, K. Jungjohann, B. Boyce, T. Zhu, J. Kacher, O.N. Pierron, Correction: In situ TEM measurement of activation volume in ultrafine grained gold, *Nanoscale*. 13 (2021) 9040. <https://doi.org/10.1039/d1nr90099d>.
- [94] D.S. Gianola, D.H. Warner, J.F. Molinari, K.J. Hemker, Increased strain rate sensitivity due to stress-coupled grain growth in nanocrystalline Al, *Scr. Mater.* 55 (2006) 649–652.
- [95] Y. Zhang, K. Ding, S. Stangebye, D. Chen, J. Kacher, O. Pierron, T. Zhu, Atomistic modeling of surface and grain boundary dislocation nucleation in FCC metals, *Acta Mater.* 237 (2022) 118155. <https://doi.org/10.1016/J.ACTAMAT.2022.118155>.
- [96] R.W. Armstrong, N. Balasubramanian, Unified Hall-Petch description of nano-grain nickel hardness, flow stress and strain rate sensitivity measurements, *AIP Adv.* 7 (2017). <https://doi.org/10.1063/1.4996294>.
- [97] J. Han, S.L. Thomas, D.J. Srolovitz, Grain-boundary kinetics: A unified approach, *Prog. Mater. Sci.* 98 (2018) 386–476.
- [98] H. Zhang, M.I. Mendelev, D.J. Srolovitz, Computer simulation of the elastically driven migration of a flat grain boundary, *Acta Mater.* 52 (2004) 2569–2576.
- [99] D.L. Olmsted, E.A. Holm, S.M. Foiles, Survey of computed grain boundary properties in face-centered cubic metals — II: Grain boundary mobility, *Acta Mater.* 57 (2009) 3704–3713. <http://dx.doi.org/10.1016/j.actamat.2009.04.015>.
- [100] A. Barrios, Y. Zhang, X. Maeder, G. Castelluccio, O. Pierron, T. Zhu, Abnormal grain growth in ultrafine grained Ni under high-cycle loading, *Scr. Mater.* 209 (2022) 114372. <https://doi.org/10.1016/j.scriptamat.2021.114372>.
- [101] P. Zhao, B. Chen, J. Kelleher, G. Yuan, B. Guan, X. Zhang, S. Tu, High-cycle-fatigue induced continuous grain growth in ultrafine-grained titanium, *Acta Mater.* 174 (2019) 29–42. <https://doi.org/10.1016/j.actamat.2019.05.038>.
- [102] O. Glushko, M.J. Cordill, The driving force governing room temperature grain coarsening in thin gold films, *Scr. Mater.* 130 (2017) 42–45. <https://doi.org/10.1016/J.SCRIPTAMAT.2016.11.012>.
- [103] M. Razeghi, *Fundamentals of Solid State Engineering*, 3rd ed., Springer Science & Business Media, 2009.

- [104] D. Porter, K. Easterling, M. Sherif, Phase Transformations in Metals and Alloys, 3rd ed., Taylor & Francis Group, LLC, 2009.
- [105] H. Grimmer, W. Bollmann, D.H. Warrington, Coincidence-site lattices and complete pattern-shift in cubic crystals, *Acta Crystallogr. Sect. A.* 30 (1974) 197–207.
- [106] H. Fukutomi, T. Kamijo, Grain boundary sliding-migration of aluminum $\langle 110 \rangle \Sigma 11 \{113\}$ symmetric tilt coincidence grain boundary and its interpretation based on the motion of perfect DSC dislocations, *Scr. Metall.* 19 (1985) 195–197.
- [107] T. Gorkaya, D.A. Molodov, G. Gottstein, Stress-driven migration of symmetrical $\langle 100 \rangle$ tilt grain boundaries in Al bicrystals, *Acta Mater.* 57 (2009) 5396–5405.
- [108] T. Gorkaya, K.D. Molodov, D.A. Molodov, G. Gottstein, Concurrent grain boundary motion and grain rotation under an applied stress, *Acta Mater.* 59 (2011) 5674–5680.
- [109] K.G.F. Janssens, D. Olmsted, E.A. Holm, S.M. Foiles, S.J. Plimpton, P.M. Derlet, Computing the mobility of grain boundaries, *Nat. Mater.* 5 (2006) 124–127.
- [110] D. V. Bachurin, D. Weygand, P. Gumbsch, Dislocation-grain boundary interaction in $\langle 111 \rangle$ textured thin metal films, *Acta Mater.* 58 (2010) 5232–5241.
- [111] W. Bollmann, General Geometrical Theory of Crystalline Interfaces, in: *Cryst. Defects Cryst. Interfaces*, Springer Berlin Heidelberg, Berlin, Heidelberg, 1970: pp. 143–185. https://doi.org/10.1007/978-3-642-49173-3_12.
- [112] M.F. Ashby, Boundary defects, and atomistic aspects of boundary sliding and diffusional creep, *Surf. Sci.* 31 (1972) 498–542. [https://doi.org/10.1016/0039-6028\(72\)90273-7](https://doi.org/10.1016/0039-6028(72)90273-7).
- [113] J.P. Hirth, R.W. Balluffi, On grain boundary dislocations and ledges, *Acta Metall.* 21 (1973) 929–942. [https://doi.org/10.1016/0001-6160\(73\)90150-8](https://doi.org/10.1016/0001-6160(73)90150-8).
- [114] C. Wei, S.L. Thomas, J. Han, D.J. Srolovitz, Y. Xiang, A Continuum Multi-Disconnection-Mode model for grain boundary migration, *J. Mech. Phys. Solids.* 133 (2019) 103731. <https://doi.org/10.1016/j.jmps.2019.103731>.
- [115] Q. Zhu, G. Cao, J. Wang, C. Deng, J. Li, Z. Zhang, S.X. Mao, In situ atomistic observation of disconnection-mediated grain boundary migration, *Nat. Commun.* 10 (2019) 156.
- [116] S. Miura, S. Hashimoto, T. Fujii, Effect of the triple junctions on grain-boundary sliding in Aluminum tricrystals, *J. Phys. Colloq.* (1988) C5-599-C5-604. <https://doi.org/10.1051/jphyscol:1988575i>.
- [117] S.L. Thomas, C. Wei, J. Han, Y. Xiang, D.J. Srolovitz, Disconnection description

- of triple-junction motion, *Proc. Natl. Acad. Sci. U. S. A.* 116 (2019) 8756–8765.
- [118] M. Upadhyay, L. Capolungo, V. Taupin, C. Fressengeas, Grain boundary and triple junction energies in crystalline media: A disclination based approach, *Int. J. Solids Struct.* 48 (2011) 3176–3193. <https://doi.org/10.1016/j.ijsolstr.2011.07.009>.
- [119] S. Kobayashi, S. Tsunekawa, T. Watanabe, A new approach to grain boundary engineering for nanocrystalline materials, *Beilstein J. Nanotechnol.* 7 (2016) 1829–1849.
- [120] G. Gottstein, L.S. Shvindlerman, B. Zhao, Thermodynamics and kinetics of grain boundary triple junctions in metals: Recent developments, *Scr. Mater.* 62 (2010) 914–917.
- [121] U. Czubyko, V.G. Sursaeva, G. Gottstein, L.S. Shvindlerman, Influence of triple junctions on grain boundary motion, *Acta Mater.* 46 (1998) 5863–5871.
- [122] M. Upmanyu, D.J. Srolovitz, L.S. Shvindlerman, G. Gottstein, Triple junction mobility: A molecular dynamics study, *Interface Sci.* 7 (1999) 307–319.
- [123] K.L. Merkle, L.J. Thompson, F. Phillipp, In-situ HREM studies of grain boundary migration, in: *Interface Sci.*, Springer, 2004: pp. 277–292. <https://link.springer.com/article/10.1023/B:INTS.0000028657.72527.5b> (accessed September 23, 2020).
- [124] S.J. Zinkle, G.S. Was, Materials challenges in nuclear energy, *Acta Mater.* 61 (2013) 735–758. <https://doi.org/10.1016/J.ACTAMAT.2012.11.004>.
- [125] S.J. Zinkle, J.T. Busby, Structural materials for fission & fusion energy, *Mater. Today*. 12 (2009) 12–19. [https://doi.org/10.1016/S1369-7021\(09\)70294-9](https://doi.org/10.1016/S1369-7021(09)70294-9).
- [126] O. Malinkiewicz, M. Imaizumi, S.B. Sapkota, T. Ohshima, S. Öz, Radiation effects on the performance of flexible perovskite solar cells for space applications, *Emergent Mater.* 3 (2020).
- [127] N. Khiara, F. Onimus, S. Jublot-Leclerc, T. Jourdan, T. Pardoën, J.P. Raskin, Y. Bréchet, In-situ TEM irradiation creep experiment revealing radiation induced dislocation glide in pure copper, *Acta Mater.* 216 (2021) 117096. <https://doi.org/10.1016/J.ACTAMAT.2021.117096>.
- [128] M. Wurmshuber, D. Frazer, M. Balooch, I. Issa, A. Bachmaier, P. Hosemann, D. Kiener, The effect of grain size on bubble formation and evolution in helium-irradiated Cu-Fe-Ag, *Mater. Charact.* 171 (2021) 110822. <https://doi.org/10.1016/J.MATCHAR.2020.110822>.
- [129] C. Zheng, E.R. Reese, K.G. Field, T. Liu, E.A. Marquis, S.A. Maloy, D. Kaoumi, Microstructure response of ferritic/martensitic steel HT9 after neutron irradiation: Effect of temperature, *J. Nucl. Mater.* 528 (2020) 151845.

<https://doi.org/10.1016/J.JNUCMAT.2019.151845>.

- [130] J.E. Pawel, A.F. Rowcliffe, D.J. Alexander, M.L. Grossbeck, K. Shiba, Effects of low temperature neutron irradiation on deformation behavior of austenitic stainless steels, *J. Nucl. Mater.* 233–237 (1996) 202–206. [https://doi.org/10.1016/S0022-3115\(96\)00218-8](https://doi.org/10.1016/S0022-3115(96)00218-8).
- [131] A. Reichardt, A. Lupinacci, D. Frazer, N. Bailey, H. Vo, C. Howard, Z. Jiao, A.M. Minor, P. Chou, P. Hosemann, Nanoindentation and in situ microcompression in different dose regimes of proton beam irradiated 304 SS, *J. Nucl. Mater.* 486 (2017) 323–331. <https://doi.org/10.1016/J.JNUCMAT.2017.01.036>.
- [132] Y. Matsukawa, M. Briceno, I.M. Robertson, Combining in situ transmission electron microscopy and molecular dynamics computer simulations to reveal the interaction mechanisms of dislocations with stacking-fault tetrahedron in nuclear materials, *Microsc. Res. Tech.* 72 (2009) 284–292. <https://pubmed.ncbi.nlm.nih.gov/19189314/> (accessed May 18, 2022).
- [133] J. Kacher, G.S. Liu, I.M. Robertson, In situ and tomographic observations of defect free channel formation in ion irradiated stainless steels, *Micron*. 43 (2012) 1099–1107. <https://doi.org/10.1016/J.MICRON.2012.01.017>.
- [134] D. Kiener, P. Hosemann, S.A. Maloy, A.M. Minor, In situ nanocompression testing of irradiated copper, *Nat. Mater.* 10 (2011) 608–613. <https://doi.org/10.1038/NMAT3055>.
- [135] F. Tan, F. Li, Q. Fang, J. Li, H. Feng, Grain boundary migration and deformation mechanism influenced by heterogeneous precipitate, *J. Mater. Sci.* 56 (2021) 9458–9469. <https://doi.org/10.1007/S10853-021-05843-Z/FIGURES/9>.
- [136] E.H. Lee, T.S. Byun, J.D. Hunn, M.H. Yoo, K. Farrell, L.K. Mansur, On the origin of deformation microstructures in austenitic stainless steel: part I—microstructures, *Acta Mater.* 49 (2001) 3269–3276. [https://doi.org/10.1016/S1359-6454\(01\)00193-8](https://doi.org/10.1016/S1359-6454(01)00193-8).
- [137] A. Alsabbagh, R.Z. Valiev, K.L. Murty, Influence of grain size on radiation effects in a low carbon steel, *J. Nucl. Mater.* 443 (2013) 302–310. <https://doi.org/10.1016/J.JNUCMAT.2013.07.049>.
- [138] G.M. Cheng, W.Z. Xu, Y.Q. Wang, A. Misra, Y.T. Zhu, Grain size effect on radiation tolerance of nanocrystalline Mo, *Scr. Mater.* 123 (2016) 90–94. <https://doi.org/10.1016/J.SCRIPTAMAT.2016.06.007>.
- [139] N.A. Enikeev, V.K. Shamardin, B. Radiguet, Radiation Tolerance of Ultrafine-Grained Materials Fabricated by Severe Plastic Deformation, *Mater. Trans.* 60 (2019) 1723–1731. <https://doi.org/10.2320/MATERTRANS.MF201931>.
- [140] X. Zhang, K. Hattar, Y. Chen, L. Shao, J. Li, C. Sun, K. Yu, N. Li, M.L. Taheri, H.

- Wang, J. Wang, M. Nastasi, Radiation damage in nanostructured materials, *Prog. Mater. Sci.* 96 (2018) 217–321. <https://doi.org/10.1016/J.PMATSCI.2018.03.002>.
- [141] M. Rose, A.G. Balogh, H. Hahn, Instability of irradiation induced defects in nanostructured materials, *Nucl. Instruments Methods Phys. Res. Sect. B Beam Interact. with Mater. Atoms.* 127–128 (1997) 119–122. [https://doi.org/10.1016/S0168-583X\(96\)00863-4](https://doi.org/10.1016/S0168-583X(96)00863-4).
- [142] N. Nita, R. Schaeublin, M. Victoria, R.Z. Valiev, Effects of irradiation on the microstructure and mechanical properties of nanostructured materials, *Philos. Mag.* 85 (2006) 723–735. <https://doi.org/10.1080/14786430412331319965>.
- [143] B.N. Singh, A.J.E. Foreman, Calculated grain size-dependent vacancy supersaturation and its effect on void formation, *Philos. Mag.* 29 (1974) 847–858. <https://doi.org/10.1080/14786437408222075>.
- [144] M. Samaras, P.M. Derlet, H. Van Swygenhoven, M. Victoria, Radiation damage near grain boundaries, *Philos. Mag.* 83 (2003) 3599–3607. <https://doi.org/10.1080/14786430310001600222>.
- [145] X.M. Bai, A.F. Voter, R.G. Hoagland, M. Nastasi, B.P. Uberuaga, Efficient annealing of radiation damage near grain boundaries via interstitial emission, *Science* (80-.). 327 (2010) 1631–1634. https://doi.org/10.1126/SCIENCE.1183723/SUPPL_FILE/BAI.SOM.PDF.
- [146] O. El-Atwani, E. Martinez, E. Esquivel, M. Efe, C. Taylor, Y.Q. Wang, B.P. Uberuaga, S.A. Maloy, Does sink efficiency unequivocally characterize how grain boundaries impact radiation damage?, *Phys. Rev. Mater.* 2 (2018) 113604. <https://doi.org/10.1103/PhysRevMaterials.2.113604>.
- [147] H.A. Atwater, C. V. Thompson, H.I. Smith, Ion-bombardment-enhanced grain growth in germanium, silicon, and gold thin films, *J. Appl. Phys.* 64 (1998) 2337. <https://doi.org/10.1063/1.341665>.
- [148] D.C. Bufford, F.F. Abdeljawad, S.M. Foiles, K. Hattar, Unraveling irradiation induced grain growth with in situ transmission electron microscopy and coordinated modeling, *Appl. Phys. Lett.* 107 (2015) 191901. <https://doi.org/10.1063/1.4935238>.
- [149] K. Sugio, Y. Shimomura, T.D. De La Rubia, Computer Simulation of Displacement Damage Cascade Formation near Sigma 5 Twist Boundary in Silver, *J. Phys. Soc. Japan.* 67 (1998) 882–889. <https://doi.org/10.1143/JPSJ.67.882>.
- [150] M. Samaras, P.M. Derlet, H. Van Swygenhoven, M. Victoria, Atomic scale modelling of the primary damage state of irradiated fcc and bcc nanocrystalline metals, *J. Nucl. Mater.* 351 (2006) 47–55. <https://doi.org/10.1016/J.JNUCMAT.2006.02.030>.
- [151] K.Y. Yu, D. Bufford, C. Sun, Y. Liu, H. Wang, M.A. Kirk, M. Li, X. Zhang,

Removal of stacking-fault tetrahedra by twin boundaries in nanotwinned metals, *Nat. Commun.* 4 (2013) 1377. <https://doi.org/10.1038/ncomms2382>.

- [152] V. Borovikov, X.-Z. Tang, D. Perez, X.-M. Bai, B.P. Uberuaga, A.F. Voter, Coupled motion of grain boundaries in bcc tungsten as a possible radiation-damage healing mechanism under fusion reactor conditions, *Nucl. Fusion.* 53 (2013) 063001. <https://doi.org/10.1088/0029-5515/53/6/063001>.
- [153] L. Zhang, C. Lu, K. Tieu, Y. Shibuta, Dynamic interaction between grain boundary and stacking fault tetrahedron, *Scr. Mater.* 144 (2018) 78–83. <https://doi.org/10.1016/J.SCRIPTAMAT.2017.09.027>.
- [154] L. Zhang, Y. Shibuta, C. Lu, X. Huang, Interaction between nano-voids and migrating grain boundary by molecular dynamics simulation, *Acta Mater.* 173 (2019) 206–224. <https://doi.org/10.1016/J.ACTAMAT.2019.05.020>.
- [155] L. Yang, H.L. Zhou, H. Liu, F. Gao, X.T. Zu, S.M. Peng, X.G. Long, X.S. Zhou, Dynamics of defect-loaded grain boundary under shear deformation in alpha iron, *Model. Simulations Mater. Sci. Eng.* 26 (2018) 025006. <https://doi.org/10.1088/1361-651X/aa9aca>.
- [156] S. Gupta, O.N. Pierron, MEMS based nanomechanical testing method with independent electronic sensing of stress and strain, *Extrem. Mech. Lett.* 8 (2016) 167–176.
- [157] S. Gupta, O.N. Pierron, A MEMS Tensile Testing Technique for Measuring True Activation Volume and Effective Stress in Nanocrystalline Ultrathin Microbeams, *Microelectromechanical Syst.* 26 (2017) 1082–1092.
- [158] E. Hosseini, S. Gupta, O.N. Pierron, M. Legros, Size effects on intergranular crack growth mechanisms in ultrathin nanocrystalline gold free-standing films, *Acta Mater.* 143 (2018) 77–87.
- [159] S. Gupta, Characterization of Plastic Deformation Mechanisms in Ultrafine Grained FCC Metals Using MEMS Based Nanomechanical Testing Methods, Georgia Institute of Technology, 2019.
- [160] R.E. Stoller, M.B. Toloczko, G.S. Was, A.G. Certain, S. Dwaraknath, F.A. Garner, On the use of SRIM for computing radiation damage exposure, *Nucl. Instruments Methods Phys. Res. Sect. B.* 310 (2013) 75–80. <https://doi.org/10.1016/J.NIMB.2013.05.008>.
- [161] K. Nordlund, A.E. Sand, F. Granberg, S.J. Zinkle, R. Stoller, R.S. Averback, T. Suzudo, L. Malerba, F. Banhart, W.J. Weber, F. Willaime, S. Dudarev, D. Simeone, *Primary Radiation Damage in Materials*, 2015.
- [162] D.B. Williams, C.B. Carter, *Transmission Electron Microscopy*, 2nd ed., Springer Science & Business Media, 2009.

- [163] R.F. Egerton, R. McLeod, F. Wang, M. Malac, Basic questions related to electron-induced sputtering in the TEM, *Ultramicroscopy*. 110 (2010) 991–997.
- [164] E.A. Kenik, T.E. Mitchell, Orientation dependence of the threshold displacement energy in copper and vanadium, *Philos. Mag.* 32 (1975) 815–831.
- [165] N. Braidy, Z.J. Jakubek, B. Simard, G.A. Botton, Quantitative energy dispersive X-ray microanalysis of electron beam-sensitive alloyed nanoparticles, *Microsc. Microanal.* 14 (2008) 166–175.
- [166] C.M. Wang, D.R. Baer, J.E. Amonette, M.H. Engelhard, J.J. Antony, Y. Qiang, Electron beam-induced thickening of the protective oxide layer around Fe nanoparticles, *Ultramicroscopy*. 108 (2007) 43–51.
- [167] B. Muntifering, R. Dingreville, K. Hattar, J. Qu, Electron beam effects during in-situ annealing of self-ion irradiated nanocrystalline nickel, *Mater. Res. Soc. Symp. Proc.* 1809 (2015) 13–18.
- [168] S.Y. Lee, K.R. Park, S. gyu Kang, J.H. Lee, E. chae Jeon, C.H. Shim, J.P. Ahn, D.I. Kim, H.N. Han, Y.C. Joo, C. Kim, I.S. Choi, Selective crack suppression during deformation in metal films on polymer substrates using electron beam irradiation, *Nat. Commun.* 10 (2019) 4454.
- [169] M. Jin, A.M. Minor, E.A. Stach, J.W. Morris Jr., Direct observation of deformation-induced grain growth during nanoindentation of ultrafine-grained Al at room temperature, *Acta Mater.* 52 (2004) 5381–5387.
- [170] W. Kang, M.T.A. Saif, A novel method for in situ uniaxial tests at the micro/nano scalepart I: Theory, *J. Microelectromechanical Syst.* 19 (2010) 1309–1321.
- [171] J.R. Welty, G.L. Rorrer, D.G. Foster, *Fundamentals of Momentum, Heat, and Mass Transfer*, 6th ed., John Wiley & Sons, Inc., 2013.
- [172] I. Jenčič, M.W. Bench, I.M. Robertson, M.A. Kirk, Electron-beam-induced crystallization of isolated amorphous regions in Si, Ge, GaP, and GaAs, *J. Appl. Phys.* 78 (1995) 974–982.
- [173] K. Maeda, S. Takeuchi, Enhancement of Dislocation Mobility in Semiconducting Crystals by Electronic Excitation, in: *Dislocations in Solids*, 1996: pp. 445–500. <https://doi.org/10.1525/9780520959743-054>.
- [174] R. Sarkar, C. Rentenberger, J. Rajagopalan, Electron beam induced artifacts during in situ TEM deformation of nanostructured metals, *Sci. Rep.* 5 (2015) 16345.
- [175] M. Gaumé, P. Baldo, F. Mompiau, F. Onimus, In-situ observation of an irradiation creep deformation mechanism in zirconium alloys, *Scr. Mater.* 154 (2018) 87–91. <https://doi.org/10.1016/j.scriptamat.2018.05.030>.

- [176] S. Stangebye, Y. Zhang, S. Gupta, E. Hosseini, F. Yu, C. Barr, K. Hattar, O.N. Pierron, T. Zhu, J. Kacher, Grain growth of nanocrystalline aluminum under tensile deformation: a combined in situ TEM and atomistic study, *Materialia*. 16 (2021) 101068.
- [177] H.G.F. Wilsdorf, The ductile fracture of metals: A microstructural viewpoint, *Mater. Sci. Eng.* 59 (1983) 1–39.
- [178] H.G.F. Wilsdorf, The role of glide and twinning in the final separation of ruptured gold crystals, *Acta Metall.* 30 (1982) 1247–1258.
- [179] K. Hattar, J. Han, M.T.A. Saif, I.M. Robertson, In situ transmission electron microscopy observations of toughening mechanisms in ultra-fine grained columnar aluminum thin films, *J. Mater. Res.* 20 (2005) 1869–1877. <https://doi.org/10.1557/JMR.2005.0233>.
- [180] K. Zhang, J.R. Weertman, J.A. Eastman, Rapid stress-driven grain coarsening in nanocrystalline Cu at ambient and cryogenic temperatures, *Appl. Phys. Lett.* 87 (2005) 061921.
- [181] M. He, S. Samudrala, G. Kim, P. Felfer, A. Breen, J. Cairney, D. Gianola, Linking stress-driven microstructural evolution in nanocrystalline aluminium with grain boundary doping of oxygen, *Nat. Commun.* 7 (2016) 11225.
- [182] T.A. Furnish, B.L. Boyce, J.A. Sharon, C.J. O'Brien, B.G. Clark, C.L. Arrington, J.R. Pillars, Fatigue stress concentration and notch sensitivity in nanocrystalline metals, *J. Mater. Res.* 31 (2016) 740–752.
- [183] X.-M. Luo, X.-F. Zhu, G.-P. Zhang, Nanotwin-assisted grain growth in nanocrystalline gold films under cyclic loading, *Nat. Commun.* 5 (2014). <https://doi.org/10.1038/ncomms4021>.
- [184] S. Chu, P. Liu, Y. Zhang, X. Wang, S. Song, T. Zhu, Z. Zhang, X. Han, B. Sun, M. Chen, In situ atomic-scale observation of dislocation climb and grain boundary evolution in nanostructured metal, *Nat. Commun.* 13 (2022) 4151. <https://doi.org/10.1038/s41467-022-31800-8>.
- [185] J.X. Hou, X.Y. Li, K. Lu, Orientation dependence of mechanically induced grain boundary migration in nano-grained copper, *J. Mater. Sci. Technol.* 68 (2021) 30–34. <https://doi.org/10.1016/j.jmst.2020.08.018>.
- [186] P.F. Rottmann, K.J. Hemker, Experimental quantification of mechanically induced boundary migration in nanocrystalline copper films, *Acta Mater.* 140 (2017) 46–55.
- [187] E.Y. Chen, P. Hamilton, B.L. Boyce, R. Dingreville, The heterogeneous nature of mechanically accelerated grain growth, *J. Mater. Sci.* (2022). <https://doi.org/10.1007/S10853-022-07974-3>.

- [188] S.E. Babcock, R.W. Balluffi, Grain boundary kinetics-II. In situ observations of the role of grain boundary dislocations in high-angle boundary migration, *Acta Metall.* 37 (1989) 2367–2376. [https://doi.org/10.1016/0001-6160\(89\)90034-5](https://doi.org/10.1016/0001-6160(89)90034-5).
- [189] J.M. Zhang, K.W. Xu, V. Ji, Dependence of strain energy on the grain orientations in an FCC-polycrystalline film on rigid substrate, *Appl. Surf. Sci.* 185 (2002) 177–182. [https://doi.org/10.1016/S0169-4332\(01\)00586-4](https://doi.org/10.1016/S0169-4332(01)00586-4).
- [190] J. Zhang, W. Ludwig, Y. Zhang, H.H.B. Sørensen, D.J. Rowenhorst, A. Yamanaka, P.W. Voorhees, H.F. Poulsen, Grain boundary mobilities in polycrystals, *Acta Mater.* 191 (2020) 211–220. <https://doi.org/10.1016/J.ACTAMAT.2020.03.044>.
- [191] M.L. Jenkins, Z. Zhou, S.L. Dudarev, A.P. Sutton, M.A. Kirk, Electron microscope weak-beam imaging of stacking fault tetrahedra: Observations and simulations, *J. Mater. Sci.* 41 (2006) 4445–4453. <https://doi.org/10.1007/S10853-006-0089-5/FIGURES/13>.
- [192] D. Kaoumi, V. Jammot, Insights into the plastic behavior of irradiated Ni-based alloy through in-situ TEM experiments: Formation and evolution of defect-free channels, *J. Nucl. Mater.* 523 (2019) 33–42. <https://doi.org/10.1016/J.JNUCMAT.2019.05.037>.
- [193] M. Xu, K. Chen, F. Cao, L. Velasco, T.M. Kaufman, F. Ye, H. Hahn, J. Han, D.J. Srolovitz, X. Pan, Disconnection-mediated Twin/Twin-junction migration in FCC metals, *Acta Mater.* 240 (2022) 118339. <https://doi.org/10.1016/J.ACTAMAT.2022.118339>.
- [194] L. Zhang, J. Han, D.J. Srolovitz, Y. Xiang, Equation of motion for grain boundaries in polycrystals, *Npj Comput. Mater.* 7 (2021) 1–8. <https://doi.org/10.1038/s41524-021-00532-6>.
- [195] O. Glushko, G. Dehm, Initiation and stagnation of room temperature grain coarsening in cyclically strained gold films, *Acta Mater.* 169 (2019) 99–108. <https://doi.org/10.1016/J.ACTAMAT.2019.03.004>.
- [196] F.J. Humphreys, M. Hatherly, *Recrystallization and Related Annealing Phenomena*, Elsevier, (2004). https://books.google.com/books?hl=en&lr=&id=Kt1lV4m2bqEC&oi=fnd&pg=PP1&ots=RrzQRmhoyB&sig=X_xTEz7beacbjgMh_v8ACh8X2v8#v=onepage&q&f=false (accessed November 4, 2022).
- [197] T. Zhu, J. Li, A. Samanta, A. Leach, K. Gall, Temperature and strain-rate dependence of surface dislocation nucleation, *Phys. Rev. Lett.* 100 (2008) 025502.
- [198] Y. Zhang, I.P. Fulfillment, *Mechanics of Heterogeneous Metallic Materials*, Georgia Institute of Technology, 2021.
- [199] T. Zhu, J. Li, A. Samanta, H.G. Kim, S. Suresh, Interfacial plasticity governs strain

- rate sensitivity and ductility in nanostructured metals, *Proc. Natl. Acad. Sci.* 104 (2007) 3031–3036. <https://doi.org/10.1073/PNAS.0611097104>.
- [200] T. Zhu, J. Li, S. Yip, Atomistic Reaction Pathway Sampling: The Nudge Elastic Band Method and Nanomechanics Applications, in: *Nano Cell Mech. Fundam. Front.*, 2013: pp. 313–338.
- [201] F.R.N. Nabarro, Cottrell-stokes law and activation theory, *Acta Metall. Mater.* 38 (1990) 161–164. [https://doi.org/10.1016/0956-7151\(90\)90044-H](https://doi.org/10.1016/0956-7151(90)90044-H).
- [202] D.S. Gianola, B.G. Mendis, X.M. Cheng, K.J. Hemker, Grain-size stabilization by impurities and effect on stress-coupled grain growth in nanocrystalline Al thin films, *Mater. Sci. Eng. A.* 483–484 (2008) 637–640. <https://doi.org/10.1016/j.msea.2006.12.155>.